Searching for the Light Supersymmetric Top Quark with the ATLAS Experiment

Anna Thuy Trang Phan

Submitted in total fulfilment of the requirements
of the degree of Doctor of Philosophy

March 2011

School of Physics
The University of Melbourne

Abstract

The nature of dark matter and the source of the matter-antimatter asymmetry in the universe are two of the most important questions in particle physics and cosmology. The current Standard Model of particle physics, while being a very successful description of the observed fundamental particles and their interactions, cannot fully account for either of these phenomena. Theoretical extensions of the Standard Model, however, possibly can. One such extension is the Minimal Supersymmetric Standard Model (MSSM).

This thesis begins by exploring the MSSM parameter space in which the matter-antimatter asymmetry of the universe is dynamically generated through electroweak baryogenesis. In this scenario, one of the supersymmetric partners to the top quark, the light stop quark, must be lighter than the top quark. It is found that this parameter space region is highly constrained by experimental limits on the electric dipole moment of the electron and the branching ratio of a bottom quark into a strange quark and a photon. If the additional requirement of matching the observed dark matter abundance by the relic density of the lightest supersymmetry particle is necessitated, the allowed MSSM parameter space is further constrained.

The focus of the thesis then moves to the investigation of the collider phenomenology of supersymmetric electroweak baryogenesis, in particular, the evaluation of the discovery potential of light stop quark pair production at the LHC using the ATLAS experiment. This study assumes a light stop decay topology involving the lightest chargino and neutralino where the visible final state products mimic those from top quark pair production. Feasibility studies are performed for proton-proton collisions at $\sqrt{s} = 10$ TeV and an integrated luminosity of 1 fb^{-1}, concentrating on the dileptonic and semileptonic decay channels where there are two or one charged leptons in the final state. It is found that signal points with stop masses $\lesssim 120$ GeV and stop-neutralino mass differences $\gtrsim 60$ GeV have the greatest discovery potential in the dileptonic decay channel, while the semileptonic decay channel is swamped by backgrounds and requires detailed understanding of the detector and backgrounds in order to extract a signal. Finally, a preliminary study is conducted on 41.4 pb^{-1} of data collected at collisions at $\sqrt{s} = 7$ TeV in the dielectron decay channel, focusing on the understanding of selection variables and backgrounds.

Declaration

This is to certify that

1. this thesis comprises only my original work towards the PhD except where indicated in the Preface,
2. due acknowledgement has been made in the text to all other material used,
3. the thesis is less than 100,000 words in length, exclusive of tables, bibliographies and appendices.

Anna Thuy Trang Phan

Preface

Achieving the goals of modern experimental particle physics requires a large group of scientists who collaborate closely together. ATLAS is one of the largest collaborative efforts ever attempted in the physical sciences. In such a collaboration it is rare that an individual performs any substantial body of work in isolation. The standard procedure is to work within groups that are assigned specific roles in the collaboration. The work presented in this thesis was undertaken within various ATLAS working groups.

The exception to this is the work presented in Chapter 3, which was performed outside the ATLAS collaboration and is the complete work of the author with theoretical guidance from C. Balazs, C.E.M. Wagner and M.S. Carena.

The work in the first part of Chapter 5 is a review of the relevant sections in Reference [78]. This work is presented in order to set the scene for the results in Section 5.3 which is the sole work of the author. This work was performed within the ATLAS e/γ trigger working group.

The work in Chapters 6 to 10 was executed within the ATLAS supersymmetry working group and the results are the complete work of the author except for the work in Chapter 8, which is a modified version of an ATLAS internal physics note [153] which the author coauthored with P. Urquijo.

The work in the first part of Appendix B is a modified version of the relevant sections in Reference [78] which the author had direct involvement in producing. This work is presented to set the scene for the results in Section B.3 which is the sole work of the author. This work was performed within the ATLAS missing transverse energy working group.

Acknowledgements

If I have seen further it is only by standing on the shoulders of giants. – Isaac Newton

This work would not have been possible without the help, support and love of many different people. This makes it impossible to thank every person for their individual contribution.

First and foremost, I wish to express my deepest gratitude to my supervisor, Elisabetta Barberio, for her invaluable support, guidance, encouragement and patience. Thank you for nurturing the researcher within me and making me the scientist I am today. I would also like to thank my other Melbourne based supervisors, Geoff Taylor and Stuart Wyithe for their advice over the years.

I would like to acknowledge the other people in the Melbourne experimental particle physics group, who I have worked with and who have helped me in various software and physics matters: Tim Dyce, Tom Fifield, Martin White, Tony Limosani, Anthony Morley, Nadia Davidson, Will Davey, David Peake, Tony Shao and David Jennens. Special thanks to Vivien Lee, Stefanie Leong and T'Mir Julius for help in printing and binding this thesis. I also have to thank the members of the Sydney high energy physics group who have had to put up with me in the Australian apartment, especially Jason Lee, Anthony Waugh, Nikhul Patel and Aldo Saavedra.

Moving now across the world, I am greatly indebted to my overseas supervisor Allan Clark. Thank you for welcoming, accepting and treating me as one of your own students. My gratitude also goes to the other people in the Geneva nuclear and particle physics group for their help in software and physics issues: Szymon Gadomski, Xin Wu, Andrew Hamilton, Sergei Gonzalez Sevilla, Till Eifert, Andree Robichaud-Veronneau, Moritz Backes, Clemencia Mora Herrera, Valerio Dao, Francesca Bucci, Elina Berglund and Antonella Succurro. I am particularly indebted to Phillip Urquijo, without whom this thesis would have been greatly diminished. I also want to acknowledge Olivier Lombard for all his help with the required Swiss administration and my Vernier flatmates Agustina Bayley, Andry Rahaniraka and Nicole Vontobel for being my family away from home.

I thank all my collaborators in the ATLAS experiment. Having worked in multiple working groups, I have had the opportunity to collaborate with many different people, too numerous to mention here. Special thanks go to Donatella Cavalli, Naoko Kanaya and Iacopo Vivarelli from the missing transverse energy group, Monika Wielers, Denis Damazio and Bertrand Laforge from the electron and calorimeter trigger groups and Giacomo Polesello, Tommaso Lari, Paul de Jong and George Redlinger from the supersymmetry group.

I am deeply obliged to my theorist collaborators who have enlightened me on everything light stop related: Csaba Balazs, Marcela Carena and Carlos Wagner. I also want to thank Nicholas Setzer who was willing to answer all my supersymmetry questions, no matter how basic and Kalliopi Petraki for proofreading my theory chapters.

I am also very grateful to my family and friends, who have had a great influence over me and have helped me fully realise my ambitions. And last but certainly not least, I would like to thank William Tran for all his sacrifices, support and encouragement despite the many periods of separation. Words can't even begin to express my gratitude to you.

To my family, for their love and support.

Table of Contents

List of Tables

List of Figures

The worthwhile problems are the ones you can really solve or help solve,
the ones you can really contribute something to.

– Richard Feynman

1

Introduction

When the universe is observed, the most easily studied objects are planets, stars and interstellar gas, which are made up of protons, neutrons and electrons. The amount of these particles is known as the baryon content of the universe. However, it has been established that approximately 73% of the energy density of the universe is in a form of matter with negative pressure, perhaps a cosmological constant, and another 23% is in the form of some non-baryonic matter, referred to as dark matter. The observed baryons make up a mere 4% of the total energy density of the universe.

Another striking observation is that the 4% of baryonic matter in the universe is almost entirely devoid of any antibaryonic matter. There is a cosmological excess of matter over antimatter which is at odds with the theoretical symmetry between them. This symmetry suggest that should exist astronomically large regions of antimatter, which is not what is observed.

The Standard Model of particle physics, while being a very successful description of the observed fundamental particles and their interactions, does not explain either of these observations and hence a new, more complete theory is required. Many theoretical extensions of the Standard Model have been suggested, however, they typically address only one of these problems.

One popular extension of the Standard Model is Supersymmetry, in which a new symmetry between bosons and fermions is introduced. This symmetry leads to new particles, not yet observed. With the introduction of a new conservation law, the lightest supersymmetric particle is stable and a candidate for dark matter. In addition, this model can be constructed to explain the generation of observed matter-antimatter asymmetry via electroweak baryogenesis. An important consequence of this scenario is that one of the supersymmetric partners to the top quark, the light stop quark, must be lighter than the top quark. Chapter 2 provides an introduction to the Standard Model, Supersymmetry and electroweak baryogenesis, laying the foundations for Chapter 3 which probes the bounds of the supersymmetric electroweak baryogenesis parameter space, otherwise known as the light stop scenario.

The ATLAS experiment at the Large Hadron Collider (LHC) is designed to look for the Higgs boson and search for new physics beyond the Standard Model, such as Supersymmetry. The LHC is a proton-proton collider designed to provide centre of mass energies of up to 14 TeV[1] to recreate the conditions of the universe down to 10^{-34} seconds after the Big Bang. A basic description of the LHC and the ATLAS detector is given in Chapter 4 while Chapter 5 is dedicated to the ATLAS electron trigger system for which the author developed an alternative algorithm for seeding electromagnetic clusters.

If supersymmetry exists at energy scales compatible with the LHC, supersymmetric particles will be produced, and studied. In particular, light stop decays are a prime candidate for early supersymmetry searches at the LHC, due to their high production cross section and clean event topologies. The remainder of this thesis, from Chapter 6 to Chapter 10, is dedicated to analysing light stop quark pair production at the ATLAS experiment in the scenario where the detectable light stop quark decay products mimic those from top quark pair production.

---

[1] Natural units for physics quantities are the convention in particle physics and this thesis. The reduced Planck constant, speed of light and Boltzmann constant are normalised to unity, $\hbar = c = k_B = 1$. Energy, momentum and mass are expressed in electron volts (eV).

Tapestries are made by many artisans working together. The contributions of separate workers cannot be discerned in the completed work, and the loose and false threads have been covered over. So it is in our picture of particle physics.

– Sheldon Lee Glashow

2

Background Theory

Particle physics is the quest to understand the fundamental nature of matter. The Standard Model is a theoretical framework that explains many of the currently existing observations of fundamental particles and forces. However, there are specific problems with the theory leading to the belief that it is only an effective theory, unable to describe physics at arbitrarily high energies. Theories that extend the Standard Model, such as Supersymmetry, may provide solutions to these problems and establish a more complete description of matter. This chapter presents a brief overview of the Standard Model and its limitations, followed by an outline of Supersymmetry and how it resolves some of the shortcomings of the Standard Model.

2.1. Standard Model

The Standard Model (SM) [1, 2, 3] provides the best known description of fundamental particles and their interactions, excluding gravity. It has made many successful predictions [4] and has been experimentally probed to very high precision. The SM is a gauge quantum field theory which describes the interaction of point-like fermions, whose interactions are mediated by gauge bosons.

2.1.1. Matter

The particles that constitute matter have spin-$\frac{1}{2}$ and can be divided into two categories: those that feel the strong force; quarks, and those that do not; leptons. In total there are six known quarks and six known leptons, whose properties are shown in Table 2.1.

The six quark types or flavours, are arranged into three distinct families, also known as generations. The first generation is comprised of the up quark, and the slightly heavier down quark. These have fractional electric charges of $+\frac{2}{3}$ and $-\frac{1}{3}$ respectively. The two following generations are successively more massive and likewise consist of a doublet of an up-type and a down-type quark. The second generation consists of the whimsically named charm and strange quarks, while the third generation includes the prosaically named top and bottom quarks. Free quarks have never been observed directly, they are confined inside composite systems known as hadrons. The most commonplace hadrons are the proton and the neutron, three-quark systems made up of the lightest two quarks, up and down.

The six leptons are similarly classified into three generations. The first generation consists of the familiar electron-type leptons, while the subsequent generations consist of the heavier muon-type and tau-type leptons. Each lepton generation consists of a doublet of a charged lepton and its corresponding neutral neutrino. In the SM, neutrinos are considered massless, however observations of neutrino flavour oscillations from solar [5], atmospheric [6], reactor [7] and long-baseline accelerator experiments [8] have shown that neutrinos must have some small mass.

Table 2.1. The fermions of the Standard Model with their electric charges and masses [4].

Leptons			Quarks		
Flavour	Electric Charge	Mass (GeV)	Flavour	Electric Charge	Approximate Mass (GeV)
e	-1	5.11×10^{-4}	u	2/3	0.002
ν_e	0	$< 2 \times 10^{-9}$	d	-1/3	0.005
μ	-1	0.1057	c	2/3	1.3
ν_μ	0	$< 1.9 \times 10^{-4}$	s	-1/3	0.1
τ	-1	1.7768	t	2/3	172
ν_τ	0	$< 1.82 \times 10^{-2}$	b	-1/3	4.2

2.1.2. Forces

The SM describes the electromagnetic, weak and strong forces as the exchange of vector bosons between the fermions. The type of exchanged boson determines the type of interaction. The electromagnetic force is mediated by the massless photon, the strong force is mediated by eight massless coloured gluons, and the weak force is mediated by the massive $W^{\pm}$ and Z bosons. These forces couple to electric charge, colour and weak isospin, respectively. Table 2.2 shows the vector bosons and their properties.

The fourth fundamental force, gravity, is conspicuously absent from the SM. In principle gravitational interactions could also be described in terms of the exchange of a graviton gauge boson, however attempts to create a satisfactory quantum field theory of gravity and incorporate this into the SM have so far failed. Fortunately, for most purposes in experimental particle physics, gravity can be neglected as it is much weaker than the other forces at the energy scales being probed.

The Electromagnetic Force

With the exception of gravity, electromagnetism is probably the most familiar force in everyday life. The quantum field theory of electromagnetism, quantum electrodynamics (QED), is the oldest, simplest and most successful of the dynamical theories that were eventually brought together to form the SM; all the other theories are modelled on it.

Table 2.2. The bosons of the Standard Model with their electric charges and masses [4].

Force	Particle	Electric Charge	Mass (GeV)
Strong	g	0	0
Electromagnetic	γ	0	0
Weak	$W^{\pm}$	±1	80.399
	Z	0	91.1876

QED is an abelian gauge field theory with the symmetry group $U(1)_Q$ which describes the interaction between charged fermions and the massless photon. The QED Lagrangian is:

$$\mathcal{L}_{\text{QED}} = \bar{\psi}_q(i\gamma^{\mu}\not{D}_{\text{QED},\mu} - m_q)\psi_q - \frac{1}{4}F_{\mu\nu}F^{\mu\nu},$$

where a fermion field of mass m_q and charge q is represented as ψ_q and the field is given by $F_{\mu\nu}$. To maintain local $U(1)_Q$ gauge invariance, the covariant derivative $\not{D}_{\text{QED},\mu}$ requires the introduction of the photon gauge field, A_{μ}:

$$\not{D}_{\text{QED},\mu} = \partial_{\mu} + iQA_{\mu},$$

where Q is the generator of the $U(1)_Q$ group and can be identified with e, electric charge. The electromagnetic field in $\mathcal{L}_{\text{QED}}$ is expressed in terms of the photon field:

$$F_{\mu\nu} = \partial_{\mu}A_{\nu} - \partial_{\nu}A_{\mu}.$$

The abelian structure of $U(1)_Q$ does not allow any self-interaction terms for the photon field.

The Strong Force

Quantum chromodynamics (QCD) describes all phenomena related to strongly interacting particles, quarks and gluons. It can be constructed in full analogy to QED, but with the important difference that the local gauge group, $SU(3)_C$ is larger and non-abelian. Similarly to the QED Lagrangian, the QCD Lagrangian is:

$$\mathcal{L}_{\text{QCD}} = \sum_{n} \bar{\psi}^{a}_{n}(i\gamma^{\mu}\not{D}_{\text{QCD},\mu} - m_n)\psi^{a}_{n} - \frac{1}{4}G^{\alpha}_{\mu\nu}G^{\mu\nu}_{\alpha},$$

where the gluon field is given by $G^{\alpha}_{\mu\nu}$ where α=(1,2,3,4,5,6,7,8) and a quark field of mass m_n represented as ψ^{a}_{n}. The flavour assignment is labelled by the index n, which takes on six values: n=(u,d,c,s,t,b). The colour charge is labelled by a=(1,2,3). The quarks and antiquarks are identified with the **3** and **3*** representations of $SU(3)$ while the gluons are assigned to the **8** fundamental representation. Note that the gluon field does not have a flavour index and so QCD has an approximate flavour symmetry, which is broken by the differing quark masses. To maintain local $SU(3)_C$ gauge invariance, the covariant derivative, $\not{D}_{\mathrm{QCD},\mu}$ requires the introduction of the gluon gauge field A^{α}_{μ}:

$$\not{D}_{\mathrm{QCD},\mu} = \partial_{\mu} + ig_s A^{\alpha}_{\mu}\lambda_{\alpha},$$

where λ_{α} are the $SU(3)_C$ group generators. The commutator of the generators is proportional to the antisymmetric structure constant of $SU(3)_C$, $f^{\alpha\beta\gamma} = f_{\alpha\beta\gamma} = f^{\gamma}_{\alpha\beta}$:

$$[\lambda_{\alpha}, \lambda_{\beta}] = if^{\gamma}_{\alpha\beta}\lambda_{\gamma}.$$

The non-abelian nature of this commutation relationship allows for the self-interaction of gluon fields. The gluon field in $\mathcal{L}_{\mathrm{QCD}}$ differs to the electromagnetic field in that is not just expressed in terms of the gluon gauge field, but also the $SU(3)_C$ structure constant and the coupling constant of quarks and gluons g_s:

$$G^{\alpha}_{\mu\nu} = \partial_{\mu}A^{\alpha}_{\nu} - \partial_{\nu}A^{\alpha}_{\mu} - g_s f^{\alpha}_{\beta\gamma}A^{\beta}_{\mu}A^{\gamma}_{\nu}.$$

An essential feature dictating the phenomenology of QCD is that the coupling constant g_s decreases as the renormalisation scale μ increases:

$$\mu\frac{\partial g_s(\mu)}{\partial\mu} = -\left(11 - \frac{2n_f}{3}\right)\frac{g_s(\mu)^3}{16\pi^2} + \mathcal{O}(g_s(\mu)^5),$$

where n_f is the number of flavours at or below the renormalisation scale μ. This feature of QCD, that the coupling strength decreases at large μ or short distances, is known as asymptotic freedom. This results in non-perturbative effects at distances of size $\mathcal{O}(1/\Lambda_{\mathrm{QCD}})$, where Λ_{QCD} is generated in the solution to the above differential equation:

$$\alpha_s(\mu) \equiv \frac{g_s^2(\mu)}{4\pi} = \frac{4\pi}{\beta_0 \ln[\mu^2/\Lambda^2_{\mathrm{QCD}}]} + \mathcal{O}\left(\frac{1}{\ln[\mu^2/\Lambda^2_{\mathrm{QCD}}]^2}\right), \quad \text{where } \beta_0 = 11 - 2\frac{n_f}{3}.$$

The scale of Λ_{QCD} is where the theory becomes strongly coupled and perturbation theory fails to be valid.

The final distinction between QCD and QED is that whilst free particles with net electric charge are observed in nature, no particles with net colour have ever been observed. Coloured particles are confined to colourless bound states leading to the phenomenon of quark confinement, whereby isolated quarks are never observed. Confinement has important consequences for the phenomenology of collider signatures where quarks or gluons are produced, resulting in the production of collimated jets of hadrons in the final state.

The Weak Force and Electroweak Unification

The third force described by the SM is weak force, responsible for, among other processes, nuclear beta decay. Like QED and QCD, the theory of the weak force is arrived at by the requirement that the appropriate Lagrangian remain locally gauge invariant. In this case it is required that the Lagrangian describing the interactions of left handed fermion doublets is invariant under $SU(2)_L$ transformations in the vector space of weak isospin, I.

The SM describes the electromagnetic and weak interactions as two different aspects of a unified electroweak interaction [9, 10, 11] with the gauge group $SU(2)_L \otimes U(1)_Y$ where the gauge group $U(1)_Y$ of weak hypercharge Y is defined by $Q = Y + I_3$ where Q is the electric charge and I_3 is the third component of weak isospin. The free field electroweak Lagrangian before symmetry breaking is:

$$\mathcal{L}_{\mathrm{EW},f} = \sum_f \bar{\psi}_f i\gamma^\mu \not{D}_{\mathrm{EW},\mu}\psi_f,$$

where the ψ_f are the chiral matter fields:

$$L_L^n = \begin{pmatrix} \nu_L^n \\ e_L^n \end{pmatrix}, e_R^n, \qquad Q_L^n = \begin{pmatrix} u_L^n \\ d_L^n \end{pmatrix}, u_R^n, d_R^n, \tag{2.1}$$

where the index n, runs from 1 to 3 and represents the three generations of the SM matter fields. u_L^n, d_L^n, u_R^n, d_R^n are the quark fields, and e_L^n, ν_L^n, e_R^n are the lepton fields. Note that there are no ν_R^n terms as right handed neutrinos are not seen in nature. To maintain $SU(2)_L \otimes U(1)_Y$ gauge invariance, the electroweak gauge invariant covariant derivative $\not{D}_{\mathrm{EW},\mu}$ requires the introduction of the B_μ and W_u^i gauge fields:

$$\not{D}_{\mathrm{EW},\mu} = \partial_\mu + ig\frac{Y}{2}B_\mu + ig'\frac{\tau_L^i}{2}W_\mu^i,$$

where g and g' are coupling constants and τ_L^i are the Pauli matrices, the generators of the $SU(2)_L$ group. The non-abelian nature of the Pauli matrices allows for the the self-interaction of W^i fields. The electroweak gauge fields $W_\mu^\pm$, Z_μ and A_μ are linear combinations of these four fields:

$$W_\mu^\pm = \frac{1}{\sqrt{2}}\left(W_\mu^1 \pm iW_\mu^2\right) \quad \text{and} \quad \begin{aligned} Z_\mu &= \cos\theta_W W_\mu^3 - \sin\theta_W B_\mu \\ A_\mu &= \sin\theta_W W_\mu^3 - \cos\theta_W B_\mu \end{aligned} \quad \text{where} \quad \theta_W = \cot\left(\frac{g'}{g}\right).$$

2.1.3. Mass

The theories of the strong and electroweak interactions can be combined into a single Lagrangian which is invariant under $SU(3)_C \times SU(2)_L \times U(1)_Y$ transformations. However, such a theory is missing a crucial piece. The $W^{\pm}$ and Z bosons, unlike photons and gluons, are massive. Inserting mass terms into the Lagrangian breaks the gauge invariance of the theory, leads to divergences and thus a non-renormalisable theory [12]. Therefore to obtain a successful predictive theory, the SM Lagrangian should be constructed in such a way that mass terms are included yet local gauge invariance is retained. The simplest approach that offers a solution is the Higgs mechanism [13].

The Higgs mechanism involves the generation of mass terms through the spontaneous breaking of the electroweak symmetry by the introduction of a complex scalar field ϕ which transforms as a doublet under $SU(2)_L$ with non-zero vacuum expectation value ϕ_0 to the Lagrangian:

$$\mathcal{L}_{\text{Higgs}} = (\partial_\mu \phi)^\dagger (\partial^\mu \phi) - \mu^2 \phi^\dagger \phi - \lambda (\phi^\dagger \phi)^2,$$

where $\phi = \frac{1}{\sqrt{2}} \begin{pmatrix} \phi_1 + i\phi_2 \\ \phi_3 + i\phi_4 \end{pmatrix}$ and $\phi_0 = \frac{1}{\sqrt{2}} \begin{pmatrix} 0 \\ v \end{pmatrix}$, where $v^2 = \frac{-\mu^2}{\lambda}$ and $\mu^2 < 0$.

Replacing ∂_μ in $\mathcal{L}_{\text{Higgs}}$ with the electroweak covariant derivative $\not{D}_{\text{EW},\mu}$ for gauge invariance means that when ϕ gets an expectation value, that is after electroweak symmetry breaking, the Lagrangian contains extra terms, including weak gauge boson mass terms, from which it can be calculated that:

$$m_{W^{\pm}} = \frac{1}{2} v g' \quad , \quad m_Z = \frac{v}{2} \sqrt{g^2 + g'^2} \quad , \quad m_\gamma = 0 \quad \text{and} \quad \cos\theta_W = \frac{m_W}{m_Z}.$$

Note that the complex scalar field ϕ contains four degrees of freedom, only three of which can be gauged away to give masses to the weak gauge bosons, the remaining degree of freedom is a massive scalar particle, the elusive Higgs boson, H.

The Higgs mechanism also provides a formalism for fermion masses. The non-zero vacuum expectation value of the system results in the vacuum everywhere gaining the ability to emit or absorb neutral colourless Higgs bosons that carry isospin. Therefore fermions, which can couple to this new boson, acquire mass through Yukawa couplings, $g^{i,j}_{e,u,d}$:

$$\mathcal{L}_{\text{Yukawa}} = -g_e^{i,j}\bar{L}_e^i\phi e_R^j - g_d^{i,j}\bar{Q}_L^i\phi d_R^j - g_u^{i,j}\bar{Q}_L^i\phi u_R^j + \text{Hermitian conjugate},$$

where the repeated indices i, j run over the three generations and are summed. These couplings induce a set of 3×3 matrices for the quarks and leptons where the weak gauge eigenstates are linear combinations of the mass eigenstates. This leads to interactions mediated by the $W^{\pm}$ bosons which change quark flavour and charged leptons into their corresponding neutrinos and vice versa. The mixing matrix acting on the charged $-\frac{1}{3}$ quarks is the Cabibbo-Kobayashi-Maskawa (CKM) matrix [14, 15].

The Higgs mechanism predicts a new scalar particle, the Higgs boson which has yet to be discovered and thus the SM remains incomplete. One of the experimental difficulties of the Higgs boson search is that the Higgs mechanism does not directly predict the Higgs boson mass, m_H. However, a direct constraint arises from considering the $W^+W^- \rightarrow W^+W^-$ elastic scattering process. To keep the cross section of this process finite, the Higgs mass must be less than ~1 TeV [16]. Other experimental measurements can also place constraints on m_H. Direct searches for the Higgs boson at LEP gave a lower limit of 114.4 GeV at 95% confidence level (CL) [17] while the Tevatron excludes a Higgs mass region between 158 GeV and 175 GeV also at 95% CL [18]. Indirect bounds are obtained through the use of fits to precision electroweak measurements. These fits currently derive an upper of 185 GeV at 95% CL [19]. These limits suggest that if the Higgs boson does exist, it should be found at the LHC.

The Higgs mechanism is not without its shortcomings. The SM predicts that the Higgs boson is affected by large radiative corrections to its mass from loop interactions with fermions and bosons. These loop corrections yield the following contributions to m_H:

$$\delta m_H^2 = \frac{\lambda_s^2}{16\pi^2}[\Lambda^2 - 2m_s^2\ln(\frac{\Lambda}{m_s}) + \ldots] - \frac{|\lambda_f|^2}{16\pi^2}[2\Lambda^2 + 6m_f^2\ln(\frac{\Lambda}{m_f}) + \ldots], \qquad (2.2)$$

where the first term defines the correction due to scalars of mass m_s and Higgs coupling λ_s and the second term is the equivalent for fermions of mass m_f and Higgs coupling λ_f, and where Λ is the energy cutoff scale to which the theory is valid. If the SM is valid up the Plank scale, then $\Lambda \equiv \Lambda_{\text{Planck}} \sim 10^{19}$ GeV. This leads to extremely large corrections to the Higgs mass, such that fine tuning of parameters is required to some thirty orders of magnitude to keep the Higgs boson light as required by unitarity. This is considered unnatural, and is known as the fine tuning problem.

There are other reasons to believe that the SM is incomplete. Connected to the fine tuning problem is the hierarchy problem, which is the question why the Planck scale is so much larger than the electroweak scale. The SM also does not explain why there are three generations of fermions or contain a mechanism for the generation of neutrino masses; it also does not predict particle masses or the elements of the CKM mixing matrix or the values of any of the coupling constants.

Aside from these particle physics problems, the SM also has no explanation for the astrophysical observations of dark matter or the baryon asymmetry of the universe, which some theories beyond the SM can address.

2.2. Supersymmetry

Supersymmetry (SUSY) [20, 21] is a proposed extension to the SM which postulates the existence of a new kind of fundamental symmetry between bosons and fermions. Since the Lagrangian is required to be invariant under this symmetry transformation, every fermonic degree of freedom needs a corresponding bosonic degree of freedom and vice versa. These new degrees of freedom correspond to the existence of new particles, the superpartners or sparticles, placing the observed particles in supermuliplets with the new postulated superpartners.

SUSY is a unique extension of Poincaré algebra and possesses many desirable features, including providing an elegant solution to the fine tuning problem, being a stepping stone towards the unification of the electroweak and strong forces and a theoretical framework for a quantum theory of gravity. Additionally, SUSY offers the possibility of generating the observed baryon asymmetry of the universe and provides an answer to the dark matter puzzle, which this thesis explores in detail.

That SUSY offers a solution to the fine tuning problem is evident upon inspection of Equation 2.2, where it can be seen that the fermonic and scalar terms provide similar but opposite sign corrections. The nature of the SUSY generators requires the introduction of an additional complex scalar for each SM fermion and an additional fermion for every scalar. As long as the SUSY energy scale is around 1 TeV, the correction terms from the additional SUSY particles will largely cancel the divergent corrections from the SM particles.

An interesting implication of SUSY is its natural consequence of grand unification. The gauge coupling strengths of the SM forces vary with the energy scale of interactions, and it is anticipated that they may become equal at a some grand unification scale. The evolution of the gauge coupling strengths with energy scale is dependent on the particles in the theory and it turns out that the inclusion of SUSY particles with masses at the electroweak scale possibly leads to grand unification. While grand unification is not a motivation for SUSY, it is a pleasant side effect.

By demanding gauge invariance under local supersymmetric transformations, a spin-2 massless gauge field is introduced to the theory, which can be identified as the graviton. This particle and its supersymmetric partner, the gravitino, mediate gravitational interactions, through which a quantum theory of gravity can be obtained. Unfortunately, however tantalising this supergravity theory is, like other four-dimensional theories of gravity, it is not renormalisable.

Despite these promising features, SUSY cannot be the final theory of particle phenomena. Like the SM, it does not resolve the hierarchy problem, explain why there are three generations of fermions or neutrino masses and it does not predict particle masses and mixing angles. Instead, as will be seen, it introduces many new parameters.

2.2.1. Supersymmetry Particle Spectrum

The phenomenology of the SUSY particles is derived from the fact that particles in the same supermultiplet must be in the same representation of the gauge groups, and so must have the same electric charge, weak isospin, and colour degrees of freedom. Each supermultiplet must also contain an equal number of fermion and boson degrees of freedom. The simplest possible set of multiplets is called the Minimal Supersymmetric Standard Model (MSSM). The MSSM incorporates the SM fermions into chiral supermultiplets along with a further complex scalar, and the SM gauge bosons into vector supermultiplets along with an additional fermion. The naming convention gives superpartners of fermions an 's' in front of their SM name, and are known as sfermions. For example, the partner of the top quark is called the 'stop' quark. Superpartners of bosons receive an 'ino' at the end of their names, the Higgs bosons have 'higgsino' partners, and the superpartners of the gauge bosons are called 'gauginos'. Table 2.3 summarises the sparticle content of the MSSM.

Table 2.3. The undiscovered particles of in the MSSM (assuming sfermion mixing for the first two families is negligible) [21].

Name	Spin	Gauge Eigenstates	Mass Eigenstates
Higgs bosons	0	$H_u^0\ H_d^0\ H_u^+\ H_d^-$	$h^0\ A^0\ H^0\ H^\pm$
squarks	0	$\tilde{u}_L\ \tilde{u}_R\ \tilde{d}_L\ \tilde{d}_R$ $\tilde{c}_L\ \tilde{c}_R\ \tilde{s}_L\ \tilde{s}_R$ $\tilde{t}_L\ \tilde{t}_R\ \tilde{b}_L\ \tilde{b}_R$	same same $\tilde{t}_1\ \tilde{t}_2\ \tilde{b}_1\ \tilde{b}_2$
sleptons	0	$\tilde{e}_L\ \tilde{e}_R\ \tilde{\nu}_e$ $\tilde{\mu}_L\ \tilde{\mu}_R\ \tilde{\nu}_\mu$ $\tilde{\tau}_L\ \tilde{\tau}_R\ \tilde{\nu}_\tau$	same same $\tilde{\tau}_1\ \tilde{\tau}_2\ \tilde{\nu}_\tau$
neutralinos	$\frac{1}{2}$	$\tilde{B}^0\ \tilde{W}^0\ \tilde{H}_u^0\ \tilde{H}_d^0$	$\tilde{\chi}_1^0\ \tilde{\chi}_2^0\ \tilde{\chi}_3^0\ \tilde{\chi}_4^0$
charginos	$\frac{1}{2}$	$\tilde{W}^\pm\ \tilde{H}_u^+\ \tilde{H}_d^-$	$\tilde{\chi}_1^\pm\ \tilde{\chi}_2^\pm$
gluino	$\frac{1}{2}$	$\tilde{g}$	same

In the SM only one Higgs scalar field is required to give mass to all the fermions and weak gauge bosons. The SM Higgs field is a doublet, which has four degrees of freedom, three of which are absorbed in electroweak symmetry breaking, resulting in just one Higgs boson. However, in the MSSM in order to give mass to all the sparticles, the SM Higgs sector must be extended into two Higgs doublets, comprised of four complex scalar fields with eight degrees of freedom. Three of these are absorbed in electroweak symmetry breaking, and the remainder manifest as five physical Higgs bosons, three neutral, h^0, A^0, H^0, and two charged H^+ and H^-. These Higgs fields are then classified into chiral supermultiplets with a total of four fermionic superpartners.

The MSSM also contains more particle mixing than the SM. Except for the gluino, gauginos and higgsinos have the same quantum numbers, and will therefore mix to form the physical particles. The neutral higgsinos and the neutral gauginos form the four neutralinos χ_i^0 (i=1,2,3,4), and the charged higgsinos and the wino form the charginos $\chi_i^\pm$ (i=1,2). For the sfermions, since chiral fermions have two degrees of freedom, there will be two spinless superpartners for each SM fermion, which are sometimes loosely referred to as left handed and right handed sfermions, although they have no standard handedness or chirality. Since these two sfermions have identical quantum numbers, they will mix to form the physical particles. The mixing depends on the mass of the SM fermion, and the third generation sfermions will mix most. For example, the stop quark mixing matrix, $\mathcal{M}^2_{\tilde{t}}$, is given by [22]:

$$\mathcal{M}^2_{\tilde{t}} = \begin{pmatrix} m^2_{LL} & (m^2_{LR})^* \\ m^2_{LR} & m^2_{RR} \end{pmatrix} \quad \text{where} \quad \begin{aligned} m^2_{LL} &= m^2_{\tilde{Q}_3} + m^2_Z \cos 2\beta\,(\tfrac{1}{2} - \tfrac{2}{3}\sin^2\theta_W) + m^2_t \\ m^2_{RR} &= m^2_{\tilde{U}_3} + \tfrac{2}{3} m^2_Z \cos 2\beta\, \sin^2\theta_W + m^2_t \\ m^2_{LR} &= m_t(A_t - \mu^* \cot\beta) \end{aligned} \tag{2.3}$$

and m_t is the mass of the top quark, m_Z is the mass of the Z boson, θ_W is the weak mixing angle and $m^2_{\tilde{Q}_3}$, $m^2_{\tilde{U}_3}$, μ, A_t and β are SUSY parameters which will be described later. Note that the parameters μ and A_t can take complex values:

$$A_t = |A_t|\,\mathrm{e}^{\mathrm{i}\phi_{A_t}} \quad \text{and} \quad \mu = |\mu|\,\mathrm{e}^{\mathrm{i}\phi_\mu}$$

leading to the off-diagonal elements, $m^2_{LR} = (m^2_{LR})^*$, also being complex with the phase:

$$\phi_{\tilde{t}} = \arg(m^2_{LR}) = \arg(A_t - \mu^* \cot\beta).$$

The mixing matrix, $\mathcal{M}^2_{\tilde{t}}$, can be diagonalised and the physical stop quarks $\tilde{t}_1$ and $\tilde{t}_2$ are given by:

$$\begin{pmatrix} \tilde{t}_1 \\ \tilde{t}_2 \end{pmatrix} = \begin{pmatrix} \mathrm{e}^{\mathrm{i}\phi_{\tilde{t}}}\cos\theta_{\tilde{t}} & \sin\theta_{\tilde{t}} \\ -\sin\theta_{\tilde{t}} & \mathrm{e}^{-\mathrm{i}\phi_{\tilde{t}}}\cos\theta_{\tilde{t}} \end{pmatrix} \begin{pmatrix} \tilde{t}_L \\ \tilde{t}_R \end{pmatrix},$$

where $\tilde{t}_1$ is the lighter stop quark and $\tilde{t}_2$ is the heavier one, and $\theta_{\tilde{t}}$ is the stop quark mixing angle. The masses are given by:

$$m^2_{\tilde{t}_{1,2}} = \frac{1}{2}\left(m^2_{LL} + m^2_{RR} \mp \sqrt{(m^2_{LL} - m^2_{RR})^2 + 4|m_{LR}|^2}\right),$$

while the mixing angle is given by:

$$\tan\theta_{\tilde{t}} = \frac{m^2_{LL} - m^2_{\tilde{t}_1}}{-|m^2_{LR}|}.$$

Note that if $m_{LL} < m_{RR}$ then $\tilde{t}_1$ has a predominantly left handed gauge character, otherwise if $m_{LL} > m_{RR}$ then $\tilde{t}_1$ has a predominantly right handed gauge character.

2.2.2. Supersymmetry Parameters

If SUSY was realised in nature as an unbroken symmetry then the superpartner particles would have identical mass to their SM counterparts. This is evidently not the case, as such particles would be trivial to observe. Therefore, if it exists, SUSY must be a broken symmetry.

The SUSY breaking is implemented by including explicit 'soft' mass terms to the MSSM Lagrangian $\mathcal{L}_{\text{MSSM}}$. These terms are called soft because they do not reintroduce the quadratic divergences removed by introducing SUSY. The MSSM Lagrangian then becomes:

$$\mathcal{L}_{\text{MSSM}} = \mathcal{L}_{\text{SUSY}} + \mathcal{L}_{\text{soft}},$$

where $\mathcal{L}_{\text{SUSY}}$ contains the terms invariant under SUSY transforms and $\mathcal{L}_{\text{soft}}$ contains the SUSY breaking parameters.

The parameters of $\mathcal{L}_{\text{SUSY}}$ consist of [4]:

- gauge couplings: g_1, g_2 and g_3 corresponding to the SM gauge group $SU(3)_C \times SU(2)_L \times U(1)_Y$ respectively.
- a higgsino mass parameter: μ.
- Higgs-fermion Yukawa coupling constants: λ_{u_i}, λ_{d_i} and λ_{e_i} (i=1,2,3) corresponding to the coupling of the left and right handed quarks and leptons and their superpartners to the Higgs bosons and higginos.

The parameters of $\mathcal{L}_{\text{soft}}$ consist of [4]:

- gaugino masses: M_3, M_2 and M_1 associated with the $SU(3)_C$, $SU(2)_L$ and $U(1)_Y$ subgroups of the SM.
- five scalar squared-mass parameters for the squarks and sleptons: $m^2_{\tilde{Q}_i}$, $m^2_{\tilde{U}_i}$, $m^2_{\tilde{D}_i}$, $m^2_{\tilde{L}_i}$, $m^2_{\tilde{E}_i}$ (i=1,2,3) corresponding the superpartners of the five electroweak gauge multiplets (Equation 2.1).
- Higgs-squark-squark and Higgs-slepton-slepton trilinear interaction terms, with coefficients $\lambda_{u_i}A_{u_i}$, $\lambda_{d_i}A_{d_i}$ and $\lambda_{e_i}A_{e_i}$ (i=1,2,3). It is traditional to factor out the Yukawa couplings in the definition of the trilinear couplings, so if the trilinear

couplings are of the same order compared to the other soft mass terms, only the trilinear couplings of the third generation are phenomenologically relevant.

- three parameters relating to the Higgs: the vacuum expectation values of the two Higgs fields: v_u and v_d where the more commonly used $\tan\beta$ is the ratio between them, and one physical Higgs mass: the later analysis will use the mass of the charged Higgs, $m_{H^\pm}$, though the mass of the pseudoscalar Higgs, m_{A^0} is more commonly used.

It is obvious that the total number of independent physical parameters that define the MSSM is quite large, particularly those associated with the SUSY breaking sector; in fact, the MSSM possesses 124 independent parameters [23]. To allow for the practical study of the MSSM, the number of parameters which are considered must be reduced. This can be done by assuming a mechanism of SUSY breaking, such as minimal SuperGravity (mSUGRA) [24], the most well studied model where SUSY is broken by gravitational interactions. Alternatively, restrictions on the MSSM parameter space can be made using phenomenologically motivated arguments, which is the approach that this thesis pursues.

2.2.3. *R*-Parity

The most general form of the MSSM includes gauge invariant terms that violate both baryon number (B) and lepton number (L), allowing for B and L violating processes. These processes must be very suppressed in order to reproduce experimental data, with the strongest constraint being the lifetime of the proton, τ_p experimentally measured to be $\tau_p > 1.6\times10^{33}$ years at 90% CL [25]. These terms cannot simply be forbidden by postulating that B and L are fundamental symmetries, since they are necessarily violated by non-perturbative electroweak effects [26] (though these effects are negligible for experiments at ordinary energies). A new symmetry is instead introduced, called R-parity, the conservation of which prevents both baryon and lepton violating couplings. R-parity conservation does, however, allow B and L violation if they occur in the same amounts. The R-parity of a particle, R, is defined as:

$$R = (-1)^{3(B-L)+2S}, \tag{2.4}$$

where B is the baryon number, L is the lepton number and S is the spin of the particle. All SM particles have R of +1 and all SUSY particles have R of −1. In R-parity conserving models, R is an exactly conserved, multiplicative quantum number, meaning that fast proton decay is excluded, there can be no mixing between SM and SUSY particles and that every interaction vertex must contain an even number of sparticles. R-parity conservation has a great influence over the phenomenology of the MSSM. Sparticles must be produced in pairs in interactions of SM particles; every sparticle must decay to an odd number of sparticles; and the lightest SUSY particle (LSP) will be absolutely stable. It should be noted that models without R-parity conservation can be constructed in which proton decay is adequately suppressed [27], however this thesis will only consider R-parity conserving models.

2.3. Dark Matter

Visible matter is not the only matter in the universe. The first indications of invisible matter were spiral galaxy rotation curve observations early last century. It was found that the stars in galaxies were rotating faster than what could be caused by their visible matter. A galactic halo of unseen matter was postulated to explain this phenomenon. Since then, observations of large astrophysical systems, with sizes ranging from galactic to cosmological scales, have all required the existence of a large amount of dark matter to explain results. They include observations of rotational speeds of galaxies [28], orbital velocities of galaxies within clusters [29], gravitational lensing [30], the cosmic microwave background [31], light element abundances [32] and large scale structure [33].

Recent precision measurements of temperature anisotropies in the cosmic microwave background from the Wilkinson Microwave Anisotropy Probe (WMAP) combined with the distribution of galaxies from baryonic acoustic oscillations and distance measurements from Type 1a supernovae, have allowed the matter density of the universe to be quantified with greater precision than ever before. The matter density of the universe is measured to be $\Omega_m h^2 = 0.1352 \pm 0.0036$ [31], however the visible baryonic matter density is measured to be only $\Omega_b h^2 = 0.02255 \pm 0.00054$, while the cold dark matter density is much larger at $\Omega_c h^2 = 0.1126 \pm 0.0036$. The nature of this dark matter is one of the major mysteries of particle physics and astronomy.

Although the existence of dark matter is well motivated by several lines of evidence, the exact nature of dark matter remains elusive, and there are many candidates for dark matter particles. The most popular of these are weakly interacting particles much like neutrinos, but with a much larger mass. These weakly interacting massive particles (WIMPs) should be stable, heavy, and electrically and colour neutral. As mentioned above, in R-parity conserving SUSY models, the LSP is stable and if it is neutral, it is an ideal dark matter candidate. Within a given SUSY scenario, it is possible to calculate the mass spectrum and decay widths of the SUSY particles, and use this information to obtain the relic density of the LSP. Comparing this relic density to the dark matter density, it is possible to use cosmological measurements to constrain SUSY parameters. In this thesis, it is assumed that the LSP is the lightest neutralino χ_1^0.

Detecting dark matter is essential in determining its properties and its role in the formation of structure in the universe. Many experiments have searched and are currently searching for a signal of WIMP-like dark matter using a variety of methods. Direct detection experiments have been designed to detect dark matter particles through their scattering with nuclei, while indirect detection experiments attempt to observe the annihilation products of dark matter particles.

Note that these detection techniques are complementary to collider searches for dark matter. The direct or indirect detection of dark matter particles is unlikely to provide enough information to reveal the underlying physics, though results from these experiments can be used to constrain SUSY model parameters. In contrast, collider experiments may identify a long-lived WIMP but will not be able to test its cosmological stability or abundance. Only by combining the information provided by many different experimental methods, is the nature of dark matter to be ascertained.

2.4. Baryogenesis

The most basic distinction drawn between particles in nature, is that between particles and antiparticles. Since antiparticles were first predicted and observed, it has been clear theoretically that there is a high degree of symmetry between particles and antiparticles. This is in stark contrast to what is seen in the universe at large. According to the observations, the baryon density is dominated by baryons, while antibaryons are only secondary products in high energy processes. The source of this asymmetry is one of the major puzzles of particle physics and cosmology.

2.4.1. Baryogenesis Conditions

Assuming that cosmological inflation removes any initial baryon asymmetry after the Big Bang, there should be a dynamic mechanism to generate the currently observed asymmetry. A physical process that generates an asymmetry between baryons and antibaryons from an initial baryon symmetry is called baryogenesis. Any mechanism for baryogenesis must fulfil the three Sakharov conditions [34]:

- ***B* Violation**

  Baryon number (B) violation is obviously required for baryogenesis since, starting from a baryon symmetric universe, B violation must take place in order for the universe to evolve into a baryon asymmetric universe.

  In the SM, B is violated by the triangle anomaly, which leads to the non-perturbative sphaleron process depicted in 2.1. This process involves nine left handed quark doublets and three left handed leptons, one from each generation, leading to $\Delta B = \Delta L = -3$.

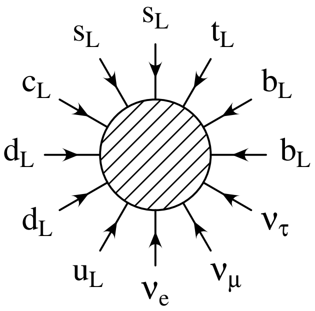

Figure 2.1. Sphaleron Process [35].

- ***C* and *CP* Violation**

  C (charge conjugation) is the symmetry between particles and anti-particles. If C is conserved, for every process which produces a particle, there will be an inverse process which produces its antiparticle at precisely the same rate, so no baryon asymmetry can be created. P (parity) is the symmetry of interactions between right handed and left handed particles. As well as C violation, CP (the combination of C and P) violation is also required to generate a baryon asymmetry because the antiparticle of a left handed particle is right handed.

  In the SM, C is maximally broken, since only the left handed electron is $SU(2)_L$ gauge coupled, while CP is violated via the inclusion of a complex phase in the CKM quark mixing matrix for three generations of quarks.

- **Departure from Thermal Equalibrium**

  Equilibrium is when the rate of a process equals the rate of the inverse process, hence a departure in equilibrium is required to generate a baryon asymmetry so that processes which produce a net baryon number will not have this destroyed by the inverse process.

Interestingly, this last baryogenesis condition can be bypassed if charge conjugation-parity-time reversal (*CPT*) is violated [36]. However, since *CPT* invariance is a fundamental symmetry of quantum field theory, guaranteed by Lorentz invariance, it is more likely that baryogenesis will occur due to a departure from equilibrium rather then *CPT* violation.

One scenario for equilibrium departure in the SM is the electroweak phase transition, which can provide a departure from thermal equilibrium if it is sufficiently strongly first order, which is the basis for electroweak baryogenesis.

2.4.2. Electroweak Baryogenesis

It is speculated that in the early hot universe, the vacuum possessed a large number of symmetries, some of which are not seen today. As the universe expanded and cooled, the vacuum underwent a series of symmetry-breaking phase transitions. The electroweak phase transition is the breaking of the $\mathrm{SU}(2)_\mathrm{L} \times \mathrm{U}(1)_\mathrm{Y}$ symmetry of the electroweak field into the $\mathrm{U}(1)_\mathrm{Q}$ symmetry of the electromagnetic field by the Higgs mechanism.

This electroweak phase transition can provide a departure from thermal equilibrium if it is sufficiently first order. The difference between first order and second order is determined by the behaviour of the Higgs potential. A first order transition proceeds via bubble nucleation, where bubbles of asymmetric phase nucleate within the symmetric phase as the universe cools below the critical temperature. These bubbles provide the necessary departure from equilibrium [37].

Inside the bubbles, the Higgs vacuum expectation value and particle masses are non-zero, while they are still vanishing in the exterior symmetric phase. As the bubbles expand to eventually collide and fill all of space, *CP* violating interactions in the bubble walls create a chiral asymmetry in the vicinity of the bubble walls, leading to an excess of left handed particles relative to right handed particles outside the wall and a compensating deficit inside the wall [38].

Sphalerons interact only with left handed particles and hence convert the chiral asymmetry outside the bubble into a net B asymmetry. To ensure the preservation of this generated baryon asymmetry, the B violating processes inside the bubble must be out of equilibrium at the nucleation temperature, T_N. To achieve this, the rate of B violating processes, which depends on the ratio of the sphaleron energy to the critical temperature, must be smaller than the expansion rate of the universe. As the sphaleron energy is proportional to the Higgs vacuum expectation value, this leads to the condition for a sufficiently strong first-order phase transition: $\phi(T_N)/T_N \gtrsim 1$, where $\phi(T_N)$ is the Higgs vacuum expectation value at T_N [39].

For a light Higgs, a first-order phase transition can be induced by the loop effects of light bosonic particles, with masses around the weak scale and large coupling to the Higgs field. The only particles in the SM which satisfy the mass conditions are the weak gauge bosons, however their Higgs couplings are not strong enough to induce a first-order transition for a Higgs mass above the current experimental limit [40].

It is however, possible to implement this electroweak baryogenesis mechanism in the MSSM because stop quarks have Higgs couplings which are proportional to the large top mass. For this mechanism to work, the lighter stop quark must be mainly right handed with $m_{\tilde{t}_1} < m_t$ leaving the heavier stop quark to be mainly left handed and thus $m_{\tilde{t}_2} \gtrsim 1$ TeV to achieve agreement with electroweak precision tests and ensure a sufficiently heavy Higgs boson compatible with the LEP limit [41]. This constrains the parameters involved in the stop mixing matrix (Equation 2.3) in the following way [42]:

$$\begin{aligned} & m_{\tilde{U}_3} \lesssim 0 & \qquad & 5 \lesssim \tan\beta \lesssim 10 \\ & m_{\tilde{Q}_3} \gtrsim 1\,\text{TeV} & \qquad & 0.3 \lesssim \frac{1}{m_{\tilde{Q}_3}} \left|A_t - \mu^* \cot\beta\right| \lesssim 0.5 \end{aligned}$$

Due to the dependence on the existence of a light stop quark for electroweak baryogenesis to be successful in the MSSM, this parameter space region is called the light stop scenario (LSS).

We are all agreed that your theory is crazy. The question which divides us is whether it is crazy enough to have a chance of being correct.

– Niels Bohr

3

The Light Stop Scenario

The Light Stop Scenario (LSS) is a parameter space region within the MSSM where the baryon asymmetry of the universe can be generated through electroweak baryogenesis. This chapter presents the results of an analysis of the constraints on the LSS parameter space from different measurements and concludes by introducing the baryogenesis inspired benchmark point studied in detail in this thesis.

A random scan of the LSS parameter space was performed using micrOmegas[1] [44] with the parameters in $\mathcal{L}_{\text{SUSY}}$ set to their SM values and the SUSY breaking parameters in $\mathcal{L}_{\text{soft}}$ using the values and bounds shown in Table 3.1. These bounds were chosen in collaboration with the authors of References [41] and [42]. This study revises the analysis found within Reference [42] using the updated theoretical calculations discussed in Reference [41].

Being a random scan, the goal of this analysis is not to understand how the parameters affect each of the physical quantities as in Reference [42], but rather to ensure that the LSS parameter space, with current theoretical calculations and experimental observations, has not been ruled out, that electroweak baryogenesis within the MSSM is still feasible.

---

[1] The CPVMSSM [43] package was used for proper treatment of ϕ_μ and ϕ_{A_t}.

Table 3.1. Light Stop Scenario parameter space scan bounds.

Squark Mass Parameters	**Slepton Mass Parameters**
2 TeV < $m_{\tilde{Q}_3}$ < 10 TeV -10 GeV < $m_{\tilde{U}_3}$ < 0 GeV 500 GeV < $m_{\tilde{D}_3}$ < 2 GeV $m_{\tilde{Q}_i}, m_{\tilde{U}_i}, m_{\tilde{D}_i}$ = 10 TeV (i=1,2)	$m_{\tilde{L}_3}, m_{\tilde{R}_3}$ = 1 TeV $m_{\tilde{L}_i}, m_{\tilde{R}_i}$ = 10 TeV (i=1,2)
Higgs Sector Parameters	**Trilinear Interaction Parameters**
200 GeV < $m_{H^\pm}$ < 2 TeV $5 < \tan\beta < 10$ 100 GeV < $\lvert\mu\rvert$ < 500 GeV $0.1 < \phi_\mu < \pi$	$A_b > 0$ $A_t > A_\tau$ $0.3 < \left\lvert A_t - \mu^* \cot\beta \right\rvert / m_{\tilde{Q}_3} < 0.5$ $\phi_{A_t} = -\pi$
Gaugino Mass Parameters	
50 GeV < M_1 < 500 GeV $M_2 = M_1$ M_3 = 1 TeV	

The requirement of successful electroweak baryogensis in agreement with current experimental results places very stringent constraints on the MSSM parameters, with bounds on all quantities relating to third generation squark soft masses and couplings as well as the Higgs sector. To further reduce the number of free parameters, the additional requirement of grand unification was assumed, relating the gaugino mass parameters by: $M_2 = (g_2^2/g_1^2)M_1 \simeq 2M_1$. Moreover, the first and generation sfermion soft masses were taken to be very large, to satisfy the electric dipole moment measurement in the presence of large phases.

In addition to these bounds on MSSM parameters, constraints were also placed on measurable quantities. The most significant of these is that of a lightest Higgs mass above the SM Higgs LEP experimental limit, $m_{h^0} > 110$ GeV. Note that this constraint is looser than the LEP limit of 114.4 GeV as higher order corrections can increase the predicted value of the Higgs mass [45]. It was also required that the lightest neutralino, $\tilde{\chi}_1^0$ was the LSP at each point with a relic density not much larger than WMAP measured dark matter density, $\Omega_{\tilde{\chi}_1^0} h^2 < 3$.

A total of 40 000 parameter space points were generated within the LSS parameter bounds with the given constraints.

3.1. Constraints from *CP* Violating Phases

A problem for successful electroweak baryogenesis in the SM is that the strength of the *CP* violating interactions are too small to have generated the large chiral asymmetries needed for the sphaleron processes to generate the baryon asymmetry [46]. The MSSM can accommodate many *CP* violating phases in addition to the CKM phase present in the SM, however, the strength of their interactions are tightly bounded by the experimental limits on the electric dipole moments (EDMs) of the electron and neutron. The one-loop contributions to these EDMs may be efficiently suppressed if the first and second generation sfermions are very heavy, with masses larger than about 10 TeV [47], leaving only the chargino and neutralino currents as the *CP* violating sources in the LSS. The charginos and neutralinos should therefore remain light and there should exist non-negligible phases between the higgsino and gaugino mass parameters. However, even in the absence of one-loop contributions, two-loop contributions to the EDMs involving the charginos and the Higgs field remain sizeable [48], where the terms relating to these contributions are the same as those that generate the baryon asymmetry. In this analysis it is shown how strongly the EDM limits constrain the LSS parameter space.

The electron EDM measurement places the strongest constraint on the chargino and neutralino phases in the LSS, being the best measured and least plagued by theoretical uncertainties. The upper bound on the electron EDM comes from measurements of the ^{205}Thallium atom EDM, and is currently $|d_e| < 1.6 \times 10^{-27}$ e cm at 90% CL [49]. As shown in Figure 3.1, of the LSS parameter space points generated, only about half are consistent with this experimental bound, and an order of magnitude improvement on the measurement would be almost sufficient to rule out this baryogenesis mechanism in the MSSM entirely. It is however reassuring that some subset of the LSS parameter space is currently consistent with experimental constraints on the electron EDM.

Other observables are sensitive to the non-negligible phases between the higgsino and gaugino mass parameters; these phases may induce effects on flavour changing neutral currents associated with the bottom quark [50]. One of the most sensitive experimental measurements is the $b \to s\gamma$ branching ratio [51]. The current experimental world average is $(3.55 \pm 0.24_{\text{exp}} \pm 0.09_{\text{model}}) \times 10^{-4}$ [52] while the next-to-next-to-leading order SM calculation yields $(3.15 \pm 0.23) \times 10^{-4}$ [53]. Figure 3.2 shows the values of the branching ratio obtained in the parameter space scan compared with the central SM and experimental values. While the experimental result does rule out a small subset of the LSS parameter space, it is more interesting to note both the constructive and destructive interference of the SUSY terms to the SM contribution.

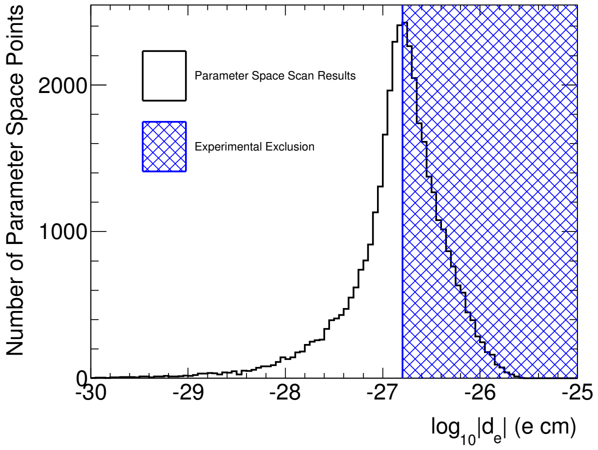

Figure 3.1. Electron EDM constraint on the LSS parameter space. Histogram shows the values of the EDM obtained in the LSS parameter space scan, while the hashed region shows the experimentally excluded values at 90% CL [49].

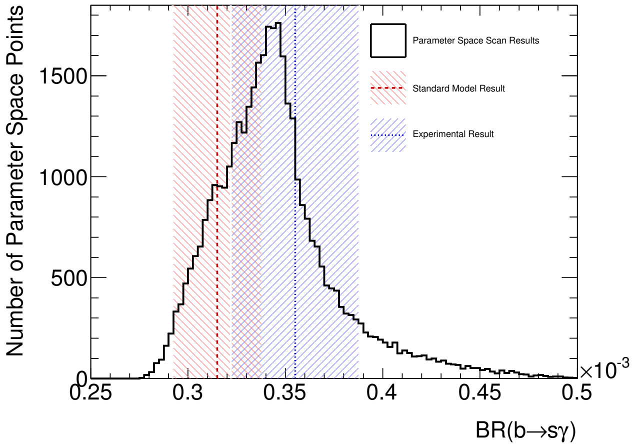

Figure 3.2. $\mathcal{B}(b \to s\gamma)$ constraint on the LSS parameter space. Histogram shows the values of the branching ratio obtained in the LSS parameter space scan, while the dotted line shows the current experimental world average [52] and the dashed line shows the SM calculation [53], both shown with hashed bands representing one sigma uncertainties.

3.2. Constraints from Neutralino Dark Matter

The baryon asymmetry of the universe is not the only cosmological problem the SM does not address, there is also the dark matter puzzle. MSSM can provide a dark matter candidate in the lightest neutralino, $\tilde{\chi}_1^0$. The conditions necessary for electroweak baryogenesis in the MSSM, which define the LSS, have important implications for neutralino dark matter.

Firstly, if the lightest neutralino is to be the source of the observed dark matter, it must be lighter than the light stop so that it is stable. Secondly, in much of the parameter space of interest the light stop is only slightly heavier than the neutralino LSP, implying that stop-neutralino coannihilation will be significant. Finally, the higgsino-gaugino phase modifies the masses of the neutralinos and their couplings to other particles.

3.2.1. Constraints from Relic Density

Neutralino annihilations are very important to the question of whether they make up all or part of the observed dark matter in the universe. Soon after the Big Bang, when the universe was very hot and dense, very energetic and massive particles were created. These particles existed in thermal equilibrium, meaning processes which converted heavy particles into lighter ones and vice versa occurred with the same rate. As the universe expanded and cooled, lighter particles no longer had sufficient kinetic energy to produce heavier particles. Therefore at some point, the density of a particular particle species becomes too low to support frequent interactions, violating the conditions for thermal equilibrium. At this point in time, the particles are said to 'freeze out' and their number remains constant. The density of a specific particle type at the time of freeze out is known as the particle relic density [54].

Figure 3.3 shows the values of the neutralino relic density, $\Omega_{\tilde{\chi}_1^0} h^2$, obtained in the LSS parameter space scan as a function of the parameters $|\mu|$ and M_1 for comparison with Reference [42]. The crosses correspond to where the relic density is consistent within two standard deviations with WMAP data [31]. The points in which the relic density is above the experimental bound and excluded by more than two standard deviations are indicated by the asterisks. The pluses denote points in which the relic density is less than the WMAP value; an additional source of dark matter, unrelated to neutralinos would be needed in these points. Finally, the empty regions are a result of the restrictions when conducting the LSS parameter space scan. The empty region in

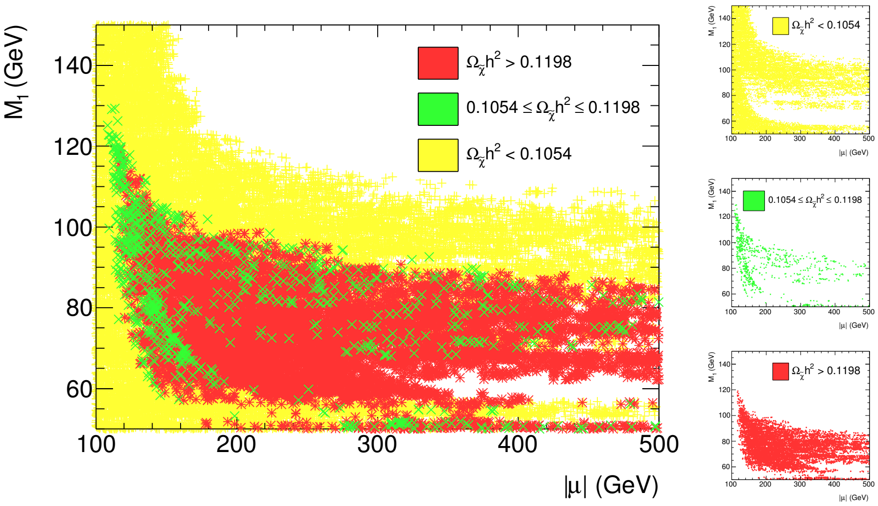

Figure 3.3. Neutralino relic density, $\Omega_{\tilde{\chi}_1^0} h^2$, in the LSS parameter space. The green crosses (centre right) correspond to where $\Omega_{\tilde{\chi}_1^0} h^2$ is consistent within two standard deviations with WMAP data [31], red asterisks (lower right) is where $\Omega_{\tilde{\chi}_1^0} h^2$ is too high while yellow pluses (upper right) is where it is too low. The empty region in the upper right of the combined datasets is where $m_{\tilde{t}_1} < m_{\tilde{\chi}_1^0}$, while other empty regions are where $\Omega_{\tilde{\chi}_1^0} h^2 > 3$ or $m_{h^0} < 110$ GeV.

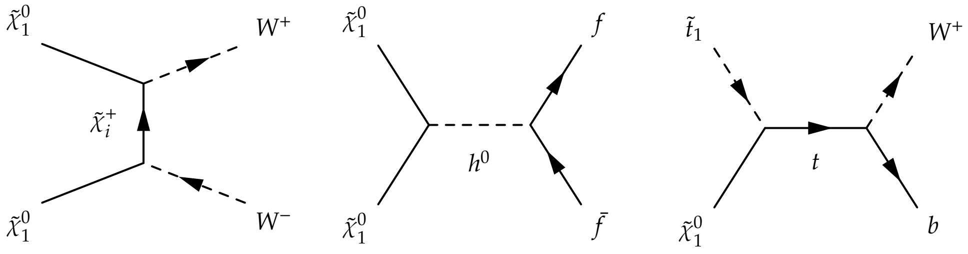

(a) Coannihilation

(b) Resonant Higgs Annihilation

(c) Chargino Exchange

Figure 3.4. Examples of processes contributing to neutralino (co)annihilation required to reduce the neutralino relic density to a level consistent with observations [55].

the upper right is where the lightest stop becomes the LSP, while the other empty areas are either where the Higgs mass is well below the LEP limit, $m_{h^0} < 110$ GeV, or where the neutralino relic density is well above the measured WMAP value, $\Omega_{\tilde{\chi}_1^0} h^2 > 3$.

As can be seen, in most of the LSS parameter space, the neutralino relic density exceeds the dark matter density. Keeping the unification motivated ratio of the gaugino mass parameters M_2/M_1 close to two along with the constraints on the Higgs sector parameters required for electroweak baryogenesis induces a lightest neutralino with mostly bino admixture. A bino typically overcloses the universe, unless there is a special situation that circumvents this [56]. For example, as shown in the Feynman diagrams depicted in Figure 3.4, neutralinos can coannihilate with sfermions of similar mass, annihilate near a Higgs resonance or acquire a sizable higginos admixture allowing for chargino exchange [55]. These processes can lower the neutralino relic density to a level that is consistent with observations; however if these processes are too efficient, the relic density is too small. Since the dark matter density has been measured to such high precision, the number of parameter space points consistent within two standard deviations is quite small, though their existence is encouraging.

3.2.2. Constraints from Direct Detection

Direct detection experiments assume that if dark matter is everywhere in the universe, then it should be travelling through the earth at all times, and although it is weakly interacting, it may occasionally interact and if a detector is sensitive and large enough then that interaction can be measured. The interaction of a dark matter particle with detector material can be classified by: elastic or inelastic and spin-dependent or spin-independent; elastic spin-independent interactions have higher cross sections [54] since they involve the interaction of the dark matter particle with the nucleus as a whole.

Figure 3.5 shows the spin independent neutralino-nucleon elastic scattering cross sections in the LSS parameter space as a function of neutralino mass compared to the experimental limits from XENON [57], CDMS [58] and ZEPLIN [59]. It can be seen that a large portion of the LSS parameter space has been ruled out by the non-observation of dark matter by these experiments, however there still remains some allowed regions.

3.2.3. Constraints from Indirect Detection

In parallel to direct detection experiments, a wide range of astrophysical indirect detection programs have developed to search for the annihilation products of dark matter particles. After freeze out, dark matter annihilation becomes greatly suppressed; however even if its impact on the dark matter relic density is negligible, the annihilation still continues and may be observable. As the annihilation rate is proportional to the square of the dark matter density, it is natural to search for dark matter annihilations

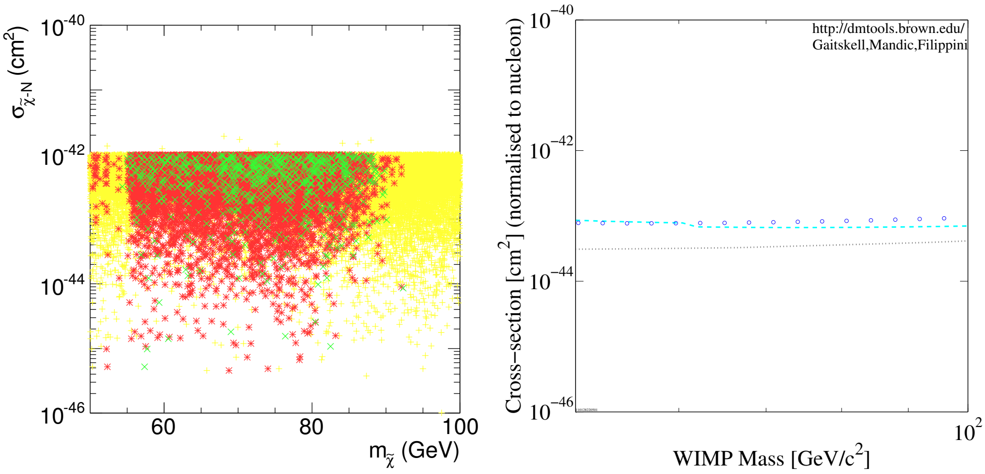

(a) $\sigma_{\tilde{\chi}_1^0-N}$ in the LSS parameter space. See Figure 3.3 for a description of the symbols.

(b) $\sigma_{\tilde{\chi}_1^0-N}$ limits from as rendered by DM Tools Limit Plot Generator [60].

Figure 3.5. Spin independent neutralino-nucleon elastic scattering cross sections in the LSS parameter space (left) as a function of neutralino mass compared to the experimental limits (right) of XENON [57] (dots), CDMS [58] (dashes) and ZEPLIN [59] (circles).

in regions of the universe expected to have high dark matter densities. Thus searches are currently underway to detect neutrinos from annihilations of gravitationally captured dark matter in the core of the Sun [61], antimatter particles from dark matter annihilations in the galactic halo [62], and photons from dark matter annihilations in galactic substructure [63].

In contrast to direct detection, there have been some reported anomalies in indirect detection, and some of these can be interpreted as possible evidence for dark matter. The most prominent example is the measurement of the flux of positrons and electrons with energies between 10 GeV and 1 TeV by PAMELA [64], ATIC [65], and Fermi-LAT [66]. These data are shown in Figure 3.6, and reveal an excess of positrons above an estimate of the expected background. While the generally accepted explanation for these data is pulsars [67]; it is still interesting to explore the possibility that the positron excess arises from dark matter annihilation.

Figure 3.7 shows the velocity averaged neutralino annihilation cross sections as a function of neutralino mass. Unfortunately, the observed fluxes are far larger than expected from the neutralinos in the LSS parameter space. As such, the current indirect detection experiments do not exclude any of the LSS parameter space region.

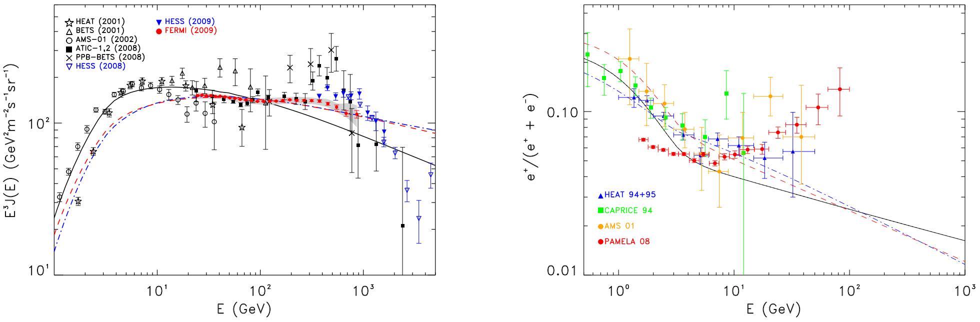

Figure 3.6. Cosmic positron excess measurements and interpretations [67]. Left is the total positron and electron flux measured by Fermi with shaded systematic errors, and other experiments. Right is the cosmic positron fraction measured by PAMELA and other experiments. In both cases, the solid line represents the prediction from a standard cosmic ray model using GALPROP [68], while the dashed lines represent the prediction after modifications are made to fit the Fermi-LAT data.

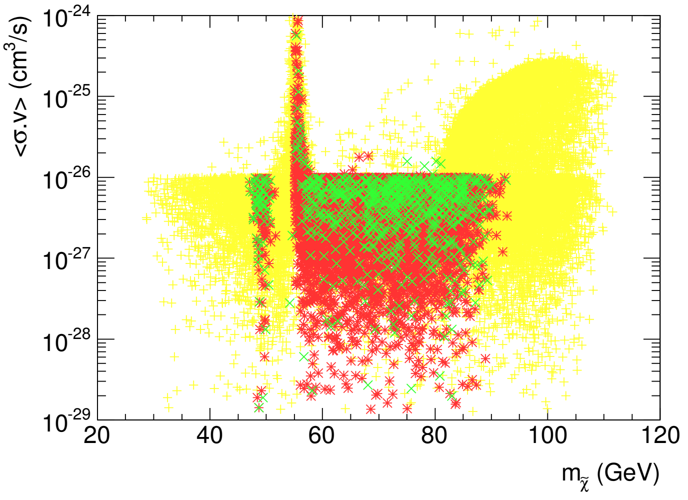

Figure 3.7. Velocity averaged neutralino annihilation cross sections as a function of neutralino mass in the LSS parameter space. See Figure 3.3 for a description of the symbols.

3.3. Light Stop Benchmark

The previous sections outlined a scenario in which the dark matter abundance and baryon asymmetry of the universe can simultaneously be achieved in the context of the MSSM. For the detailed exploration of the collider phenomenology of such a model, a particular parameter space point, or benchmark point, is chosen for further analysis.

The benchmark point chosen, $LHS2$ [56], was selected such that the baryon asymmetry of the universe and the relic density of neutralinos was predicted to be close to the dark matter density measured by WMAP and all known low energy, collider and astrophysical constraints were satisfied as discussed in the previous sections. In this benchmark point, the neutralino relic density is lowered to match the observed dark matter density though annihilation near a Higgs resonance. The MSSM parameters for this benchmark can be found in Appendix A.

The distinctive collider signature of electroweak baryogensis in the MSSM is the existence of a light stop. The $LHS2$ benchmark point features a stop that could be discovered at the LHC in early data due to the large difference between the stop and the neutralino masses. Even the heavier stop can possibly be produced at the LHC together with the third generation sleptons. However due to the resonant feature, the Higgs boson can decay into neutralinos, which reduces the visible Higgs width and makes its collider discovery more challenging. Table 3.2 gives the masses of these sparticles.

Table 3.2. Sparticle masses in the $\tilde{t}_1$ benchmark point $LHS2$ [56].

Particle	**Mass (GeV)**
$\tilde{t}_1$	137
$\tilde{t}_2$	1 510
$\tilde{\tau}_1$	998
$\tilde{\nu}_\tau$	980
$\tilde{\chi}_1^0$	58
$\tilde{\chi}_2^0$	112
$\tilde{\chi}_1^+$	111
$\tilde{\chi}_2^+$	419
h	116

An experiment is a question which we ask of Nature, who is always ready to give a correct answer, provided we ask properly, that is, provided we arrange a proper experiment.

– Charles Vernon Boys

4

The ATLAS Experiment

The ATLAS experiment is operated by a collaboration of over 3 000 physicists from more than 175 institutes spanning 38 countries. It is located at CERN, a European particle physics laboratory on the French-Swiss border, near Geneva, Switzerland. Its goals are to search for the origin of electroweak symmetry breaking and new physics beyond the SM in the proton-proton collisions provided by the LHC. This chapter gives a brief overview of the LHC accelerator and introduces the ATLAS detector, presenting all main detector components and describing the detector simulation and particle reconstruction methods required to make full use of the detector in physics analyses. Finally, the recent history of the LHC and ATLAS is summarised, providing the context in which the research of this thesis was conducted.

4.1. The Large Hadron Collider

The LHC is the world's newest and most powerful particle collider. It is designed to accelerate two separate beams of proton bunches up to an energy of 7 TeV, and then bring them into collisions with centre of mass energies of 14 TeV every 25 ns, with a peak luminosity of 10^{34} cm^{-2}s^{-1}. It will also be able to collide lead nuclei with an energy of 2.8 TeV per nucleon at a peak luminosity of 10^{27} $\text{cm}^{-2}\text{s}^{-1}$. This section will give a brief overview of the LHC machine, concentrating on proton collisions; more comprehensive descriptions can be found in References [69, 70].

The LHC provides collisions at four interaction points (IPs), shown in Figure 4.1. At each interaction point is a detector:

- *ATLAS* (A Toriodal LHC Apparatus) is a general purpose detector located at point 1 [71], see Section 4.2;
- *CMS* (Compact Muon Solenoid) is a general purpose detector located at point 5 [72];
- *LHCb* is a dedicated detector for precision measurements of CP violation and rare decays of B hadrons located at point 8 [73];
- *ALICE* (A Large Ion Collider Experiment) is a heavy ion detector designed to address the physics of strongly interacting matter and the quark gluon plasma located at point 2 [74].

The LHC has been designed to achieve the highest possible luminosity with the highest possible energy, limited by technology and costs. It is installed in the 26.7 km long tunnel that was constructed earlier for the CERN Large Electron Positron (LEP) machine, which lies between 45 m and 170 m below the surface on a plane inclined at 1.4%, and makes extensive use of previous CERN energy frontier accelerators to ramp protons to their final collision energy.

Protons to be injected into the LHC begin their journey as hydrogen atoms, stripped of their electrons. Their acceleration to LHC collision energy proceeds through a number of steps. They are first accelerated to 50 MeV by a linear accelerator, LINAC2, before being passed around three storage rings, the PS Booster, PS and SPS, where they are successively accelerated to 11.4 GeV, 26 GeV and 450 GeV and combined into bunches. They are then injected into the main LHC accelerator via two 2.5 km tunnels, where they are accelerated to the final collision energy. A schematic of the accelerator chain is shown in Figure 4.2.

To achieve the design beam energy of 7 TeV, the LHC contains 1 232 superconducting dipole magnets, which can generate magnetic fields of up to 8.33 T. The coils are made of niobium-titanium (NbTi), a material that is superconducting at 1.9 K. The magnets are twin bore, consisting of two sets of coils and beam channels within the

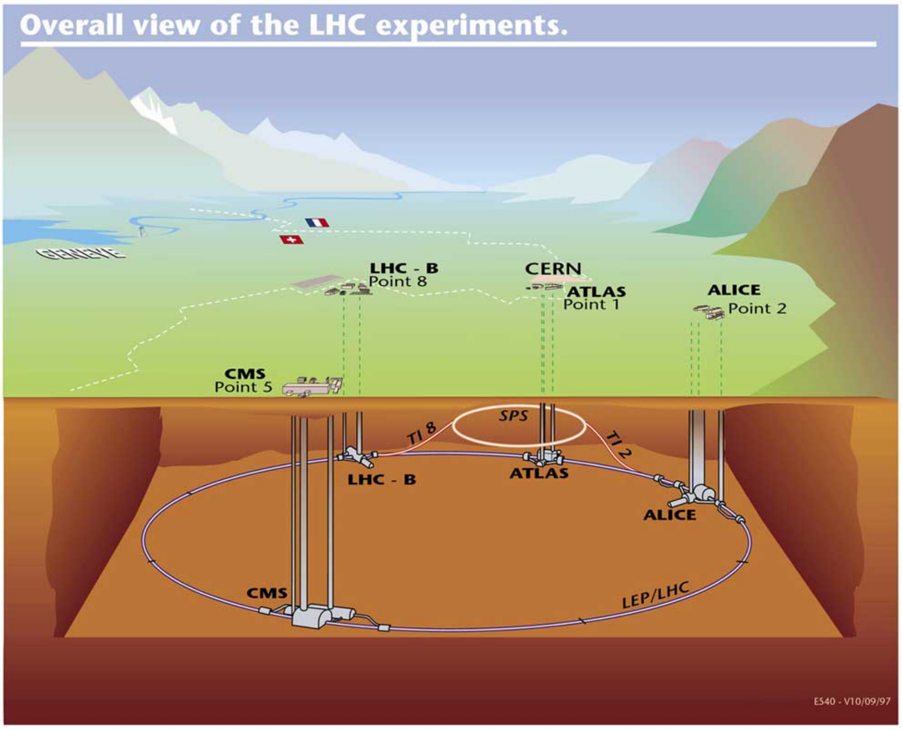

Figure 4.1. Location of the four main experiments on the LHC ring [75].

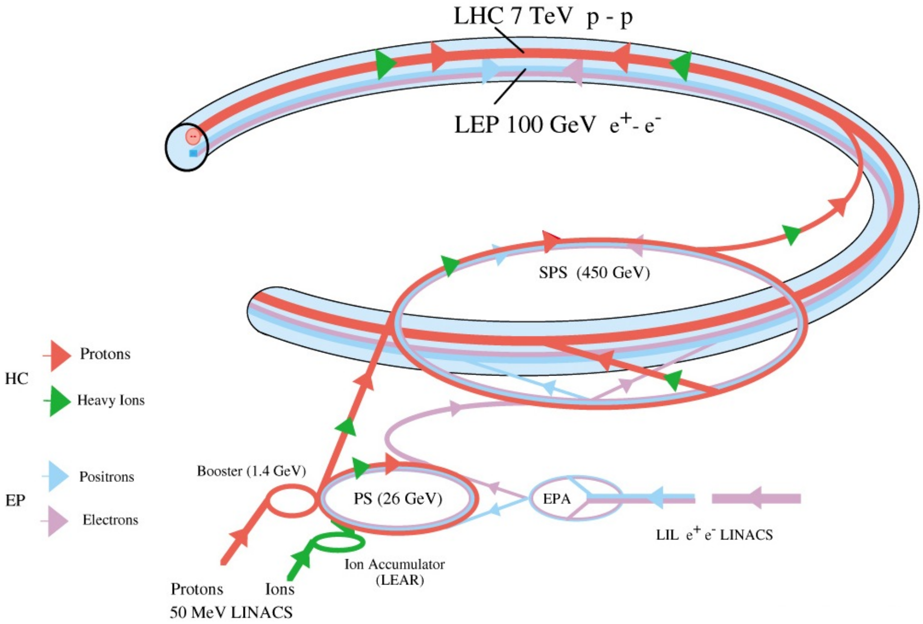

Figure 4.2. LHC/LEP injection complex, showing the different paths for protons, heavy ions and positrons and electrons [76].

same mechanical structure and cryostat. This design was required to accelerate two beams of equally charged particles in opposite directions within a small area. In addition to the dipole magnets there are quadrupole magnets for beam focusing and beam corrections, and sextupole, octupole and decapole magnets which are used to compensate for systematic non-linearities.

Along with the beam energy, the other main characteristic of an accelerator is the luminosity, the number of events per unit area it can achieve per second. For a Gaussian beam in a circular collider, this can be approximated by:

$$L = \frac{N_p^2 n_b f_{\mathrm{rev}} \gamma_r}{4\pi \epsilon_n \beta^*} F,$$

where N_p is the number of particles per bunch, n_b the number of bunches per beam, f_{rev} the revolution frequency, γ_r the relativistic gamma factor, ϵ_n the normalized transverse beam emittance, β^* the beta function at the collision point, and F the geometric luminosity reduction factor due to the crossing angle at the IP:

$$F = \left(1 + \left(\frac{\theta_c \sigma_z}{2\sigma^*}\right)^2\right)^{-1/2},$$

where θ_c is the full crossing angle at the IP, σ_z the RMS bunch length, and σ^* the transverse RMS beam size at the IP. Table 4.1 lists the key parameters for the LHC and their values for design energy and luminosity.

Increasing the luminosity is the only way to collect increased yields of events for processes with low cross sections. The LHC peak luminosity of 10^{34} cm^{-2} s^{-1} is achieved by a large number of bunches ($N_p = 2\,808$), a small bunch spacing ($1/f_{\mathrm{rev}} =$ 25 ns), a high number of protons per bunch ($Np = 1.15 \cdot 10^{11}$), and a small bunch size ($\sigma* = 16.7\mu$m). Unfortunately increasing the luminosity by increasing the number of particles per bunch, also increases the number of interactions per bunch crossing. For the design peak luminosity at nominal energy there are around 20 interactions on average per bunch crossing. This is calculated from the total inelastic proton-proton cross section, estimated to be 60 mb. The vast majority of these interactions however, generate little transverse momentum (p_{T} as they stem from long-range proton-proton interactions. These soft interactions, known as the underlying event, can be seen as noise superimposed upon all events. Furthermore, most detector elements have readout latencies that exceed the small bunch spacing of 25 ns resulting in detector signals arising from previous bunch crossings. The combination of both effects form what is denoted as pile up. The effects of pile up have had a strong impact on the design of all LHC detectors and will influence physics analyses.

Table 4.1. Summary of key LHC parameters for running in proton-proton collision mode at design energy and luminosity at the ATLAS/CMS IPs [70].

Accelerator parameters	
Circumference	26 658.883 m
Dipole magnetic field	8.33 T
Dipole magnet temperature	1.9 K
Number of dipole magnets	1 232
Number of quadrupole magnets	400
Number of other magnets	5 050
Beam parameters	
Proton energy	7 TeV
Number of protons per bunch	1.15×10^{11}
Number of bunches	2 808
Time between bunches	24.95 ns
Circulating beam current	584 mA
Stored energy per beam	362 MJ
Luminosity parameters	
RMS bunch length	7.55 cm
RMS bunch size	16.7 μm
Beta function	0.55 m
Relativistic gamma factor	7 641
Transverse normalised emittance	3.75 μm
Full crossing angle	285 μrad
Geometric luminosity reduction factor	0.836
Peak luminosity	10^{34} cm^{-2}s^{-1}
Interaction parameters	
Inelastic cross section	60 mb
Total cross section	100 mb
Events per bunch crossing	19.02

4.2. The ATLAS Detector

ATLAS has been designed to accommodate a broad physics program, ranging from precise measurements of SM parameters to the search for new physics phenomena and studying the properties of strongly interacting matter at extreme energy densities. These physics studies coupled with the challenging conditions at the LHC determine the requirements for the detector design [71]:

- Due to the experimental conditions, the detectors require fast, radiation-hard electronics and sensor elements. In addition, high detector granularity is needed to handle the particle fluxes and to reduce the influence of overlapping events.
- Large acceptance in pseudorapidity with almost full azimuthal angle coverage.
- Good charged particle momentum resolution and reconstruction efficiency in the inner tracker.
- Very good electromagnetic calorimetry for electron and photon identification and measurements, complemented by full coverage hadronic calorimetry for accurate jet and missing transverse energy measurements.
- Good muon identification and momentum resolution over a wide range of momenta and the ability to determine unambiguously the charge of high momentum muons.
- Highly efficient triggering on low transverse-momentum particles with sufficient background rejection.

Table 4.2 summarises the ATLAS detector's key performance goals required to achieve its physics aims. The overall ATLAS detector layout is shown in Figure 4.3. The largest of the LHC experiments, it is 25 m in diameter and 44 m in length and weighs approximately 7 000 tonnes. The detector is split into different subdetectors, all of which have different roles in measuring the particles created in the LHC collisions. In the following sections, the main subdetectors and components of the ATLAS experiment are introduced; a comprehensive description of the detector can be found in References [71, 77] and its expected performance in Reference [78].

Table 4.2. General performance goals of the ATLAS detector [71]. Note that for high p_T muons, the muon spectrometer performance is independent of the inner detector system. The units for E and p_T are in GeV.

Detector component	Required resolution	η coverage Measurement	 Trigger
Tracking	$\sigma_{p_T}/p_T = 0.05\% \oplus 1\%$	±2.5	-
Electromagnetic	$\sigma_E/E = 10\%/\sqrt{E} \oplus 0.7\%$	±3.2	±2.5
calorimetry	$\sigma_E/E = 10\%/\sqrt{E} \oplus 0.7\%$	±3.2	±2.5
Hadronic calorimetry			
barrel and endcap	$\sigma_E/E = 50\%/\sqrt{E} \oplus 3\%$	±3.2	±3.2
forward	$\sigma_E/E = 100\%/\sqrt{E} \oplus 10\%$	$3.1 < \|\eta\| < 4.9$	$3.1 < \|\eta\| < 4.9$
Muon spectrometer	$\sigma_{p_T}/p_T = 10\%$ at $p_T = 1$ TeV	±2.7	±2.4

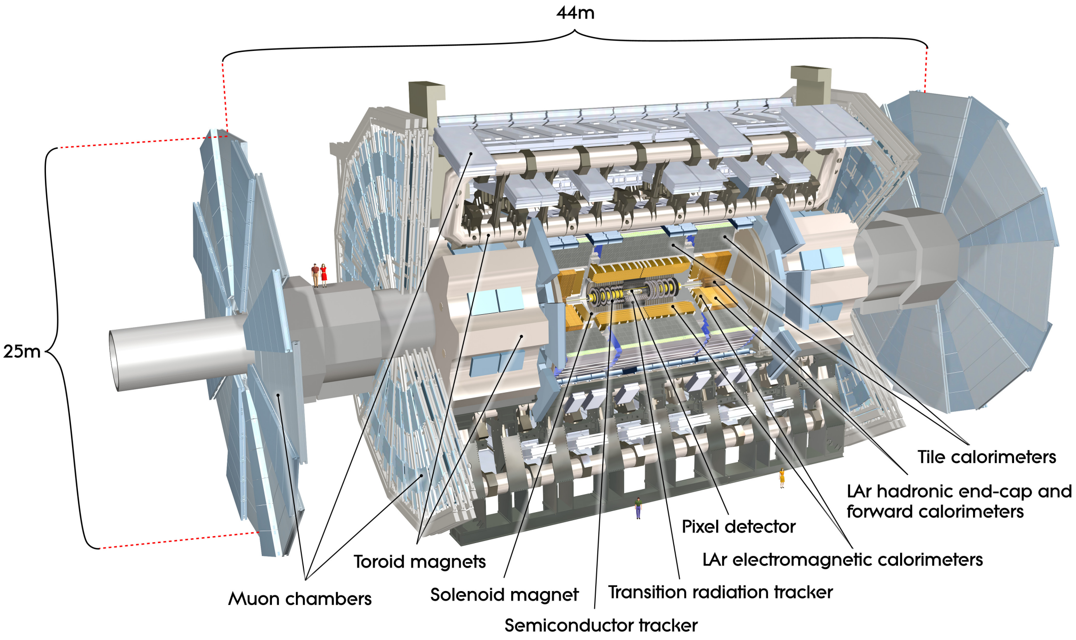

Figure 4.3. Cut away view of the ATLAS detector [71].

4.2.1. Coordinates System

A standard right handed Cartesian coordinate system, illustrated in Figure 4.4, is used for describing the ATLAS detector and the particles emerging from the proton-proton collisions. It is briefly summarised here to aid in understanding the following detector description. The origin of this coordinate system is at the nominal interaction point within the detector, where the beam direction defines the z axis and the x-y plane is transverse to the beam direction. The positive x axis is defined as pointing from the interaction point to the centre of the LHC ring and the positive y axis is defined as pointing upwards. Side A of the detector is defined as that with positive z and Side C is that with negative z.

The most convenient coordinate system to use is (R, ϕ, z), where R is the transverse radius from the beamline, ϕ is the azimuthal angle (measured from the x axis) covering the range $\phi \in [0, 2\pi)$, and the origin of z is at the interaction point. The polar angle θ can also be used, measured from the z axis and covering the range $\theta \in [0, \pi)$.

In hadron-hadron colliders, particles are often described by the parameters $(p_\mathrm{T}, \eta, \phi)$ where p_T denotes the transverse momentum in the x-y-plane and η denotes pseudorapidity, $\eta = -\ln[\tan(\frac{\theta}{2})]$, which is invariant under longitudinal Lorentz boosts[1]. These parameters are used because the cross sections of physics processes have a roughly even distribution in η and because hadrons are composite particles, in a given collision the original z momentum of the interacting constituents is unknown. Particles in the η-ϕ plane are separated by a distance $\Delta R = \sqrt{\Delta\eta^2 + \Delta\phi^2}$.

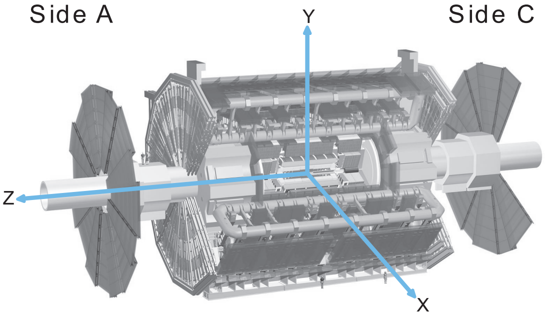

Figure 4.4. ATLAS coordinate system.

---

[1] Pseudorapidity is used instead of true rapidity, $y = \frac{1}{2}\ln[(E + p_z)(E - p_z)]$, because rapidity can not be calculated if the masses of the particles are unknown. In the relativistic limit, pseudorapidity approximates rapidity [79].

4.2.2. Magnet System

One of the key design features of the ATLAS detector is the unique hybrid superconducting magnet system [80], shown in Figure 4.5. It is an arrangement of a central solenoid surrounded by a system of three large air-core toroids, measuring 26 m in length and 20 m in diameter. This unusual configuration and large size has made the magnet system a considerable engineering challenge for the experiment and driven the design of the rest of the detector.

The central solenoid provides a 2 T axial field for the inner detector, while minimising the radiative thickness in front of the barrel electromagnetic calorimeter. The solenoid windings share a common vacuum vessel with the barrel electromagnetic calorimeter, eliminating two vacuum walls. The inner and outer diameters of the solenoid are 2.46 m and 2.56 m respectively and its axial length is 5.8 m. The flux is returned by the hadronic calorimeter and its support structure.

The barrel and two endcap toroids provide the magnetic field for the muon spectrometer. Each of the three toroids consists of eight coils arranged radially and symmetrically around the beam axis. The barrel toroid coils are housed in eight individual cryostats, the endcap coils are housed in one large cryostat, one for each side. The barrel toroid system weighs 830 tons and is 25.3 m in length with inner and outer diameters of 9.4 m and 20.1 m respectively. The two endcap toroids are each 5 m in length with an inner diameter of 1.65 m, and an outer diameter of 10.7 m.

The magnetic field of the toroid system is quite inhomogeneous. The barrel toroid provides a bending power, $\int B \, \mathrm{d}l$ of 2 to 6 Tm in the region $|\eta| < 1.4$, while the endcap toroids provide approximately a $\int B \, \mathrm{d}l$ of 4 to 8 Tm in the region $1.6 < |\eta| < 2.7$. The

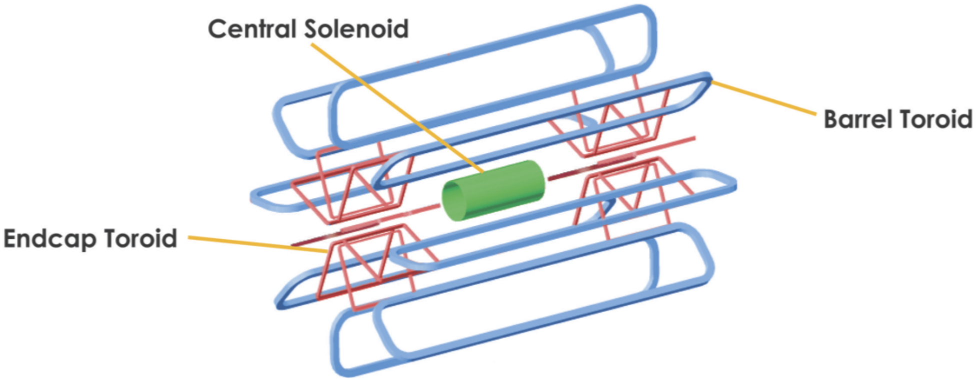

Figure 4.5. Geometry of ATLAS magnet system [81].

bending power is lower in the transition regions where the two magnets overlap ($1.3 < |\eta| < 1.6$), despite the rotation of the endcap system with respect to the barrel system, in order to provide radial overlap and optimise bending power in this region.

4.2.3. Tracking System

Approximately 1 000 particles will emerge from the interaction point every 25 ns within $|\eta| < 2.5$, creating a very large track density in the detector. Accurate measurements of the momentum and charge of these particles is performed by the ATLAS inner detector [82]. Shown in Figure 4.6, the inner detector is designed to provide hermetic and robust pattern recognition, excellent momentum resolution and accurate vertex measurements for charged tracks above a nominal p_T threshold of 0.5 GeV within the pseudorapidity range $|\eta| < 2.5$.

The inner detector consists of three independent but complementary subdetectors. Positioned closest to the beam are high resolution silicon pixel detectors and stereo pairs of silicon microstrip (SCT) detectors. These are surrounded by the transition radiation tracker (TRT), which provides continuous particle tracking using many layers of gaseous straw tubes interleaved with transition material. The combination of the two techniques gives robust pattern recognition and high precision in both ϕ and z coordinates. The straw hits at the outer radius contribute significantly to the mo-

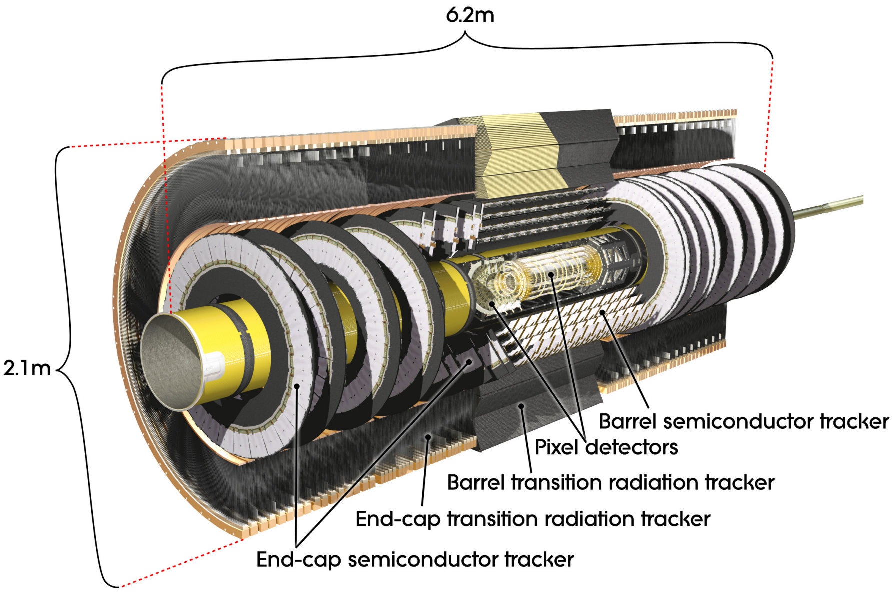

Figure 4.6. Cut away view of the ATLAS inner detector [71].

mentum measurement, since the lower precision per point compared to the silicon is compensated by the large number of measurements and the higher average radius. The relative precision of the different measurements is well matched, so that no single measurement dominates the momentum resolution.

The precision silicon tracking detectors cover the region $|\eta| < 2.5$. In the barrel region, they are arranged on concentric cylinders around the beam axis while in the endcap regions they are located on disks perpendicular to the beam axis. To reduce costs and the amount of material in front of the calorimetry system, the silicon detectors are limited to three cylindrical pixel barrel layers, three pixel endcap disks, four SCT cylindrical barrel layers and nine SCT endcap disks. Due to their high granularity and intrinsic accuracies, these two subdetectors have the highest number of readout channels of all the subdetecters, with the the pixel detector having approximately 80.4 million channels and the SCT with approximately 6.3 million channels.

The straw tubes of the TRT cover the region $|\eta| < 2.5$. In the barrel region, up to 73 layers of straw planes are interleaved with fibres, while in the endcap region, 160 straw planes are interleaved with foils, which provide the transition radiation. The barrel contains about 50 000, 144 cm long straws, each divided in two at the centre, in order to reduce the occupancy, with readout at each end. The endcaps contain 320 000 radial straws, 37 cm in length, with the readout at the outer radius. The total number of electronic channels is approximately 351 000. The TRT is operated with a non-flammable gas mixture of 70% Xe, 27% CO_2 and 3% O_2, with a total volume of 3 m^3.

4.2.4. Calorimetry System

Complementary to the measurement of a particle's momentum and charge is the measurement of its energy. This calculation is the primary function of the ATLAS calorimetry system [83], shown in Figure 4.7, which consists of a number of sampling detectors using different techniques depending on the physics requirements and radiation environment of the region they cover. The system, which has full ϕ symmetry and coverage around the beam axis, covers a pseudorapidity range of $|\eta| < 5$. It comprises of an electromagnetic calorimeter, a hadronic calorimeter and forward calorimeters.

The electromagnetic calorimeter is divided into a barrel part ($|\eta| < 1.475$) and two endcap components ($1.375 < |\eta| < 3.2$), each housed in their own cryostat. The barrel calorimeter consists of two identical half-barrels, separated by a small gap

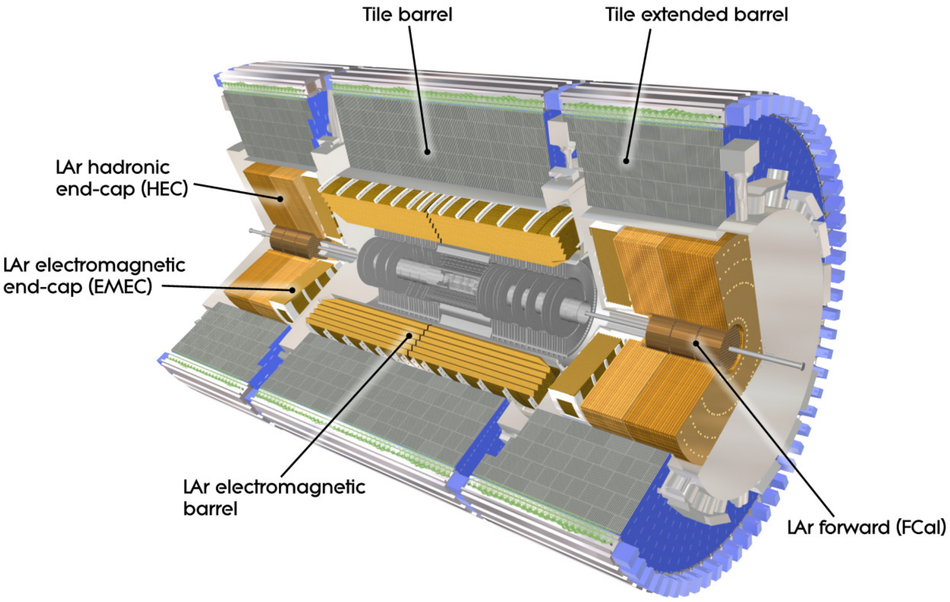

Figure 4.7. Cut away view of the ATLAS calorimeter system [71].

of 4 mm at $z = 0$, with around 110 000 readout channels together. Each endcap calorimeter is mechanically divided into two coaxial wheels: an outer wheel covering the region $1.375 < |\eta| < 2.5$, and an inner wheel covering the region $2.5 < |\eta| < 3.2$, with approximately 64 000 readout channels altogether. The total depth of the electromagnetic calorimeter is > 22 radiation lengths (X_0) in the barrel and $> 24X_0$ in the endcaps, which provides good containment for electromagnetic showers.

The electromagnetic calorimeters are lead-liquid argon detectors with accordion shape absorbers interleaved with readout electrodes, where the lead absorber thickness has been optimised as a function of η in terms of energy resolution. The accordion geometry allows the calorimeters to have several active layers in depth; three in the precision measurement region ($0 < |\eta| < 2.5$) and two in the higher-η region ($2.5 < |\eta| < 3.2$) and in the overlap region between the barrel and the endcap. Figure 4.8 shows a module in the precision measurement region, note the fine segmentation of the first layer, which provides position information of electromagnetic clusters. To account for the significant amount of material in front of the calorimeter (approximately 2 X_0 at $\eta = 0$ for example), a presampler detector covering the region $|\eta| < 1.8$ is used to correct for energy losses.

The hadronic calorimeter consists of a barrel covering the region $|\eta| < 1.0$, two extended barrels covering the region $0.8 < |\eta| < 1.7$, and two hadronic endcaps covering the

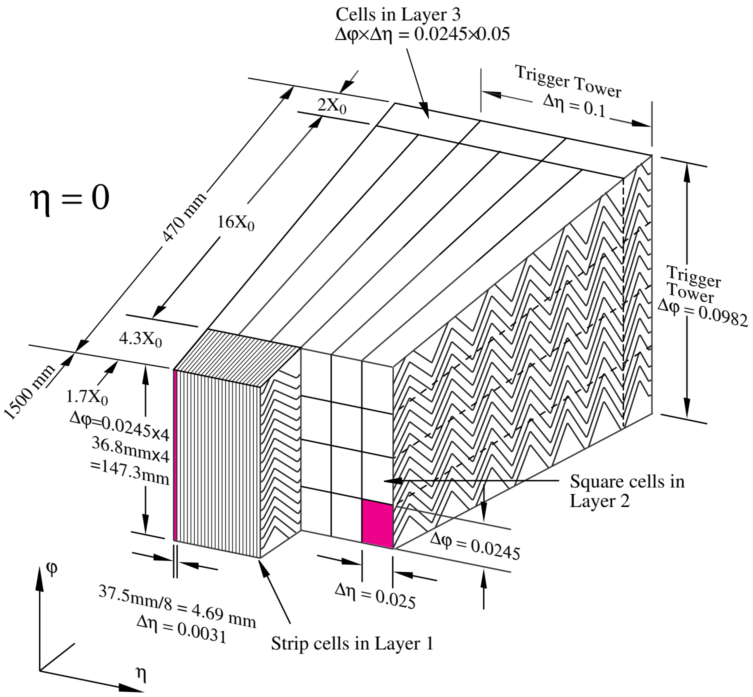

Figure 4.8. Sketch of a electromagnetic calorimeter barrel module [71]. The granularity in η and ϕ of the cells of each of the three layers and of the trigger towers is indicated.

region $1.5 < |\eta| < 3.2$. It contains 9.7 interaction lengths (λ) of active calorimeter in the barrel and 10 λ in the endcaps, to provide good containment for high energy jets. Together with the large η coverage, this thickness also ensures a good missing transverse energy measurement.

The hadronic barrel and extended barrels are sampling tile detectors using steel as the absorber and scintillating tiles as the active material. They are placed directly outside the electromagnetic calorimeter. The barrel and extended barrels are divided azimuthally into 64 modules and segmented in depth in three layers. The hadronic endcap is a copper-liquid argon sampling detector, consisting of two independent wheels per endcap, located directly behind the endcap electromagnetic calorimeter and sharing the same cryostats. Each wheel is built from 32 identical wedge-shaped modules, and divided two segments in depth, for a total of four layers per endcap.

The forward calorimeter is integrated into the endcap cryostats and provides coverage over $3.1 < |\eta| < 4.9$. It is approximately 10 λ deep, and consists of three modules in each endcap using liquid argon as the active material: the first, using copper as the absorber material, is optimised for electromagnetic measurements, while the other two, both using tungsten as the absorber material, predominantly measure the energy of hadronic interactions.

4.2.5. Muon System

Muons are very useful in searches for new physics at hadron colliders. However, being minimising ionising particles they can pass though the ATLAS calorimeter with very little energy loss, while the ATLAS inner detector is unable to provide good momentum resolution and charge determination due to the limited bending power of the ATLAS central solenoid. It falls to the ATLAS muon spectrometer [84], shown in Figure 4.9, to identify and provide precision measurements of muons. It consists of separate trigger and high precision tracking chambers, and uses the toroid magnets to deflect muon tracks that pass through it for momentum measurements. Chambers in the barrel region are located between and on the eight coils of the barrel toroid magnet, arranged in three cylindrical layers around the beam axis, while the endcap chambers are located in front and behind the two endcap toroid magnets, forming three large wheels perpendicular to the beam.

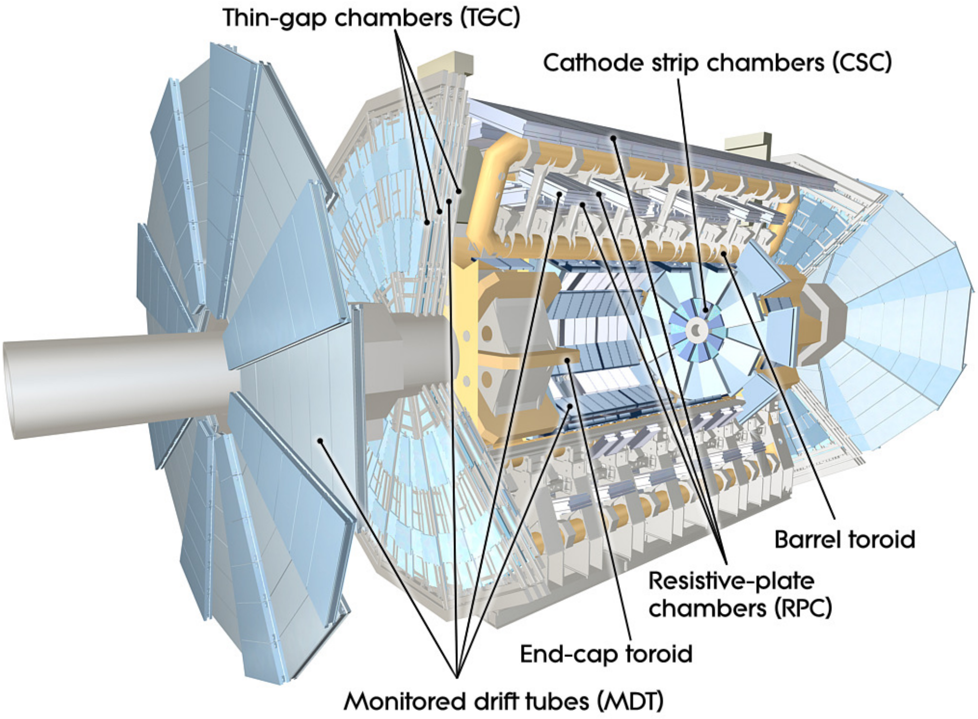

Figure 4.9. Cut away view of the ATLAS muon system [71].

Precision muon momentum measurement is performed by the Monitored Drift Tube (MDT) chambers, which consist of 3 to 8 layers of drift tubes, 3 cm in diameter, filled with an ionising gas mixture of Ar/CO_2. The 1150 MDT chambers contain 354 000 channels and cover the range $|\eta| < 2.7$, except in the innermost endcap layer where their coverage is limited to $|\eta| < 2.0$. In the forward region ($2 < |\eta| < 2.7$), 32 Cathode Strip Chambers (CSCs) are used in the innermost layer due to their higher rate capability and time resolution. The CSCs are multiwire proportional chambers with cathode planes segmented into strips in orthogonal directions with 31 000 electronic channels.

The muon trigger subsystem consists of Resistive Plate Chambers (RPCs) in the barrel and Thin Gap Chambers (TGCs) in the endcap regions. The 606 RPCs are gaseous parallel electrode plate detectors, covering the region $|\eta| < 1.05$, with 373 000 readout channels, while the 3 588 TGCs are multi-wire proportional chambers, covering the region $1.05 < |\eta| < 2.7$ with 318 000 readout channels. These chambers provide bunch-crossing identification and well-defined p_{T} thresholds for triggering, and measure the muon coordinate in the direction orthogonal to that determined by the precision-tracking chambers.

4.2.6. Trigger and Data Acquisition System

The proton-proton interaction rate at the LHC design luminosity is approximately 1 GHz, while the data recording is limited by technology to around 200 Hz. This means that only some events can be stored. ATLAS uses a specialised trigger and data acquisition (TDAQ) system, schematically shown in Figure 4.10, to select events with interesting characteristics to store for physics analysis. The required reduction factor is achieved by the three level online trigger system. Level 1 (L1) [85] is implemented in high-speed custom electronics. The subsequent two levels of reduction are provided by the High Level Trigger (HLT) [86], which is comprised of two distinct parts: Level 2 (L2), a system of programmable processors; and the Event Filter (EF), a large farm of CPUs.

The L1 trigger searches for high p_{T} muons, electrons and photons, jets, and tauons decaying into hadrons, as well as large missing and total transverse energy. Its selection is based on information from a subset of detectors. High p_{T} muons are identified using dedicated trigger chambers, RPC in the barrel and TGC in endcap regions, and the remaining particles are identified from reduced granularity information from the calorimeters. The L1 decision is made within 2.5 μs, reducing the rate to a maximum of 75 kHz.

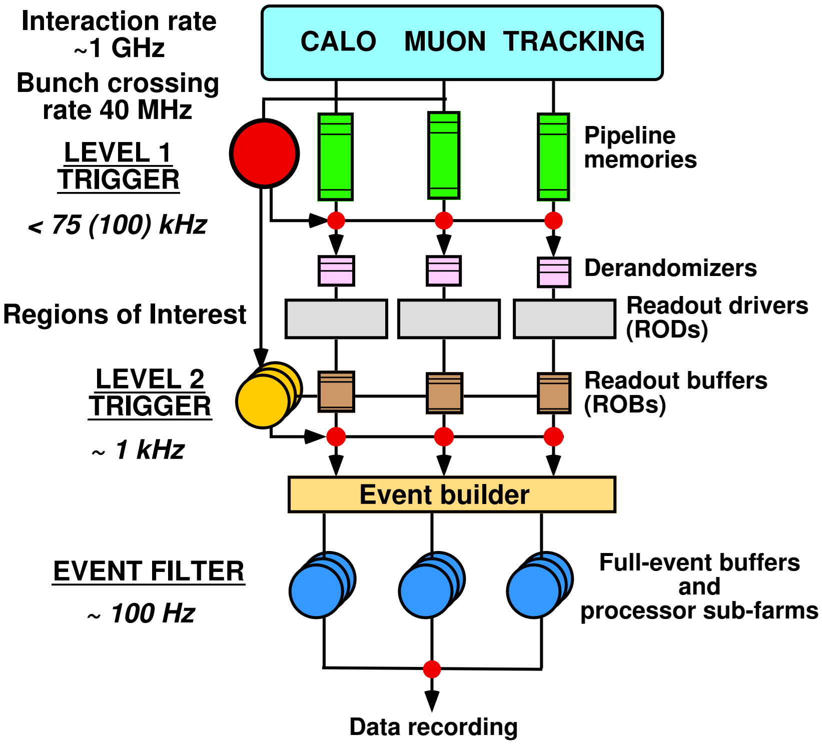

Figure 4.10. Schematic view of the ATLAS TDAQ system [77].

The L1 trigger also provides Region of Interests (RoIs), which are areas within the detector where interesting features in the event have been identified, which seed the L2 selection. The L2 trigger uses RoI information about coordinates, energy, and type of signature to limit the amount of data which must be transferred from the detector readout. It is designed to reduce the event rate to approximately 3 kHz in an average event time of 40 ms. The final stage of the event selection, the EF, reduces the event rate to about 200 Hz and has an average event processing time of order 4 s. Unlike L2, which uses specialised algorithms optimised for timing performance, the EF typically uses the same algorithms as the offline reconstruction. The use of the more complex pattern recognition algorithms and calibration developed for offline helps in providing the additional rejection needed at the EF. A detailed description of the electron trigger selection algorithms is given in Chapter 5.

The data acquisition (DAQ) controls all data movements down the trigger selection chain. This system receives and buffers the event data from the detector, at the L1 trigger acceptance rate, from the detector-specific readout electronics over point-to-point links. On request, it subsequently moves the data within the RoIs to the L2 trigger. For those events fulfilling the L2 selection criteria, it performs event building at the L2 trigger acceptance rate. The assembled events are then moved by the DAQ to the EF, and the selected events are moved to permanent storage. In addition to the movement of data, the DAQ system also provides for the configuration, control and monitoring of all hardware and software components needed for data-taking. Supervision of the detector equipment and related infrastructure is handled separately by the Detector Control System (DCS) [87].

4.3. Detector Simulation

Monte Carlo (MC) simulations are used to study detector response and performance, and develop particle reconstruction algorithms and prepare physics analyses. There are three steps involved in the simulation of ATLAS data [88]: generation of the event and immediate decays; simulation of the detector and physics interactions; and digitisation of the energy deposited in the sensitive regions of the detector into voltages and currents for comparison to the readout of the ATLAS detector

Event generators focus on the description of the physics involved in particle production and decay, using theoretical understanding of the processes involved. An assortment of MC generators exist for LHC physics simulation and are chosen according to their suitability for the required physics process. Further information about event generation is given in Chapter 7.

A single particle generator is also used for testing and evaluating the reconstruction efficiencies. Although unphysical, these generators produce events with a single primary particle, for example a muon, electron, or charged pion, at a specified energy, position, and momentum direction.

The response of the ATLAS detector to generated events is estimated using a dedicated simulation based on GEANT4 [89] using the Quark-Gluon String Precompound model [90] for the simulation of interactions of high energy hadrons and the Bertini intranuclear cascade model [91] for low energy hadrons. The simulation uses a model of the ATLAS detector which is constantly updated with revisions of detector material and conditions, such as calibrations, dead channels and misalignments from data studies.

The ATLAS digitisation software converts the records of energy depositions produced by the simulation into detector responses. Charge collection, including crosstalk, electronic noise and channel dependent variations in detector response are all modelled and tuned to reproduce results seen in laboratory tests, test beam data and cosmic ray runs. To produce a realistic model of detector response, additional effects from pileup and other beam backgrounds are also incorporated.

Due to the complicated detector geometry and detailed physics description used by the ATLAS GEANT4 simulation, it is impossible to achieve the required simulated statistics for many physics studies without faster simulation. To overcome this problem, ATLAS has developed a number of fast simulation software packages to complement the full GEANT4 simulation (commonly called 'full simulation'), each of which is useful in different physics cases.

ATLFAST-I [92] has been developed for physics parameter space scans and studies that require very large statistics but do not require the level of detail contained in the full simulation. A factor of 1000 speed increase over full simulation is achieved with sufficient detail for many feasibility studies. ATLFAST-II is a fast simulation meant to provide large statistics to supplement full simulation studies. The aim is to try to simulate events as fast as possible while still being able to run the standard ATLAS reconstruction. ATLFAST-II is made up from two components: the Fast ATLAS Tracking Simulation (Fatras) [93] for the inner detector and muon system simulation and the Fast Calorimeter Simulation (FastCaloSim) [94] for the calorimeter simulation. An improvement over full simulation time of a factor of 10 is achieved with full GEANT4 inner detector and muon simulation and FastCaloSim, and a factor of 100 is achieved with Fatras and FastCaloSim.

In both event generation and detector simulation, information called 'truth' is recorded for each event. In generation, the truth is a history of the interactions from the generator, including incoming and outgoing particles. In simulation, truth tracks and decays for certain particles are stored. This truth information can be used during analysis of simulated data to for performance studies and analysis optimisation.

4.4. Particle Reconstruction and Identification

The object of the experiment is to determine the particles created in the proton-proton collisions by identifying their decay products. Each subsystem of the ATLAS detector has a key role to play in particle reconstruction and identification. The particles which ATLAS can identify and reconstruct are: electrons, photons, muons, tauons and jets which originate from hadrons, quarks or gluons. Particles which leave no detectable signature in the detector are inferred using energy and momentum conservation, through the calculation of transverse missing energy. The reconstruction and calculation of these particles and quantities relies on the more basic observables of tracks left in the inner detector by charged particles and clusters of energy deposits in the calorimeters. Details of the general reconstruction of these quantities and basic identification of these particles in ATLAS is provided below. The final particle selections are analysis dependent and will be discussed later.

4.4.1. Track Reconstruction

Track reconstruction begins with silicon clusters which are deduced from raw hits in the inner detector. Three-dimensional space points are then formed from these clusters. Pixel clusters translate directly into space points, while SCT clusters from either side of a module are associated to form a single SCT space point.

Tracks are first identified using the 'inside-out' pattern recognition algorithm [95], which starts with the silicon space points close to the IP and extends outwards towards the TRT. Track seeds are created from three space points and use defined roads to search for hits to associate to the track. The next step refines the tracks using a more sophisticated track fitter and removes overlapping tracks. This inside-out tracking procedure selects track candidates with $p_{\mathrm{T}} > 100$ MeV. Lastly these silicon tracks are used to define roads in which a TRT extension can be attached. The inside-out sequence is followed by an outside-in sequence that runs on the remaining hits after those hits already used in a track have been removed. The 'outside-in' algorithm is seeded in the TRT and the track is extrapolated into the silicon. In this second step, tracks from secondary interactions, such as photon conversions and long-lived hadron decays, with $p_{\mathrm{T}} > 300$ MeV are recovered.

A reconstructed track can be parameterised with respect to the reconstructed vertex using the perigee representation (d_0, z_0, ϕ_0, θ, q/p), where d_0 and z_0 denote the transverse and longitudinal impact parameters, respectively. Accurate reconstruction of the impact parameter is essential for vertex reconstruction and flavour tagging.

4.4.2. Cluster Reconstruction

Clusters are built from energy deposits in calorimeter cells. There are two clustering algorithms in ATLAS: sliding window clustering and topological clustering [96]. Sliding window clustering builds fixed size clusters from seeds selected using a sliding window algorithm. This is fast and useful for objects with a well defined energy deposition pattern, such as electromagnetic showers from electrons and photons. Topological clustering groups cells based on their neighbouring cells and the significance of their energy contents. This results in clusters with a variable number of cells, which is more suited for hadron reconstruction and hence jets, since hadronic showers have a more varied energy response.

The offline sliding window cluster algorithm uses calorimeter towers as seeds. Calorimeter towers are built in bins of size $\Delta\eta \times \Delta\phi = 0.025 \times 0.025$ in the electromagnetic calorimeter and in the region $|\eta| < 2.5$ and the energy deposits are summed longitudinally within the towers. The sliding window is 5×5 towers in size and moved around the tower grid to find a local maximum in $E_{\mathrm{T}} > 3$ GeV to use as a precluster seed. If a precluster is found within 2×2 towers of another, the precluster with the largest transverse energy is kept. These preclusters act as seeds to a cluster, where the cluster size is dependent on the location of the cluster and the hypothesis of the particle type. For example, an electron cluster is $\Delta\eta \times \Delta\phi = 0.075 \times 0.175$ in size in the barrel region and$\Delta\eta \times \Delta\phi = 0.125 \times 0.125$ in size in the endcap region. Cluster energy is calculated from the amplitudes observed in the cells of the longitudinal layers of the electromagnetic calorimeter and of the presampler (where present). The calculation sums the weighted energies in these compartments, then takes into account several corrections, for example, for shower depth, lateral and longitudinal leakage and local energy modulation.

Topological clusters (topoclusters) are seeded by cells with a large signal to noise ratio, $\Gamma \equiv |E_{\mathrm{cell}}/\sigma_{\mathrm{noise,cell}}| > 4$, where σ_{noise} is the width of noise, which can either be purely electronic noise or a sum in quadrature of electronic and pileup noise. The cluster is then grown by iteratively adding neighbouring cells with $\Gamma > 2$. Finally, a ring of guard cells that satisfy $\Gamma > 0$ are added to the cluster. These 4/2/0 noise thresholds are optimised to suppress electronics noise as well as pileup from minimum bias events while keeping single pion efficiency as high as possible [97]. To prevent overlap of particle deposits, the clusters are then split between any local maxima.

4.4.3. Electron Reconstruction and Identification

An electron will leave a track in the inner detector and deposit energy in the electromagnetic calorimeter. The identification and measurement of electrons is performed using two main algorithms. The first algorithm is optimised for the reconstruction of isolated, high p_{T} electrons and is seeded by a cluster in the electromagnetic calorimeter. The second algorithm is optimised for reconstructing non-isolated, low p_{T} electrons and is seeded by a track in the inner detector. The high p_{T} algorithm is used for electron reconstruction in this thesis.

The first stage of electron reconstruction is to seed a cluster in the electromagnetic calorimeter using the aforementioned sliding window algorithm. The second stage is to match the cluster to an inner detector track with $p_{\mathrm{T}} > 0.5$ GeV. The chosen track has an extrapolated impact point in the second layer of the electromagnetic calorimeter closest to the cluster barycenter.

Electron identification makes use of a number of variables that can distinguish between electrons and background hadrons. These discriminating variables are both from the calorimeters and the inner detector. Electrons will deposit very little energy in the hadronic calorimeter compared to jets and so hadronic leakage is a good discriminator against jet background. The lateral shower shape in the second layer of the electromagnetic calorimeter can be used to distinguish the narrower showers originating from electrons compared to the wider showers of high energy pions and jets. The fine segmentation of the first layer of the electromagnetic calorimeter can be used to identify any substructure within a shower coming from pions or photons. The inner detector is used to require constraints on the electron track to reduce background from photon conversions and jets containing high p_{T} pions. The matched track must contain a minimum number of hits in the pixel and silicon detectors and point back towards the primary vertex, in addition to having a minimum distance in η to the considered cluster.

4.4.4. Muon Reconstruction and Identification

A muon will pass through the entire ATLAS detector, leaving a mark in each of the subsystems: a track in the inner detector, minimal energy deposits in the calorimeters and a track in the muon spectrometer. The identification and measurement of muons incorporates information from each of the subsystems, where for each stage of the muon reconstruction there are multiple algorithms that may be used. The details of each individual algorithm will not be discussed here, instead a broad overview will be given that will summarise the stages of muon reconstruction.

The first stage of muon reconstruction is to find a track in the muon spectrometer. A track is found from segments in the separate muon spectrometer modules using segment pattern recognition and global spectrometer track tracing through the toroidal magnetic field. The track parameters obtained from the muon spectrometer track fit are extrapolated to the interaction point taking into account both multiple scattering and energy loss in the calorimeters.

The second stage of muon reconstruction is to find a matching track in the inner detector. The third stage of muon identification is to combine the muon spectrometer and inner detector tracks. The combination algorithm [98] used in this thesis, statistically merges the independently found tracks to obtain a χ^2 value that can be used to assess the match.

4.4.5. Jet Reconstruction

High energy quarks and gluons will traverse the first three main layers of the ATLAS detector, fragmenting into a large number of collimated hadronic particles that form what is called a jet. These particles will leave tracks in the inner detector if they are charged and energy deposits in the electromagnetic and hadronic calorimeters. In this thesis, jet reconstruction is performed by two main algorithms, a seeded fixed cone finder with split and merge, and the anti-$\mathrm{k_T}$ sequential recombination algorithm, whose inputs are ‘pseudoparticles’. A pseudoparticle is created from a topocluster by assigning it a four-momentum based on its energy and spatial coordinates η and ϕ.

The seeded fixed cone jet algorithm first orders all the input pseudoparticles in decreasing p_{T}. If the highest p_{T} pseudoparticle is above the seed threshold $p_{\mathrm{T}}^{\mathrm{seed}}$, all topoclusters within a cone of fixed radius R_{cone}, are combined with the seed. A new direction is calculated from the four-momenta inside the initial cone and a new cone is centred around it. Objects are then (re-)collected in this new cone, and again the direction is updated. This process continues until the direction of the cone does not change anymore after recombination, at which point the cone is considered stable and is called a jet. At this point the next seed is taken from the input list and a new cone jet is formed with the same iterative procedure. This continues until no more seeds are available. The jets found this way can share constituents and a split and merge procedure is used to define non-overlapping exclusive jets. Jets which share constituents with more than a certain fraction f_{sm} of the p_{T} of the less energetic jet are merged, while they are split if the amount of shared p_{T} is below f_{sm}. The parameters of the cone algorithm used are $p_{\mathrm{T}}^{\mathrm{seed}} = 1$ GeV, $R_{\mathrm{cone}} = 0.4$ and $f_{\mathrm{sm}} = 0.5$ [78].

A general sequential recombination algorithm introduces distances d_{ij} between pseudoparticles, defined as $d_{ij} = \min(p_{\mathrm{T}i}^{2k}, p_{\mathrm{T}j}^{2k})\frac{\Delta_{ij}^{2}}{R^{2}}$ where $p_{\mathrm{T}i}$ is the transverse momentum of object i, $\Delta_{ij}^{2} = (\eta_i - \eta_j)^2 + (\phi_i - \phi_j)^2$, R is used to set the scale of jet radii and k is used to set the relative power of the momentum (p) and distance (Δ) scales. An ordered list of all the distances and relative transverse momenta between the input pseudoparticles is generated. If the smallest item in the list is a d_{ij}, then pseudoparticles i and j are added together to form a new pseudoparticle and the list is updated. It the smallest item is a p_{ti}^{2k}, pseudoparticle i is labelled a jet and removed from the list. The anti-k$_{\mathrm{T}}$ algorithm is the special case when $k = -1$ [99], and the cone size used in this thesis is $R = 0.4$.

4.4.6. Flavour Tagging

The identification of jets that originate from the fragmentation and hadronisation of b quarks can help discriminate different processes. When b quarks are produced in interactions, they fragment to form b hadrons. Due to the relatively high masses of the b quark and the b hadrons, this fragmentation is hard and the b hadron retains about 70% of the b quark momentum. Additionally due to their mass, the b hadron decay products also may have a large momentum transverse to the b hadron flight path and the opening angle of the decay products is large enough to allow separation. Due to the relatively long lifetime of hadrons containing a b quark, the b hadron will travel a measurable distance before decaying. Such displaced vertices can be identified by measuring the impact parameters of the tracks from the b hadron decay products or explicitly reconstructed. Spatial flavour tagging algorithms use the impact parameters of tracks associated to jets and/or reconstruction of secondary vertices to discriminate between jets originating from b quarks from those initiated by light quarks or gluons.

The more sophisticated spatial favour tagging algorithms use a combination of impact parameter and secondary vertex information. IP3D+SV1 is one such algorithm, combining the likelihoods of the IP3D and SV1 algorithms. The IP3D tagging algorithm combines the significance of the longitudinal and transverse impact parameters of all the tracks inside a jet into a discriminant. The SV1 secondary vertexing algorithm combines the significance of the invariant mass of all tracks associated to the vertex, the ratio of the sum of the energies of the tracks participating to the vertex to the sum of the energies of all tracks in the jet and the number of two-track vertices into a discriminant.

The simpler spatial flavour tagging algorithms only use one discriminating variable rather than a combination. The SV0 tagging algorithm involves placing a cut on the signed decay length significance $L/\sigma(L)$, of a reconstructed secondary vertex, where L is the decay length of the secondary vertex and $\sigma(L)$ its uncertainty. The sign of $L/\sigma(L)$ is given by the sign of the projection of the decay length vector on the jet axis.

Flavour tagging can also be performed by identifying the lepton from semileptonic b hadron decays. Due to the hard fragmentation and high mass of b hadrons, the lepton will have a relatively large transverse momentum and also a large momentum relative to the jet axis and thus can be identified. However, these lepton flavour tagging algorithms are statistically limited by the semileptonic b branching ratio and will not be used in the analyses presented in this thesis.

4.4.7. Missing Transverse Energy Reconstruction

In a detector, the detection and measurement of particles depends on their interactions with the material of the detector. However there exist particles, such as neutrinos, which do not interact and thus do not leave a direct signature in the detector. These particles leave an indirect signature, which is the energy that is not detected but expected because of energy and momentum conservation.

In a hadron collider the initial momentum of the colliding particles along the beam axis is unknown, due to the composite nature of a hadron, so the total amount of missing energy cannot be calculated. However, the initial momentum transverse to the beam axis is zero, so any net momentum in that direction indicates transverse missing energy, or $E_{\mathrm{T}}^{\mathrm{miss}}$. This quantity is also easier to study in a hadron collider than the total missing energy since it is not affected by all the activity which occurs in the forward regions from soft scatterings of the partons in the beam.

The $E_{\mathrm{T}}^{\mathrm{miss}}$ reconstruction in ATLAS is based on the energy deposited in each calorimeter cell calibrated to an associated reconstructed particle $E_{\mathrm{T.calo}}^{\mathrm{miss}}$ and an estimate of energy lost by particles entering the cryostat $E_{\mathrm{T.cryo}}^{\mathrm{miss}}$. An additional correction $E_{\mathrm{T.muon}}^{\mathrm{miss}}$ is required for muons which are minimum ionising particles and thus do not deposit much energy in the calorimeters. The total $E_{\mathrm{T}}^{\mathrm{miss}}$ is the sum of these three terms:

$$E_{\mathrm{T}}^{\mathrm{miss}} = E_{\mathrm{T.calo}}^{\mathrm{miss}} + E_{\mathrm{T.cryo}}^{\mathrm{miss}} + E_{\mathrm{T.muon}}^{\mathrm{miss}}.$$

See Appendix B for a detailed description of the $E_{\mathrm{T}}^{\mathrm{miss}}$ reconstruction algorithm and a study of its expected performance in minimum bias events at $\sqrt{s} = 14$ TeV performed by the author. Only the major steps will be outlined here.

The $E_{\mathrm{T.muon}}^{\mathrm{miss}}$ term is calculated from the momenta of the muons measured using standalone muon spectrometer reconstruction. This insures that energy lost by muons in the calorimeter is not double counted. Only good quality muons with a matched track in the inner detector are considered.

The $E_{\mathrm{T.cryo}}^{\mathrm{miss}}$ term corrects for energy lost in the cryostat between the liquid argon electromagnetic calorimeter and the tile hadronic calorimeter. This energy loss is recovered using the correlation between energies of the final layer of the liquid argon calorimeter and the first layer of the hadronic calorimeter.

The $E_{\mathrm{T.calo}}^{\mathrm{miss}}$ term is the dominant contribution to $E_{\mathrm{T}}^{\mathrm{miss}}$. It is calculated using cells in topoclusters calibrated to the reconstructed particle they are associated with. Only cells in topoclusters are used to take advantage of the 4/2/0 noise thresholds. The association of calorimeter cells to particles is performed by filling an association map, starting from reconstructed particles in the chosen order, navigating back to their component clusters (sliding window clusters for electrons/γs, combined clusters for taus and topoclusters for jets and b jets) and back again to their cells. If a cell belongs to more than one kind of reconstructed particle, the first association is taken, in the chosen order of the reconstructed objects. If a cell belongs to more than one object of the same kind, all associations are taken and the geometrical weights are also included. Cells within topoclusters which are not associated to any reconstructed particle are calibrated using global calibration weights.

Complementary to the reconstruction of $E_{\mathrm{T}}^{\mathrm{miss}}$ is total transverse energy, ΣE_{T}, which is the scalar sum of the transverse energy, as opposed to $E_{\mathrm{T}}^{\mathrm{miss}}$ which is the vector sum, and is calculated using the same quantities.

4.5. Detector Operation

Installation of the ATLAS detector at point 1 began in 2005. Each part of the detector was lowered into the cavern, connected to its required services and electronic readout channels and integrated into the ATLAS TDAQ system. All components were extensively tested, some using test beams, prior to the insitu commissioning [71].

The ATLAS detector was largely operational and prepared for the first LHC start up in September 2008. It had been collecting cosmic ray events in combined mode and was kept fully operational from the end of July 2008. The envisaged target energy for the LHC in 2008 was 5 TeV per proton beam, with a luminosity target of 10^{32} cm^{-2} s^{-1}. It is against this backdrop that the feasibility studies presented in this thesis were conducted.

The LHC start up on the 10th of September 2008 went smoothly. Protons with energies of 450 GeV were successfully injected into the LHC from the accelerator complex. The LHC machine was operated with a single proton beam, both directions were operated successively, with and without capturing. However, due to an incident on the 19th of September, further beam commissioning was stopped for repairs.

The ATLAS detector continued recording cosmic ray events through 2008 and 2009, obtaining a dataset of 7.6 million events, which were used for commissioning and initial calibration and performance studies. Performance close to design goals was obtained for all the different detector systems, indicating their readiness for LHC collision data [100, 101, 102, 103].

LHC repairs continued until December 2009, when a series of runs at centre of mass energies of 0.9 TeV and 2.36 TeV was performed. When the beams were colliding and declared to be stable by the LHC operators, all main ATLAS detector components were fully operational and all levels of the trigger and data acquisition system performed as expected, assuring smooth and well monitored data taking with around 90% efficiency. The data sample at 0.9 TeV contains nearly 400 000 events recorded with high quality calorimeter and tracking information, corresponding to an integrated luminosity of approximately 9 μb^{-1}. The data sample at 2.36 TeV, contains 36 000 events, corresponding to approximately 0.7 μb^{-1}. Although the p_{T} spectrum of the particles produced in these collisions was well below the range for which ATLAS was designed, the performance of the detector was found to be remarkably good [104].

In January 2010, a decision was made for the LHC to run at an energy of 3.5 TeV per proton beam, with a luminosity target of 10^{32} cm^{-2} s^{-1}, with the goal of providing experiments with 1 fb^{-1} by the end of 2011. 7 TeV proton-proton collisions began on the 30th of March and ended for 2010 on the 4th of November to start again in March 2011. Almost all machine performance milestones were met, even exceeded in some cases. The LHC parameters for one of the last runs of the year, compared to design energy and luminosity, is given in Table 4.3. Note that the achieved number of protons per bunch and emittance are both better than design.

During the seven month period of $\sqrt{7}$ = 7 TeV proton-proton collisions in 2010, a total luminosity of 48.9 pb^{-1} was delivered to ATLAS during stable beam periods by the LHC. The instantaneous luminosity over this time increased from ~10^{27} cm^{-2}s^{-1} to ~10^{32} cm^{-2}s^{-1} as different bunch configurations were used. ATLAS recorded 45.0 pb^{-1} worth of data, inferring a total data taking efficiency of 92.0%. The inefficiency accounts for the turn on of the high voltage of the pixel, SCT and some of the muon detectors (2.0%) and any inefficiencies due to deadtime or due to individual problems with a given subdetector that prevent the ATLAS data taking to proceed (4.4%). Some of these inefficiencies can be recovered by offline data reprocessing. This is exceptional performance for a detector in its first year of operation.

Table 4.3. Comparison of LHC parameters reached running in proton-proton collision mode in 2010 compared to design energy and luminosity at the ATLAS interaction point.

Beam parameters		
Proton energy	3.5 TeV	7 TeV
Number of protons per bunch	~1.2×10^{11}	1.15×10^{11}
Number of bunches	368	2,808
Time between bunches	150 ns	25 ns
Circulating beam current	~81 mA	584 mA
Stored energy per beam	~25 MJ	360 MJ
Luminosity parameters		
Peak luminosity	~10^{32} cm^{-2}s^{-1}	10^{34} cm^{-2}s^{-1}
Relativistic gamma factor	3,731	7,641
Beta function	~3.5 m	0.55 m
Emittance	~2.4 μm	3.75 μm
Crossing angle	~100 μrad	285 μrad
Transverse beam size	~60 μm	16.7 μm

There is no promised road leading to definite results. What's important is how to keep open as many options as possible.

– Makoto Kobayashi

5

Electron Triggering

The ATLAS trigger system is based on three levels of selection to capture interesting physics events with cross sections many orders of magnitude smaller than the total LHC proton-proton cross section. The trigger selections must provide sufficient rejection power to reduce the data rate to be compatible with offline computing resources while retaining rare physics processes of interest. At the LHC, signatures with leptons in their final states are easy to detect and disentangle from backgrounds. In particular, electrons are important for many analyses, from SM precision physics to searches for new physics. This chapter describes the strategy, implementation and performance of the electron trigger selection, following Reference [78], focusing on an alternative algorithm for seeding clusters at L2 which the author developed. This alternate algorithm was constructed to identify events containing collimated electrons, such as boosted $J/\psi \to e^+e^-$ decays.

5.1. Electron Trigger Requirements

Events featuring electrons in their final states are important signatures for many physics analyses at the LHC, from SM measurements of top quark properties to

Table 5.1. Examples of important processes requiring good electron trigger selection [78].

Momentum Range	**Process**
Low p_T $\sim 5 - 20$ GeV	$J/\psi \to e^+e^-$ $\Upsilon \to e^+e^-$ $\gamma^* \to e^+e^-$
High p_T $\sim 20 - 100$ GeV	$Z \to e^+e^-$ $W \to e^+\nu_e$ $t \to bW^+ \to be^+\nu_e$ $H \to ZZ^{(*)} \to e^+e^-e^+e^-, e^+e^-\mu^+\mu^-$
Very high p_T $\sim 100 - 1000$ GeV	$Z' \to e^+e^-$ $W' \to e^+\nu_e$

searches for new physics such SUSY. Furthermore, the electron trigger must be highly efficient for benchmark SM processes such as $Z \to e^+e^-$ and $W^+ \to e^+\nu_e$, which are crucial for understanding the detector performance, calibration and alignment. Table 5.1 lists important physics channels yielding electrons in the final state with their various transverse momenta ranges. To select electrons from all these processes, electron trigger algorithms need to be optimised for high signal efficiency and background rejection over a wide range of transverse momenta, from a few GeV to several TeV.

The electron trigger algorithms also need to provide the required reduction in event rate within the constraints of the online environment. They need to be robust against detector effects such as miscalibration, misalignment, dead and noisy read-out cells or sectors, as well as changes in luminosity and beam conditions. The challenging online environment of the LHC, with an average of 23 inelastic events per bunch crossing, separated by only 25 ns at design luminosity, places tight constraints on execution time and data requirements of the algorithms, which should aim to reject background processes as early as possible in order to optimise the usage of the available resources.

5.2. Electron Trigger Selection

Each of the ATLAS triggers can be viewed as a series of selection steps of increasing complexity, and the electron trigger is no different. At L1, electrons are selected using calorimeter information with reduced granularity. After receiving the L1 RoI positions, the L2 trigger reconstructs clusters using the full calorimeter granularity within the RoI and associates these clusters with a track in the inner detector, requiring a match in position. Electron candidates passing the L2 selection criteria are retained to be examined by the EF. In the EF, electrons are selected with a strategy very similar to that of L2. The main differences arise from the availability of calibration data and the possibility to use more sophisticated reconstruction algorithms with access to the detector data for the full event. This results in sharper thresholds and better background rejection. Each of these steps and the systems involved are described in more detail in the following subsections, and distributions of the selection variables will be shown, comparing candidates from 482 000 signal single electron events with a distribution flat in E_T between 7 and 80 GeV produced using a single particle generator, to candidates from 499 000 QCD multijet background events generated by PYTHIA with at least one jet with $E_T > 17$ GeV.

5.2.1. Level 1 Electron Trigger Selection

The L1 trigger, shown in Figure 5.1, uses three main components to make its decisions. The Level 1 Muon Trigger (L1Muon) uses track information from dedicated, fast muon chambers to identify high p_T muon candidates. The Level 1 Calorimeter Trigger (L1Calo) uses calorimeter energy deposits to identify various high E_T particles and calculate total event energy sums. Results from both of these systems are then processed by the Central Trigger Processor (CTP). The CTP selects events based on a predefined list of trigger items using logical combinations of results from L1Calo and L1Muon.

The L1 decision is made within 2.5 μs, reducing the event rate from the possible initial 40 MHz to a maximum of 75 kHz. The decision time includes the transmission of signals between the detector and the trigger electronics. During the L1 trigger processing, the data from all detector systems are held in pipeline memories. Once an event has been accepted, the data are read out, formatted and initial preprocessing applied before they are stored in readout buffers (ROBs) for use by the L2 and EF.

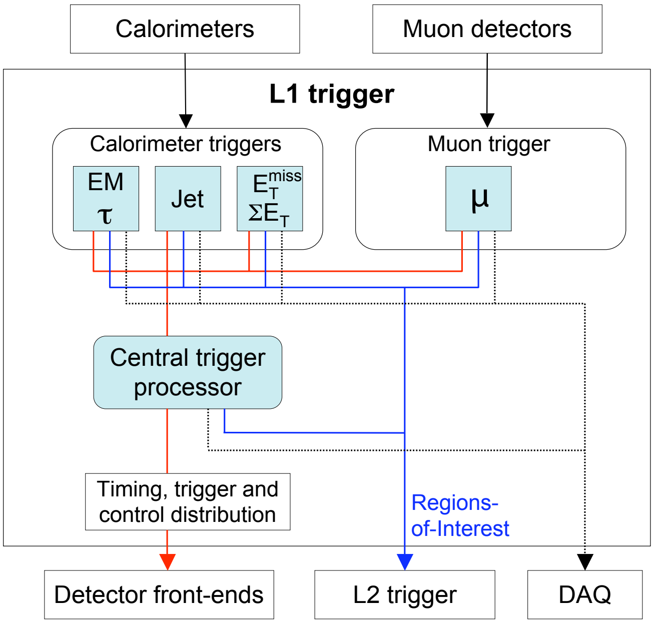

Figure 5.1. Block diagram of the ATLAS L1 trigger [105].

The L1 trigger also provides the important functionality of uniquely identifying the bunch crossing of interest, where each trigger signal has to be correctly mapped to one bunch crossing. The short bunch crossing interval, physical size of the muon spectrometer and the long pulse shape of the calorimeter signals makes this a non-trivial task.

At L1, electron candidates are identified using the L1Calo triggers [105] which obtain information from both the electromagnetic and hadronic calorimeters in the barrel, endcap and forward regions up to $|\eta| < 2.5$. The granularity of the information used however, is reduced by the use of trigger towers which merge several calorimeter cells, yielding a region of 0.1×0.1 in $\Delta\eta \times \Delta\phi$ in most areas of the calorimeter. An example of a trigger tower in the barrel of the electromagnetic calorimeter is shown in Figure 4.8. In these towers, all the cells are summed separately over the full depth of the electromagnetic and hadronic calorimeters.

The L1 electron selection algorithm, schematically shown in Figure 5.2, searches for narrow, high E_T showers using a sliding window of 4×4 towers provided by the L1Calo triggers. For a 4×4 window to contain an electron candidate, the central 2×2 core must be a local E_T maximum and the sum of one of the four possible 1×2 and 2×1 combinations within the core region is required to pass the electromagnetic cluster E_T threshold, E_T^{EM}.

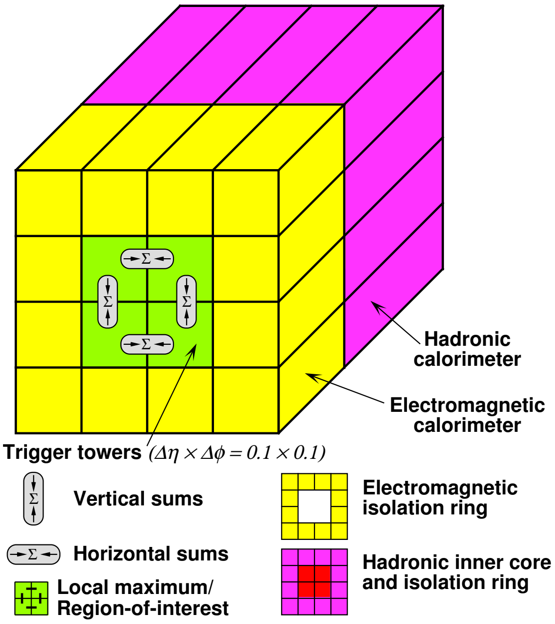

Figure 5.2. Schematic view of the ATLAS L1 electron trigger algorithm [71].

The main background for the L1 electron selection algorithm is from the overwhelming rate of hadronic jets. Therefore, extra requirements that can be used to enhance the selection are transverse and hadronic isolation. Transverse isolation is defined by requiring that the total E_{T} for the 12 electromagnetic towers surrounding the core 2×2 region is less than the electromagnetic isolation E_{T} threshold, $E_{\mathrm{isol}}^{\mathrm{EM}}$. Hadronic isolation is defined by two requirements: that the total E_{T} for the 12 hadronic towers surrounding the 2×2 core region is less than the hadronic isolation E_{T} threshold, $E_{\mathrm{isol}}^{\mathrm{HAD}}$; and that the total E_{T} for the 4 hadronic calorimeters behind the 2×2 core region is less that the hadronic core E_{T} threshold, $E_{\mathrm{core}}^{\mathrm{HAD}}$.

The distributions of these isolation variables for signal and background are shown in Figure 5.3. It can be seen that isolation is a good discriminator between signal electrons and background jets. However since isolation depends on the topology and energy distribution of the event as well as luminosity and beam conditions, these variables need to be well understood before being used for selection during data taking.

5.2.2. Level 2 Electron Trigger Selection

The software based L2 trigger provides the next stage of event selection after the hardware based L1 trigger. It is an asynchronous, distributed system running on farms built from commodity computing and network technology. The L2 trigger is

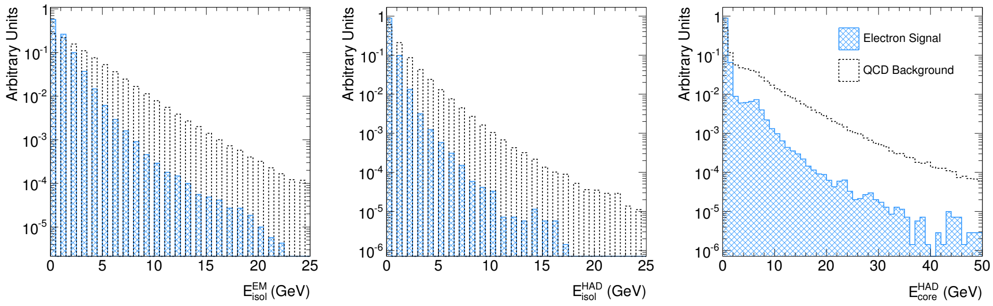

(a) Electromagnetic isolation **(b)** Hadronic isolation **(c)** Hadronic core energy

Figure 5.3. L1 electron isolation variables for simulated single electrons with E_T between 7 and 80 GeV (solid line, hatched histogram) compared with simulated background candidates from a filtered QCD multijet sample with at least one jet with E_T > 17 GeV (dashed line, hollow histogram). For the background, only clusters that do not match to a true electron within a ΔR of 0.1 are considered. All distributions have been normalised to unit area.

designed to select and reject events with an average time per event of 40 ms, reducing the event rate of the L1 trigger from 75 kHz to approximately 3 kHz. In order to operate within this time budget, the L2 trigger uses a sequence of highly optimised algorithms that only access a fraction of the event data, using RoI information provided by the L1 trigger. This includes information of the η and ϕ position and transverse energy thresholds passed by candidates and total event energy sums. This enables the L2 algorithms to select precisely the region of the detector in which the interesting features reside and therefore the ROBs from which to request the data for analysis. Data requests may be done several times per event by different L2 algorithms that progressively refine the selection. At any stage in the processing an event may be rejected. Each L2 processor can analyse several events concurrently.

In L2, electron candidates are selected using information from the calorimeters and inner detector. An electromagnetic cluster is built from the calorimeter using L1 RoI position information. From this, transverse electromagnetic cluster energy, various shower shape variables and hadronic leakage are calculated and corrected using basic position and energy calibration tools, including an amendment for the transition region between the barrel and endcap calorimeters. Various selections are applied to these variables to identify electron candidates. The inner detector is then used to search for a track in the RoI and electron candidates are selected by requiring a match in position between the cluster and associated track.

L2 calorimeter reconstruction is seeded by the η and ϕ positions provided by L1. Calorimeter cells in a region of $\Delta\eta \times \Delta\phi = 0.4 \times 0.4$ centred on the L1 coordinates are retrieved. The default algorithm for seeding clusters scans the cells in the second layer of the electromagnetic calorimeter and searches for the cell with the highest E_{T} within $\Delta\eta \times \Delta\phi = 0.15 \times 0.15$ of the L1 coordinates. An alternative algorithm was developed by the author which searches for seeds using a sliding window algorithm in the second layer of the electromagnetic calorimeter, including energy contributions from the first layer. The windows used are 3×3 cells in size, which corresponds to $\eta \times \phi = 0.075 \times 0.075$ where $|\eta| < 1.4$ and $\eta \times \phi = 0.225 \times 0.075$ where $|\eta| \geq 1.4$ in the barrel region and $\eta \times \phi = 0.025 \times 0.025$ where $|\eta| < 2.5$ and $\eta \times \phi = 0.3 \times 0.3$ where $|\eta| \geq 2.5$ in the endcap region of the electromagnetic calorimeter. Cluster seeds are identified as windows with total E_{T} above a programmable threshold. This energy sum is calculated for all possible 3×3 windows, which means that the windows overlap and electron clusters built in neighbouring windows can satisfy the selection criteria, but actually originate from the same physical particle. Multiple counting of clusters is avoided by requiring that seed windows be a local maximum and a programmable distance from another identified seed window, to avoid problems in comparing sums with identical values. This behaviour better resembles the cluster seeding at L1, EF and in the offline reconstruction. The algorithm is also more robust against detector and beam noise, however consumes more computing resources than the default algorithm. The sliding window algorithm is also able to identify multiple cluster seeds per RoI for collimated electron signatures, such as boosted $J/\psi \rightarrow e^{+}e^{-}$ decays. The performance of the alternative L2 sliding window cluster seeding algorithm is compared to the default hot cell algorithm in Section 5.3.

Once a cluster seed has been identified, a cluster of 0.075×0.175 in $\eta \times \phi$ (3×7 cells) is built around it. The larger cluster size in ϕ reduces the low energy tails resulting from photon conversions and electron bremsstrahlung. Various shower shape variables and hadronic leakage, described below, are then calculated to differentiate electromagnetic clusters from hadronic jets. The simplest selection variable is the transverse energy of the cluster, $E_{\mathrm{T}}^{\mathrm{EM}}$. Since the jet cross section is dependent on energy, a cut on $E_{\mathrm{T}}^{\mathrm{EM}}$ provides the best rejection against jet background for a given high momentum signal process such as $Z \rightarrow e^{+}e^{-}$.

Showers from electrons are typically narrower in the η direction with respect to showers from jets, and the shower shape variable R_{η} reflects this. This variable is defined as the ratio of the energy deposited in 3×7 cells divided by that in 7×7 cells in the second layer of the electromagnetic calorimeter. This quantity peaks towards one for electrons whose energy is well contained within 3×7 cells. Note that the value of

R_η can be above one due to the electric pulse shaping function used to calculate the energy deposited in each cell, which has been implemented in such a way that noise contributions fluctuate around zero instead of producing an offset. This means that for small signals, the total energy deposited in 3×7 cells can be larger than that in 7×7 cells since cell energies can be negative.

Electrons typically deposit nearly all their energy in the electromagnetic calorimeter. The selection variable that shows this difference between the signal and the background is hadronic leakage, defined as the ratio of the transverse energy deposited in the first layer of the hadronic calorimeter divided by the total transverse cluster energy, $E_{\mathrm{T}}^{\mathrm{HAD}}/E_{\mathrm{T}}^{\mathrm{EM}}$.

After applying selections on these quantities, only jets with very little hadronic activity and narrow showers remain. The fine granularity in the first layer of the electromagnetic calorimeter can observe substructures within a shower for further rejection of backgrounds, such as π^0 or η mesons decaying to photons. This is particularly important in the low E_{T} regime due to the higher background rate. In the L2 electron selection, the variable that can be exploited for this discrimination is R_ϕ. This is measured by scanning the first layer of the electromagnetic calorimeter within the shower in the η direction for the first and second local maxima, and then calculating the ratio between the difference between these energies divided by the sum, $R_\phi = (E_{\mathrm{1st}}^{\mathrm{max}} - E_{\mathrm{2nd}}^{\mathrm{max}})/(E_{\mathrm{1st}}^{\mathrm{max}} + E_{\mathrm{2nd}}^{\mathrm{max}})$. This ratio tends to one for isolated electrons and tends to zero for photons originating from π^0 or η meson decay.

The distributions of the cluster variables described above are shown in Figure 5.4 for signal and background. The shower shape variables R_η and R_ϕ in the first and second layers of the calorimeter provide good discriminating power above 0.8, since these ratios tend towards one for isolated electrons.

If all the criteria of the calorimeter based electron selection are fulfilled, a search for a track to match the cluster is performed within the RoI in the inner detector. The baseline pattern recognition for L2 tracking is seeded by the silicon detectors and subsequently extended to the TRT. There is also a track reconstruction algorithm based on only TRT information for robustness and complementarity.

There are two different tracking algorithms based on the silicon detectors available at L2, called 'SiTrack' and 'IdScan'. They both perform fast pattern recognition and track reconstruction using space points of the silicon clusters in the detectors, but with different approaches. IdScan first determines the z position of the interaction point

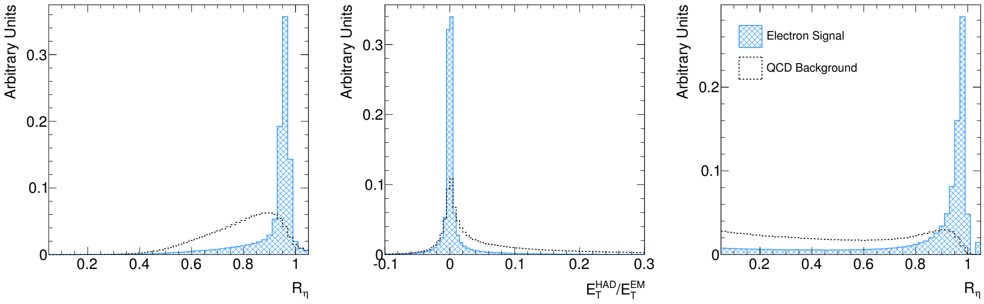

(a) R_η **(b)** $E_{\mathrm{T}}^{\mathrm{HAD}}/E_{\mathrm{T}}^{\mathrm{EM}}$ **(c)** R_ϕ

Figure 5.4. L2 cluster selection variables for simulated single electrons with E_{T} between 7 and 80 GeV (solid line, hatched histogram) compared with simulated background candidates from a filtered QCD multijet sample with at least one jet with $E_{\mathrm{T}} > 17$ GeV (dashed line, hollow histogram). For the background, only clusters that do not match to a true electron within a ΔR of 0.1 are considered. All distributions have been normalised to unit area.

along the beam axis and then performs combinatorial tracking inside groups of space points that point back to that position. SiTrack employs a combinatorial pattern recognition approach, grouping space points according to ‘logical layers’, corresponding to physical detector layers. It seeds tracks by pairing space points from the innermost two logical layers and then extrapolating the tracks to outer logical layers. Both algorithms use a Kalman filtering technique [106] to perform track fitting within the silicon detectors and extrapolation to the TRT is performed by using the Probabilistic Data Association Filter method [107].

A further rate reduction, while maintaining high electron efficiency, can be achieved by combining the cluster and track information from the calorimeter and the inner detector. The background rate can be reduced by a close match between the position of the track extrapolated to the calorimeter surface and the position of the cluster. As shown in Figure 5.5, these distributions are narrower for electrons than for jets, particularly the η difference. Another useful quantity is the ratio of cluster E_{T} and the track p_{T}, which should be around one for electrons. However, this ratio is affected by bremmstrahlung which causes a high tail in the distribution, as can be seen in Figure 5.5, so no upper threshold on $E_{\mathrm{T}}/p_{\mathrm{T}}$ is planned for early data taking.

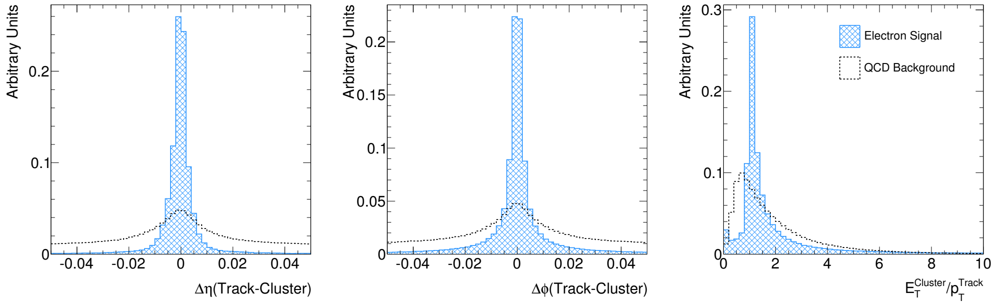

(a) $\Delta\eta$(Track – Cluster) **(b)** $\Delta\phi$(Track – Cluster) **(c)** $E_{\mathrm{T}}^{\mathrm{Cluster}}/p_{\mathrm{T}}^{\mathrm{Track}}$

Figure 5.5. L2 electron selection variables based on combined calorimeter and inner detector information. Simulated signal, single electrons with E_{T} between 7 and 80 GeV (solid line, hatched histogram) is compared with simulated background candidates from a filtered QCD multijet sample with at least one jet with $E_{\mathrm{T}} > 17$ GeV (dashed line, hollow histogram). For the background, only clusters that do not match to a true electron within a ΔR of 0.1 are considered. All distributions have been normalised to unit area.

5.2.3. Event Filter Electron Trigger Selection

The last level of online trigger selection system is the EF, which works at the L2 accept rate with an average event processing time of 4 s to reduce the event rate to approximately 200 Hz. Similarly to the L2, the EF is built on farms of commodity computers and network technology. Once the L2 trigger accepts an event, all the fragments from the ROBs are combined and sent to one EF processor for further consideration. The EF further refines the classification of L2 using the extra time to run more sophisticated reconstruction and identification algorithms and employ more detailed calibration information. Events rejected by the EF are discarded by ATLAS and those accepted are sent to permanent storage.

For EF electron selection, offline reconstruction algorithms are used where possible, with a few significant differences. The most important difference stems from the limited computing resources available to the EF. The offline reconstruction runs once per event and accesses the whole detector, while the EF uses a seeded approach, where the reconstruction runs several times per event, once for each L2 identified electron candidate, accessing only the corresponding region of the detector.

There are currently two offline electron reconstruction algorithms, of which only the standard one is used in the EF. This algorithm starts from clusters reconstructed in the calorimeters and then builds the identification variables based on information from the inner detector and calorimeters. The other algorithm is seeded from inner detector tracks and is optimised for electrons with energies as low as a few GeV and non-isolated electrons. These are a small subset of electron signatures used in physics analyses, and the limited resources available mean that this algorithm is not viable to run in the EF.

In the EF, cluster seeds are found by using the offline sliding window algorithm to find a local energy maximum with trigger tower granularity within the L2 identified RoI of $\Delta\eta \times \Delta\phi = 0.4 \times 0.4$. From these seeds, rectangular clusters are formed with a fixed size of $0.1.25 \times 0.125$ in $\eta \times \phi$, in contrast to the offline algorithm, which creates several collections of clusters corresponding to different window sizes. Also note that for offline electron reconstruction, only data from the electromagnetic calorimeter are used, whilst in the EF as in L2 and L1, hadronic energy is also computed and used to discriminate against jet backgrounds. Once the clusters have been formed, the cluster parameters and shower shape variables are calculated and further refined by a set of calibration tools, including a correction for the inactive material in front of and around the electromagnetic calorimeter and transition gap between the barrel and endcap regions.

Track reconstruction at the EF is performed using the offline inside-out tracking reconstruction algorithm, operated in a RoI seeded mode with the simplest Kalman filtering based track fitting technique due to time constraints. There is the possibility to attempt bremsstrahlung and photon conversion recovery using more sophisticated methods, but this option is not foreseen for early running where the selection criteria are sufficiently loose to be insensitive to any performance improvements

The EF electron identification is very similar to that used offline. All electron candidates have to pass a series of selection criteria based on the shower shape properties in different compartments of the calorimeter as well as track parameters and variables combining inner detector and calorimeter information. These criteria include selections on the cluster such as transverse energy, hadronic leakage, R_η, R_ϕ as in L2, as well as other shower shape variables, and on the track such as number of Pixel and SCT hits and distance of closest approach and on combined variables such as the η distance between cluster and matching track. Distributions for the EF shower shape variables and track-cluster variables which are common to both the L2 and EF are shown in Figure 5.6. The distributions are very similar to those calculated at L2, shown previously in Figures 5.4 and 5.5, but tend to have more discrimination between electrons and jets due to the more refined algorithms and calibrations available.

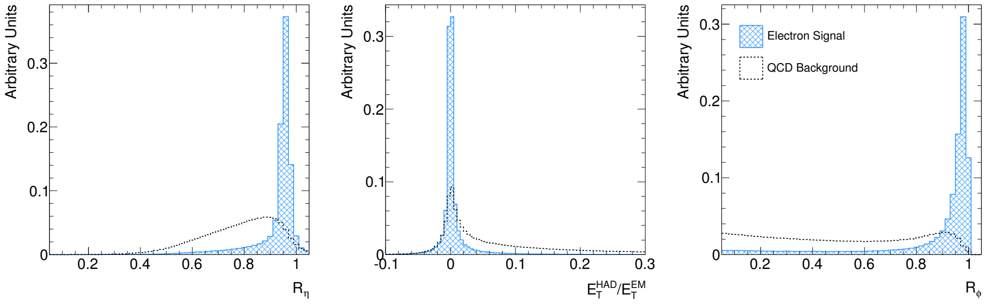

(a) R_η **(b)** $E_{\mathrm{T}}^{\mathrm{HAD}}/E_{\mathrm{T}}^{\mathrm{EM}}$ **(c)** R_ϕ

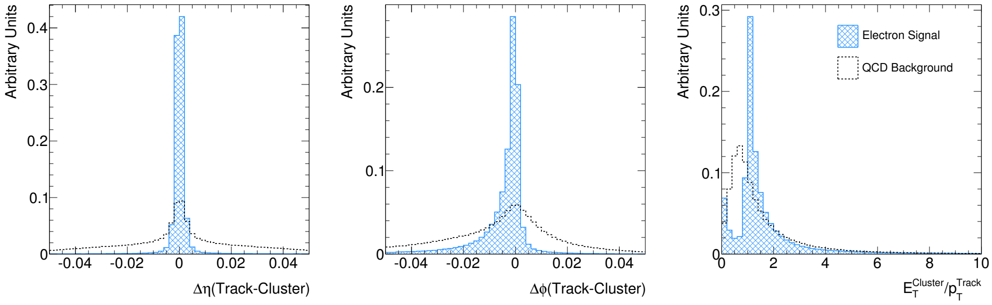

(d) $\Delta\eta$(Track − Cluster) **(e)** $\Delta\phi$(Track − Cluster) **(f)** $E_{\mathrm{T}}^{\mathrm{Cluster}}/p_{\mathrm{T}}^{\mathrm{Track}}$

Figure 5.6. EF electron selection variables. Simulated signal, single electrons with E_{T} between 7 and 80 GeV (solid line, hatched histogram) is compared with simulated background candidates from a filtered QCD multijet sample with at least one jet with $E_{\mathrm{T}} > 17$ GeV (dashed line, hollow histogram). For the background sample, only electron candidates that do not match to a true electron within a ΔR of 0.1 are considered. All distributions have been normalised to unit area.

5.3. Electron Trigger Algorithm Performance Comparison

The performance of a trigger is determined by several factors: efficiency for signal, background rate which depends on luminosity and is constrained by bandwidth, and execution time at each trigger level. This section presents a comparison of the performance of the alternative L2 sliding window cluster seeding algorithm to the original L2 hot cell cluster seeding algorithm in simulation and data.

5.3.1. Electron Trigger Performance Comparison in Simulation

The primary technical performance issue of trigger algorithms is processing time. This is governed primarily by the amount of data required by the algorithm. However as the alternative algorithm uses the same RoI based tools as the original algorithm, data access will not be the main contributing factor to differences in processing times. Instead it is expected that the sliding window algorithm will require more time than the hot cell one. Additional processing time is needed to perform the energy sums in each of the 3×3 windows and to identify the windows which pass the criteria to become cluster seeds. More subtly, the additional functionality of being able to identify multiple cluster seeds per L1 RoI means that the overall time for a L2 decision will depend on how many cluster seeds are found, since the subsequent L2 cluster and tracking algorithms need to be performed for each cluster seed. Moreover to identify multiple clusters per L1 RoI, all L1 RoIs need to be processed at once, meaning that the sliding window algorithm is less parallelisable than the hot cell algorithm. This may lead to problems in busy events with many L1 RoIs.

Average L2 acceptance and rejection processing times for the hot cell and sliding window L2 cluster seeding algorithms are given in Table 5.2. The time taken for an event to be accepted or rejected by L2 is shown in Figure 5.7. Results are presented for 1 000 single electron events with E_T between 7 and 80 GeV produced using a single particle generator and 1 000 filtered top pair events with leptons with $p_T > 1$ GeV generated using MC@NLO. Files were prepared in a format similar to ATLAS raw data and the timing test was performed running only the electron trigger. It can be seen that time taken for the different algorithms to process single electron events are equivalent, while the sliding window algorithm requires additional time to process top pair events compared to the hot cell algorithm. This is the expected result, since top pair events can have up to 6 jets per event, which can potentially pass the L1 electron selections. Note that the average L2 acceptance times are higher than the expected L2 average of 40 ms stated in Section 5.2.2, even for the original hot cell algorithm. This is due to the computer on which the test was conducted, using a desktop rather than a dedicated machine.

The physics performance of a trigger is a compromise between signal efficiency and background rate, which is constrained by bandwidth. The expected efficiency of the hot cell and sliding window L2 cluster seeding algorithms was determined using single electron, $Z \to e^+e^-$ and $J/\psi \to e^+e^-$ samples, while the expected background rejection was tested using non-diffractive minimum bias and filtered QCD samples, the details of which can be found in Table 5.3.

Figure 5.8 shows the efficiencies of a 10 GeV electron trigger as a function of E_T and η for L1, L2 and EF using single electron events using both the hot cell and sliding window

Table 5.2. Average processing times for the hot cell and sliding window L2 cluster seeding algorithms analysing single electron events with E_T between 7 and 80 GeV and filtered top pair events with leptons with $p_T > 1$ GeV. All times are in ms.

Algorithm	L2 accept time	L2 reject time
Single electron events		
Hot cell	52 ± 1	8 ± 2
Sliding window	51 ± 1	8 ± 2
Top pair events		
Hot cell	54 ± 2	9.9 ± 0.4
Sliding window	65 ± 2	16.0 ± 0.5

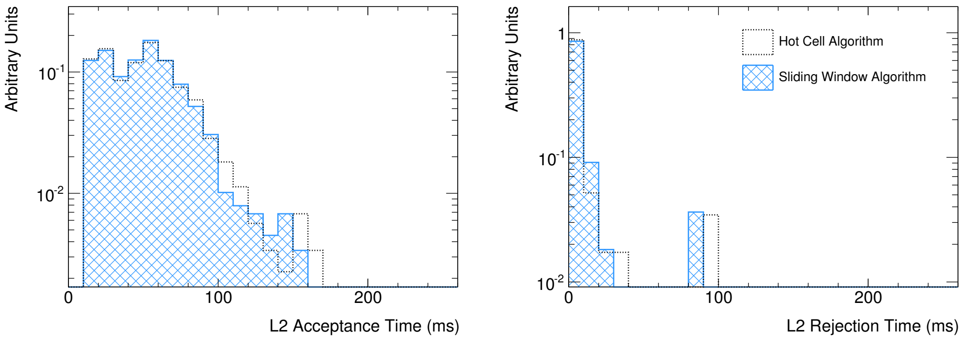

(a) Single electron events

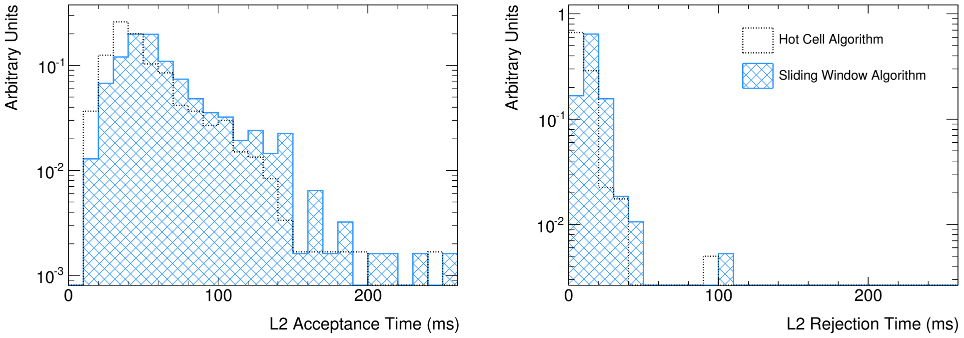

(b) Top pair events

Figure 5.7. A comparison of the time taken to accept (right) and reject (left) events by the hot cell (dotted line, hollow histogram) and sliding window (solid line, hashed histogram) L2 cluster seeding algorithms. Results are shown for single electron events with E_T between 7 and 80 GeV (upper) and filtered top pair events with leptons with $p_T > 1$ GeV (lower). All times are in ms.

Table 5.3. Details of the simulated samples used to compare the performance of the sliding window L2 cluster seeding algorithm and the hot cell L2 cluster seeding algorithm. Electron events were generated using a single particle generator while all other processes were simulated using PYTHIA.

Process	Events
Single Electrons: 7 GeV $< E_T <$ 80 GeV	482 000
$Z \to ee$	93 000
$J/\psi \to e + X$	100 000
Minimum bias	637 000
QCD: 1 jet > 17 GeV	499 000

algorithms. Efficiencies are shown with respect to electrons reconstructed offline using similar selections where trigger candidates are matched to offline electrons within $\Delta R < 0.2$. For both algorithms, the efficiency reaches a plateau value for $E_T \gtrsim 15$ GeV and is uniform as a function of η, except for a 5-10% dip in the transition region between the barrel and endcap calorimeters. The $|\eta| > 2$ region is the only area where there is a visible difference between the two algorithms. The reason is that the sliding window algorithm uses energy deposited in both the first and second sampling layers to seed a cluster, while the hot cell algorithm only uses energy deposited in the second layer. In this high η region, there is more material in front of the calorimeter [71] and some electrons will only deposit energy in the first sampling layer of the calorimeter; the hot cell algorithm will not identify these candidates. The difference between the two algorithms is quantified in Table 5.4, where their percentage efficiencies for offline reconstructed electrons with $E_T > 10$ GeV from single electron events and $Z \to e^+e^-$ events is given. It is clear that the overall expected performance of the two algorithms for these types of events is equivalent. This is not surprising, given the simple event topology. Each event contains only one or two high E_T, isolated electrons, hence in most L1 RoIs, the hottest cell is the same as the highest energy 3×3 window.

The comparison between the two algorithms was also performed using $J/\psi \to e^+e^-$ events and the results are shown in Table 5.5. These events typically contain two low E_T electrons which can be close together, so some differences between the two L2 cluster seeding algorithms are expected. It is thus surprising to find that the trigger efficiencies with respect to offline reconstructed electrons are so similar. This can be understood by looking at the trigger efficiencies with respect to true electrons. The sliding window algorithm selects more true electrons at L2, however these tend to be

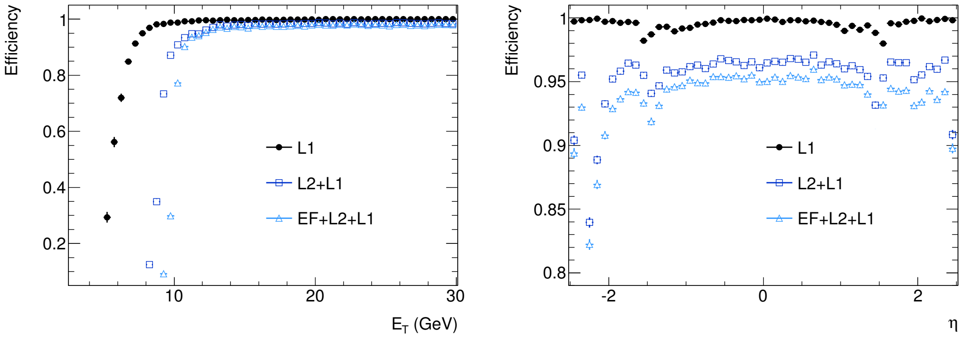

(a) Hot cell algorithm

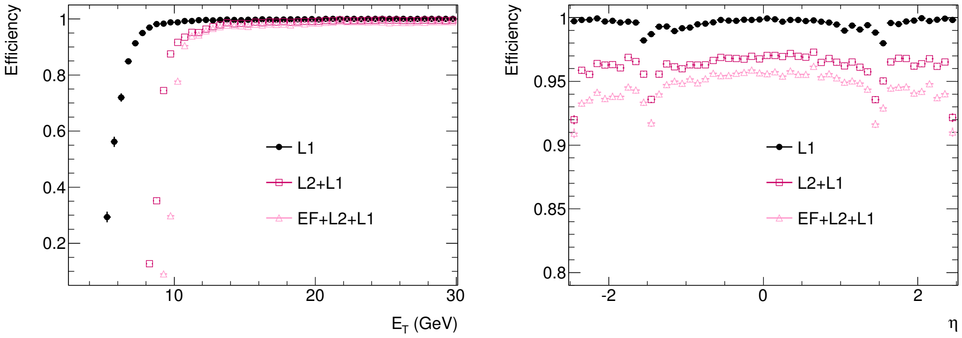

(b) Sliding window algorithm

Figure 5.8. Trigger efficiencies at L1 (solid circles), L2 (open squares) and EF (open triangles) as a function of reconstructed electron E_{T} (left) and $|\eta|$ (right) of a 10 GeV trigger for single electron events with E_{T} between 7 and 80 GeV using the hot cell (upper) and sliding window (lower) L2 cluster seeding algorithms. Trigger candidates are matched to offline electrons within $\Delta R < 0.2$.

Table 5.4. Percentage efficiencies of the hot cell and sliding window L2 cluster seeding algorithms for a 10 GeV trigger compared to offline reconstructed electrons with $E_{\mathrm{T}} > 10$ GeV for single electron events with E_{T} between 7 and 80 GeV and $Z \to e^+e^-$ events. Trigger candidates are matched to offline electrons within $\Delta R < 0.2$.

Efficiency	**Single electron events**		**$Z \to e^+e^-$ events**	
%	**Hot cell**	**Sliding window**	**Hot cell**	**Sliding window**
Offline	80 715		22 511	
L1/Offline	99.76 ± 0.02		99.67 ± 0.04	
L2/L1	97.84 ± 0.05	98.44 ± 0.04	98.56 ± 0.08	98.65 ± 0.08
EF/L2	98.83 ± 0.04	98.82 ± 0.04	99.01 ± 0.07	99.06 ± 0.06
EF/Offline	96.46 ± 0.07	97.04 ± 0.06	97.3 ± 0.1	97.4 ± 0.1

Table 5.5. Percentage efficiencies of the hot cell and sliding window L2 cluster seeding algorithms for a 5 GeV trigger compared to offline reconstructed and true electrons with $E_{\mathrm{T}} > 5$ GeV for $J/\psi \to e^{+}e^{-}$ events. Trigger candidates are matched to offline and true electrons within $\Delta R < 0.2$.

Efficiency %	**Hot cell**	**Sliding window**	**Efficiency %**	**Hot cell**	**Sliding Window**
Offline	29 746		**Truth**	56 597	
L1/Offline	95.6 ± 0.1		**L1/Truth**	80.4 ± 0.2	
L2/L1	96.4 ± 0.1	96.8 ± 0.1	**L2/L1**	81.3 ± 0.2	84.0 ± 0.2
EF/L2	96.8 ± 0.1	96.9 ± 0.1	**EF/L2**	76.4 ± 0.2	74.4 ± 0.2
EF/Offline	89.3 ± 0.2	89.7 ± 0.2	**EF/Truth**	50.0 ± 0.2	50.3 ± 0.2

Table 5.6. Percentage efficiencies of the hot cell and sliding window L2 cluster seeding algorithms for a 5 GeV trigger for non-diffractive minimum bias and filtered QCD events with jets with $E_{\mathrm{T}} > 17$ GeV. Events containing offline reconstructed electrons with $E_{\mathrm{T}} > 5$ GeV have been excluded.

Efficiency %	**Minimum bias events**		**Filtered QCD events**	
	Hot cell	**Sliding window**	**Hot cell**	**Sliding window**
Events	636 960		498 623	
L1/Events	15.81 ± 0.05		92.14 ± 0.04	
L2/L1	20.4 ± 0.1	23.9 ± 0.1	24.93 ± 0.06	31.14 ± 0.04
EF/L2	1.8 ± 0.1	1.7 ± 0.1	3.22 ± 0.05	2.70 ± 0.04
EF/Events	0.058 ± 0.003	0.063 ± 0.003	0.74 ± 0.01	0.78 ± 0.01

poorly reconstructed candidates which do not pass the more rigorous selections at the EF. This results in the final trigger efficiency being equivalent to that of the hot cell algorithm.

The signal efficiency of the sliding window L2 cluster seeding algorithm has been found to be similar to the hot cell L2 cluster seeding algorithm. Table 5.6 provides the efficiency of a 5 GeV trigger for background non-diffractive minimum bias and filtered QCD events with jets with $E_{\mathrm{T}} > 17$ GeV. Events containing offline reconstructed electrons with $E_{\mathrm{T}} > 5$ GeV have been excluded. It can be seen that the sliding window algorithm selects more background events compared to the hot cell algorithm, particularly at L2.

Since the performance comparisons of two L2 cluster seeding algorithms on various simulated samples have shown that the sliding window algorithm requires more processing time than the hot cell algorithm, while not improving the signal efficiency significantly or increasing background rejection, the decision was thus taken not to run the sliding window L2 cluster seeding algorithm during the initial data taking.

5.3.2. Electron Trigger Performance Comparison in Data

In December 2009, ATLAS recorded approximately 20 μb^{-1} of proton-proton collision data at $\sqrt{s}$ = 900 GeV with around 9 μb^{-1} of the data taken under stable beam conditions. During the whole of the 2009 period, the L1 trigger was running online, while the L2 and EF algorithms were commissioned during the stable beam periods by being run online in transparent mode, where they did not reject events. The performance of the electron and photon trigger during this period, summarised here, is described in Reference [108], supplemented by Reference [109], which describes the performance of the inner detector trigger algorithms and Reference [110] which gives an overview of the electron and photon offline performance. Due to the low energy of the collisions, only the 5 GeV trigger electron trigger was operational. The L1 calorimeter trigger ran reliably and behaved according to predictions, reaching > 95% efficiency for raw cluster energies above 6 GeV. Comparisons of the electron selection variables between the different trigger levels and offline reconstruction revealed good agreement for the shower shape variables at L2 and EF and cluster track matching quantities at EF. The differences between L2 and offline reconstruction for track related variables were more pronounced and are expected due to differences in the track reconstruction algorithms. These studies were an important step in the commissioning of the electron trigger. They showed that the trigger was performing correctly, even when most of the clusters originate from backgrounds which in normal running would be discarded.

During the course of seven months in 2010, ATLAS recorded approximately 45 pb^{-1} of proton-proton collision data at $\sqrt{s}$ = 7 TeV under stable beam conditions. During this period, the instantaneous luminosity increased from $\sim 10^{27}$ $cm^{-2}s^{-1}$ to $\sim 10^{32}$ $cm^{-2}s^{-1}$. In the initial months of data taking, as in the 900 GeV data taking period, the L1 trigger was running online, while the L2 and EF algorithms ran in transparent mode. When the instantaneous luminosity reached $\sim 10^{29}$ $cm^{-2}s^{-1}$, the triggers with the highest rates were activated, rejecting events which did not satisfy their requirements. One of the activated triggers was the 5 GeV electron trigger. Subsequently, the full trigger system was deployed when the instantaneous luminosity reached $\sim 10^{30}$ $cm^{-2}s^{-1}$. Even if the alternative L2 sliding window cluster seeding algorithm was not included in the online trigger running, its performance can still be studied offline using the collected data sample.

In order to evaluate the trigger performance, the level of agreement between data and simulation, and between trigger and offline reconstruction variables needs to be assessed. This is performed for the default hot cell L2 cluster seeding algorithm, to which the performance of the alternate sliding window L2 cluster seeding algorithm will then be compared.

The trigger performance was evaluated using 1.15 pb^{-1} of data recorded between March 30, 2010 and April 25, 2010. This data was compared to a simulated sample, consisting of 482 000 minimum bias events generated using PYTHIA. Trigger candidates from a 5 GeV electron trigger were matched to offline electron candidates, requiring a minimal distance $\Delta R < 0.15$. Electrons in the transition region of the calorimeter were excluded. The distributions of discriminating variables were compared from the different trigger levels to the offline distributions as well as with the expectations from simulations. Since no identification criteria were applied to offline reconstructed electron candidates, the distributions were dominated by backgrounds. For the following comparisons, the simulation distributions were normalised to the number of events in the data sample.

Figure 5.9(a) displays distributions of R_η, one of the shower shape selection variables at L2 and EF, for data and simulation. As described in Section 5.2, this quantity is expected to peak towards one for showers initiated from isolated electrons. It can be seen that there is reasonable agreement between data and simulation, and similar behaviour is seen for other discriminating variables. The small shift in the data to slightly lower values of R_η can partially be explained by simulation crosstalk modelling in the second sampling layer of the electromagnetic calorimeter. Figure 5.9(b) also displays the differences between the online trigger levels and offline reconstruction for R_η. For most of the clusters, trigger and offline calculations agree well. The broader resolution at L2 is due to the less refined clustering algorithms and calibrations used. For both trigger levels the resolution is below a few percent. The results, for the presented selection variable and other discriminating variables, provide evidence that the trigger selection criteria implementation is safe and robust.

Having established that the performance of the electron trigger algorithm in data is understood, the comparison of the alternate sliding window L2 cluster seeding

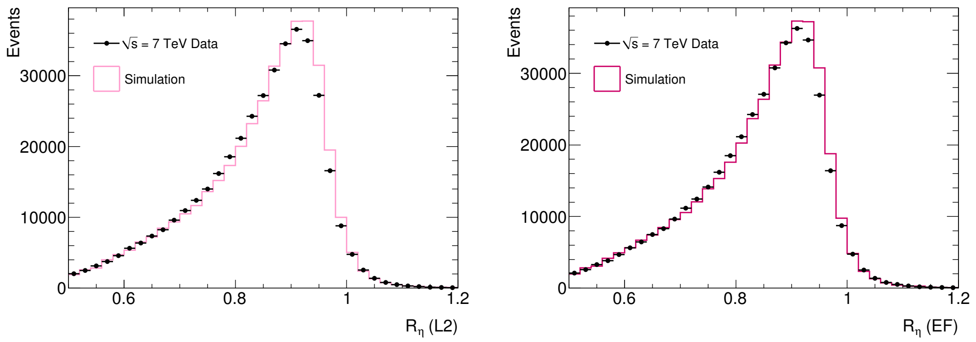

(a) R_η calculated at L2 and EF in data (points) compared to simulation (solid, hollow histograms). Simulation distributions are normalised to the number of events in the data sample.

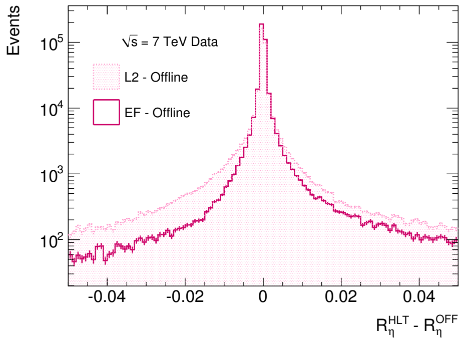

(b) L2 and EF resolution with respect to offline reconstruction for R_η. Trigger candidates are matched to offline electrons within $\Delta R < 0.15$.

Figure 5.9. R_η calculated at L2 and EF for 1.15 pb^{-1} of data compared to simulation and offline reconstruction.

algorithm to the default hot cell L2 cluster seeding algorithm can be made without need of simulation.

For the following efficiency analysis, performed on 985 $\mu\mathrm{b}^{-1}$ of data recorded during a special ATLAS trigger studies run in June 2010, trigger candidates from 5 GeV electron triggers using the hot cell and sliding window L2 algorithms were matched to offline reconstructed electrons passing similar selections, requiring a minimal distance $\Delta R < 0.15$. Table 5.7 gives the trigger efficiency for the algorithms with respect to offline electrons. As in simulation, there is little difference between the two algorithms. This is more evident in Figure 5.10 where the efficiencies of the two algorithms are compared at L2 and EF as a functions of E_T and η. The efficiency differences seen at $|\eta| > 2$ in simulation are not repeated in data. This is due to the updated L2 calibrations used during data taking.

Table 5.7. Percentage efficiencies of the hot cell and sliding window L2 cluster seeding algorithms for a 5 GeV trigger compared to offline reconstructed electrons with $E_{\mathrm{T}} > 5$ GeV for 985 μb^{-1} of data recorded at $\sqrt{s} = 7$ TeV in June 2010. Trigger candidates are matched to offline electrons within $\Delta R < 0.15$.

Efficiency	Hot cell	Sliding window
Offline	3283	
L1/Offline	72.0 ± 0.8	
L2/L1	91.5 ± 0.6	92.4 ± 0.5
EF/L2	95.3 ± 0.5	95.4 ± 0.4
EF/Offline	62.8 ± 0.8	63.5 ± 0.8

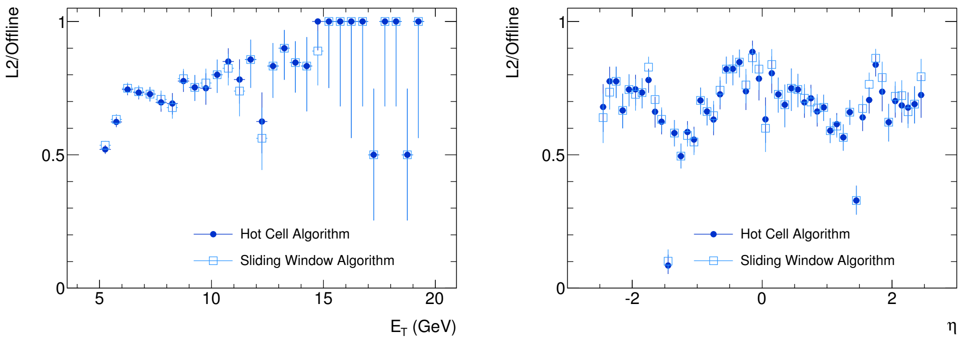

(a) L2

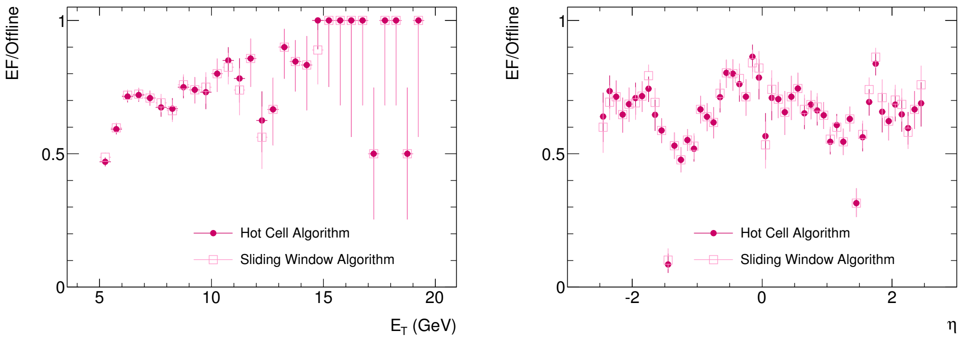

(b) EF

Figure 5.10. Trigger efficiencies at L2 (above) and EF (below) as a function of reconstructed electron E_{T} (left) and η (right) of a 5 GeV trigger for 985 μb^{-1} of data recorded at $\sqrt{s} = 7$ TeV in June 2010 using the hot cell (solid circles) and sliding window (open squares) L2 cluster seeding algorithms. Trigger candidates are matched to offline electrons within $\Delta R < 0.15$.

Table 5.8. Percentage efficiencies of the hot cell and sliding window L2 cluster seeding algorithms for a 5 GeV trigger compared to events without any offline reconstructed electrons with $E_T > 5$ GeV for 985 μb^{-1} of data recorded at $\sqrt{s} = 7$ TeV in June 2010.

Efficiency	Hot cell	Sliding window
Events	679 835	
L1/Events	17.6 ± 0.4	
L2/L1	21.7 ± 0.1	34.7 ± 0.1
EF/L2	4.4 ± 0.1	3.7 ± 0.1
EF/Events	0.169 ± 0.005	0.225 ± 0.006

Using the same dataset, the background rejection of the two different algorithms was also compared, by looking the trigger efficiency of events without any offline reconstructed electrons. The results are shown in Table 5.8 where it can be seen, as in simulation, the sliding window algorithm selects more background events compared to the hot cell algorithm.

5.4. Electron Trigger Summary

An alternate algorithm for seeding clusters at L2 using a sliding window algorithm was developed to identify signatures in which two electrons are found in the same L1 RoI. This alternate algorithm was modelled on the sliding window cluster seeding algorithms used at L1, EF and in the offline reconstruction.

The signal efficiency of the default hot cell and alternate sliding window algorithms was compared using single electron, $Z \rightarrow e^+e^-$ and $J/\psi \rightarrow e^+e^-$ simulated samples, where efficiencies for both algorithms were found to be comparable. The background rejection of the two algorithms was examined using minimum bias and QCD simulated samples, where it was found the sliding window algorithm accepts more background events compared to the hot cell algorithm. In $\sqrt{s} = 7$ TeV data, the signal efficiency of the two algorithms was equivalent, while background rejection of the sliding window algorithm was worse.

Future work should be directed to further optimisation of the sliding window algorithm in terms of background rejection. Potential uses of such a trigger are new physics signatures with collimated electrons, such as dark photons from hidden valley models [111].

Science walks forward on two feet, namely theory and experiment. Sometimes it is one foot that is put forward first, sometimes the other, but continuous progress is only made by the use of both.

– Robert Millikan

6

The Light Stop

The stop is the superpartner of the heaviest quark in the SM - the top quark. A stop quark lighter than the top quark is a necessary requirement for the generation of the observed baryon asymmetry in the universe via electroweak baryogenesis within the framework of the MSSM. This chapter first describes the stop production and decay modes for stop masses below and above the top mass, followed by an overview of the current status of relevant experimental searches. Note that while subsequent analyses will concentrate on searching for a stop quark lighter than the top quark as motivated by electroweak baryogenesis, analysis techniques will also be tested on stop quarks heavier than the top quark since the final state products remain the same.

6.1. Light Stop Production at the LHC

At the LHC, pairs of light stops will be produced through quark-antiquark annihilation ($q\bar{q} \rightarrow \tilde{t}_1\bar{\tilde{t}}_1$) and gluon fusion ($gg \rightarrow \tilde{t}_1\bar{\tilde{t}}_1$) at leading order, as described in the Feynman diagrams depicted in Figure 6.1. The cross sections for these subprocesses can be

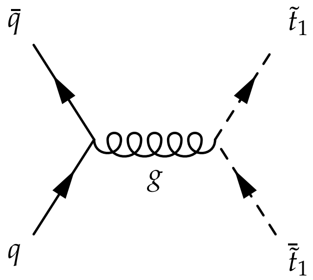

(a) quark-antiquark annihilation

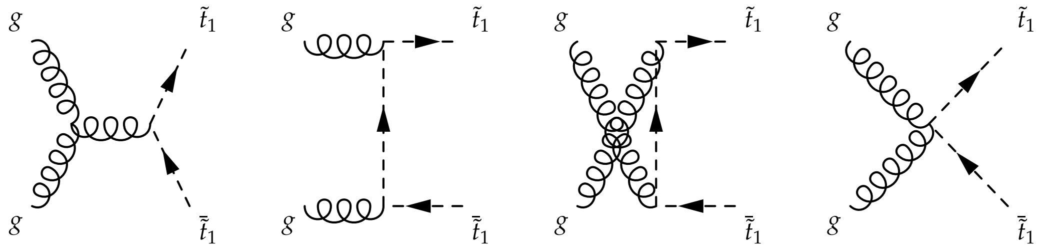

(b) gluon fusion

Figure 6.1. Leading order Feynman diagrams contributing to production of $\tilde{t}_1$ pairs [112].

written as [112]:

$$\sigma(q\bar{q} \to \tilde{t}_1\bar{\tilde{t}}_1) = \frac{\alpha_s^2\pi}{s}\frac{2}{27}\beta_1^3 \tag{6.1}$$

$$\sigma(gg \to \tilde{t}_1\bar{\tilde{t}}_1) = \frac{\alpha_s^2\pi}{s}\left\{\beta_1^3\left(\frac{5}{48}+\frac{31m_{\tilde{t}_1}^2}{24s}\right)+\left(\frac{2m_{\tilde{t}_1}^2}{3s}+\frac{m_{\tilde{t}_1}^4}{6s^2}\right)\log\left(\frac{1-\beta_1}{1+\beta_1}\right)\right\} \tag{6.2}$$

where $\sqrt{s}$ is the center of mass energy of the subprocess and $\beta_1 = \sqrt{1-4m_{\tilde{t}_1}^2/s}$. The cross section for light stop pair production at next-to-leading-order as a function of $m_{\tilde{t}_1}$ at various $\sqrt{s}$ is shown in Figure 6.2, calculated using PROSPINO [113] with CTEQ6.6 [114] parton distribution functions.

The cross section is dominated by the leading order processes and thus only depends on the mass of the stop particles, as expressed in Equations 6.1 and 6.2. Other SUSY parameters, such as gluino masses and the stop mixing angle only affect high order corrections, two of which are shown in Figure 6.3. Note that mixed stop pairs, $\tilde{t}_1\bar{\tilde{t}}_2$ and $\bar{\tilde{t}}_1\tilde{t}_2$ cannot be produced at leading order.

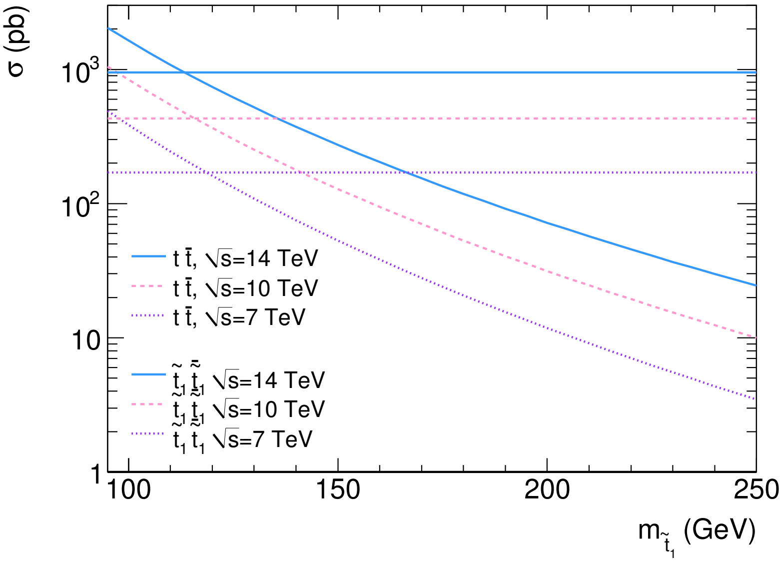

Figure 6.2. $\tilde{t}_1$ pair production cross section (varying lines) as a function of $m_{\tilde{t}_1}$ and t pair production cross section (constant lines) at $\sqrt{s}$ =14 TeV (solid lines), 10 TeV (dashed lines) and 7 TeV (dotted lines).

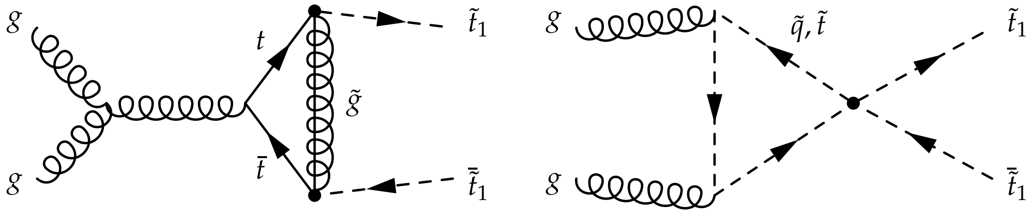

Figure 6.3. Examples of higher order Feynman diagrams contributing to production of $\tilde{t}_1$ pairs including stop mixing (dotted vertices) [112].

It is important to note that the cross section for stop quark pair production for a stop quark of the same mass as a top quark is an order of magnitude lower than that of top pair quark production. This suppression is due to the fact that the stop quark is a scalar while the top quark is a fermion.

6.2. Light Stop Decay Modes

The light stop can have different decay modes depending on the sparticle mass spectrum [115, 116, 117, 118].

- **Two body decay modes**
  If $m_{\tilde{t}_1} > m_t$, there are two possible tree-level two body stop decay modes: either through the strong interaction, $\tilde{t}_1 \to \tilde{g}t$, if $m_{\tilde{t}_1} > m_t + m_{\tilde{g}}$; or through the weak interaction $\tilde{t}_1 \to \tilde{\chi}^0_1 t$, if $m_{\tilde{t}_1} > m_t + m_{\tilde{\chi}^0_1}$. Both of these decays modes are strongly suppressed due the large top mass. Otherwise, if $m_{\tilde{t}_1} > m_{\tilde{\chi}^\pm_1} + m_b$, the two body decay $\tilde{t}_1 \to \tilde{\chi}^+_1 b$ becomes available. For $m_{\tilde{t}_1} < m_t$ and $m_{\tilde{t}_1} < m_{\tilde{\chi}^\pm_1} + m_b$, the only two body decay available is the loop decay, $\tilde{t}_1 \to \tilde{\chi}^0_1 c$.

  In the parameter space where the transition $\tilde{t}_1 \to \tilde{\chi}^+_1 b$ is dominant, the decay modes of the lightest chargino become important. It has five possible tree-level two body decay modes: $\tilde{\chi}^+_1 \to \tilde{\chi}^0_1 W^+$, $\tilde{\chi}^+_1 \to \tilde{\chi}^0_1 H^+$, $\tilde{\chi}^+_1 \to \bar{\tilde{d}}_L u$, $\tilde{\chi}^+_1 \to \bar{d}\tilde{u}_L$ and $\tilde{\chi}^+_1 \to \bar{d}\tilde{u}_R$ where u denotes up-type fermions (the neutrinos and the u,c,t quarks) with superpartners $\tilde{u}_L$, $\tilde{u}_R$ and similarly d denotes down-type fermions (the charged leptons and the d,s,b quarks) and their superparters. It also has the three body decay mode: $\tilde{\chi}^\pm_1 \to \tilde{\chi}^0_1 f\bar{f}'$ where f is a light quark or lepton through either a virtual W^+ or H^+. The branching fractions of each decay mode depends on relative masses of the virtual and real particles involved [119].

- **Three body decay modes**
  If $m_{\tilde{\chi}^\pm_1} > m_{\tilde{t}_1} - m_b$, that is all two body decays at tree-level are kinematically forbidden, the three body tree-level stop decays become relevant: $\tilde{t}_1 \to \tilde{\chi}^0_1 W^+ b$, $\tilde{t}_1 \to \tilde{\chi}^0_1 H^+ b$, $\tilde{t}_1 \to \tilde{\ell}^+ \nu_\ell b$ and $\tilde{t}_1 \to \tilde{\nu}_\ell \ell^+ b$ where ℓ=e,μ,τ; where the branching fractions of each decay mode depends on the relative masses of the virtual and real particles involved.

- **Four body decay modes**
  If the sleptons and sneutrinos are heavier than the stop quark, the four body tree-level stop decay becomes relevant: $\tilde{t}_1 \to \tilde{\chi}^0_1 b f\bar{f}'$.

6.3. Light Stop Search Topology

The relevant stop and chargino decay modes for the search presented in this thesis are listed in Table 6.1, with the corresponding Feynman diagrams in Figures 6.4 and 6.5. It is assumed that the only particles involved in the decays are the lightest stop quark, the lightest chargino, the lightest neutralino, the top quark, the W boson and their decay products. These decays then all produce the same final state: $b\chi^0_1 f\bar{f}'$ where the

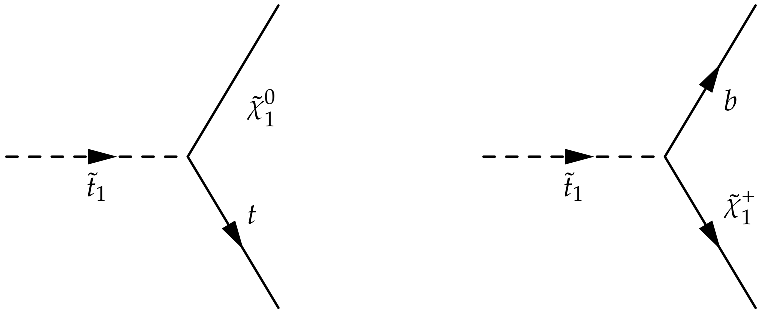

(a) Two Body

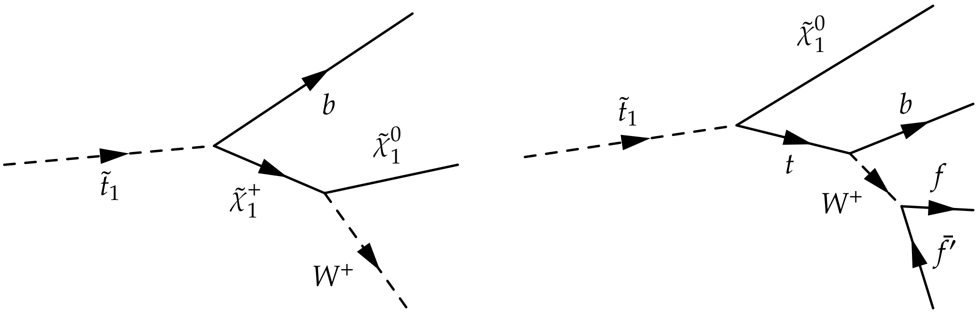

(b) Three Body **(c)** Four Body

Figure 6.4. Relevant $\tilde{t}_1$ decay modes.

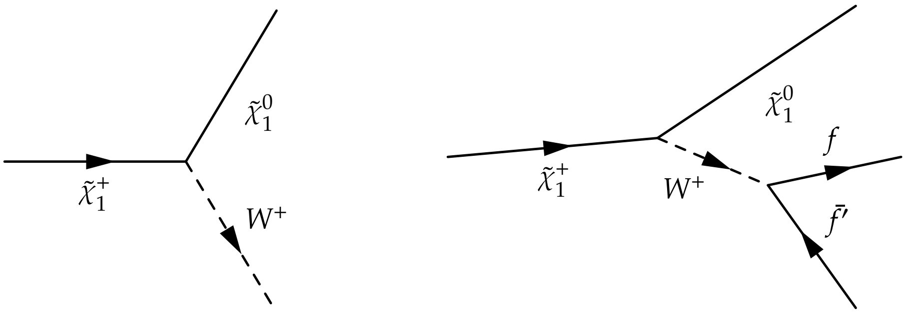

(a) Two Body **(b)** Three Body

Figure 6.5. Relevant $\tilde{\chi}_1^{\pm}$ decay modes.

Table 6.1. Relevant $\tilde{t}_1$ and $\tilde{\chi}_1^\pm$ decay modes for various mass differences.

Mass difference	Decay mode
$m_{\tilde{t}_1} \geq m_{\tilde{\chi}_1^0} + m_t$	$\tilde{t}_1 \rightarrow \tilde{\chi}_1^0 t$
$m_{\tilde{t}_1} \geq m_{\tilde{\chi}_1^\pm} + m_b$	$\tilde{t}_1 \rightarrow \tilde{\chi}_1^\pm b$
$m_{\tilde{\chi}^\pm} - m_{\tilde{\chi}^0} \geq m_{W^\pm}$	$\tilde{\chi}_1^\pm \rightarrow \tilde{\chi}_1^0 W^\pm$
$m_{\tilde{\chi}_1^\pm} < m_{\tilde{\chi}_1^0} + m_{W^\pm}$	$\tilde{\chi}_1^\pm \rightarrow \tilde{\chi}_1^0 f\bar{f}'$
$m_{\tilde{\chi}_1^\pm} + m_b + m_{W^+} \geq m_{\tilde{t}_1} < m_{\tilde{\chi}_1^\pm} + m_b$	$\tilde{t}_1 \rightarrow \tilde{\chi}_1^0 bW^+$
$m_{\tilde{t}_1} < m_{\tilde{\chi}_1^\pm} + m_b + m_{W^+}$	$\tilde{t}_1 \rightarrow \tilde{\chi}_1^0 bf\bar{f}'$

fermion flavour is determined by the W boson. The W boson decays about one third of the time into a charged lepton and corresponding neutrino and in the remaining two thirds of the time, it decays into a quark-antiquark pair.

From an experimental point of view, stop pair decays can be characterised by the decay modes of the W bosons:

- *Fully leptonic:* is about one ninth of the $\tilde{t}\bar{\tilde{t}}$ events. Both W bosons decay into a lepton-neutrino pair, resulting in a final state with two charged leptons, two neutrinos, two neutralinos and two b quarks. This mode can be identified by requiring two high p_T leptons, two jets and the presence of missing transverse energy.

- *Fully hadronic:* is about four ninths of the $\tilde{t}\bar{\tilde{t}}$ events. Both W bosons decay hadronically, which results in two neutralinos and six quarks in the final state, two b quarks and four light quarks from the W boson decay. In this case, there are no high p_T leptons to trigger on, and the signal is not easily distinguishable from the abundant SM QCD multijet production, which is orders of magnitude larger than the signal.

- *Semileptonic:* is about four ninths of the $\tilde{t}\bar{\tilde{t}}$ events. One W boson decays into a lepton-neutrino pair, while the other decays hadronically. This results in a final state of two neutralinos, two b quarks, one neutrino, one charged lepton and two light jets. This mode can be identified by requiring one high p_T lepton, four jets and the presence of missing transverse energy.

In this thesis, stop pair production is studied in the semileptonic and fully leptonic (dileptonic) decay modes, where the charged leptons are electrons or muons.

The kinematics of the visible observables depends on the sparticle masses $m_{\tilde{t}_1}$, $m_{\tilde{\chi}_1^\pm}$ and $m_{\tilde{\chi}_1^0}$, as demonstrated in Figures 6.6, 6.7, and 6.8 where the generated lepton p_{T}, b quark p_{T} and $E_{\mathrm{T}}^{\mathrm{miss}}$ spectra are shown for different sparticle mass combinations. Kinematic variations deriving from different $m_{\tilde{t}_1}$, $m_{\tilde{\chi}_1^\pm}$ and $m_{\tilde{\chi}_1^0}$ combinations are studied by keeping all other SUSY parameters constant. It can be seen that lepton p_{T} and $E_{\mathrm{T}}^{\mathrm{miss}}$ spectra are sensitive to $m_{\tilde{t}_1} - m_{\tilde{\chi}_1^0}$, whereas the b quark p_{T} spectrum is sensitive to $m_{\tilde{\chi}_1^\pm} - m_{\tilde{\chi}_1^0}$. A larger mass difference means a harder p_{T} spectrum while a smaller mass difference denotes a softer p_{T} spectrum.

Analyses will need to take the varying particle spectra into account as different $m_{\tilde{t}_1}$, $m_{\tilde{\chi}_1^\pm}$ and $m_{\tilde{\chi}_1^0}$ combinations are explored. The sparticle masses probed should also cover the LSS parameter space. Figure 6.9 displays the neutralino relic density in the LSS parameter space projected onto $m_{\tilde{t}_1}$, $m_{\tilde{\chi}_1^\pm}$ and $m_{\tilde{\chi}_1^0}$ and their differences. It can be seen that the range of the sparticle masses is quite restricted, and thus will be easily covered in the following analyses.

6.3.1. Sources of Background

Top pair events are the most challenging background in the search for light stop pairs due to their topological similarity. In fact, the decay mode choices for the light stop and the lightest chargino creates a situation where the decay products of light stop pairs mimic those from the decay of top quark pairs, but with more missing energy due to the two neutralinos in the final state. Furthermore, top pair events have a higher production cross section than light stop pair events for most values of $m_{\tilde{t}}$. This means that top pair production will be an irreducible background in all stop channels for all $m_{\tilde{t}_1}$, $m_{\tilde{\chi}_1^\pm}$ and $m_{\tilde{\chi}_1^0}$ combinations and will need special treatment in this analysis.

Other important sources of background for the stop signal are single top quark production, and Z/γ^* and W boson production in association with jets (Z/γ^* or W+jets). How much these background sources contribute to the background depends on the stop decay mode.

Single top quarks are produced by three different mechanisms at leading order: (i) W boson and gluon fusion which includes the t-channel contribution where the final state is a t quark and an associated b or light quark, (ii) associated production

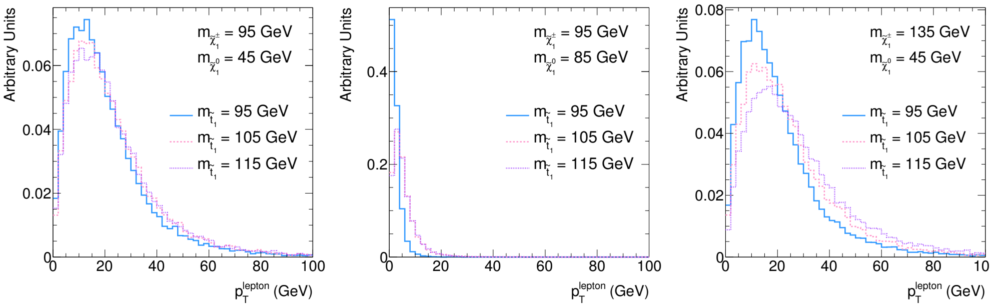

(a) **(b)** **(c)**

Figure 6.6. Truth lepton p_T distributions for various $m_{\tilde{t}_1}$, $m_{\tilde{\chi}_1^\pm}$ and $m_{\tilde{\chi}_1^0}$. Subfigure **(a)** demonstrates stop mass dependence, $m_{\tilde{t}_1}$ = 95 (solid line), 105 (dashed line) and 115 GeV (dotted line) for $m_{\tilde{\chi}_1^\pm}$ = 95 GeV and $m_{\tilde{\chi}_1^0}$ = 45 GeV; **(b)** demonstrates a shift of the neutralino mass from 45 GeV to 85 GeV; and **(c)** demonstrates a shift of the chargino mass from 95 GeV to 135 GeV. All distributions have been normalised to unit area.

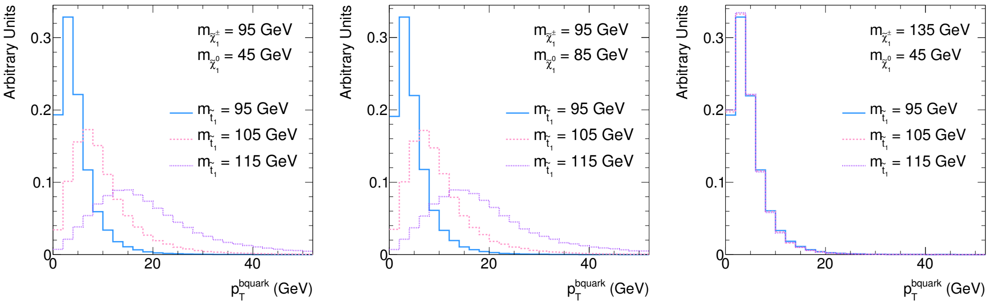

(a) **(b)** **(c)**

Figure 6.7. Truth b quark p_T distributions for various $m_{\tilde{t}_1}$, $m_{\tilde{\chi}_1^\pm}$ and $m_{\tilde{\chi}_1^0}$. See Figure 6.6 for a description of the subfigures.

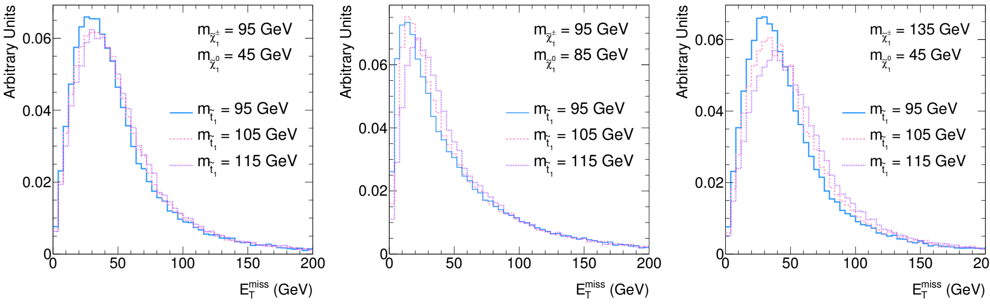

(a) **(b)** **(c)**

Figure 6.8. Truth E_T^{miss} distributions for various $m_{\tilde{t}_1}$, $m_{\tilde{\chi}_1^\pm}$ and $m_{\tilde{\chi}_1^0}$. See Figure 6.6 for a description of the subfigures.

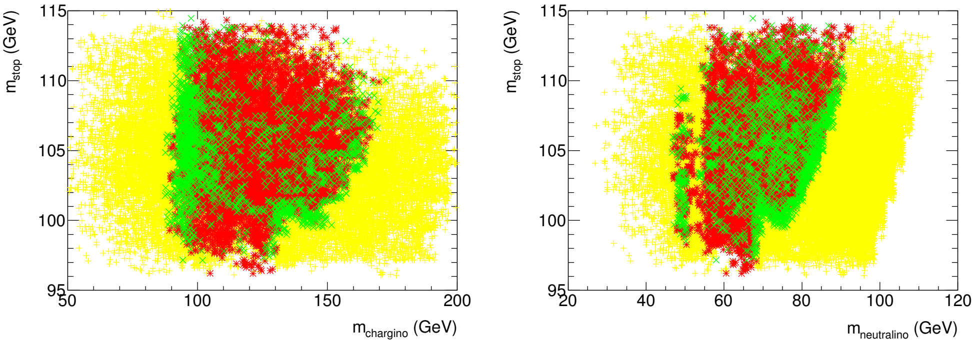

(a) Neutralino relic density projected in terms of $m_{\tilde{t}_1}$, $m_{\tilde{\chi}_1^\pm}$ and $m_{\tilde{\chi}_1^0}$

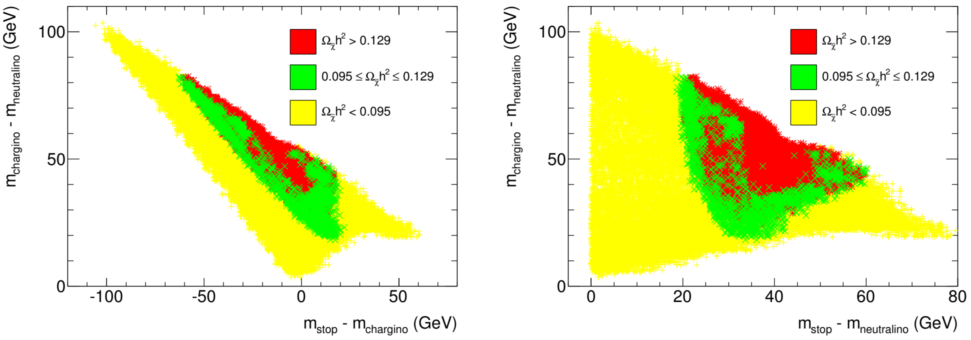

(b) Neutralino relic density projected in terms of the differences between $m_{\tilde{t}_1}$, $m_{\tilde{\chi}_1^\pm}$ and $m_{\tilde{\chi}_1^0}$

Figure 6.9. Neutralino relic density in the LSS parameter space projected onto $m_{\tilde{t}_1}$, $m_{\tilde{\chi}_1^\pm}$ and $m_{\tilde{\chi}_1^0}$ and their differences. The green crosses correspond to where the relic density is consistent within two standard deviations with WMAP data, red asterisks is where the relic density is too high while yellow pluses is where it is too low.

of a t quark and a W boson and (iii) s-channel production, where the final state is a t quark and associated b quark. All three production mechanisms contribute to the background of the semileptonic search channel. The t- and s-channels only contribute to the background of the dileptonic search channel if one of the jets is misidentified as an isolated lepton.

W+jets production where the W boson decays leptonically contain one isolated lepton and thus contribute more to the background of the semileptonic channel. In the dileptonic channel, W+jets production contribute to the background only if one of the jets is misidentified as an isolated lepton.

Z/γ^*+jets production where the Z/γ^* boson decays leptonically contain two isolated leptons and thus contribute more to the background of the dileptonic search channel rather than the semileptonic one.

Smaller contributions to the background arise from QCD multijet events and diboson (WW, ZZ and WZ) production. The contribution from diboson events is negligible due to the small production cross sections. QCD multijet events only contribute when one or more of the jets in the event is misidentified as an isolated lepton. While the lepton identification fake rate is low, the large cross section for this process means that additional selection criteria is required to reduce this background, particularly events which contain b quarks that decay leptonically. Fortunately the topology of QCD multijet events is quite distinct from stop pair events, hence this background is predicted to be small in the signal regions.

In the SUSY parameter space studied in this thesis, the stop is one of the lightest sparticles, hence other SUSY production cross sections are generally much lower than the light stop signal, and thus the background contribution from other SUSY processes can be neglected.

6.4. Experimental Limits on Light Stop Production

Searches for sparticles have been conducted at LEP and Tevatron, where the lack of any evidence has set direct constraints on their masses. Table 6.2 shows the most general limits on the relevant sparticle masses to the search conducted in this thesis.

In more detail, experiments at LEP searched for the light stop in the $\tilde{t}_1 \to \tilde{\chi}_1^0 c$ and $\tilde{t}_1 \to \tilde{\ell}^+ \nu_\ell b$ decay channels [120, 121, 122, 123]. Lower limits on $m_{\tilde{t}_1}$ have been set at 95% CL for two different values of θ_t, 0° and 56° using a combination of data from different LEP experiments. These limits correspond to the highest and lowest cross section scenarios (maximum and minimum $\tilde{t}_1 - Z$ coupling). For the $\tilde{t}_1 \to \tilde{\chi}_1^0 c$ decay channel, stop masses in the range 96 to 99 GeV, depending on the neutralino mass, are

Table 6.2. $\tilde{t}_1$, $\tilde{\chi}_1^\pm$ and $\tilde{\chi}_1^0$ mass limits [4]. Relevant assumptions include that the $\tilde{\chi}_1^0$ is the LSP, R-parity is conserved and gaugino masses unify at the grand unification scale.

Limit	Conditions
$m_{\tilde{t}} > 95.7$ GeV, CL=95%	all $\theta_{\tilde{t}}$, $m_{\tilde{t}} - m_{\tilde{\chi}_1^0} > 10$ GeV
$m_{\tilde{\chi}_1^\pm} > 94$ GeV, CL=95%	$\tan\beta < 40$, $m_{\chi^\pm} - m_{\tilde{\chi}_1^0} > 3$ GeV, all m_0
$m_{\tilde{\chi}_1^0} > 46$ GeV, CL=95%	all $\tan\beta$, all $m_{\tilde{\chi}_2^\pm} - m_{\tilde{\chi}_1^\pm}$, all m_0

excluded as long as $m_{\tilde{t}_1} - m_{\tilde{\chi}_1^0} - m_c > 5$ GeV. In the $\tilde{t}_1 \rightarrow \tilde{\ell}^+ \nu_\ell b$ decay channel, a stop mass lower limit of 96 GeV was obtained for sneutrino masses smaller than 86 GeV. Both of these limits are for the lowest cross section scenario, $\theta_t = 56°$.

At the Tevatron, both CDF and DØ collaborations have searched for the light stop in the $\tilde{t}_1 \rightarrow \tilde{\chi}_1^0 c$, $\tilde{t}_1 \rightarrow \tilde{\ell}^+ \nu_\ell b$ and $\tilde{t}_1 \rightarrow \tilde{\chi}_1^+ b$ decay channels [124, 125, 126, 127, 128, 129]. The most recent search in the $\tilde{t}_1 \rightarrow \tilde{\chi}_1^0 c$ decay channel, based on 2.6 fb^{-1} of data by CDF, excludes $m_{\tilde{t}_1} < 180$ GeV for $m_{\tilde{\chi}_1^0} = 95$ GeV at 95% CL [124]. Using 5.4 fb^{-1} of data, DØ excludes stop pair production in the $\tilde{t}_1 \rightarrow \tilde{\ell}^+ \nu_\ell b$ decay channel for $m_{\tilde{t}_1} < 210$ GeV when $m_{\tilde{\nu}} < 110$ GeV and the difference $m_{\tilde{t}_1} - m_{\tilde{\nu}} > 30$ GeV at 95% CL [127]. Finally, in the $\tilde{t}_1 \rightarrow \tilde{\chi}_1^+ b$ decay channel, the one studied in this thesis, CDF excludes stop masses between 128 and 135 GeV for $m_{\tilde{\chi}_1^\pm} = 105.8$ GeV and $m_{\tilde{\chi}_1^0} = 47.6$ GeV at 95% CL using 2.7 fb^{-1} of data [128]. Figure 6.10 shows the exclusions set in the three stop search channels by LEP, CDF and DØ collaborations. These limits only cover a restricted region of the $m_{\tilde{t}_1}$, $m_{\tilde{\chi}_1^\pm}$ and $m_{\tilde{\chi}_1^0}$ phase space. At the LHC, with its higher collision energies and higher resolution detectors, it will be possible to cover almost all the available phase space.

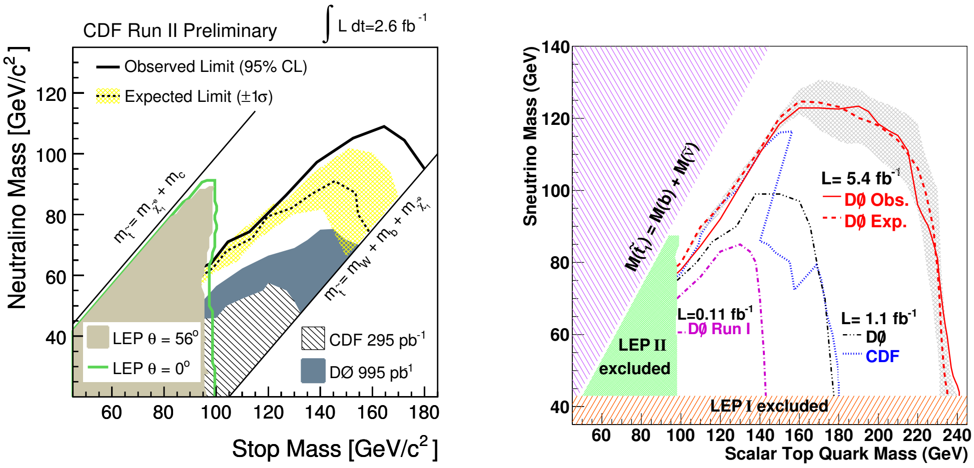

(a) Exclusion region in the $m_{\tilde{t}_1}$ and $m_{\tilde{\chi}_1^0}$ plane [124] **(b)** Exclusion region in the $m_{\tilde{t}_1}$ and $m_{\tilde{\nu}}$ plane [127]

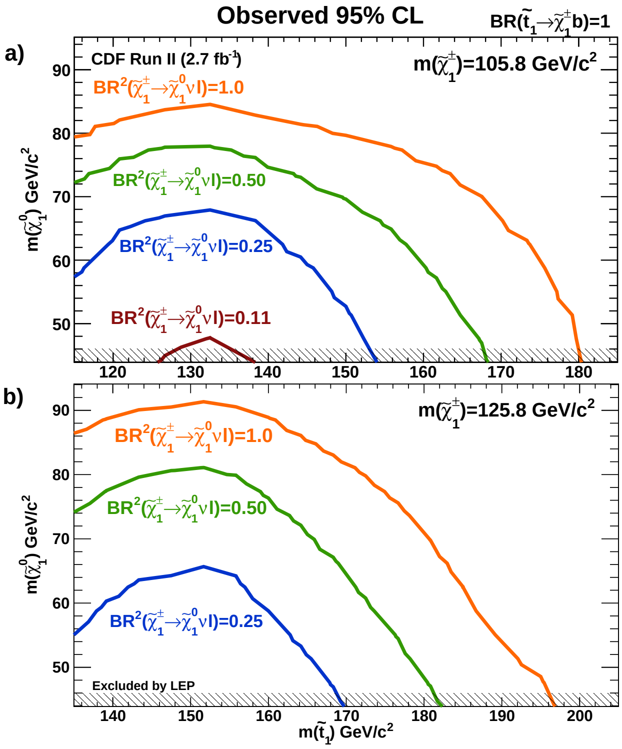

(c) Exclusion region in the $m_{\tilde{t}_1}$ and $m_{\tilde{\chi}_1^0}$ plane for several values of $\mathcal{B}(\tilde{\chi}_1^{\pm} \to \tilde{\chi}_1^0 \ell^{\pm} \nu)$ and $m_{\tilde{\chi}_1^{\pm}}$ [128]

Figure 6.10. Regions excluded by the LEP, CDF and DØ collaborations at 95% CL using the **(a)** $\tilde{t}_1 \to \tilde{\chi}_1^0 c$, **(b)** $\tilde{t}_1 \to \tilde{\ell}^+ \nu_\ell b$ and **(c)** $\tilde{t}_1 \to \tilde{\chi}_1^+ b$ decay channels.

The only object of theoretical physics is to calculate results that can be compared with experiment.

– Paul Dirac

7

Light Stop Simulation and Data Samples

The analysis presented in this thesis was prepared and optimised using simulated data at $\sqrt{s} = 10$ TeV. The distributions of the quantities used for disentangling signal from background was then compared between $\sqrt{s} = 7$ TeV simulation and data. This chapter describes how the simulated samples for signal and background processes at $\sqrt{s} = 10$ and 7 TeV are produced followed by the details of the data sample recorded at $\sqrt{s} = 7$ TeV.

7.1. Simulation

The generation of events is a multistep process which proceeds roughly as: initial state parton generation, final state parton generation, showering, radiation and hadronisation of the final state partons.

The momentum carried by the partons which interact in the proton-proton collisions varies collision to collision. This variation is described by parton distribution functions which are functions of the type and flavour of the parton and the momentum transfer in the interaction, Q^2. Event generation begins with picking initial state partons probabilistically according to the parton distribution functions. CTEQ [130] parton distribution functions were used to describe the substructure of the proton for all simulated samples.

Once the initial state partons have been generated, the hard scattering process must then be simulated to create final state partons. The event generators employed in this thesis are PYTHIA [131], HERWIG [132], ALPGEN [133], AcerMC [134] and MC@NLO [135]. Apart from MC@NLO, which includes next-to-leading order processes, these programs all use leading order matrix elements.

To obtain the final state hadrons of a process, the showering, radiation and hadronisation of the final state partons also needs to be simulated. Parton showering consists of adding initial and final state radiation as well as effects from beam remnants and multiple scatterings to a given matrix element. The radiation consists of emissions of gluons from the parent partons, with initial state radiation starting from small Q^2 and increasing as the hard scattering approaches, while final state radiation starts at larger Q^2 and decreases away from the hard scattering. Shower generation is based on probabilistically choosing which partons will split into a pair of child partons. This process is repeated until all partons reach a predefined energy threshold at which point hadronisation takes place. Hadronisation, or fragmentation, describes the process of coloured partons being transformed into colourless hadrons. Parton level generators ALPGEN, MC@NLO and AcerMC use either PYTHIA or HERWIG/JIMMY for hadronisation. HERWIG hadronisation is complemented by JIMMY [136]. These processes are non-perturbative and modelled by phenomenological models tuned to experimental data [137]. QED radiation is treated specially using PHOTOS [138].

7.1.1. Simulation of the Light Stop Signal

The light stop signal was generated in several steps. The *LHS*2 mass spectrum was produced using DarkSUSY [139] with a modified version of ISAJET [140] using the parameters in Table A.1. The program SDecay [141] was then used to calculate the decay widths and branching ratios of the SUSY particles, as shown in Table 7.1. The full set of supersymmetric masses and the decay table were input to either HERWIG [142] or PYTHIA.

The $\sqrt{s} = 10$ TeV analysis is based on the *LHS*2 benchmark point, for which 50 000 events were simulated using the HERWIG event generator and the full ATLAS detecter simulation, and 100 000 events generated using HERWIG and the ATLFAST-II detector

Table 7.1. Decay table for $\tilde{t}_1$ benchmark point *LHS*2. Only non-zero entries relevant to $\tilde{t}_1$ decay are shown. Note that $m_{\tilde{\chi}_1^\pm} < m_{\tilde{\chi}_1^0} + m_{W^\pm}$ so the $\tilde{\chi}_1^\pm$ decay proceeds through an off-shell W.

Particle	Mass (GeV)	Width (GeV)	Decay	Branching Ratio
$\tilde{t}$	137	7.63×10^{-3}	$\tilde{t} \to \tilde{\chi}_1^\pm + b$	1.00
$\tilde{\chi}_1^\pm$	111	9.69×10^{-6}	$\tilde{\chi}_1^\pm \to \tilde{\chi}_1^0 + u + \bar{d}$	0.33
			$\tilde{\chi}_1^\pm \to \tilde{\chi}_1^0 + c + \bar{s}$	0.33
			$\tilde{\chi}_1^\pm \to \tilde{\chi}_1^0 + e^+ + \nu_e$	0.11
			$\tilde{\chi}_1^\pm \to \tilde{\chi}_1^0 + \mu^+ + \nu_\mu$	0.11
			$\tilde{\chi}_1^\pm \to \tilde{\chi}_1^0 + \tau^+ + \nu_\tau$	0.11
$\tilde{\chi}_1^0$	58	0	-	-

simulation. The cross section of stop pair production of the *LHS*2 benchmark point at $\sqrt{s} = 10$ TeV where $m_{\tilde{t}} = 137$ GeV at $\sqrt{s} = 10$ TeV is (199 ± 2) pb as calculated at next-to-leading order by PROSPINO with CTEQ6.6 parton distribution functions.

To study the sensitivity of the analysis to different final state particle kinematics, events were also generated with various stop, chargino and neutralino masses using the PYTHIA event generator[1] and the ATLFAST-II detector simulation, with the remaining parameters set to those of the *LHS*2 benchmark point.

At $\sqrt{s} = 10$ TeV, two separate mass grids were generated, with 50 000 events per point, with $m_{\tilde{t}_1}$, $m_{\tilde{\chi}_1^\pm}$ and $m_{\tilde{\chi}_1^0}$ as given in Equation 7.1. For the neutralino to be a dark matter candidate, an additional condition that the neutralino is the LSP was imposed, meaning $m_{\tilde{t}_1} > m_{\tilde{\chi}_1^0}$ and $m_{\tilde{\chi}_1^\pm} > m_{\tilde{\chi}_1^0}$, resulting in 22 and 12 points each for the two grids. The grid points covered all the various allowed decay processes and mass differences. The cross section of each of the points was calculated at next-to-leading order by PROSPINO with CTEQ6.6 parton distribution functions and depends only

---

[1] PYTHIA is used since it can simulate four body decays.

on the stop mass. The cross section values are given in Table 7.2.

$$\begin{pmatrix} m_{\tilde{t}_1} & = & 120, 150, 180, 240 \\ m_{\tilde{\chi}_1^\pm} & = & 95, 155, 215 \\ m_{\tilde{\chi}_1^0} & = & 45, 105, 165 \end{pmatrix} , \begin{pmatrix} m_{\tilde{t}_1} & = & 95, 105, 115 \\ m_{\tilde{\chi}_1^\pm} & = & 95, 135 \\ m_{\tilde{\chi}_1^0} & = & 45, 85 \end{pmatrix} \tag{7.1}$$

At $\sqrt{s} = 7$ TeV, the *LHS*2 benchmark point and one mass grid were generated with 20 000 events per point after the application of a single lepton filter. The sparticle masses for this grid are given in Equation 7.2; these were chosen to cover the region with the highest discovery potential in early data as determined by the 10 TeV analysis. The *LHS*2 benchmark point was generated using HERWIG, while the mass grid was generated using PYTHIA and all events were simulated using the full ATLAS detector simulation. The cross section of stop pair production of the *LHS*2 benchmark point at $\sqrt{s} = 7$ TeV is (84.4 ± 0.7) pb while the cross section of each of the grid points is given in Table 7.2. All cross sections are calculated at next-to-leading order by PROSPINO with CTEQ6.6 parton distribution functions.

$$\begin{pmatrix} m_{\tilde{t}_1} & = & 95, 115, 135, 155 \\ m_{\tilde{\chi}_1^\pm} & = & 95, 155 \\ m_{\tilde{\chi}_1^0} & = & 45, 60, 75, 90 \end{pmatrix} \tag{7.2}$$

Table 7.2. Cross sections of the $m_{\tilde{t}}$ grid of $\tilde{t}$ signal samples as calculated at next-to-leading order by PROSPINO with CTEQ6.6 parton distribution functions.

10 TeV High Mass Grid	
$m_{\tilde{t}_1}$ (GeV)	**σ (pb)**
120	360
150	129
180	60
240	12

10 TeV Low Mass Grid	
$m_{\tilde{t}_1}$ (GeV)	**σ (pb)**
95	1040
105	668
115	443

7 TeV Mass Grid	
$m_{\tilde{t}_1}$ (GeV)	**σ (pb)**
95	490
115	306
135	90
155	45

7.1.2. Generation of Light Stop Background Sources

The background samples used for the analyses at $\sqrt{s}$ = 10 and 7 TeV were simulated using the full ATLAS detector simulation.

Top pair events at $\sqrt{s}$ = 10 and 7 TeV were generated using MC@NLO [143] interfaced with HERWIG for the hadronisation step. MC@NLO uses hard scattering processes at next-to-leading order in QCD perturbation theory. The next-to-leading order top pair cross sections calculated by MC@NLO were normalised to the next-to-next-to-leading order predictions of References [144, 145] using k factors.

The production of single top quarks at $\sqrt{s}$ = 10 TeV was simulated using AcerMC interfaced with PYTHIA for the hadronisation phase. AcerMC is a leading order event generator for SM processes in proton-proton collisions. The single top quark cross sections were normalised to next-to-leading order predictions using MCFM [146, 147]. Single top production at $\sqrt{s}$ = 7 TeV was simulated using MC@NLO [148, 149] where HERWIG was used for the hadronisation process, to take advantage of the greater accuracy of the next-to-leading order calculations compared to the leading order calculations of AcerMC.

Details of the 10 TeV top pair and single top data samples is given in Table 7.3, while details for the 7 TeV top pair and single top data samples is given in Table 7.4.

Additional top pair and single top datasets were simulated at $\sqrt{s}$ = 10 TeV to study the systematic effects of different event generators, hadronisation methods, and initial and final state radiation effects. The details of these datasets are given in Table 7.5.

Table 7.3. Details of 10 TeV top background samples. Note the s-channel single top process is not listed as its cross section is negligible.

Process	**Generator**	$\sigma \times \epsilon_F$ **(pb)**	k	**Events**
$t\bar{t}$: ℓ inclusive	MC@NLO + HERWIG/JIMMY	202.86	1.07	1 990 000
$t\bar{t}$: hadronic	MC@NLO + HERWIG/JIMMY	170.74	1.07	748 000
t: Wt channel: ℓ inclusive	AcerMC + PYTHIA	14.41	0.99	4 000
t: t channel: ℓ inclusive	AcerMC + PYTHIA	41.12	1.05	30 000

Table 7.4. Details of 7 TeV top background samples. All samples were generated using MC@NLO + HERWIG/JIMMY. Quoted cross sections are calculated at next-to-next-to-leading order.

Process	$\sigma \times \epsilon_F$ **(pb)**	**Events**
$t\bar{t}$: ℓ inclusive	89.40	200 000
$t\bar{t}$: hadronic	71.39	150 000
t: t channel $W \to e\nu_e$	7.0	10 000
t: t channel $W \to \mu\nu_\mu$	7.0	10 000
t: t channel $W \to \tau\nu_\tau$	7.0	10 000
t: s channel $W \to e\nu_e$	0.47	10 000
t: s channel $W \to \mu\nu_\mu$	0.47	10 000
t: s channel $W \to \tau\nu_\tau$	0.47	10 000
t: Wt channel, all W decays	13	15 000

The $W/Z/\gamma^*$+jets production at $\sqrt{s}$ = 10 and 7 TeV was simulated using ALPGEN interfaced with HERWIG. ALPGEN produces final states with different jet multiplicites, using the parton showering and matrix element matching technique in Reference [150]. The Z/γ^*+jets sample was filtered using the invariant mass of the fermion pair, 40 GeV $< m(\ell^\pm, \ell^\mp) <$ 2 TeV, so that production was dominated by Z boson propagators. The cross sections were normalised using the calculations in Reference [151] through k factors. Details of the W+jets data samples are given in Table 7.6 while details of the Z/γ^*+jets data samples are given in Table 7.7.

For the $\sqrt{s}$ = 10 TeV dataset, ALPGEN interfaced with HERWIG was used for diboson and QCD multijet production. Details of these data samples are given in Tables 7.8 and 7.10 respectively.

For the $\sqrt{s}$ = 7 TeV dataset, HERWIG was used for diboson production with details given in Table 7.11. For QCD multijet production, PYTHIA was used with filters for the generation of heavy flavour quarks decaying to electrons to increase the QCD contribution in signal regions. Details for this dataset are given in Table 7.12. An additional sample for Z/γ^*+jets was generated using PYTHIA with 8 GeV $< m(\ell^\pm, \ell^\mp) <$ 60 GeV, to include γ propagators with details in given Table 7.13.

For the $\sqrt{s}$ = 7 TeV simulated samples, to match the luminosity conditions of the $\sqrt{s}$ = 7 TeV data sample, events were generated with an average of two primary interactions per event for the primary datasets - top pair, single top and $W/Z/\gamma^*$+jets.

Table 7.5. Details of 10 TeV top background samples used for studying systematic uncertainties.

Process	**Generator**	**Simulation**	$\sigma \times \epsilon_F$ **(pb)**	k	**Events**
$t\bar{t}$: ℓ inclusive	AcerMC+PYTHIA	Full	108.64	2.01	392 000
$t\bar{t}$: ℓ inclusive	AcerMC+PYTHIA	Fast	108.64	2.01	400 000
$t\bar{t}$: ℓ inclusive	AcerMC+Herwig	Full	108.64	2.01	394 000
$t\bar{t}$: ℓ inclusive + ISR	AcerMC+PYTHIA	Fast	108.64	2.01	399 000
$t\bar{t}$: ℓ inclusive + FSR	AcerMC+PYTHIA	Fast	108.64	2.01	390 000
t: t channel $W \to e\nu_e$	MC@NLO+HERWIG	Full	14.46	1.00	50 000
t: t channel $W \to \mu\nu_\mu$	MC@NLO+HERWIG	Full	14.46	1.00	50 000
t: t channel $W \to \tau\nu_\tau$	MC@NLO+HERWIG	Full	14.46	1.00	50 000

Table 7.6. Details of W+jets background samples. All samples were generated using ALPGEN + HERWIG/JIMMY.

Process	**10 TeV**			**7 TeV**		
	$\sigma \times \epsilon_F$ **(pb)**	k	**Events**	$\sigma \times \epsilon_F$ **(pb)**	k	**Events**
$W \to e\nu_e + 0j$	10 006.58	1.22	1 221 000	6 913.3	1.199	1 382 000
$W \to e\nu_e + 1j$	2 003.50	1.22	262 000	1 293.0	1.199	258 000
$W \to e\nu_e + 2j$	623.31	1.22	776 000	377.1	1.199	189 000
$W \to e\nu_e + 3j$	179.01	1.22	224 000	100.9	1.199	50 000
$W \to e\nu_e + 4j$	46.58	1.22	59 000	25.3	1.199	13 000
$W \to e\nu_e + 5j$	13.56	1.22	17 000	6.9	1.199	4 000
$W \to \mu\nu_\mu + 0j$	10 226.12	1.22	418 000	6 913.3	1.199	1 386 000
$W \to \mu\nu_\mu + 1j$	2 017.48	1.22	262 000	1 293.0	1.199	255 000
$W \to \mu\nu_\mu + 2j$	625.76	1.22	780 000	377.1	1.199	188 000
$W \to \mu\nu_\mu + 3j$	172.47	1.22	223 000	100.9	1.199	50 000
$W \to \mu\nu_\mu + 4j$	46.77	1.22	59 000	25.3	1.199	13 000
$W \to \mu\nu_\mu + 5j$	13.37	1.22	17 000	6.9	1.199	4 000
$W \to \tau\nu_\tau + 0j$	10 117.47	1.22	1 326 000	6 913.3	1.199	1 365 000
$W \to \tau\nu_\tau + 1j$	2 004.41	1.22	247 000	1 293.0	1.199	255 000
$W \to \tau\nu_\tau + 2j$	634.27	1.22	793 000	377.1	1.199	188 000
$W \to \tau\nu_\tau + 3j$	174.34	1.22	223 000	100.9	1.199	50 000
$W \to \tau\nu_\tau + 4j$	47.77	1.22	59 000	25.3	1.199	13 000
$W \to \tau\nu_\tau + 5j$	13.22	1.22	17 000	6.9	1.199	4 000
$W + b\bar{b} + 0j$: $W \to \ell\nu_\ell$	5.13	1.22	16 000	3.2	1.22	7 000
$W + b\bar{b} + 1j$: $W \to \ell\nu_\ell$	5.01	1.22	15 000	2.6	1.22	6 000
$W + b\bar{b} + 2j$: $W \to \ell\nu_\ell$	2.89	1.22	9 000	1.4	1.22	3 000
$W + b\bar{b} + 3j$: $W \to \ell\nu_\ell$	1.61	1.22	5 000	0.6	1.22	2 000

Table 7.7. Details of Z+jets background samples. Dileptons have invariant mass 40 GeV < $m(\ell^{\pm}, \ell^{\mp})$ < 2000 GeV. All samples were generated using ALPGEN + HERWIG/JIMMY.

Process	**10 TeV**			**7 TeV**		
	$\sigma \times \epsilon_F$ **(pb)**	k	**Events**	$\sigma \times \epsilon_F$ **(pb)**	k	**Events**
$Z \to ee + 0j$	898.44	1.22	269 000	664.1	1.25	304 000
$Z \to ee + 1j$	197.80	1.22	62 000	133.0	1.25	62 000
$Z \to ee + 2j$	62.26	1.22	217 000	40.23	1.25	19 000
$Z \to ee + 3j$	18.76	1.22	63 000	11.14	1.25	5 000
$Z \to ee + 4j$	4.97	1.22	18 000	2.899	1.25	1 000
$Z \to ee + 5j$	1.43	1.22	6 000	0.753	1.25	500
$Z \to \mu\mu + 0j$	895.27	1.22	270 000	664.1	1.25	304 000
$Z \to \mu\mu + 1j$	198.59	1.22	62 000	133.0	1.25	63 000
$Z \to \mu\mu + 2j$	63.49	1.22	197 000	40.23	1.25	19 000
$Z \to \mu\mu + 3j$	18.70	1.22	65 000	11.14	1.25	5 000
$Z \to \mu\mu + 4j$	4.99	1.22	18 000	2.899	1.25	1 000
$Z \to \mu\mu + 5j$	1.37	1.22	5 000	0.753	1.25	500
$Z \to \tau\tau + 0j$	893.00	1.22	271 000	664.1	1.25	303 000
$Z \to \tau\tau + 1j$	97.71	1.22	63 000	133.0	1.25	63 000
$Z \to \tau\tau + 2j$	62.63	1.22	210 000	40.23	1.25	19 000
$Z \to \tau\tau + 3j$	18.86	1.22	63 000	11.14	1.25	5 000
$Z \to \tau\tau + 4j$	4.98	1.22	19 000	2.899	1.25	1 000
$Z \to \tau\tau + 5j$	1.39	1.22	5 000	0.753	1.25	500

Table 7.8. Details of 10 TeV diboson background samples. Note ZZ processes are not listed as their cross sections are negligible. All samples were generated using ALPGEN + HERWIG/JIMMY.

Process	$\sigma \times \epsilon_F$ **(pb)**	k	**Events**
$WW + 0j, W \to \ell\nu_\ell$	3.23	1.21	31 000
$WW + 1j, W \to \ell\nu_\ell$	1.71	1.21	17 000
$WW + 2j, W \to \ell\nu_\ell$	0.87	1.21	8 000
$WW + 3j, W \to \ell\nu_\ell$	0.32	1.21	4 000
$WZ + 0j, Z \to \ell\ell$	1.05	1.21	9 000
$WZ + 1j, Z \to \ell\ell$	0.73	1.21	6 000
$WZ + 2j, Z \to \ell\ell$	0.43	1.21	5 000
$WZ + 3j, Z \to \ell\ell$	0.20	1.21	2 000

Table 7.9. The p_T slices used in QCD production. Values are given in GeV.

Name	p_T(min)	p_T(max)
J0	8	17
J1	17	35
J2	35	70
J3	70	140
J4	140	280
J5	280	560
J6	560	1 120
J7	1 120	2 240
J8	2 240	∞

Table 7.10. Details of 10 TeV QCD multijet background samples. JX refers to the p_T slices given in Table 7.9. All samples were generated using ALPGEN + HERWIG/JIMMY.

Process	$\sigma \times \epsilon_F$ (pb)	Events
QCD +2j J2	30 114 236.6	3 002 000
QCD +3j J2	9 835 389.5	978 000
QCD +4j J2	1 494 832.2	149 000
QCD +5j J2	249 184.8	25 000
QCD +2j J3	1 116 548.7	1 115 000
QCD +3j J3	1 486 726.3	1 483 000
QCD +4j J3	552 311.1	551 000
QCD +5j J3	189 793.0	188 000
QCD +2j J4	31 872.0	318 000
QCD +3j J4	65 508.9	654 000
QCD +4j J4	49 028.2	489 000
QCD +5j J4	24 249.3	242 000
QCD +6j J4	11 571.7	116 000
QCD +2j J5+	750.2	334 000
QCD +3j J5+	1 944.8	579 000
QCD +4j J5+	2 149.9	642 000
QCD +5j J5+	1 392.8	417 000
QCD +6j J5+	972.6	291 000

Process	$\sigma \times \epsilon_F$ (pb)	Events
QCD $b\bar{b} + 0j$ J2	137 665.3	137 000
QCD $b\bar{b} + 1j$ J2	193 821.1	193 000
QCD $b\bar{b} + 2j$ J2	53 806.5	54 000
QCD $b\bar{b} + 3j$ J2	13 470.9	13 000
QCD $b\bar{b} + 0j$ J3	5 398.1	5 000
QCD $b\bar{b} + 1j$ J3	27 239.6	27 000
QCD $b\bar{b} + 2j$ J3	18 592.0	18 000
QCD $b\bar{b} + 3j$ J3	9 460.5	9 000
QCD $b\bar{b} + 0j$ J4	147.9	1 000
QCD $b\bar{b} + 1j$ J4	1 078.6	11 000
QCD $b\bar{b} + 2j$ J4	1 430.0	15 000
QCD $b\bar{b} + 3j$ J4	1 021.2	10 000
QCD $b\bar{b} + 4j$ J4	706.5	8 000
QCD $b\bar{b} + 0j$ J5+	3.2	1 000
QCD $b\bar{b} + 1j$ J5+	25.2	7 000
QCD $b\bar{b} + 2j$ J5+	50.0	15 000
QCD $b\bar{b} + 3j$ J5+	52.9	16 000
QCD $b\bar{b} + 4j$ J5+	55.5	17 000

Table 7.11. Details of 7 TeV diboson background samples. All samples were generated using HERWIG. Quoted cross sections are calculated at next-to-leading order.

Process	$\sigma \times \epsilon_F$ (pb)	Events
WW: 1 lepton filter	17.43	250 000
ZZ: 1 lepton filter	1.265	250 000
WZ: 1 lepton filter	5.553	250 000

Table 7.12. Details of 7 TeV QCD multijet background sample. Sample was generated using PYTHIA.

Process		$\sigma \times \epsilon_F$ (pb)	Events
QCD $b\bar{b}$	$p_{\mathrm{T}}(e) > 15$ GeV	75 126.6	4 448 000

Table 7.13. Details of 7 TeV γ^*+jets background samples. All samples were generated using PYTHIA.

Process		$\sigma \times \epsilon_F$ (pb)	Events
$\gamma^* \to \mu\mu$	15 GeV $< m(\ell^\pm, \ell^\mp) <$ 60 GeV	1 252.9	1 000 000
$\gamma^* \to ee$	15 GeV $< m(\ell^\pm, \ell^\mp) <$ 60 GeV	1 253.0	1 000 000
$\gamma^* \to \mu\mu$	8 GeV $< m(\ell^\pm, \ell^\mp) <$ 15 GeV	4 407.0	500 000
$\gamma^* \to ee$	8 GeV $< m(\ell^\pm, \ell^\mp) <$ 15 GeV	4 406.1	500 000

7.2. Data

The data used in the preliminary results presented in these thesis were collected at $\sqrt{s} = 7$ TeV between the 22nd of September and the 28th of October, 2010 corresponding to a total luminosity of $\int \mathcal{L} = (41.4 \pm 4.6)\ \mathrm{pb}^{-1}$. For this analysis, the data was required to satisfy basic beam, detector and data quality requirements. These requirements include optimal detector high voltage and nominal solenoid and toroid settings. It is also mandatory that the status of the subdetectors be sufficiently good that electron, muon, and jet identification as well as energy and momentum computations do not deviate significantly from expectation. This includes the systems needed for missing transverse momentum reconstruction, as well as the lepton trigger systems. These basic data quality requirements reduced the total integrated luminosity to $\int \mathcal{L} = (31.7 \pm 3.5)\ \mathrm{pb}^{-1}$. The uncertainty on the luminosity determination is estimated to be 11% [152].

7.2.1. Vertex Reweighting

With the instantaneous luminosity varying between 10^{30} cm^{-2}s^{-1} to 10^{32} cm^{-2}s^{-1} during the data taking period, the number of interactions per event fluctuated; there is typically between one and four interactions. The simulated samples were generated with an average of two interactions per event. The number of interactions per event can be determined by the number of good vertices per event, where a good vertex is defined as a vertex associated with at least five tracks. Figure 7.1 compares the number of good vertices per event in data to simulation for events passing event and dielectron selection criteria. As expected, the two distributions are quite different.

The discrepancies between data and simulation are corrected by reweighting the primary vertex multiplicity distribution in simulation to match that in data. The weights are shown in Figure 7.2 as a function of the number of good primary vertices. A single weight is used for events with ≥ 7 primary vertices due to the increased statistical error on the weight when considering numbers of primary vertices beyond this. Figure 7.3 presents the corrected simulation primary vertex multiplicity distribution compared to data. Note that while the corrected simulation distribution is very similar to that seen in data, it does not match exactly. This is because the primary vertex distributions are not exactly identical for each sample, however they are similar enough that a sample by sample reweighting is not necessary for this study.

For the simulated samples generated without any extra interactions, that is the diboson, low mass γ^*+jets and QCD multijet samples, no pileup weights are applied.

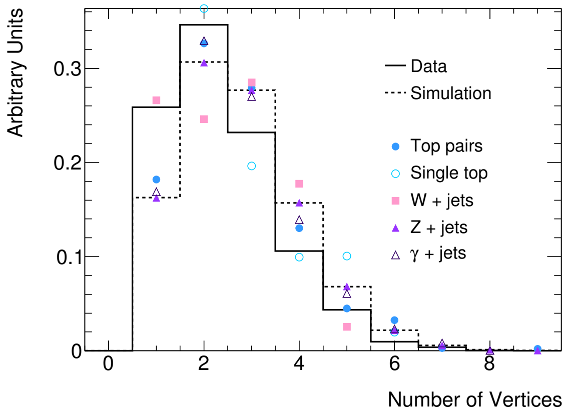

Figure 7.1. Number of good primary vertices in data (solid line) and simulation (dashed line). Individual simulated sample distributions are also shown for comparison (different shaped points). All distributions have been normalised to unit area.

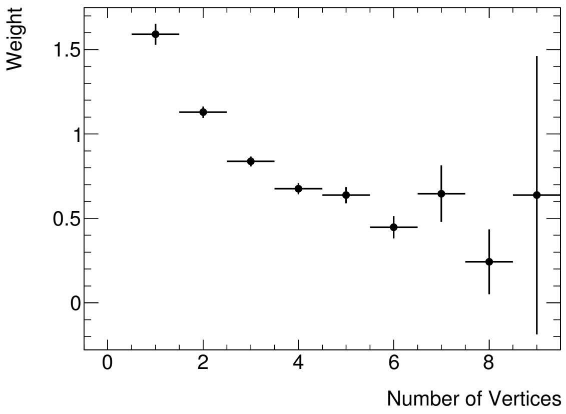

Figure 7.2. Weights to be applied to 7 TeV simulated samples generated with multiple interactions per event as a function of the number of good primary vertices. Due to the increasing statistical errors, a single weight of ~0.57 was used for events with ≥ 7 primary vertices.

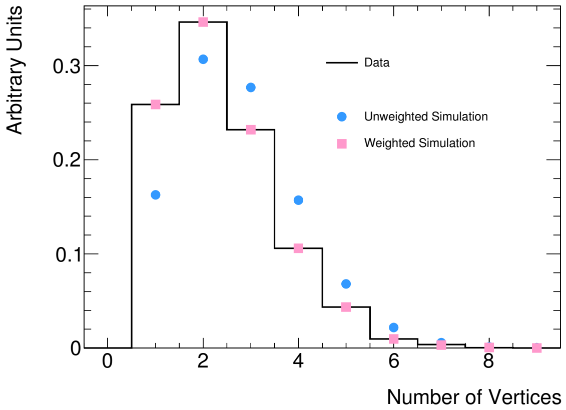

Figure 7.3. Number of good primary vertices in data (solid line) and simulation before (solid circles) and after (solid squares) reweighting.

Whether you can observe a thing or not depends on the theory which you use. It is the theory which decides what can be observed.

– Albert Einstein

8

Dileptonic Light Stop Search

This chapter presents a feasibility study of a search for light stop quark pair production in the dileptonic final state topology in 1 fb^{-1} of data at $\sqrt{s} = 10$ TeV as presented by the author in Reference [153]. An example of a decay scenario leading to a dileptonic final state is shown in Figure 8.1. The event signature of such a final state is two high p_T isolated leptons, two b jets and transverse missing energy from the two neutrinos and two neutralinos. This analysis only considers the cases where the lepton is an electron or muon. While this search channel has a lower branching ratio than both the semileptonic and fully hadronic channels, it has the advantage of relatively low and well controlled backgrounds.

8.1. Particle Selection Criteria at $\sqrt{s} = 10$ TeV

To detect the stop dileptonic final state, well reconstructed electrons, muons and jets are required. These final state particles need to be within detector acceptance and isolated from other particles for good momentum and energy measurements. The particle selection criteria required to meet these requirements are collectively referred to as 'preselection' criteria and are summarised in Table 8.1. Details of the preselection

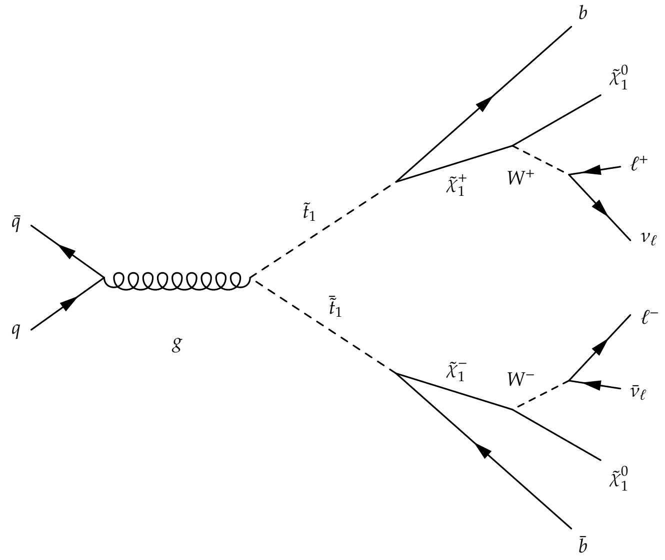

Figure 8.1. Possible $\tilde{t}_1\bar{\tilde{t}}_1$ production and decay scenario leading to the dileptonic final state.

Table 8.1. Summary of $\sqrt{s} = 10$ TeV preselection criteria.

	Electrons	**Muons**	**Jets**
p_T	> 10 GeV	> 10 GeV	> 10 GeV
η	$0 \leq \lvert\eta\rvert \leq 1.37$ or $1.37 \leq \lvert\eta\rvert \leq 2.5$	$\lvert\eta\rvert < 2.5$	$\lvert\eta\rvert < 2.5$
Energy Isolation	$E_\mathrm{T} < 6$ GeV in $\Delta R < 0.2$	$E_\mathrm{T} < 6$ GeV in $\Delta R < 0.2$	–

criteria for each of the particle types and their efficiency for *LHS*2 stop pair events are provided below.

Additionally, to aid in identifying stop events, flavour tagging is used, as well as measurements of missing and total transverse energy. Details of the algorithms used and their performance is given in the following.

8.1.1. Electron Selection Criteria for $\sqrt{s} = 10$ TeV

The electron candidates are required to have $p_\mathrm{T} > 10$ GeV and pseudorapidity in the range $0 \leq |\eta| \leq 2.5$ to match the coverage of the inner detector, and not be found in

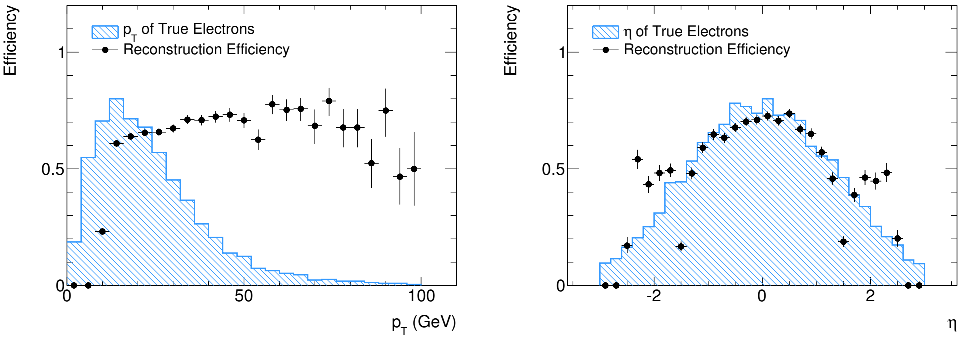

Figure 8.2. Electron reconstruction efficiencies for electrons originating from stop decays in the *LHS*2 benchmark point at $\sqrt{s} = 10$ TeV as a function of electron p_T (left) and η (right). The hashed histograms show the p_T and η distributions of true electrons. Reconstructed electrons are matched to true electrons within $\Delta R < 0.1$.

the calorimeter crack region $1.37 < |\eta| < 1.52$. The candidates are also required to be isolated: the additional transverse energy E_T in a cone $\Delta R < 0.2$ around the electron axis is required to be less than 6 GeV.

The reconstruction efficiency for electrons with these requirements in *LHS*2 stop pair events is shown in Figure 8.2. The plots are produced by taking all true electrons from a chargino, and counting how many are matched with $\Delta R < 0.1$ to good reconstructed electrons. The efficiency is the ratio of the two numbers. True electrons were not required to pass the p_T or η selection criteria and hence Figure 8.2 also includes detector acceptance.

8.1.2. Muon Selection Criteria for $\sqrt{s} = 10$ TeV

Muon candidates are defined as the best match combination from information attained from the muon chambers and tracking system, have $p_\mathrm{T} > 10$ GeV, be in the $|\eta| < 2.5$ range and are required to be isolated based on the same criteria as that for electrons. Muons which are close to the jets defined below, within a cone of radius $\Delta R < 0.3$, are rejected to remove those muons which arise from decays of hadrons inside jets which have the potential to degrade resolution in invariant mass combinations. The reconstruction efficiency, including detector acceptance, for muons in *LHS*2 stop pair events is shown in Figure 8.3.

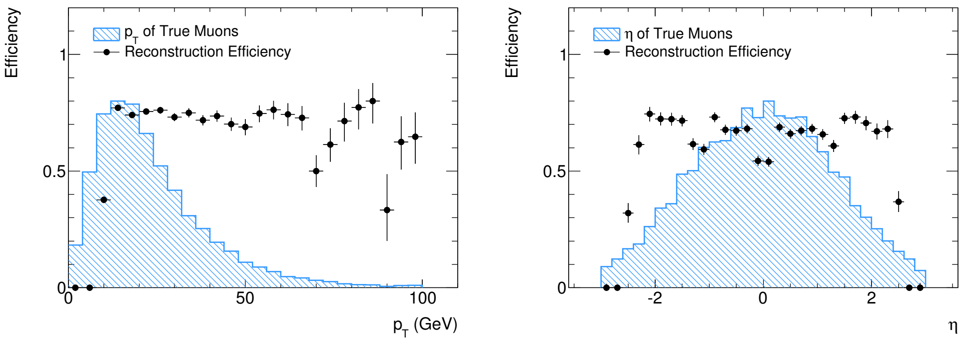

Figure 8.3. Muon reconstruction efficiencies for muons originating from stop decays in the *LHS*2 benchmark point at $\sqrt{s} = 10$ TeV as a function of muon p_T (left) and η (right). The hashed histograms show the p_T and η distributions of true muons. Reconstructed muons are matched to true muons within $\Delta R < 0.1$.

8.1.3. Jet Selection Criteria for $\sqrt{s} = 10$ TeV

Jets are reconstructed with the seeded fixed cone algorithm. Their energy is calibrated cell by cell using weights based on cell energy density and location in the calorimeter, then summed using weighting functions which account for detector effects. An extra correction factor depending on p_T and η is then applied to account for the different parameters of the seeded fixed cone algorithm used compared to that used to extract the calibration constants.

The jets are restricted to the pseudorapidity region $|\eta| < 2.5$ and must have $p_T > 10$ GeV. Since many electron candidates are also reconstructed as jets, if a jet overlaps with an electron within $\Delta R < 0.2$, the jet is removed. The jet reconstruction efficiencies, including detector acceptance, for jets with these requirements in *LHS*2 stop pair events is shown in Figure 8.4.

8.1.4. Flavour Tagging Performance at $\sqrt{s} = 10$ TeV

Jets originating from b quarks are identified using the IP3D+SV1 algorithm and are used to define both signal and background control regions. Reference [78] quotes a light jet rejection, defined as the inverse of the light jet misidentification rate, of 633 ± 7 for an efficiency of 50% using a weight threshold of > 6 for top pair events with this algorithm. To ensure maximal acceptance of the softer b quarks from light stop decays, while applying a threshold of $p_T > 15$ GeV, a flavour weight threshold of > 3 was used.

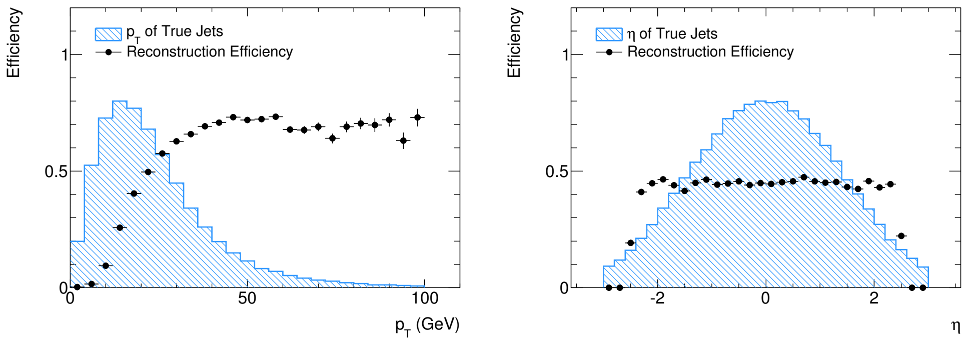

Figure 8.4. Jet reconstruction efficiencies for jets originating from stop decays in the *LHS*2 benchmark point at $\sqrt{s} = 10$ TeV as a function of jet p_{T} (left) and η (right). The hashed histograms show the p_{T} and η distributions of true jets. Reconstructed jets are matched to true jets within $\Delta R < 0.1$.

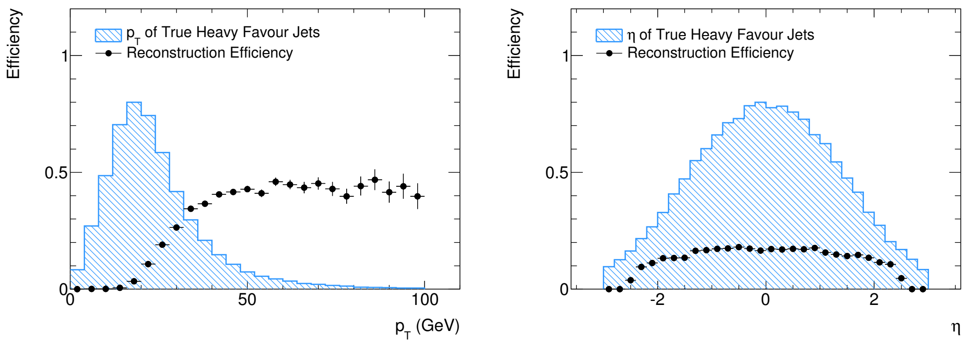

Figure 8.5. Flavour tagging efficiencies for heavy flavour jets originating from stop decays in the *LHS*2 benchmark point at $\sqrt{s} = 10$ TeV as a function of jet p_{T} (left) and η (right). The hashed histograms show the p_{T} and η distributions of true jets. Reconstructed jets are matched to true jets within $\Delta R < 0.1$.

Lowering the threshold further would increase the fake b jet contribution of W+jet and QCD multijet backgrounds. The flavour tagging efficiencies for b jets in *LHS*2 stop pair events is shown in Figure 8.5. It can be seen that the efficiency of identifying b jets in light stop events is fairly low, even with the loosening of the weight threshold.

8.1.5. $E_{\mathrm{T}}^{\mathrm{miss}}$ Reconstruction Performance at $\sqrt{s} = 10$ TeV

The refined cell-based $E_{\mathrm{T}}^{\mathrm{miss}}$ reconstruction algorithm, where cells are calibrated according to the reconstructed particle they are assigned to, is used in this analysis. The performance and resolution of the algorithm for *LHS*2 stop pair events is shown in

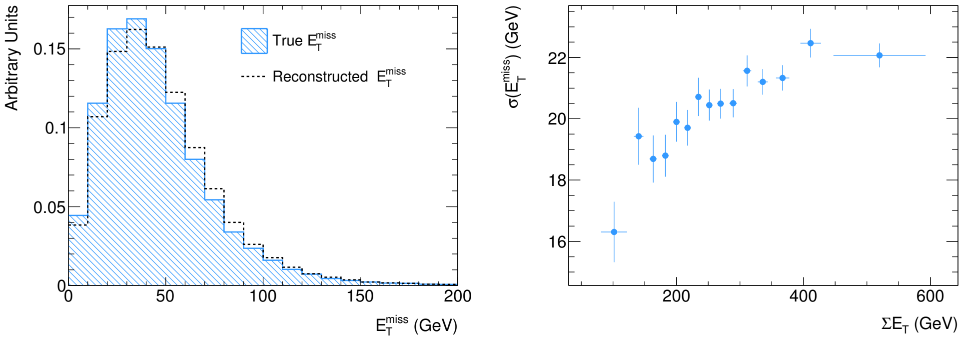

(a) $E_{\mathrm{T}}^{\mathrm{miss}}$ true and reconstructed **(b)** $E_{\mathrm{T}}^{\mathrm{miss}}$ resolution versus ΣE_{T}

Figure 8.6. $E_{\mathrm{T}}^{\mathrm{miss}}$ reconstruction performance in stop decays in the *LHS*2 benchmark point for $\sqrt{s}$ = 10 TeV.

Figure 8.6. It can be seen that the performance of the algorithm is as expected, with the reconstructed distribution being a little broader than the true and the $E_{\mathrm{T}}^{\mathrm{miss}}$ resolution degrading and plateauing as ΣE_{T} increases.

8.2. Trigger Selection at $\sqrt{s}$ = 10 TeV

Considering the relatively soft jet p_{T} and $E_{\mathrm{T}}^{\mathrm{miss}}$ in light stop events, it is anticipated that efficient triggering on dileptonic light stop events can only be provided by single and double lepton triggers. It is expected that for a 1 fb^{-1} data sample, the lowest p_{T} thresholds on single lepton triggers will be 20 GeV and 10 GeV for double lepton triggers. The exact thresholds will depend on detector running conditions.

Figure 8.7 shows the 10 GeV single lepton trigger efficiencies as a function of the reconstructed lepton p_{T} and η for *LHS*2 stop pair events. The efficiencies are measured with respect to the offline preselections described above. As can be seen, the 10 GeV single lepton trigger efficiencies are at plateau for $p_{\mathrm{T}} \gtrsim$12 GeV and are relatively flat in η. The efficiencies for the 20 GeV single lepton triggers are similar but with a higher p_{T} turn on, plateauing at $p_{\mathrm{T}} \gtrsim$ 22 GeV. The efficiencies for the 10 GeV double lepton triggers are the product of the single lepton triggers since the triggers are independent in events with isolated leptons.

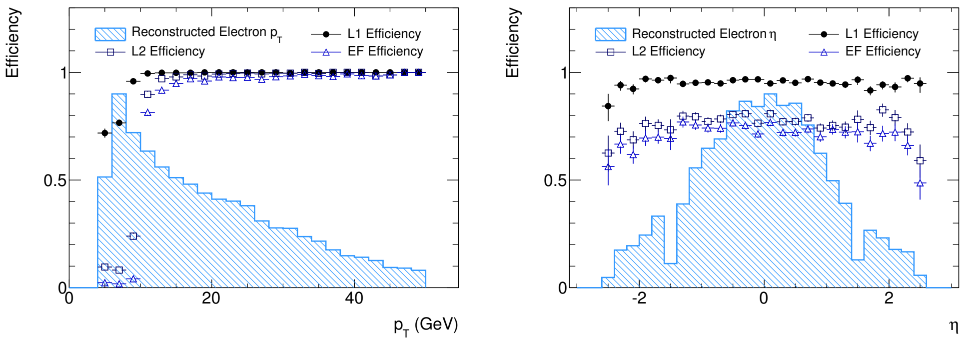

(a) Single electron trigger efficiency

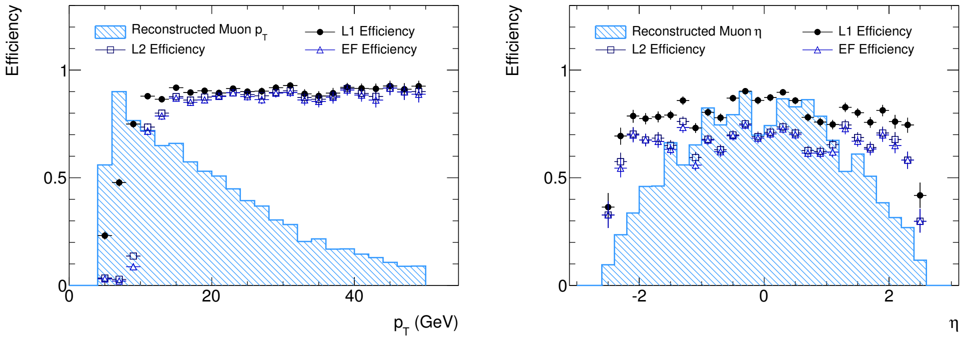

(b) Single muon trigger efficiency

Figure 8.7. Single lepton trigger efficiencies at L1 (solid circles), L2 (open squares) and EF (open triangles) for 10 GeV electron (upper) and muon (lower) triggers as a function of reconstructed lepton p_{T} (left) and η (right) in *LHS*2 stop pair events at $\sqrt{s}$ = 10 TeV. The hashed histograms show the p_{T} and η distributions of reconstructed leptons that match true leptons within $\Delta R = 0.1$. The efficiencies are measured with respect to the offline lepton preselections described above the exception of the p_{T} selection.

8.3. Dileptonic Event Selection at $\sqrt{s}$ = 10 TeV

Signal selection must take into account the varying signal topologies caused by the many possible stop-chargino-neutralino mass differences; for example, a small stop-chargino mass difference will produce very soft b jets, while a large stop-neutralino mass difference will give rise to high p_{T} leptons. Therefore multiple signal regions must be identified to clearly isolate as many stop signatures as possible.

The main challenge is to use appropriate selection criteria that do not incur large systematic uncertainties from detector effects such as the energy resolution of the

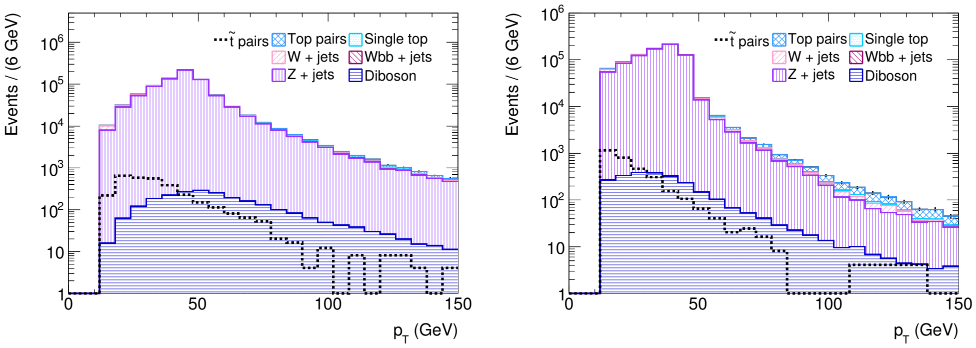

(a) $p_\mathrm{T}(\ell_1^\pm)$ **(b)** $p_\mathrm{T}(\ell_2^\pm)$

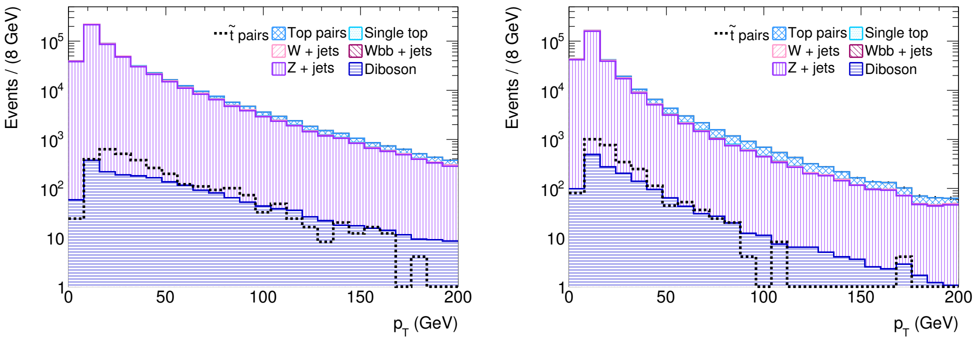

(c) $p_\mathrm{T}(\mathrm{jet}_1)$ **(d)** $p_\mathrm{T}(\mathrm{jet}_2)$

Figure 8.8. Dileptonic observables at 10 TeV normalised to 1 fb^{-1} for high p_T SM backgrounds (solid, filled histograms) superimposed with the *LHS*2 benchmark point (hollow, dashed histogram) after lepton selection.

calorimeters, or from model effects on the shape of the backgrounds, but still maintain sufficiently high signal to background ratio.

In this thesis, two signal regions have been studied, covering two different situations: (i) large stop-chargino mass differences, giving rise to high p_T b jets (b-jet region), and (ii) large stop-neutralino mass differences, giving rise to high p_T leptons and large $E_\mathrm{T}^\mathrm{miss}$ (high $E_\mathrm{T}^\mathrm{miss}$ region). Herein the selection criteria used is described in detail, and summarised in Table 8.2.

Events are first selected by requiring two opposite sign leptons with $p_\mathrm{T} > 12$ GeV. The lepton p_T thresholds are chosen to be as low as is allowed by the trigger to maximise efficiency. Missing transverse energy $E_\mathrm{T}^\mathrm{miss}$ and its significance defined as $E_\mathrm{T}^\mathrm{miss} / \sqrt{\sum E_\mathrm{T}}$, clean up a large fraction of Z+jets and QCD multijet events. These criteria are used in combination to improve background suppression at low $E_\mathrm{T}^\mathrm{miss}$. The angular separation between the two oppositely charged leptons $\Delta\phi(\ell_1^\pm, \ell_2^\mp) < (\pi - 0.4)$, has been used to

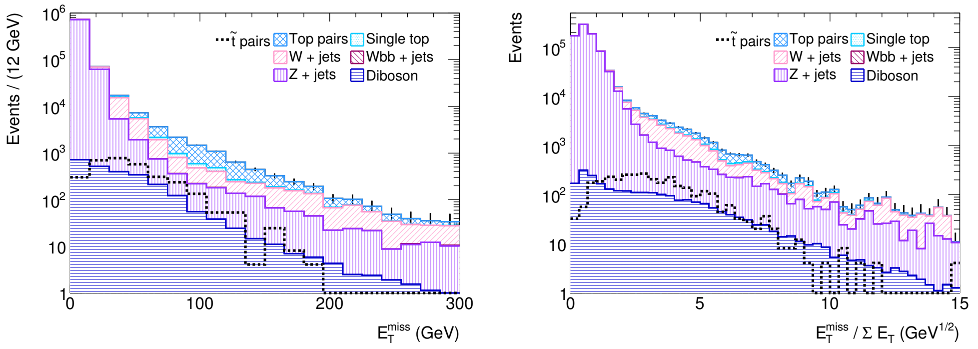

(a) $E_{\mathrm{T}}^{\mathrm{miss}}$ **(b)** $E_{\mathrm{T}}^{miss}/\sqrt{\sum E_{\mathrm{T}}}$

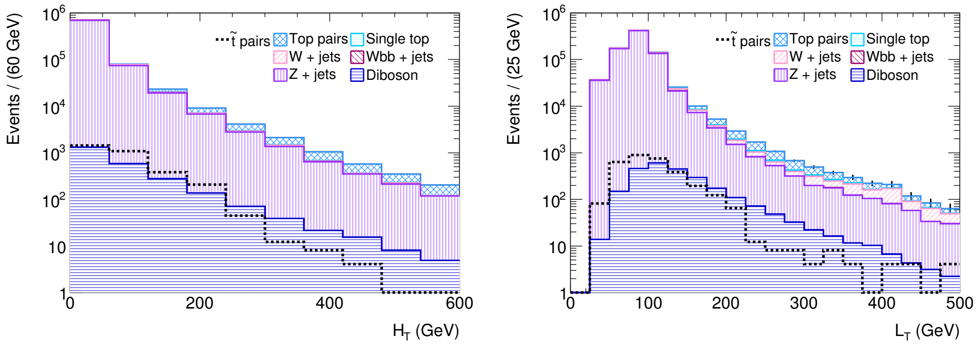

(c) H_{T} **(d)** L_{T}

Figure 8.9. More dileptonic observables at 10 TeV normalised to 1 fb^{-1} for high p_{T} SM backgrounds (solid, filled histograms) superimposed with the *LHS*2 benchmark point (hollow, dashed histogram) after lepton selection.

separate the more back-to-back W/Z+jets events from the more spherical signal events. A minimum dilepton invariant mass threshold on the oppositely charged lepton pair is imposed $m(\ell_1^{\pm}, \ell_2^{\mp}) > 5$ GeV, to suppress backgrounds arising from two calorimeter clusters pointing to the same inner detector track leading to a double counting of the same electron in the event. This requirement also removes backgrounds originating from photon conversions and Dalitz decay. A further selection of $m(\ell_1^{\pm}, \ell_2^{\mp})$ not being within the Z mass window $m_Z \pm 10$ GeV, is applied to remove Z+jets. To further suppress QCD multijet backgrounds, a requirement is placed on the minimum angular separation between the missing energy and the first two or three jets in the event, in the ϕ plane. Figures 8.8 and 8.9 show a comparison of some of these observables after dilepton requirements for the *LHS*2 benchmark point, top and other other high p_{T} SM (W+jets, Z+jets, diboson) background samples normalised to an integrated luminosity of 1 fb^{-1}.

Table 8.2. Summary of the 10 TeV dileptonic event selection criteria.

Criterion	b jet region	high $E_{\mathrm{T}}^{\mathrm{miss}}$ region
$p_{\mathrm{T}}(\ell_1^{\pm}), p_{\mathrm{T}}(\ell_2^{\mp})$	> 12 GeV	> 12 GeV
$E_{\mathrm{T}}^{\mathrm{miss}}$	> 20 GeV	> 20 GeV
$E_{\mathrm{T}}^{\mathrm{miss}} / \sqrt{\sum E_{\mathrm{T}}}$	> 2.0 GeV$^{1/2}$	> 7.0 GeV$^{1/2}$
$\Delta\phi(\ell_1^{\pm}, \ell_2^{\mp})$	$< (\pi - 0.4)$	$< (\pi - 0.4)$
$m(\ell_1^{\pm}, \ell_2^{\mp})$	> 5 GeV, $\ni m_Z \pm 10$ GeV	> 5 GeV, $\ni m_Z \pm 10$ GeV
$p_{\mathrm{T}}(b\mathrm{jet}_1)$	> 15 GeV	–
$p_{\mathrm{T}}(\mathrm{jet}_1)$	–	> 20 GeV
$p_{\mathrm{T}}(\mathrm{jet}_2)$	> 10 GeV	> 10 GeV
$\Delta\phi(\mathrm{jet}_{1,2,3}, E_{\mathrm{T}}^{\mathrm{miss}})$(min.)	> 0.3	> 0.3
$m_{b\mathrm{jet},\ell}$(max.)	< 85 GeV	–
$m_{b\mathrm{jet},\ell}$(min.)	< 55 GeV	–
L_{T}	< 170 GeV	–
H_{T}	< 250 GeV	–

The differences in the selection criteria of the two signal regions are as follows:

- ***b* jet region:** require at least one b jet with $p_{\mathrm{T}} > 15$ GeV and a secondary jet with $p_{\mathrm{T}} > 10$ GeV. The latter is to suppress background processes with low jet multiplicities. Upper thresholds are enforced on the maximum and minimum invariant masses formed between the b jet and the leptons, and on the transverse scalar sums $L_{\mathrm{T}} \equiv \sum_{\ell} p_{\mathrm{T}} + E_{\mathrm{T}}^{\mathrm{miss}}$ and $H_{\mathrm{T}} \equiv \sum_{\mathrm{jets}} p_{\mathrm{T}}$. The maximum invariant mass has a greater resolution for the heavier background top events, whereas the minimum invariant mass has a better resolution for the softer stop events. This is because the angle between the b jet and lepton depends on the virtuality of the W boson; in the stop decay, the W boson is virtual and so the b jet and lepton are closer together and the minimum invariant mass is smaller, while in top events the W boson is real.

- **$E_{\mathrm{T}}^{\mathrm{miss}}$ region:** require a leading jet with $p_{\mathrm{T}} > 20$ GeV, and a subleading jet with $p_{\mathrm{T}} > 10$ GeV. Tighter selection on $E_{\mathrm{T}}^{\mathrm{miss}} / \sqrt{\sum E_{\mathrm{T}}}$.

The event yield expectations are shown for the b jet and high $E_{\mathrm{T}}^{\mathrm{miss}}$ signal regions in Table 8.3 for the *LHS*2 benchmark point, top and other other SM (W+jets, Z+jets,

Table 8.3. Dileptonic event yields at 10 TeV for the *b* jet and high $E_{\mathrm{T}}^{\mathrm{miss}}$ signal regions for 1 fb^{-1} with the *LHS*2 benchmark point and SM backgrounds. Errors are statistical only.

Process	*b* jet region	high $E_{\mathrm{T}}^{\mathrm{miss}}$ region
$t\bar{t}$	279 ± 6	432 ± 7
single t	45 ± 3	38 ± 2
$W \to e\nu + j$	6 ± 2	8 ± 3
$W \to \mu\nu + j$	1 ± 1	17 ± 4
$W \to \tau\nu + j$	0	5 ± 2
$W \to \ell\nu + b$	3 ± 1	0
$Z \to ee + j$	0	0
$Z \to \mu\mu + j$	0.4 ± 0.4	30 ± 5
$Z \to \tau\tau + j$	10 ± 3	34 ± 4
Diboson	1.6 ± 0.4	28 ± 2
QCD	0	0
QCD bb	0	0
Signal	220 ± 30	50 ± 10
Backgrounds	345 ± 7	590 ± 10

Table 8.4. Dileptonic event yields at 10 TeV for the *b* jet and high $E_{\mathrm{T}}^{\mathrm{miss}}$ signal regions with 1 fb^{-1} for selected $m_{\tilde{t}_1}$, $m_{\tilde{\chi}_1^\pm}$, $m_{\tilde{\chi}_1^0}$ grid points. Errors are statistical only.

$m_{\tilde{t}_1}/m_{\tilde{\chi}_1^\pm}/m_{\tilde{\chi}_1^0}$ (GeV)	*b* jet region	high $E_{\mathrm{T}}^{\mathrm{miss}}$ region
95/95/45	90 ± 50	1 000 ± 200
95/135/45	50 ± 30	800 ± 100
105/95/45	70 ± 30	480 ± 80
105/135/45	20 ± 20	500 ± 90
115/95/45	380 ± 60	390 ± 60
115/135/45	10 ± 10	420 ± 60
120/95/45	450 ± 60	320 ± 50
120/215/45	20 ± 10	320 ± 50
150/95/45	59 ± 9	60 ± 10
150/215/45	10 ± 5	270 ± 30
180/95/45	5 ± 4	270 ± 30
180/215/45	0	150 ± 10
240/95/45	3 ± 1	27 ± 3
240/215/45	6 ± 1	62 ± 4

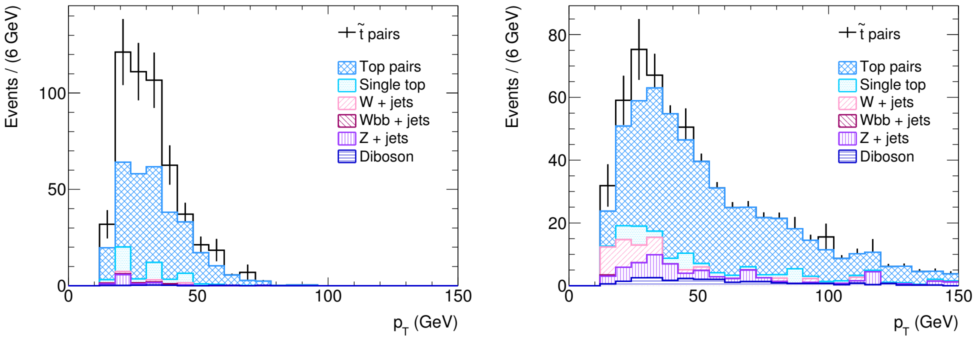

(a) Leading lepton p_{T}

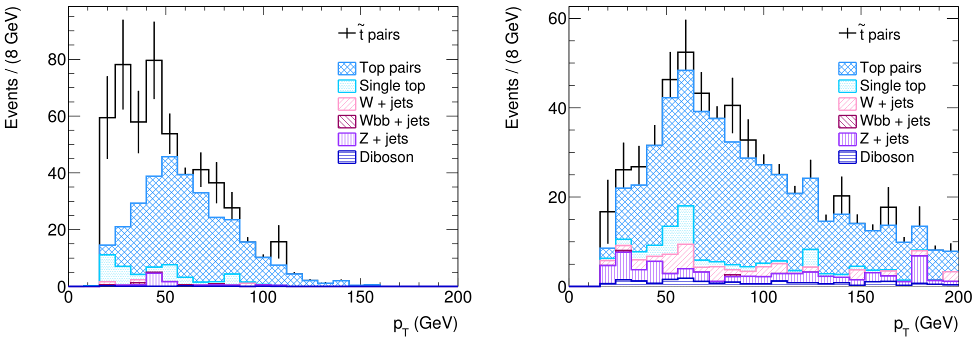

(b) Leading jet p_{T}

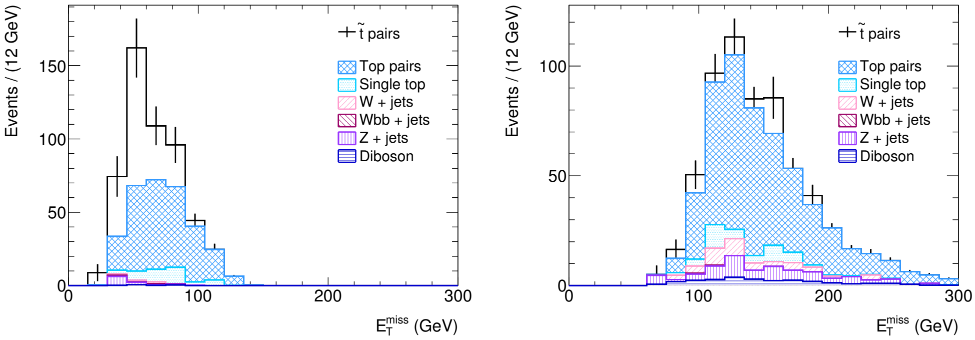

(c) $E_{\mathrm{T}}^{\mathrm{miss}}$

Figure 8.10. Dileptonic observables at 10 TeV for the b jet (left) and high $E_{\mathrm{T}}^{\mathrm{miss}}$ (right) signal regions for 1 fb^{-1} with the *LHS*2 benchmark point (hollow histogram) and SM backgrounds (patterned histograms).

diboson, QCD multijet, including $b\bar{b}$) background samples for an integrated luminosity of 1 fb^{-1}. Top pair production dominates the background contribution to both signal regions. Note the differing *LHS*2 event yields in the two signal regions; in this benchmark point, the relatively large stop-chargino mass difference, $m_{\tilde{t}_1} - m_{\tilde{\chi}_1^\pm} \simeq 25$ GeV $\gg m_b$, implies observable b jets, while the chargino-neutralino mass difference, $m_{\tilde{\chi}_1^\pm} - m_{\tilde{\chi}_1^0} \simeq 50$ GeV $\ll m_W$, implies relatively low $E_{\mathrm{T}}^{\mathrm{miss}}$ significance. This is clearer in Figure 8.10, where the same observables are displayed for both signal regions. Table 8.4 shows the event yield expectations for the b jet and high $E_{\mathrm{T}}^{\mathrm{miss}}$ signal regions for selected stop grid points for an integrated luminosity of 1 fb^{-1}. Unfortunately, these numbers are dominated by statistical errors after luminosity normalisation, particularly for points with low $m_{\tilde{t}_1}$. Note the varying event yields for the different sparticle masses and signal regions.

8.4. Dileptonic Background Estimation

Data driven approaches were developed to estimate normalisation of the major backgrounds. This approach was taken due to the difficulties associated with modelling possible instrumental effects and involving tails of distributions.

The contribution from W+jets production is an example of a background which could be challenging to simulate, as these events only mimic the dileptonic stop signal if a jet has been misidentified as a lepton. Consequently, this contribution will be controlled by direct measurements from data using the method described in detail in Section 10.4. For this analysis, the assumption was made that the W+jets background could be determined with 50% accuracy at 200 pb^{-1}, dominated by statistical errors, and 20% accuracy at 1 fb^{-1}, dominated by systematic effects.

The contribution of the QCD multijet and $b\bar{b}$ processes is also difficult to assess. As can be seen in Table 8.3, no simulated events from these backgrounds survive the signal region selection criteria. Note that due to large simulation scaling factors, this result is not very meaningful.

An estimation for the contributions from these processes can be made under the assumption of 'factorisable' efficiencies for the selection criteria. The event selection can be broken into three components, lepton, jets (and b jets) and $E_{\mathrm{T}}^{\mathrm{miss}}$ selection. The probability for finding two leptons ($\epsilon_{2\ell}$), two jets ($\epsilon_{2\mathrm{jet}}$), one b jet ($\epsilon_{b\mathrm{jet}}$), and $E_{\mathrm{T}}^{\mathrm{miss}}$ and its significance ($\epsilon_{E_{\mathrm{T}}^{\mathrm{miss}}}$) in an event are determined from the simulated samples. Criteria pertaining to angular separation and invariant masses between leptons of the same type are also considered in these efficiencies. The minimum azimuthal angle between the jets and $E_{\mathrm{T}}^{\mathrm{miss}}$ is correlated with the $E_{\mathrm{T}}^{\mathrm{miss}}$ criteria and included that efficiency.

Based on the factorised efficiencies, the expected yield for QCD multijet and $b\bar{b}$ backgrounds is calculated as:

$$\begin{aligned} b\,\text{jet region}: \quad N_{\text{expected}}(2\ell + b\text{jet} + E_{\mathrm{T}}^{\mathrm{miss}}) &= \sigma \times \mathcal{L} \times \epsilon_{2\ell} \times \epsilon_{b\text{jet}} \times \epsilon_{E_{\mathrm{T}}^{\mathrm{miss}}} \\ &= 35 \pm 8\,\text{events} \end{aligned}$$

$$\begin{aligned} \text{high}\,E_{\mathrm{T}}^{\mathrm{miss}}\,\text{region}: \quad N_{\text{expected}}(2\ell + 2\text{jets} + E_{\mathrm{T}}^{\mathrm{miss}\prime}) &= \sigma \times \mathcal{L} \times \epsilon_{2\ell} \times \epsilon_{2\text{jet}} \times \epsilon_{E_{\mathrm{T}}^{\mathrm{miss}\prime}} \\ &= 0.4 \pm 0.2\,\text{events} \end{aligned}$$

This yield is relatively insignificant and thus QCD multijet and $b\bar{b}$ backgrounds are neglected for the remainder of this analysis. The normalisation and shapes of these backgrounds will ultimately be determined directly from data using a method similar to Reference [154] which was developed for similar lepton selection criteria.

The shape of the expected contribution from the top backgrounds ($t\bar{t}$ and single t) is determined using simulation. The normalisation of the background will be derived from data using the ratio of expected top events in a sideband region defined for each of the signal regions. For the b jet signal region, the top sideband region is defined by $m_{b\text{jet},\ell}(\text{max.}) > 110$ GeV as shown in Figure 8.11(a), while all the other selection criteria remain the same as the signal region. For the high $E_{\mathrm{T}}^{\mathrm{miss}}$ signal region, the top sideband is defined by the presence of a b jet with $p_{\mathrm{T}} > 15$ GeV, as depicted in Figure 8.11(b). This is done to enhance the top contribution which is characterised by high p_{T} b jets.

To estimate $Z \to ee$ and $Z \to \mu\mu$ backgrounds deriving from Z events with invariant mass outside the Z mass window, the simulation contribution is normalised to the measured yield inside the Z mass window, shown in Figure 8.11(c), after subtracting the top background. Typically only a few Z events lie within the signal regions, but this technique is used to ensure control over this background.

Table 8.5 displays the yields in the top and Z sidebands for the *LHS*2 benchmark signal point and all SM background samples, excluding QCD multijet backgrounds. Note

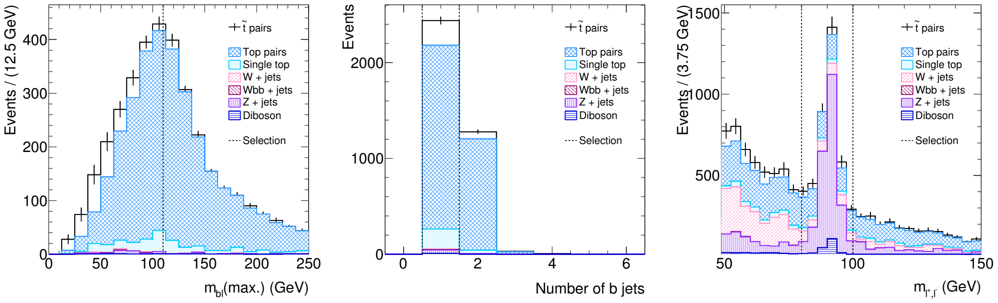

(a) $m_{b\text{jet},\ell}$(max.) for b jet signal region t sideband selection **(b)** Number of b jets for high $E_{\mathrm{T}}^{\mathrm{miss}}$ signal region t sideband selection **(c)** $m_{\ell^+\ell^-}$ for Z sideband selection

Figure 8.11. Dilepton top and Z sideband region selection variables at 10 TeV for the b jet and high $E_{\mathrm{T}}^{\mathrm{miss}}$ signal regions for 1 fb^{-1} with the *LHS*2 benchmark point (hollow histogram) and SM backgrounds (patterned histograms).

the insignificant contribution of the *LHS*2 signal to each of these regions. This can also be seen in Figure 8.11 where relevant selection variables in each of the sideband regions is shown. It is clear that the estimation of the Z background must follow the top background due to contamination. Selected stop signal grid points are given in Table 8.6. Points with high stop-chargino mass differences will contaminate the top sideband region while points with high chargino-neutralino mass differences will contaminate the Z sideband region.

The remaining backgrounds are primarily from $Z \rightarrow \tau\tau$, $Wb\bar{b}$, and diboson events. These backgrounds are estimated using simulation. These processes have two reconstructed opposite sign high p_{T} prompt leptons. The calculated number of expected background events from a process is given by: $N_{\text{expected}} = \sigma_{\text{process}} \times \mathcal{L} \times \epsilon$ where the acceptance, $\epsilon = N_{\text{passed}}/N_{\text{total}}$, is the fraction of events that passed the selection criteria. For data, the differences in particle selection efficiencies between simulation and data will need to be taken into account.

Table 8.5. Dileptonic event yields at 10 TeV for the top and Z sideband regions for both signal regions for 1 fb^{-1} with the *LHS*2 benchmark point and SM backgrounds.

Process	**b jet signal region**		**high $E_{\mathrm{T}}^{\mathrm{miss}}$ signal region**	
	t sideband	**Z sideband**	**t sideband**	**Z sideband**
$t\bar{t}$	699 ± 9	720 ± 9	343 ± 6	687 ± 9
single t	59 ± 3	96 ± 5	19 ± 1	125 ± 5
$W \to e\nu + j$	0	1 ± 1	0	38 ± 9
$W \to \mu\nu + j$	0	0	0	21 ± 6
$W \to \tau\nu + j$	0	0	0	2 ± 2
$W \to \ell\nu + b$	0	8 ± 2	1 ± 1	6 ± 2
$Z \to ee + j$	0	2 020 ± 30	0	327 000 ± 900
$Z \to \mu\mu + j$	5 ± 3	1 640 ± 30	1 ± 1	310 300 ± 900
$Z \to \tau\tau + j$	8 ± 2	1 ± 1	2 ± 1	50 ± 10
Diboson	2 ± 1	93 ± 3	2 ± 1	1 040 ± 10
Signal	30 ± 10	50 ± 10	16 ± 8	150 ± 20
Background	772 ± 9	41 000 ± 5 000	367 ± 6	760 000 ± 20 000

Table 8.6. Dileptonic event yields at 10 TeV for the top and Z sideband regions for both signal regions with 1 fb^{-1} for selected $m_{\tilde{t}_1}$, $m_{\tilde{\chi}_1^\pm}$, $m_{\tilde{\chi}_1^0}$ grid points.

$m_{\tilde{t}_1}/m_{\tilde{\chi}_1^\pm}/m_{\tilde{\chi}_1^0}$ (GeV)	**b jet signal region**		**high $E_{\mathrm{T}}^{\mathrm{miss}}$ signal region**	
	t sideband	**Z sideband**	**t sideband**	**Z sideband**
95/95/45	20 ± 20	0	110 ± 50	310 ± 80
95/135/45	50 ± 30	20 ± 20	50 ± 30	500 ± 100
105/95/45	30 ± 20	60 ± 30	70 ± 30	240 ± 60
105/135/45	20 ± 20	20 ± 20	60 ± 30	320 ± 70
115/95/45	10 ± 10	120 ± 30	90 ± 30	330 ± 60
115/135/45	10 ± 10	20 ± 10	0	310 ± 60
120/95/45	20 ± 10	100 ± 30	110 ± 30	150 ± 30
120/215/45	7 ± 7	0	10 ± 10	210 ± 40
150/95/45	70 ± 9	35 ± 7	23 ± 5	35 ± 7
150/215/45	3 ± 3	0	217 ± 7	150 ± 20
180/95/45	5 ± 4	5 ± 4	10 ± 5	140 ± 20
180/215/45	2 ± 2	2 ± 2	7 ± 3	90 ± 10
240/95/45	17 ± 2	7 ± 1	18 ± 2	7 ± 1
240/215/45	1 ± 1	6 ± 1	20 ± 2	17 ± 2

8.5. Dileptonic Background Subtraction

Once the background yields and shapes are determined, they are subtracted from the signal following the procedure described here. The results from the factorisation study in the previous section suggests that the QCD multijet contribution is small and can be neglected in this analysis in both signal regions. The top background is determined as described previously and subtracted from the signal and Z sideband regions. The Z contribution is then subtracted after rescaling as described above. Finally, the backgrounds estimated from simulation are subtracted, that is, backgrounds due to jets misidentified as leptons, and the backgrounds from $Z \to \tau\tau$, $Wb\bar{b}$, and diboson production. Table 8.7 shows the breakdown of the different backgrounds using the *LHS*2 benchmark as the signal. The presence of signal in the sideband region causes some overestimate of the top background in the signal region.

8.6. Systematic Uncertainties

The sources of systematic error which can affect the analysis presented in these thesis are outlined here, with their expected uncertainties taken from Reference [78] unless otherwise stated. The systematics are generally considered to be uncorrelated.

Table 8.7. Dileptonic background breakdowns at 10 TeV for both signal regions for 1 fb^{-1} with *LHS*2 as the signal component after background estimation. Statistical errors are derived from sideband rescaling.

Component	**Yield b jet region**	**Yield high $E_{\mathrm{T}}^{\mathrm{miss}}$ region**
Total Background	370 ± 10	620 ± 10
t Background	320 ± 20	490 ± 30
Z Background	9 ± 4	63 ± 9
Fake Background	59 ± 8	22 ± 5
Other Background	4 ± 4	27 ± 6
Total Estimate	390 ± 20	600 ± 30

8.6.1. Leptons

For electrons, the uncertainty on the identification efficiency is expected to be of the order of 0.5% and assumed to be p_{T} independent. For muons with $p_{\mathrm{T}} < 100$ GeV, a 1% uncertainty on identification efficiency is estimated. Both lepton identification uncertainties include the uncertainty on trigger identification efficiency and are independent of η. In this analysis, identification and efficiency uncertainties are determined by randomly removing the respective particles according to their nominal uncertainties.

The uncertainty on the electron energy scale is estimated to be 0.2% and resolution to be 1%, independent of p_{T} and η. For muons, the uncertainty on the p_{T} scale is estimated to be 0.2% and on the p_{T} resolution is estimated to be 4% for $p_{\mathrm{T}} < 100$ GeV, independently of η. Since the energy scale uncertainties are global changes to the overall energies of the particles, all particles of a given type are varied simultaneously. The uncertainties deriving from the resolution are derived by smearing the respective quantities with a single Gaussian.

8.6.2. Jets

The determination of the jet energy scale is rather challenging as it depends on a variety of detector and physics effects including nonlinearities in the calorimeter response due to the noncompensating nature of hadronic calorimeter, energy loss in inactive material and energy lost outside the jet cone.

To estimate the sensitivity of the analyses to the jet energy scale uncertainty, the energies of reconstructed jets are scaled by 5%. To account for jet energy resolution, the energy of each jet is smeared by $60\%/\sqrt{E} \oplus 5\%$. These uncertainties are assumed to be independent of p_{T} and η. Jet energies are modified prior to the selection of analysis objects in order to mimic the situation with real data. The resulting variation in the measurement from the analyses gives a good measure of the systematic uncertainty due to the jet energy scale.

This systematic is one of the largest ones contributing to the analysis due to the multiple jets in the signal region and use of jet combinations in selection criteria.

8.6.3. Missing Transverse Energy

The $E_{\mathrm{T}}^{\mathrm{miss}}$ can be affected by a number of causes. It is expected that the cell-based $E_{\mathrm{T}}^{\mathrm{miss}}$ reconstruction algorithm, is affected primarily by the jet and lepton energy scales and resolution. In this analysis, $E_{\mathrm{T}}^{\mathrm{miss}}$ is recalculated according to the systematic variations for the jet and lepton energy scales and resolutions. An additional rescaling is also necessary to account for the uncertainty in the measurement of the low p_{T} contribution to the $E_{\mathrm{T}}^{\mathrm{miss}}$ calculation. A 10% rescaling on this low p_{T} contribution is applied.

This dependence of the $E_{\mathrm{T}}^{\mathrm{miss}}$ calculation on the jet and lepton energy scales and resolution means that uncertainties on these measurements will affect analyses in multiple ways, increasing their associated systematic errors.

8.6.4. Flavour Tagging

The efficiency of the identification of b jets and related rejection of light favour jets depends on the performance of the tracking algorithms in reconstructing the impact parameter and secondary vertex. For integrated luminosities of 1 fb^{-1}, the relative error on the b tagging efficiency is assumed to be 5% while the light flavour rejection relative error is assumed to be 10%. As b jets are used in event selection, analyses will be very sensitive to uncertainties in flavour tagging. The b jet efficiency and light quark rejection variations are implemented by randomly rejecting b tagged jets or by randomly changing the tag of light flavour jets.

8.6.5. Jets Misidentified as Leptons

The largest systematic uncertainty associated with jets faking leptons arises from measuring the fake rate in control samples and extrapolating it to the signal region. Based on the of this background in References [155, 156], conservative estimates of the error on the fake rates from muons and electrons are taken to be 20% at 1 fb^{-1} and 50% at 200 pb^{-1}.

8.6.6. Background Simulation and Estimation

The uncertainties on top pair and single top quark production will affect the analysis the most, and thus were studied in detail. To estimate the uncertainty on predicted kinematic distributions, predictions from different generators were compared. It was found that only the rate of background processes was affected and not the shapes, and thus this uncertainty can be neglected. To evaluate the systematic effect of initial and final state QCD radiation (ISR and FSR), which impact the jet multiplicity and transverse momenta of particles in an event, studies were performed varying Λ_{QCD} from 0.192 GeV to 0.096 GeV (ISR) and 0.0384 GeV (FSR) in top background samples [157].

The uncertainties on the background cross sections used in the normalisation of the background processes will affect the signal to background ratios and propagate into the estimated signal yields. Following Reference [157], these cross section uncertainties were estimated to be: 10% for top pair, 20% for single top quark, W+jets and Z+jets and 100% for diboson and QCD multijet events.

8.6.7. Total Systematic Error

The total systematic error on the background estimation is 14% for the b jet region and 8% for the high $E_{\mathrm{T}}^{\mathrm{miss}}$ region. The results are mostly insensitive to the choice of signal hypothesis considered. A breakdown of the systematic uncertainties on the background estimation for both signal regions is given in Table 8.8. The systematic uncertainties are larger in the b jet signal region due to numerous selection criteria based on jet kinematics and flavour tagging weights. This tight selection window incurs dependence on the jet energy scale, allowing migration of top events between signal and sideband regions. The very tight requirement on the missing energy significance in the high $E_{\mathrm{T}}^{\mathrm{miss}}$ region results in relatively small error contributions. Further studies will need to be performed to reduce the systematics associated with the choices of signal region.

Table 8.8. Dileptonic systematic errors in % on background estimation at 10 TeV for 1 fb^{-1} for both signal regions.

Systematic	Error b jet region	Error high $E_{\mathrm{T}}^{\mathrm{miss}}$ region
E_e scale	0.51	0.13
E_e resolution	0.80	0.00
e identification efficiency	0.01	0.05
p_μ scale	0.16	0.03
p_μ resolution	0.42	1.00
μ identification efficiency	0.86	0.07
E_{jet} scale	8.50	4.41
E_{jet} resolution	3.92	0.42
flavour tagging efficiency	6.11	2.69
flavour tagging rejection	1.48	2.66
$t\bar{t}$ generation	1.74	1.14
$t\bar{t}$ fragmentation	5.21	3.36
$t\bar{t}$ ISR/FSR	5.25	1.14
single$-t$ generation/fragmentation	0.75	0.39
$\sigma(t\bar{t})$	0.30	0.23
$\sigma(\mathrm{single}-t)$	0.60	0.46
$\sigma(z)$	0.00	0.00
$\sigma(\mathrm{QCD})$, $\sigma(\mathrm{Diboson})$	0.98	4.53
Fake rate	3.02	0.71
Total	14.09	8.41

8.7. Dileptonic Search Results

The discovery potential for 1 fb^{-1} of integrated luminosity for the b jet and high $E_{\mathrm{T}}^{\mathrm{miss}}$ signal regions in various sparticle mass scenarios is shown in Figure 8.12, calculated following the procedure in Reference [158]. The signal significance taking into account statistical and systematic errors for the *LHS*2 benchmark and selected grid points is given in Tables 8.9 and 8.10. The two signal regions are sensitive to different signal points, with many points above 3σ in significance. Signal points with stop masses $\lesssim 120$ GeV and stop-neutralino mass differences $\gtrsim 60$ GeV have the greatest discovery potential. The signal points with significance $\gtrsim 10$ have the potential for exclusion with $\sim 200\ \mathrm{pb}^{-1}$ of data.

Table 8.9. Discovery potential at 10 TeV for the *b* jet signal region with 1 fb^{-1} for *LHS*2 and selected $m_{\tilde{t}_1}$, $m_{\tilde{\chi}_1^\pm}$, $m_{\tilde{\chi}_1^0}$ grid points.

Signal	**Yield (events)**	**Statistical Error (%)**	**Systematic Error (%)**	**Significance**
*LHS*2	212	14	26	3.1
95/95/45	90	29	61	1.4
95/135/45	45	57	130	0.6
105/95/45	74	35	74	1.1
105/135/45	15	170	360	0.2
115/95/45	374	8.3	14	10.4
115/135/45	10	250	540	0.1
120/95/45	451	7.2	12	12.4
120/215/45	22	120	250	0.3
150/95/45	61	40	95	0.9
150/215/45	10	240	515	0.1
180/95/45	5	470	1 000	0.0
180/215/45	0	–	–	–
240/95/45	2	1 000	2 200	0.0
240/215/45	6	410	890	0.0

Table 8.10. Discovery potential at 10 TeV for the high $E_{\mathrm{T}}^{\mathrm{miss}}$ signal region with 1 fb^{-1} for *LHS*2 and selected $m_{\tilde{t}_1}$, $m_{\tilde{\chi}_1^\pm}$, $m_{\tilde{\chi}_1^0}$ grid points.

Signal	**Yield (events)**	**Statistical Error (%)**	**Systematic Error (%)**	**Significance**
*LHS*2	53	74	100	0.8
95/95/45	697	7.1	8.6	12.1
95/135/45	562	8.2	9.9	10.6
105/95/45	238	18	24	3.2
105/135/45	360	12	16	4.7
115/95/45	268	17	22	3.5
115/135/45	239	17	22	3.4
120/95/45	180	25	33	2.4
120/215/45	209	20	26	3.0
150/95/45	36	110	150	0.5
150/215/45	215	19	25	3.1
180/95/45	214	19	25	3.1
180/215/45	131	31	41	1.9
240/95/45	20	190	270	0.3
240/215/45	44	90	130	0.6

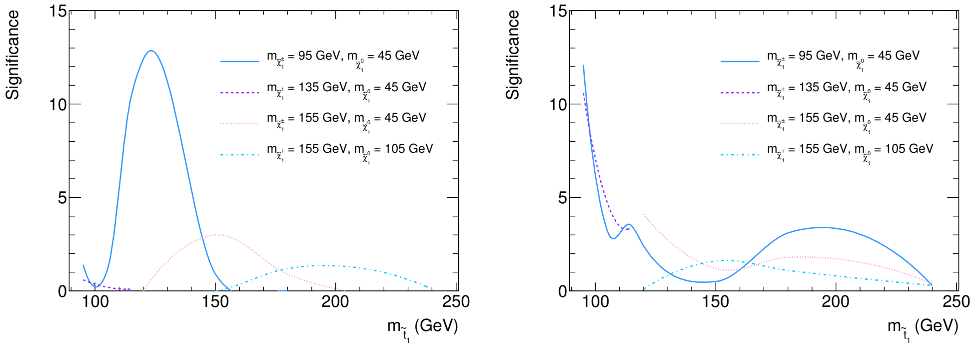

(a) b jet signal region

(b) High $E_{\mathrm{T}}^{\mathrm{miss}}$ signal region

Figure 8.12. Discovery potential at 10 TeV for the b jet and high $E_{\mathrm{T}}^{\mathrm{miss}}$ signal regions in various sparticle mass scenarios with 1 fb^{-1}.

8.8. Stop Contribution to Top Analyses

In the investigated light stop decay scenarios, the light stop decay products are identical to those from the decay of top quarks, but with two extra neutralinos in the final state (compare Figure 8.13 to Figure 8.1). Therefore, if nature allows this possibility, stop quark events affect the measurement of the top quark cross section. This section explores the possible contribution of the stop signal to the semileptonic and dileptonic top cross section analyses detailed in References [155] and [156] respectively.

The basic top event selections consist of a series of kinematic requirements on the reconstructed particles, which are listed in Table 8.11. The event yield expectations

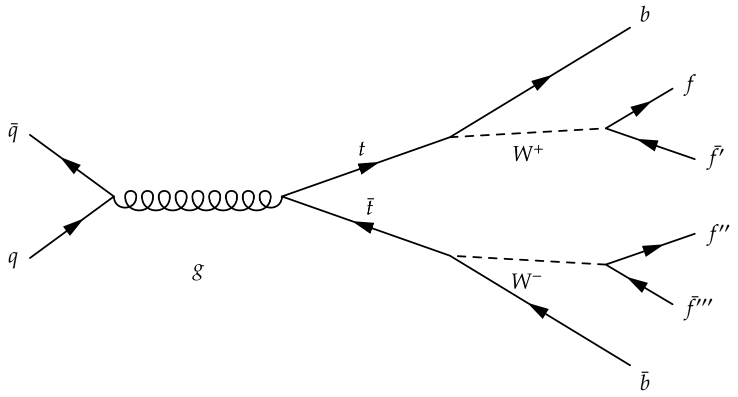

Figure 8.13. $t\bar{t}$ production and decay.

Table 8.11. Summary of 10 TeV basic top selection criteria.

Criterion	Semileptonic Selection	Dileptonic Selection
Leptons	$p_{\mathrm{T}}(\ell_1^{\pm}) > 20$ GeV	$p_{\mathrm{T}}(\ell_1^{\pm}), p_{\mathrm{T}}(\ell_2^{\mp}) > 20$ GeV $m(\ell_1^{\pm}, \ell_2^{\mp}) \ni m_Z \pm 5$ GeV
Jets	$p_{\mathrm{T}}(\mathrm{jet}_1), p_{\mathrm{T}}(\mathrm{jet}_2), p_{\mathrm{T}}(\mathrm{jet}_3) > 40$ GeV $p_{\mathrm{T}}(\mathrm{jet}_4) > 20$ GeV	$p_{\mathrm{T}}(\mathrm{jet}_1), p_{\mathrm{T}}(\mathrm{jet}_2) > 20$ GeV
Missing Transverse Energy	$E_{\mathrm{T}}^{\mathrm{miss}} > 20$ GeV	$E_{\mathrm{T}}^{\mathrm{miss}} > 35$ GeV (ee, $\mu\mu$) $E_{\mathrm{T}}^{\mathrm{miss}} > 20$ GeV ($e\mu$)

Table 8.12. Top basic selection event yields at 10 TeV 1 fb^{-1} with the *LHS*2 benchmark point and SM backgrounds. Errors are statistical only.

Process	Semileptonc Selection	Dileptonic Selection
$t\bar{t}$	28 570 ± 10	3 620 ± 20
single t	2 500 ± 200	292 ± 6
$W \rightarrow e\nu + j$	4 550 ± 40	75 ± 10
$W \rightarrow \mu\nu + j$	5 020 ± 40	110 ± 10
$W \rightarrow \tau\nu + j$	780 ± 20	8 ± 3
$W \rightarrow \ell\nu + b$	268 ± 2	1 ± 1
$Z \rightarrow ee + j$	340 ± 3	16 ± 3
$Z \rightarrow \mu\mu + j$	268 ± 2	117 ± 7
$Z \rightarrow \tau\tau + j$	296 ± 2	190 ± 9
Diboson	57 ± 1	110 ± 4
Signal	240 ± 20	280 ± 30
Backgrounds	42 600 ± 200	4 560 ± 30

are shown for both analyses in Table 8.12 for the *LHS*2 benchmark point together with top and other other high-p_{T} SM background processes for an integrated luminosity of 1 fb^{-1}. Top pair production is the dominant contribution, being 67% and 75% of the events passing the semileptonic and dileptonic selections respectively, while the *LHS*2 contribution is insignificant, making up 0.56% and 5.8% of the events.

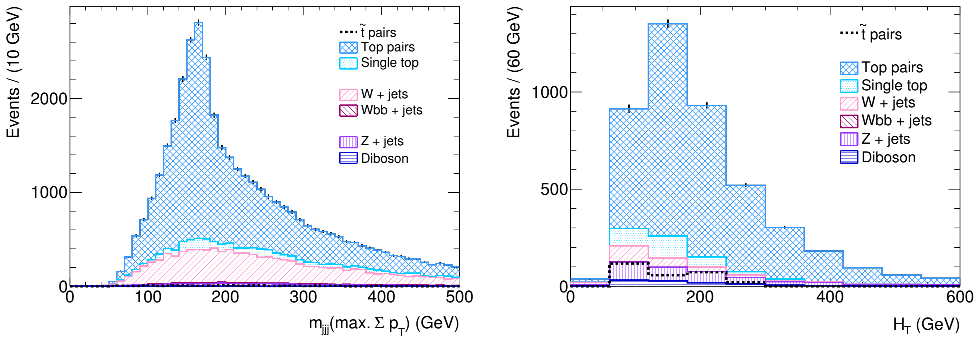

(a) Hadronic top mass **(b)** H_T

Figure 8.14. Top signal selection variables at 10 TeV for the semileptonic search channel (left) and the dileptonic search channel (right) normalised to 1 fb^{-1} for high p_T SM backgrounds (solid, filled histograms) superimposed with the *LHS*2 benchmark point (hollow, dashed histogram) after basic top selections.

In the top analyses, further selection criteria are used to increase the proportion of top events. These include selections on reconstructed quantities such as hadronic top mass (defined as the invariant mass of the three jet combination whose total p_T is the highest amongst all three jet combinations) in the semileptonic analysis [155] shown in Figure 8.14(a), or $H_\mathrm{T} \equiv \Sigma_\mathrm{jets} p_\mathrm{T}$ in the dileptonic analysis [156] shown in Figure 8.14(b). These particular variables have an effect on the stop events, further reducing their contribution to the top cross section. This implies that the stop signal will not be seen in top cross section measurements for most of the sparticle masses explored in this thesis, as shown in Table 8.13. This result motivates the necessity of specialised analyses to search for light stop signatures.

8.9. Dileptonic Stop Search Summary

Light stop events have highly varied final state kinematics depending on the stop, neutralino and chargino masses and mass differences. Despite the decay products of light stop pairs being identical to those from the decay of top quark pairs, due to either the low production cross sections or the low p_T of the final state products, stop pair events will not be seen in top cross section measurements. Thus, specialised analyses are necessary for light stop signatures.

Table 8.13. Top basic selection event yields at 10 TeV with 1 fb^{-1} for selected $m_{\tilde{t}_1}$, $m_{\tilde{\chi}_1^\pm}$, $m_{\tilde{\chi}_1^0}$ grid points. Errors are statistical only.

$m_{\tilde{t}_1}/m_{\tilde{\chi}_1^\pm}/m_{\tilde{\chi}_1^0}$ (GeV)	Semileptonic Selection	Dileptonic Selection
95/95/45	5 000 ± 1 000	1 000 ± 200
95/135/45	100 ± 200	900 ± 100
105/95/45	100 ± 200	800 ± 100
105/135/45	800 ± 100	700 ± 100
115/95/45	900 ± 300	780 ± 90
115/135/45	2 940 ± 70	680 ± 80
120/95/45	1 120 ± 40	780 ± 10
120/215/45	23 ± 7	530 ± 60
150/95/45	1 390 ± 5	230 ± 20
150/215/45	570 ± 3	450 ± 30
180/95/45	6 000 ± 8 000	440 ± 30
180/215/45	70 ± 900	240 ± 20
240/95/45	5 000 ± 4 000	57 ± 4
240/215/45	300 ± 500	88 ± 5

In this thesis, two signal regions were defined to take into account the varying signal topologies. Two sideband regions were defined for each signal region for data driven background estimation of Z boson and top quark backgrounds. For proton-proton collision energies of 10 TeV and an integrated luminosity of 1 fb^{-1} it was determined that signal points with low stop mass and high stop-neutralino mass differences had the greatest discovery potential. These signal points also have the potential for exclusion with $\sim$ 200 pb^{-1} of data.

Future studies must look towards refining the techniques used for background subtraction from sideband information and on ensuring the analysis be robust against systematic uncertainties from the selection criteria for the signal region. Significance may also be improved through studies of the expected shape of a null signal hypothesis in the signal region.

What we observe is not nature itself, but nature exposed to our method of questioning

– Werner Heisenberg

9

Semileptonic Light Stop Search

This chapter presents a feasibility study of extracting a signal for light stop pair production in the semileptonic final state topology in 1 fb^{-1} of data at $\sqrt{s} = 10$ TeV. Figure 9.1 shows a possible light stop production and decay scenario leading to the semileptonic final state, characterised by an isolated high p_{T} lepton, two b jets, two light quark jets and missing transverse energy.

The semileptonic channel has a higher branching ratio than the dileptonic channel and if the light stop is discovered, it offers the possibility of extracting the stop, neutralino and chargino masses by measuring kinematic endpoints of various quantities, as detailed in Appendix D. The shortcoming of this channel is the very large irreducible top background.

Note that this analysis uses the same particle preselection criteria as the previously discussed dileptonic analysis and these details will not be repeated here.

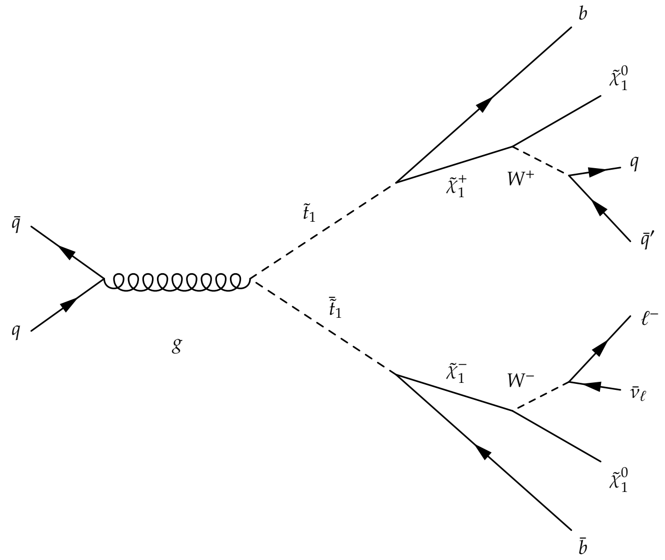

Figure 9.1. Possible $\tilde{t}_1\bar{\tilde{t}}_1$ production and decay scenario leading to the semileptonic final state.

Table 9.1. Summary of the 10 TeV semileptonic event selection criteria.

Criterion	Selection
Leptons	$p_T(\ell_1^\pm) > 20$ GeV
Jets	$p_T(\mathrm{jet}_1), p_T(\mathrm{jet}_2) > 10$ GeV $p_T(b\mathrm{jet}_1), p_T(\mathrm{bjet}_2) > 15$ GeV $H_T < 300$ GeV
Missing Transverse Energy	$E_T^{\mathrm{miss}} > 20$ GeV

9.1. Semileptonic Event Selection

Due to the similarity of stop pair decay to top pair decay, event selection is based on that defined for the measurement of the top cross section in the semileptonic channel in Reference [155], but with softer requirements on the kinematics to match the stop signal. Table 9.1 provides the stop event selection criteria. Both the top and stop analyses begin by requiring at least one lepton with $p_T > 20$ GeV. This requirement reduces the signal efficiency, but is necessary due to trigger requirements;

it is expected for 1 fb^{-1} of integrated luminosity, the lowest single lepton trigger will have a p_{T} threshold of 20 GeV. Figure 9.2 shows a comparison of some of the basic event observables after trigger and lepton requirements for the *LHS*2 benchmark point, and top and other other SM (W+jets, Z+jets, diboson) background processes normalised to an integrated luminosity of 1 fb^{-1}. Of note is the missing transverse energy distribution in Figure 9.2(e). Unlike the canonical SUSY collider signature of a number of high p_{T} jets and large missing transverse energy, stop pair events tend to be more spherical in shape, meaning the neutralinos in the final state balance one another and the missing transverse energy is not large. The missing transverse energy selection is therefore left at 20 GeV to suppress Z and QCD multijet backgrounds. Thus the jet p_{T} thresholds are the only selections to be lowered for the softer signal kinematics. However, lowering the required jet p_{T} thresholds allows more QCD multijet events to pass selections and so the additional requirement of two b tagged jets is added to improve signal purity. To decrease the higher energy top pair background, an upper threshold is placed on the scalar sum of the p_{T} of the jets passing preselection criteria, $H_{\text{T}} \equiv \sum_{\text{jets}} p_{\text{T}} <$ 300 GeV, shown in Figure 9.2(f). The event yield expectations after event selection are shown for the signal region in Table 9.2 for the *LHS*2 benchmark point, and top and other SM (W+jets, Z+jets, diboson) background processes normalised to an integrated luminosity of 1 fb^{-1}.

Table 9.2. Semileptonic signal region event yields at 10 TeV for 1 fb^{-1} with the *LHS*2 benchmark and SM backgrounds. Errors are statistical only.

Process	Yield
$t\bar{t}$	10 762 ± 6
single t	1 200 ± 100
$W \to e\nu + j$	150 ± 20
$W \to \mu\nu + j$	140 ± 30
$W \to \tau\nu + j$	20 ± 10
$W \to \ell\nu + b$	222 ± 2
$Z \to ee + j$	4 ± 1
$Z \to \mu\mu + j$	18 ± 5
$Z \to \tau\tau + j$	10 ± 1
Diboson	3 ± 1
Signal	300 ± 20
Backgrounds	12 500 ± 100

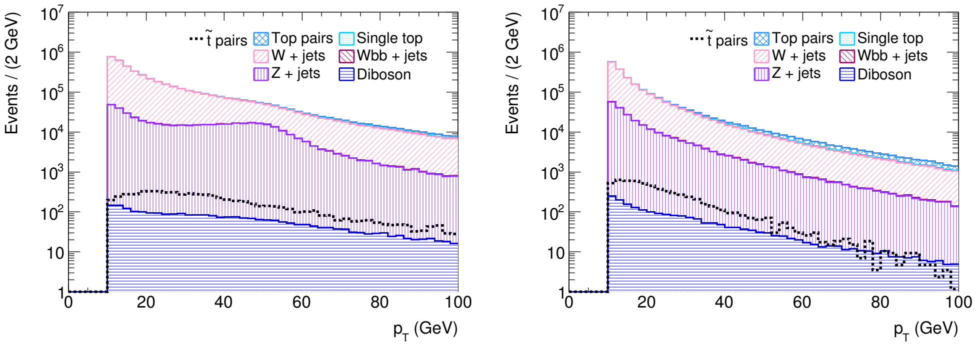

(a) $p_{\mathrm{T}}(\mathrm{jet}_1)$ **(b)** $p_{\mathrm{T}}(\mathrm{jet}_2)$

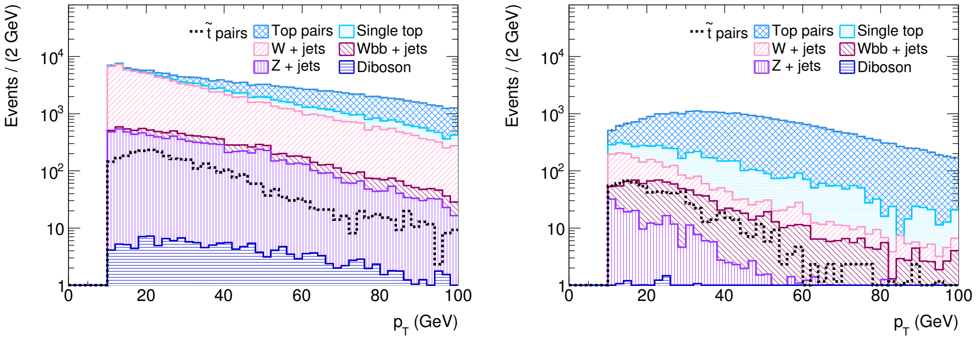

(c) $p_{\mathrm{T}}(\mathrm{bjet}_1)$ **(d)** $p_{\mathrm{T}}(\mathrm{bjet}_2)$

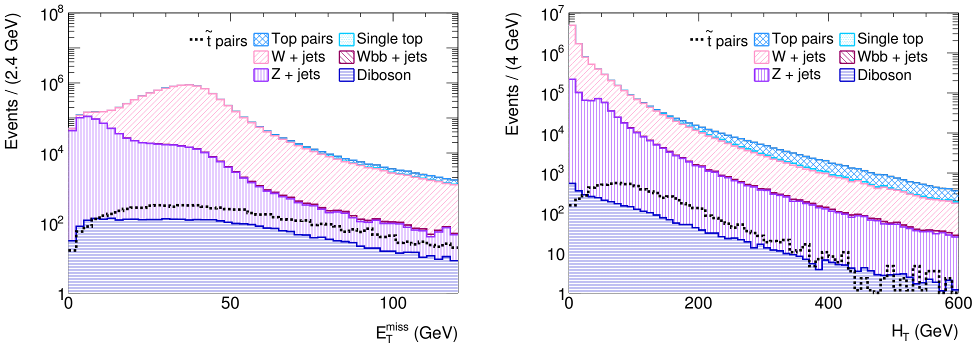

(e) $E_{\mathrm{T}}^{\mathrm{miss}}$ **(f)** H_{T}

Figure 9.2. Semileptonic observables at 10 TeV normalised to 1 fb^{-1} for high p_{T} SM backgrounds (solid, filled histograms) superimposed with the *LHS*2 benchmark (hollow, dashed histogram) after lepton trigger and selection.

9.2. Semileptonic Background Estimation

After event selection, the expected dominant background to the light stop pair signal is still top pair production. Smaller contributions to the background arise from single top quark, W/Z+jets and QCD multijet production. Single top quark events are the most similar to the light stop signal, requiring only the mistagging of a light favour jet as a b jet to mimic the signal. W+jets events only contribute to the background if two jets are identified as b jets while Z+jets events only contribute to the background if at least 20 GeV of $E_{\mathrm{T}}^{\mathrm{miss}}$ is reconstructed, one of the leptons is not identified and two jets are identified as b jets. QCD multijet events only constitute a background if at least 20 GeV of $E_{\mathrm{T}}^{\mathrm{miss}}$ is reconstructed and if a jet is mistakenly identified as a lepton or if it contains a semileptonic decay of a heavy quark, as well as two jets that are identified as b jets. Given the substantial uncertainty in the theoretical prediction of QCD multijet processes with heavy flavour quarks and the difficulty in reliably modelling lepton misreconstruction and flavour mistagging, data driven estimation is required for all these backgrounds. In this analysis, the contributions from single top quark, W/Z+jets and QCD multijet backgrounds will be neglected since the contribution from top pair production is an order of magnitude higher, as seen in Table 9.2.

9.2.1. Semileptonic Top Background Estimation

The top pair background can be estimated from data by exploiting the fact that one of the W bosons decays into two light jets and the other decays into a charged lepton and its corresponding neutrino, $t\bar{t} \rightarrow b\bar{b}W^{+}W^{-} \rightarrow b\bar{b}\bar{q}q\ell\nu_{\ell}$. Two pure top samples can thus be selected, with minimum contribution from the stop signal, by separately applying strict selection criteria on each of the two branches.

An essential step to estimate this background is to reconstruct all selected events assuming a semileptonic top pair hypothesis. The hadronic top candidate is defined as the combination of one tagged b jet and two light jets those combined total p_{T} is the highest. The reconstruction of the leptonic top candidate is a little more complicated due to the neutrino in the final state. However since the neutrino is the only source of missing energy, it can be assumed that the transverse missing momentum measured belongs to the neutrino. The longitudinal momentum of the neutrino can then be calculated by assuming that the W-boson which the neutrino and lepton decayed from was on-shell, and applying the W mass constraint. For $m_{\mathrm{T}} \equiv 2|p_{\ell_{\mathrm{T}}}||E_{\mathrm{T}}^{\mathrm{miss}}| - 2\vec{p}_{\ell_{\mathrm{T}}} \cdot \vec{E}_{\mathrm{T}}^{\mathrm{miss}} \leq$

m_W, there is a quadratic equation and two solutions for p_{ν_z} exist[1]. Simulation studies show that the solution closest to the truth kinematics is the one with the smallest absolute value, hence is the one chosen in this analysis. For $m_T > m_W$, $p_{\ell_z} = E_T^{miss}/p_{\ell_T}$ is used. This calculated p_{ν_z} is combined with the x and y components of E_T^{miss}, the remaining b jet and highest p_T lepton in the event to create the leptonic top candidate. This method associates the correct b jet with the appropriate decay branch 87% of the time in top events and 79% in stop pair events.

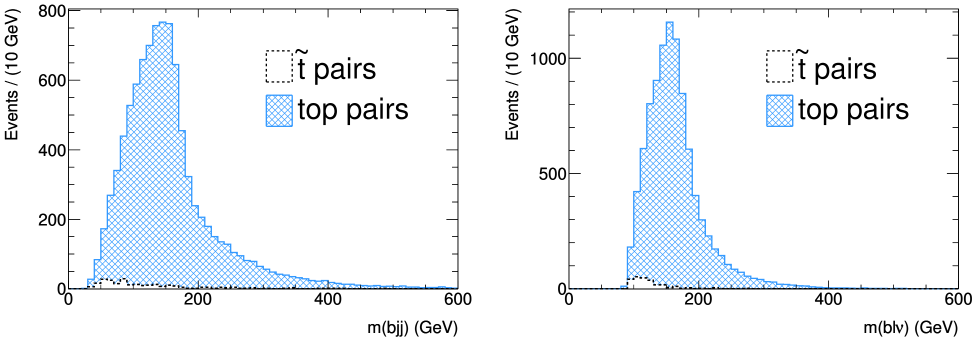

(a) Hadronic top mass, m(bjj) **(b)** Leptonic top mass, m($b\ell\nu$)

Figure 9.3. Reconstructed hadronic and leptonic top masses for semileptonic top (solid line, hashed histogram) and *LHS*2 stop (dashed line, hollow histogram) pairs for 1 fb^{-1} at 10 TeV.

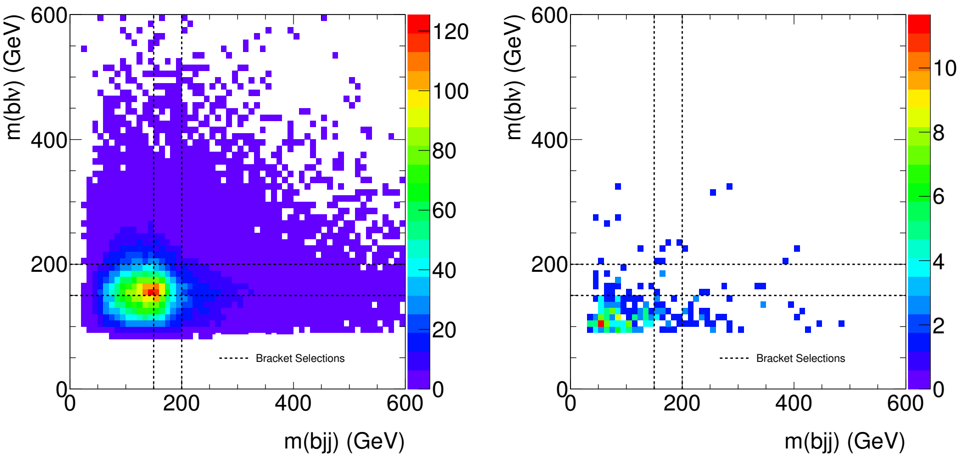

(a) Semileptonic Top Pairs **(b)** Semileptonic Stop Pairs

Figure 9.4. Reconstructed hadronic and leptonic top masses for semileptonic top (left) and *LHS*2 stop (right) pairs for 1 fb^{-1} at 10 TeV. Dashed lines show top sample selections from Reference [159].

---

[1] Details of this calculated can be found in Appendix E.

The distributions of the reconstructed hadronic and leptonic top masses, m(bjj) and m($b\ell\nu_\ell$), are shown in Figures 9.3 and 9.4 for semileptonic top and *LHS*2 stop pairs. The top mass peak at ≈ 175 GeV is clearly visible in the top sample, while the stop contributes only to the lower mass regions. The leptonic top mass distribution is narrower than the hadronic top mass as a consequence of the neutrino momentum calculation.

Top pair background estimation will nominally proceed as follows. A hadronic top sample is chosen in data using selections on the leptonic branch, the sample is then normalised to the number of events in the background, and finally the scaled sample is subtracted from the observed hadronic top distribution to extract the signal. Similarly for a leptonic top sample selected using the hadronic branch. In a previous ATLAS semileptonic stop pair analysis [159], the hadronic top sample was chosen to satisfy the following conditions on the leptonic branch: m($b\ell\nu_\ell$) = (175 ± 25) GeV and m($b\ell$) $>$ 60 GeV, while the leptonic top sample was chosen to satisfy the following conditions on the hadronic branch: m(bjj) = (175 ± 25) GeV and m(jj) $>$ 60 GeV. However the bracket selection criteria around the top mass are too narrow and would bias the background samples as can be seen in Figure 9.4(a). Moreover, due to the broad jet resolution, the leptonic top sample does not include most of the events in the hadronic top peak. If the background sample distribution is not representative of the full background distributions, the estimate of the background under the stop signal is incorrect. As shown in Reference [159], the background subtraction will result in a distribution that does not reproduce the real signal, biasing the endpoint measurements.

In this analysis, top pair background estimation will thus proceed as follows. A top sample is selected using the leptonic branch of the event, requiring m($b\ell\nu$) $>$ 150 GeV. This top sample is then used to estimate the shape of the hadronic background distribution, m(bjj). Figure 9.5(a) displays the sample distribution compared to the background distribution for semileptonic top pair events and all high p_T background (single top, W/Z+jets and diboson) processes. The sample distributions have been rescaled so that the integral of the sample and background distributions are the same. It can be seen that the top sample matches the background distribution well, as expected. Including the other background samples introduces a bias in the low mass region, due to the contributions of single top quark and W+jets events, which can be seen quantitively in Table 9.3. Further work will be required to reduce the bias. In this analysis it is assumed that the shape of the contribution of the single top and W+jets events is well reproduced by the simulation and this background can be accounted for by using the fitted linear function, shown in Figure 9.5(b). Thus the background estimation method will contain an extra step, where the sample in data will be corrected

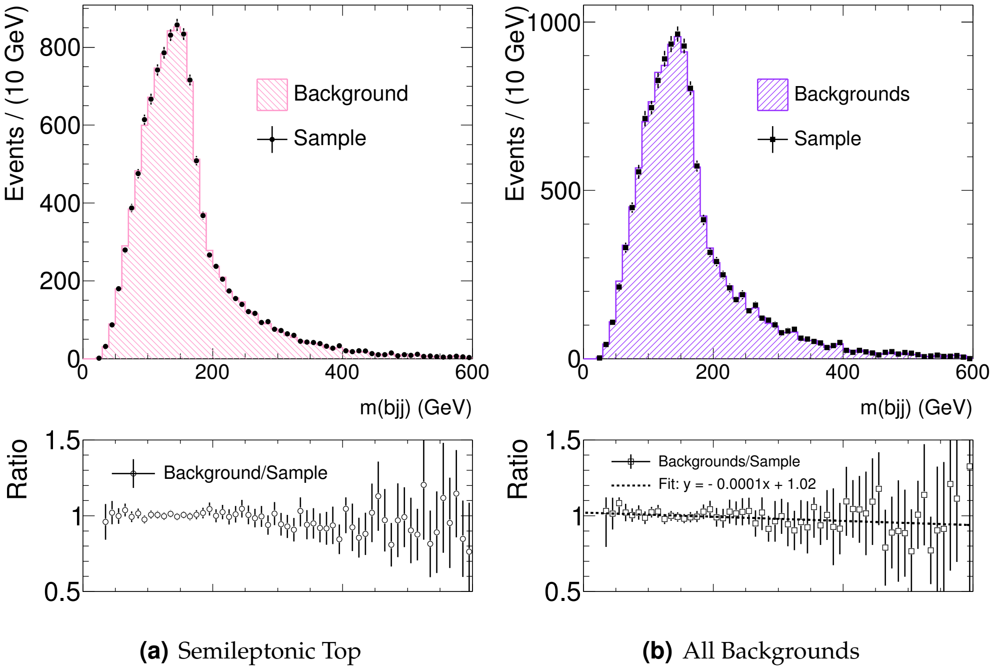

(a) Semileptonic Top **(b)** All Backgrounds

Figure 9.5. Semileptonic top estimation samples (solid points) compared to background distributions (hashed histograms) for 1 fb^{-1} at 10 TeV. Sample distributions have been rescaled to match the background distributions. The lower half of the figures presents the ratio of the sample to the background (hollow points).

using the fit from simulation. The corrected distribution will then be scaled to match the number of events in the background distribution, using the integral of the upper halves of the distributions, 300 GeV $<$ m(bjj) $<$ 600 GeV, where there is no signal expected as seen in Figure 9.3(a). Finally, the sample will be subtracted from the observed distribution to extract the signal.

9.3. Semileptonic Background Estimation Results

To test the sensitivity of the above background estimation method , the detector systematic uncertainties were applied as explained in the previous chapter. The percentage change in the event yield in the background samples is shown in Table 9.4. As can be seen, the method is very sensitive to systematic uncertainties related to jet reconstruction with a 40% change in event yield due to jet energy scale and a 13% change due to jet energy resolution. Inaccuracies in measuring jet energy affect the analysis in

Table 9.3. Semileptonic top sample region event yields at 10 TeV for 1 fb^{-1} with the *LHS*2 benchmark and SM backgrounds. Errors are statistical only.

Process	Yield
$t\bar{t}$	4 809 ± 4
single t	640 ± 70
$W \to e\nu + j$	61 ± 8
$W \to \mu\nu + j$	54 ± 8
$W \to \tau\nu + j$	11 ± 15
$W \to \ell\nu + b$	97 ± 1
$Z \to ee + j$	2 ± 1
$Z \to \mu\mu + j$	8 ± 4
$Z \to \tau\tau + j$	3 ± 1
Diboson	1 ± 1
Signal	90 ± 10
Backgrounds	5 680 ± 70

multiple ways, the most obvious way being the jet related particle, event and sample selections. More subtly, changes in jet energies also affect missing transverse energy measurements which this method relies on to reconstruct the leptonic top candidate. The dependence on energy scale could be reduced by explicitly reconstructing the hadronic W boson and quantifying the energy shift from the expected mass peak and correct for this. The dependence on energy resolution could be reduced by fitting for the top peak. Thus while there is potential in the semileptonic stop pair decay channel, it is not a viable analysis until the experiment is mature and some light stop signal has been discovered using the dileptonic channel as the detector and backgrounds need to be well understood, particularly as some of the variations in the background estimation due to systematic uncertainties are greater than the *LHS*2 signal expectation.

9.4. Semileptonic Stop Search Summary

If evidence for new physics is found following the dileptonic search procedure detailed in the previous chapter, it will not necessarily indicate the presence of a light stop. Further information about the mass scale and nature of the underlying physics in the event must be extracted from measurements of the kinematic endpoints for example in the semileptonic decay mode.

Table 9.4. Semileptonic systematic errors in % on semileptonic background estimation at 10 TeV for 1 fb^{-1}.

Systematic	**Background Estimation**
E_e scale	0.089
E_e resolution	0.005
e identification efficiency	0.436
p_μ scale	0.088
p_μ resolution	0.780
μ identification efficiency	0.531
E_{jet} scale	40.454
E_{jet} resolution	13.363
flavour tagging efficiency	4.209
flavour tagging rejection	0.300
Total	42.825

This chapter investigated a simple method for data driven background estimation for the semileptonic stop search channel exploiting the two different decay branches to select pure top samples by reconstructing events assuming a semileptonic top pair hypothesis. It was found that for an integrated luminosity of 1 fb^{-1} at $\sqrt{s} = 10$ TeV, the semileptonic decay channel is overwhelmed by backgrounds and requires detailed understanding of the detector and backgrounds in order to extract a signal. In particular, jet resolution and energy scale need to be known at an accuracy of 1%.

The light stop semileptonic decay mode is thus not a discovery channel, and only worth pursuing after some sort of new physics signal is seen using in the more sensitive dileptonic decay mode.

Although we often hear that data speak for themselves, their voices can be soft and sly.

– Frederick Mosteller

10

Preliminary Data Studies

The amount of good quality data recorded by ATLAS at $\sqrt{s} = 7$ TeV in 2010 is insufficient to perform a complete light stop study, particularly with the reliance of the analysis on lower p_{T} electrons, muons and jets compared to the published ATLAS SM W, Z/γ^{*} and top cross sections [160, 161] and SUSY one lepton search [162]. The busy LHC collision environment and material heavy ATLAS detector means that lower p_{T} particles are more challenging to identify and their properties are more difficult to determine accurately. This chapter presents some preliminary results, focusing on understanding the selection variables and backgrounds in the dileptonic search channel where both leptons are electrons.

10.1. Particle Selection Criteria at $\sqrt{s} = 7$ TeV

The preselection criteria used to select electrons, muons and jets for analysis at $\sqrt{s} = 7$ TeV and the algorithms used for flavour tagging and missing transverse energy reconstruction are described in this section. The preselection criteria and algorithms used are based on those used in the SUSY dilepton search [163]. These criteria are different than those at $\sqrt{s} = 10$ TeV due to the updated reconstruction algorithms and the modifications required to match the $\sqrt{s}$ = 7 TeV detector running conditions of 2010. Of note is the increase in the lepton p_{T} thresholds to 15 GeV to ensure that selected events are not affected by trigger turn on.

10.1.1. Electron Selection Criteria for $\sqrt{s}$ = 7 TeV

The electron candidates are required to have $p_{\mathrm{T}} > 15$ GeV and pseudorapidity in the range $0 \leq |\eta| \leq 2.47$. The pseudorapidity range has been restricted slightly compared to the preselection at $\sqrt{s}$ = 10 TeV as it was found that energy measurements of electrons near the transition region of the electromagnetic calorimeter were not well measured. Candidate electrons are discarded if there are any problematic cells within their electromagnetic cluster; due to hardware issues [101], the signal cannot be read out from ~2% of the electromagnetic calorimeter cells. The reconstruction efficiency for the electrons passing these requirements in *LHS*2 stop pair events is shown in Figure 10.1. The effect of the problematic electromagnetic calorimeter regions can be seen in the asymmetry in the η efficiency.

For the final selection in the signal and control regions, the electron candidates are required to pass additional requirements based on: at least one hit in the first pixel layer, the number of TRT hits, the ratio of high threshold TRT hits to the total number of TRT hits and the ratio of cluster energy to track momentum. These additional selections remove secondary electrons from photon conversions as well as hadrons misidentified as electrons. To reduce the number of fakes electron and electrons imbedded in jets, the electron candidates are also required to be isolated based on calorimeter energy: the

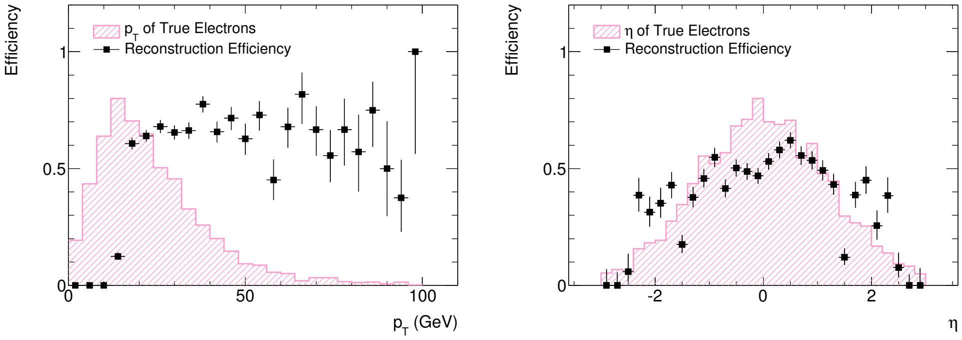

Figure 10.1. Electron reconstruction efficiencies for electrons originating from stop decays in the *LHS*2 benchmark scenario at $\sqrt{s}$ = 7 TeV as a function of electron p_{T} (left) and η (right). The hashed histograms show the p_{T} and η distributions of true electrons. Reconstructed electrons are matched to true electrons within $\Delta R < 0.1$.

ratio of the additional transverse energy E_{T} in a cone $\Delta R < 0.2$ around the electron axis to electron p_{T} is required to be less than 0.15. Simulated events containing electrons are reweighted using η dependent event weights which correct for differences in electron reconstruction efficiencies between data and simulation.

10.1.2. Muon Selection Criteria for $\sqrt{s} = 7$ TeV

Muon candidates at $\sqrt{s} = 7$ TeV are required to be identified either in both the muon spectrometer and the inner detector, or as a match between an extrapolated inner detector track and one or more segments in the muon spectrometer, as opposed to muon candidates at $\sqrt{s} = 10$ TeV, which had to be identified in both subdetectors. This new approach is used to recover efficiency losses in detector regions with poor muon spectrometer coverage. The inner detector track is required to have a at least 1 pixel and 6 SCT hits, and an η dependent number of TRT hits. For combined muons, the χ^2 of the match between the inner detector and muon spectrometer tracks must be < 150, and the difference between the p_{T} estimates must be compatible within the resolution of the subdetector systems. The track quality selections are designed to reject both muons originating from cosmic rays and inflight decays of π and K mesons, while the isolation requirement reduces both these and the contribution from b and c quark decays.

All muon candidates are also required to to be less then 10 mm in the z coordinate from the primary vertex to discriminate against muons from cosmic rays. Only muons with $p_{\mathrm{T}} > 15$ GeV and $|\eta| < 2.4$ are considered. In simulated events, each component

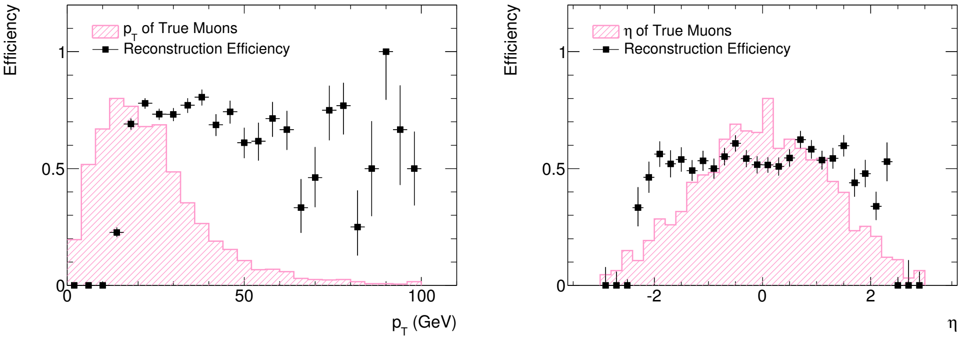

Figure 10.2. Muon reconstruction efficiencies for muons originating from stop decays in the *LHS*2 benchmark scenario at $\sqrt{s} = 7$ TeV as a function of muon p_{T} (left) and η (right). The hashed histograms show the p_{T} and η distributions of true muons. Reconstructed muons are matched to true muons within $\Delta R < 0.1$.

of the muon p_T is shifted and smeared in order to reproduce the p_T resolution in data [164]. The resolution in data is worse than in simulation because both the muon spectrometer and inner detector do not yet have the ultimate alignment and calibration constants. The reconstruction efficiency for muons in *LHS*2 stop pair events is shown in Figure 10.2. For the final selection in the signal and control regions, the muon candidates are required to be isolated based on surrounding track momentum: the sum of the transverse momenta of tracks in a cone $\Delta R < 0.2$ around the muon axis is required to be less than 1.8 GeV.

10.1.3. Jet Selection Criteria for $\sqrt{s} = 7$ TeV

Jets are reconstructed with the anti-k_T sequential algorithm with parameters $R = 0.4$ and $k = -1$ [99]. Their energy is measured at the electromagnetic scale and corrected for the effects of calorimeter non-compensation and inhomogeneities by using p_T and η dependent calibration factors [165].

Only jets with $p_T > 15$ GeV and $|\eta| < 2.5$ are considered. If a jet and an electron are both identified within a distance $\Delta R < 0.2$, the jet is discarded. Furthermore, identified electrons or muons are only considered if they satisfy $\Delta R > 0.4$ with respect to the closest jet. This helps to remove leptons which arise from decays of hadrons inside jets. The jet reconstruction efficiencies for jets with these requirements in *LHS*2 stop pair events is shown in Figure 10.3.

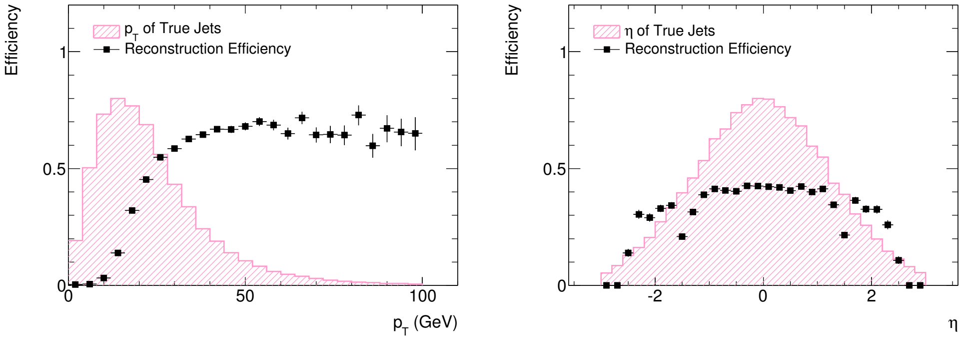

Figure 10.3. Jet reconstruction efficiencies for jets originating from stop decays in the *LHS*2 benchmark scenario at $\sqrt{s} = 7$ TeV as a function of jet p_T (left) and η (right). The hashed histograms show the p_T and η distributions of true jets. Reconstructed jets are matched to true jets within $\Delta R < 0.1$.

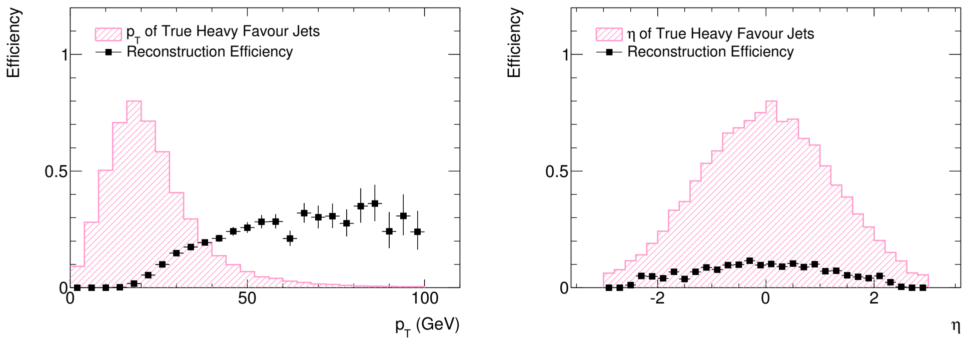

Figure 10.4. Flavour tagging efficiencies for heavy flavour jets originating from stop decays in the *LHS*2 benchmark scenario at $\sqrt{s} = 7$ TeV as a function of jet p_T (left) and η (right). The hashed histograms show the p_T and η distributions of true jets. Reconstructed jets are matched to true jets within $\Delta R < 0.1$.

10.1.4. Flavour Tagging Performance at $\sqrt{s} = 7$ TeV

Jets originating from b quarks are identified using the SV0 algorithm for this analysis and it is anticipated for early results to be used only to define the top control region. A jet is considered a b jet if it has $p_\mathrm{T} > 15$ GeV and contains a secondary vertex with $L/\sigma(L) > 5.72$. This operating point yields a 50% efficiency in simulated top pair events [166]. The tagging efficiencies for b jets in *LHS*2 stop pair events is shown in Figure 10.4. The efficiency is overall much lower than at $\sqrt{s} = 10$ TeV due to the operating point chosen and the simpler, more robust algorithm used.

10.1.5. $E_\mathrm{T}^\mathrm{miss}$ Reconstruction Performance at $\sqrt{s} = 7$ TeV

A simpler version of the refined cell-based $E_\mathrm{T}^\mathrm{miss}$ reconstruction algorithm is used in this analysis, where jets are calibrated as described above and the low p_T energy deposits are calibrated at the electromagnetic scale. The performance and resolution of the algorithm for *LHS*2 stop pair events is shown in Figure 10.5. The resolution is larger than that seen at $\sqrt{s} = 10$ TeV due to the simpler energy calibrations used.

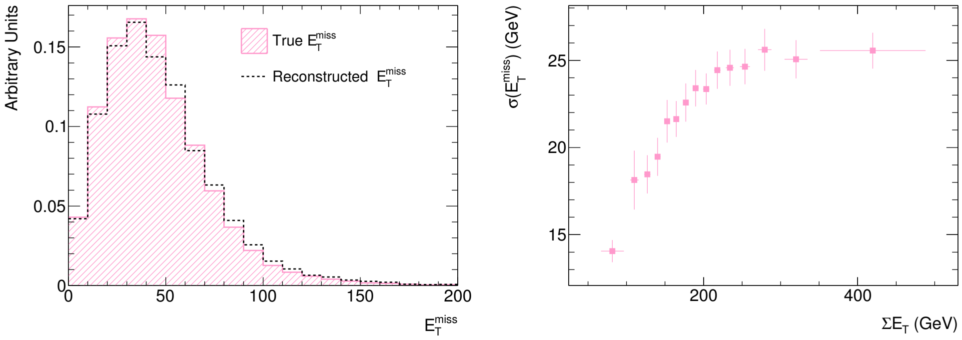

(a) $E_{\mathrm{T}}^{\mathrm{miss}}$ true and reconstructed **(b)** $E_{\mathrm{T}}^{\mathrm{miss}}$ resolution versus ΣE_{T}

Figure 10.5. $E_{\mathrm{T}}^{\mathrm{miss}}$ reconstruction performance in stop decays in the *LHS*2 benchmark scenario for $\sqrt{s} = 7$ TeV.

10.2. Trigger Selection at $\sqrt{s} = 7$ TeV

In the 7 TeV data running period in 2010, the lowest p_{T} thresholds on single and double electron triggers evolved with the luminosity. The single electron trigger began on a threshold of $p_{\mathrm{T}} = 10$ GeV and evolved to a threshold of $p_{\mathrm{T}} = 15$ GeV. The double electron trigger began on thresholds of $p_{\mathrm{T}} = 3$ GeV for both leptons, evolved to thresholds of $p_{\mathrm{T}} = 5$ GeV and ended with thresholds of $p_{\mathrm{T}} = 10$ GeV. For this analysis, events were selected using a dielectron trigger with a threshold of $p_{\mathrm{T}} = 10$ GeV on both electrons. This trigger is operational for the entire data taking period used in this study. The electron trigger efficiency plateaued at $p_{\mathrm{T}} \sim 15$ GeV which is the p_{T} threshold used in the study presented here.

Table 10.1 gives the overall efficiency for reconstructed electrons with $p_{\mathrm{T}} > 10$, 15, 20 and 25 GeV while Figure 10.6 shows the 15 GeV single electron trigger efficiencies as a function of the reconstructed electron p_{T} and η for data and simulation. Unfortunately the 10 GeV single electron trigger was not operational during this period due to high trigger rates. However, the performance of the 10 GeV trigger can be inferred by studying the 15 GeV trigger, as both triggers rely on the same underlying algorithm.

The trigger efficiencies were measured with the 'tag and probe' method using $Z \to e^+e^-$ events. The tag and probe electrons are defined as the two highest p_{T} leptons in the events. They must have opposite sign and are required to be reconstructed according to the basic electron preselection criteria. The invariant mass of the two electrons is required to be in the interval 80 – 100 GeV. The tag offline electron is required to be

Table 10.1. Single 15 GeV electron trigger efficiencies in percentage with respect to the given number of reconstructed electrons with $p_T > 10$, 15, 20 and 25 GeV in data and simulation. Errors are statistical.

	Data		**Simulation**	
	Efficiency	**# of Electrons**	**Simulation**	**# of Electrons**
$p_T > 10$ GeV	92.6 ± 1.3	10 825 ± 104	92.3 ± 0.4	8 504 ± 27
$p_T > 15$ GeV	95.2 ± 1.3	10 529 ± 103	93.9 ± 0.4	8 358 ± 27
$p_T > 20$ GeV	96.5 ± 1.4	9 815 ± 99	94.8 ± 0.5	7 846 ± 26
$p_T > 25$ GeV	96.6 ± 1.4	9 115 ± 95	94.9 ± 0.5	7 283 ± 25

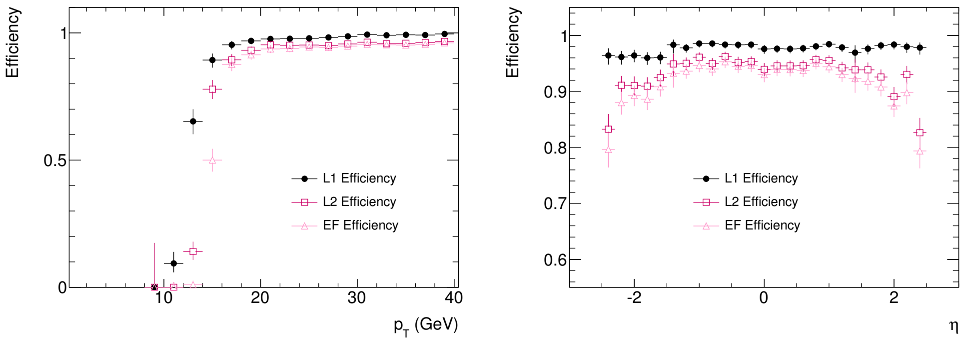

(a) 15 GeV single electron trigger efficiency in simulation

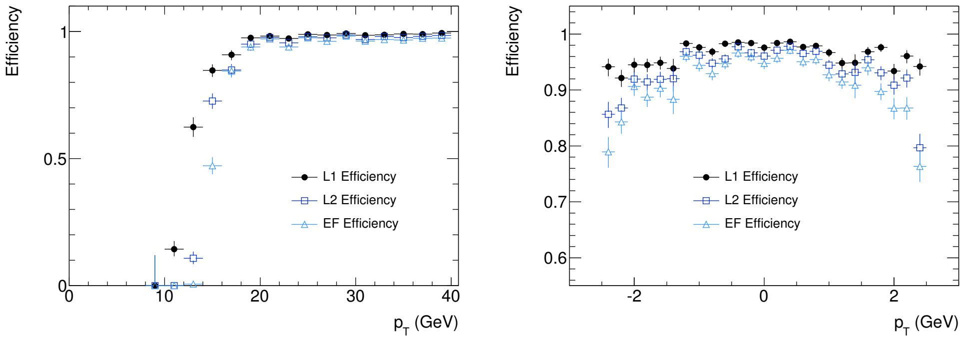

(b) 15 GeV single electron trigger efficiency in data

Figure 10.6. Single electron trigger efficiencies at L1 (solid circles), L2 (open squares) and EF (open triangles) for the 15 GeV electron trigger as a function of reconstructed lepton p_T (left) and η (right) in data (below) and simulation (above) at $\sqrt{s} = 7$ TeV. Errors are statistical.

matched to a trigger electron passing the 15 GeV threshold. For the selected events, the efficiency of the 15 GeV trigger is evaluated by measuring the rate at which the probe offline electron is matched to a trigger electron passing the 15 GeV threshold. It can be seen that the trigger plateaus at $p_{\mathrm{T}} \sim 20$ GeV and the efficiencies in data and simulation are in excellent agreement within statistics. Note that the number of electrons differs so drastically between data and simulation since this comparison is performed before the event preselection is applied.

10.3. Dileptonic Event Selection at $\sqrt{s} = 7$ TeV

Before any requirements are made on the number of leptons in the event, the following event preselection criteria are applied:

- If any jet with $p_{\mathrm{T}} > 20$ GeV fails basic quality selection criteria against detector noise and non-collision backgrounds [167], the event is discarded. These selections consider the energy fractions in the electromagnetic and hadronic endcap calorimeters, the maximum energy fraction in one calorimeter layer, the number of cells containing at least 90% of the jet energy, the fraction of cells with good quality pulse shapes and the jet mean energy averaged time.

- If any electron candidate is found in the calorimeter crack region $1.37 < |\eta| < 1.52$, the event is vetoed since the subsequent $E_{\mathrm{T}}^{\mathrm{miss}}$ and ΣE_{T} measurements can not be trusted.

- If the distance of any muon candidates to the primary vertex is more than 10 mm in the z coordinate, the event is rejected to remove cosmic ray events.

- All events must have at least one primary vertex associated to at least five tracks to discriminate against non-collision backgrounds.

After the preselection, events are required to have exactly two electrons of opposite sign. Both electrons must be isolated and pass the additional electron preselection criteria described in Section 10.1.1. Additionally, the dielectron invariant mass $m(e_1^{\pm}, e_2^{\mp})$ must exceed 10 GeV.

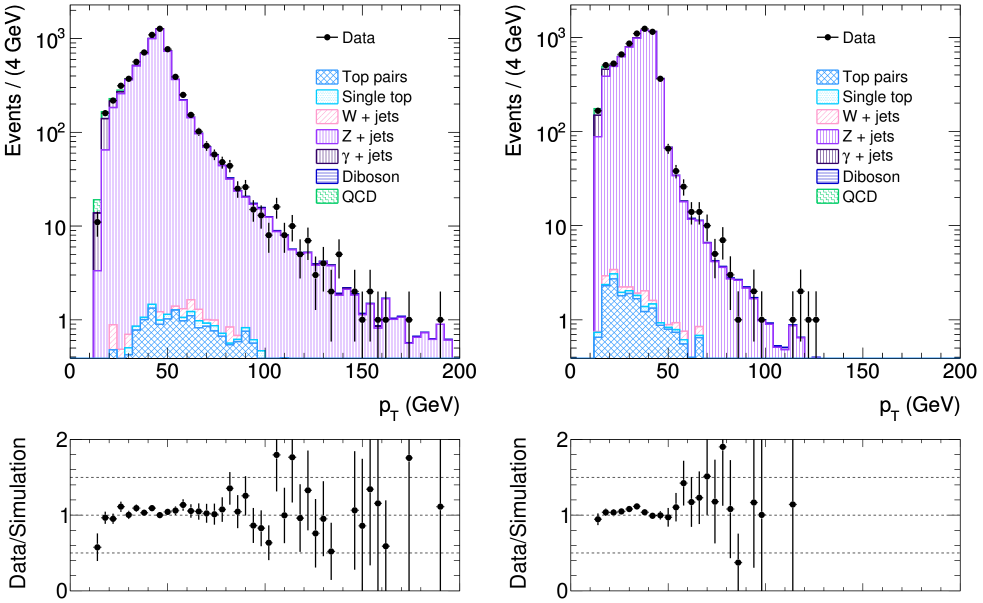

(a) $p_T(e_1^\pm)$ **(b)** $p_T(e_2^\pm)$

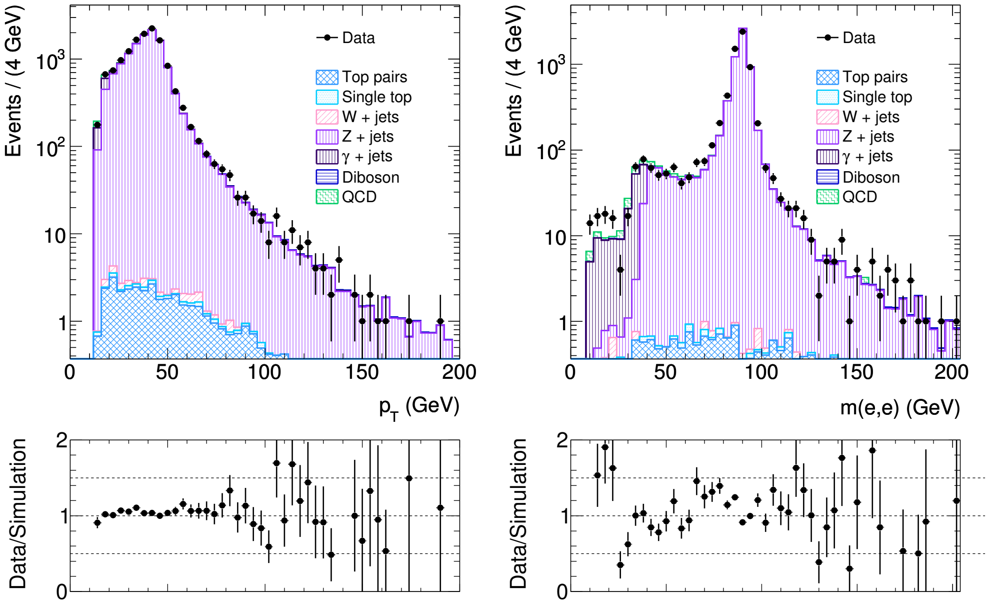

(c) $p_T(e)$ **(d)** $m(e_1^\pm, e_2^\mp)$

Figure 10.7. Dileptonic opposite sign observables at 7 TeV in data (solid circles) and simulation (patterned histograms) for 31.7 pb^{-1}. Data errors are purely statistical. No errors are shown for simulation. Ratio errors are statistical.

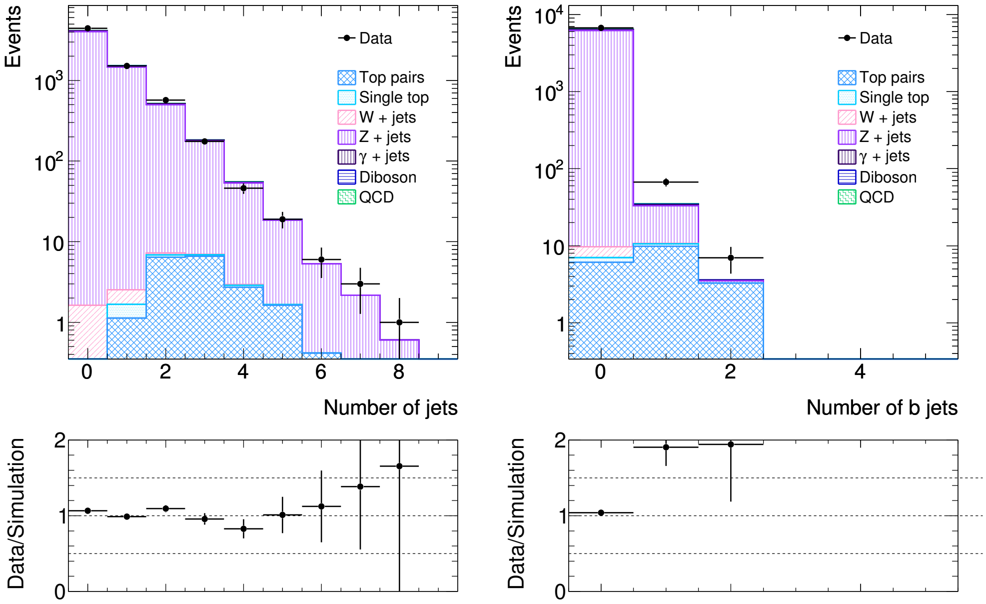

(a) Number of jets **(b)** Number of *b* jets

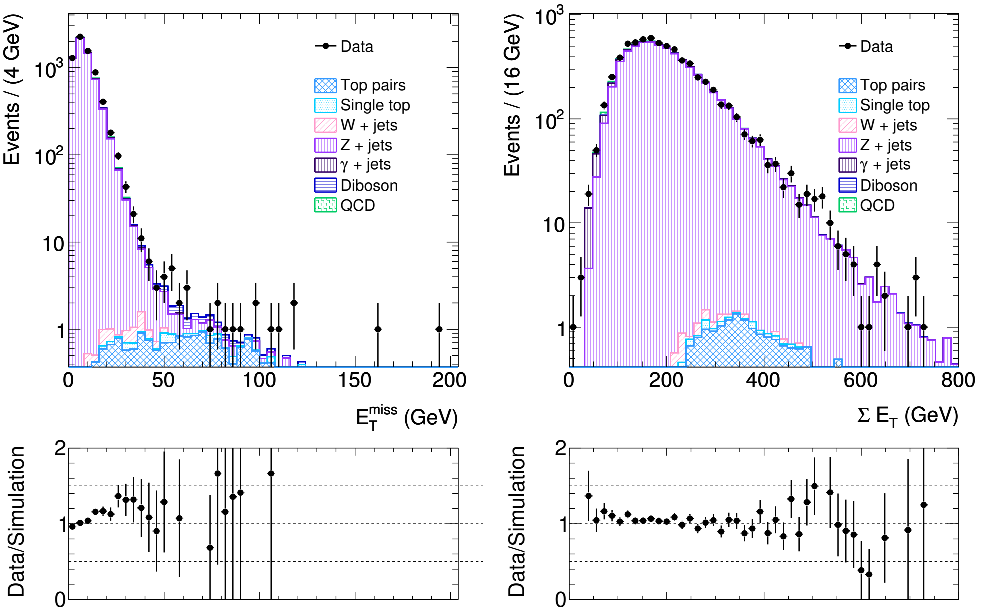

(c) $E_{\mathrm{T}}^{\mathrm{miss}}$ **(d)** ΣE_{T}

Figure 10.8. More dileptonic opposite sign observables at 7 TeV in data (solid circles) and simulation (patterned histograms) for 31.7 pb^{-1}. Data errors are purely statistical. No errors are shown for simulation. Ratio errors are statistical.

Table 10.2. Dileptonic opposite sign event yields at 7 TeV in data and simulation for 31.7 pb^{-1}. Errors are purely statistical.

Dataset	**Yield**
Data	6770 ± 80
Simulation	6490 ± 30
$t\bar{t}$	19.3 ± 0.7
single t	1.6 ± 0.2
$W \rightarrow \ell\nu + j$	2.8 ± 0.6
$Z \rightarrow \ell\ell + j$	6220 ± 20
$\gamma^* \rightarrow \ell\ell + j$	154 ± 6
Diboson	13.0 ± 0.1
QCD multijet	64 ± 6

Table 10.2 compares the number of events passing this selection in data to expectations from simulation, while Figures 10.7 and 10.8 show comparisons between data and simulation of event variables that are important for the stop search. Results for events with two electrons of same sign can be found in Appendix F. The agreement between data and simulation is good, especially since systematic uncertainties have not been considered. The most important systematic uncertainties are jet energy scale and resolution, lepton energy scale and resolution, cross section and luminosity uncertainties.

The selection is dominated by Z/γ^*+jets events as expected using the above event selection criteria. The contribution of these events can easily be reduced by further selections on the invariant mass of the electrons, missing transverse energy and the number of jets, however, this reduces the statistics such that data and simulation comparisons are uninformative.

10.4. Background Determination

There are two main backgrounds to an opposite sign dielectron search, events with two real opposite sign electrons and events with jets misidentified as electrons or electrons where the charge has been misidentified. Events with two real opposite sign electrons include Z/γ^*+jets and dileptonic top pair events. Data driven methods to estimate these backgrounds have already been discussed in Section 8.4. This section describes and tests data driven methods to estimate backgrounds from misidentified electrons and electrons where the charge has been misidentified.

10.4.1. Electron Misidentification Rate

The probability for a jet to fake an electron can be determined using Z+jets and QCD multijet events by defining a loose and tight electron selection, and measuring the probabilities r and f that a real or fake loose electron will pass tight criteria in the two data samples, one dominated by real leptons (Z+jets) and the other by fake leptons (QCD multijet).

A loose electron is defined as one which has passed the basic electron preselection with the additional requirement of one hit in the first pixel layer and the ratio of the additional transverse energy E_{T} in a cone $\Delta R < 0.2$ around the electron axis to electron p_{T} to be less than 0.5. A tight electron must pass the basic and additional electron preselection criteria and the ratio of the additional transverse energy E_{T} in a cone $\Delta R < 0.2$ around the electron axis to electron p_{T} must be less than 0.15.

The $Z +$ jets (real control) region is defined by two opposite sign electrons with invariant mass between 80 to 100 GeV, where at least one of the electrons passes the tight selection criteria. The QCD (fake control) region is identified by requiring two same sign electrons with invariant mass outside 80 to 100 GeV and at least one jet where at least one of the electrons fails the tight selection criteria. Events in both regions must pass the event preselection criteria and have $E_{\mathrm{T}}^{\mathrm{miss}} < 20$ GeV. Figures 10.9 and 10.10 show both regions prior to the invariant mass selection. As can be seen the dominant contributions to both the real and fake control regions are either Z+jets events or QCD multijet events.

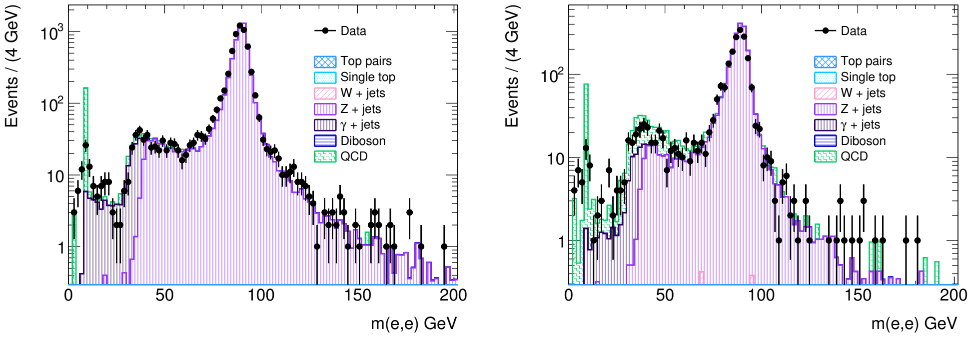

(a) $e_{\mathrm{tight}}, e_{\mathrm{tight}}$ **(b)** $e_{\mathrm{tight}}, e_{\mathrm{loose}}$

Figure 10.9. Invariant mass distributions of dielectron pairs at 7 TeV in data (solid circles) and simulation (patterned histograms) for 31.7 pb^{-1} in the real control region prior to invariant mass selection. Data errors are purely statistical. No errors are shown for simulation.

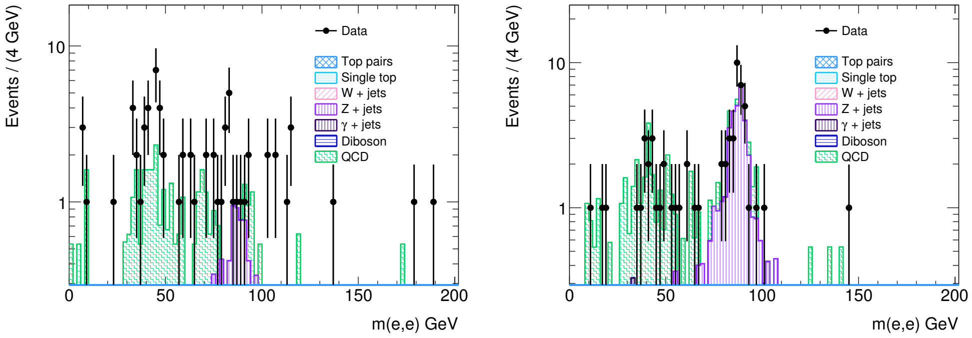

(a) $e_{\text{loose}}, e_{\text{loose}}$ **(b)** $e_{\text{loose}}, e_{\text{tight}}$

Figure 10.10. Invariant mass distributions of dielectron pairs at 7 TeV in data (solid circles) and simulation (patterned histograms) for 31.7 pb^{-1} in the fake control region prior to invariant mass selection. Data errors are purely statistical. No errors are shown for simulation.

Events in both control regions can be classified based on how many electrons are tight or loose. At reconstruction level, there are four different types of events: events with two tight electrons (N_{TT}), events with two exclusively loose electrons (N_{LL}), events where the leading electron is tight and subleading electron is exclusively loose (N_{TL}) and vice versa (N_{LT}). At truth level, there are also four different types of events: events with two real electrons (N_{RR}), events with two fake electrons (N_{FF}) and events where the leading electron is real and subleading electron is fake (N_{RF}) and vice versa (N_{FR}). These two sets of events are related to each other by the efficiency matrix:

$$\begin{bmatrix} N_{TT} \\ N_{TL} \\ N_{LT} \\ N_{LL} \end{bmatrix} = \begin{bmatrix} rr & rf & fr & ff \\ r(1-r) & r(1-f) & f(1-r) & f(1-f) \\ (1-r)r & (1-r)f & (1-f)r & (1-f)f \\ (1-r)(1-r) & (1-r)(1-f) & (1-f)(1-r) & (1-f)(1-f) \end{bmatrix} \begin{bmatrix} N_{RR} \\ N_{RF} \\ N_{FR} \\ N_{FF} \end{bmatrix}$$

This 4×4 matrix can be reduced to 3×3 since the p_{T} ordering of the electrons is not important.

The single electron efficiency r is extracted from the real control region using:

$$\tilde{r} = \frac{N_{TT}}{N_{TL} + N_{LT} + N_{TT}}$$

where $\tilde{r}$ is the pseudo-efficiency calculated using electron pairs. Using the efficiency matrix, $N_{TT} = rr \cdot N_{RR}$ and $N_{TL} = N_{LT} = r(1-r) \cdot N_{LL}$; assuming all the electrons in

Table 10.3. Electron efficiency and misidentification rate in percentage at 7 TeV in data and simulation for 31.7 pb^{-1}. Errors are purely statistical.

	Data	**Simulation**
Efficiency	77 ± 2	74 ± 1
Fake Rate	34 ± 8	57 ± 9

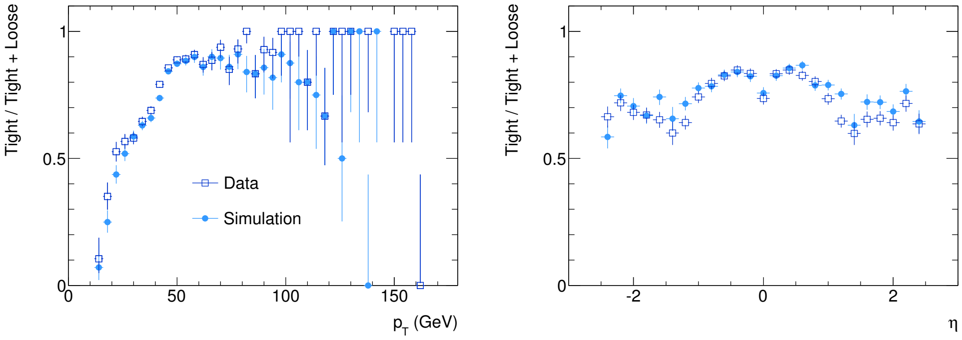

(a) p_T **(b)** η

Figure 10.11. Electron real identification efficiencies at 7 TeV from data (open squares) and simulation (solid circles) for 31.7 pb^{-1} as a function of p_T, η and E_T^{miss}. Errors are purely statistical.

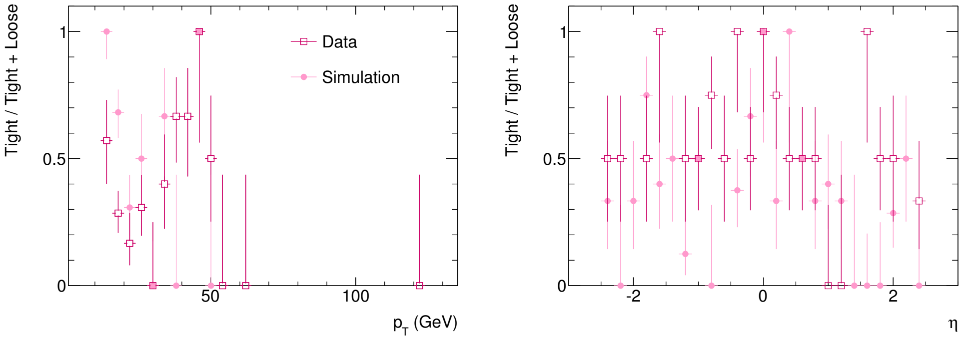

(a) p_T **(b)** η

Figure 10.12. Electron fake identification efficiencies at 7 TeV from data (open squares) and simulation (solid circles) for 31.7 pb^{-1} as a function of p_T, η and E_T^{miss}. Errors are purely statistical.

the real control region are real and should therefore pass the tight selection criteria. Hence:

$$\tilde{r} = \frac{rr}{2r(1-r)+rr} \qquad \Longrightarrow r = \frac{2\tilde{r}}{1+\tilde{r}}$$

Similarly, the single electron fake rate can be extracted from the fake control region, where the assumption is that none of the electrons are real and thus should fail the tight selection criteria:

$$\tilde{f} = \frac{N_{LT}+N_{TL}}{N_{LL}+N_{LT}+N_{TL}} = \frac{2f(1-f)}{(1-f)(1-f)+2f(1-f)} \qquad \Longrightarrow f = \frac{\tilde{f}}{2-\tilde{f}}$$

Table 10.3 shows the total efficiency and fake rate for data and simulation, while Figures 10.11 and 10.12 show the efficiency and fake rate as a function of p_{T} and η for data and simulation. It can be seen that the electron efficiency is well modelled by simulation and is around 76%. This efficiency is somewhat lower than what is seen for other ATLAS analyses. This is due to the lower p_{T} electron and jet thresholds. The fake rate is less well modelled by simulation giving a result of 55% compared to 32% from data. This is expected due to the complexity of accurately simulating the intricacies of the detector. It is very encouraging to see that the fake rate derived from data is lower than that derived from simulation.

10.4.2. Electron Charge Misidentification Rate

The electron charge identification can be measured in a data driven approach using $Z \rightarrow e^+e^-$ events. Z candidate events are identified by two electrons with invariant mass between 60 and 120 GeV passing the basic and additional electron preselection criteria described in Section 10.1.1. Additionally, the two electrons are required to be in opposite hemispheres of the detector, such that the azimuthal difference is $\Delta\phi > 3/4\pi$. To remove background contamination from W+jets and top events, $E_{\mathrm{T}}^{\mathrm{miss}} < 20$ GeV is also required.

The invariant mass of the selected lepton pair is then fitted using a Gaussian distribution convoluted with a Breit-Wigner plus an exponential function. The Breit-Wigner distribution is used to describe the $Z \rightarrow e^+e^-$ resonance, while the Gaussian accounts for detector resolution and the exponential for QED bremsstrahlung. The charge

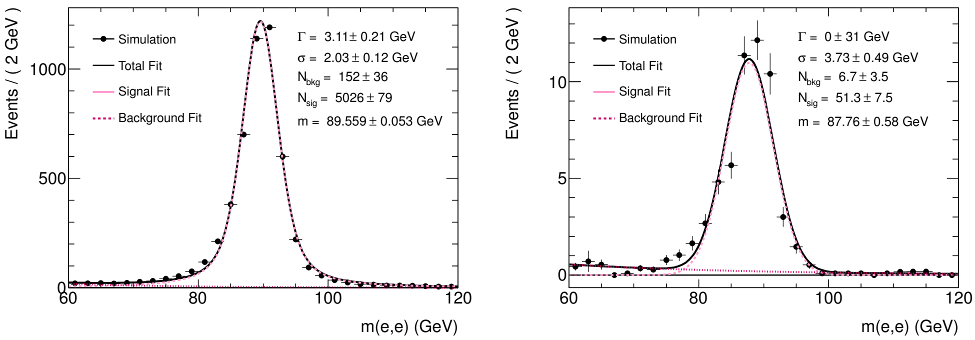

(a) Simulation

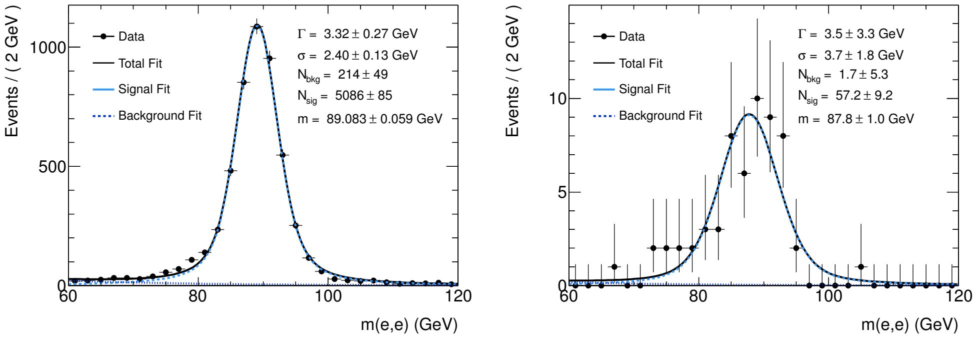

(b) Data

Figure 10.13. Dielectron opposite sign (left) and same sign (right) invariant mass distributions with fits used in electron charge misidentification rate determination at 7 GeV in data (below) and simulation (above) for 31.7 pb^{-1}. Errors are purely statistical.

misidentification rate is given by the ratio $N1/(N1 + N2)$, where $N1$ is the number of same sign events and $N2$ is the number of opposite sign events.

Figure 10.13 compares the opposite sign and same sign invariant mass distributions in data and simulation. While invariant mass distributions of the same sign distribution differ visibly between data and simulation, the derived charge misidentification rates of 1.18 ± 0.018 from data and 1.00 ± 0.16 from simulation, agree within error.

10.5. Preliminary Data Studies Summary

After years of preparation and anticipation, the LHC is operational and providing proton-proton collisions at $\sqrt{s} = 7$ TeV. This chapter studied 31.7 pb^{-1} of data, testing the prepared analysis machinery, focusing on understanding the stop selection variables and testing some of the data driven background estimation methods in the dileptonic search channel where both leptons were electrons.

It was found that the data were well modelled by simulation, although small discrepancies were observed in some distributions. However, this study did not take systematic effects into account, which are quite large considering the infancy of the experiment.

Data driven estimation techniques for backgrounds from misidentified electrons and electrons where the charge has been misidentified were also investigated. It was pleasant to discover that the electron identification efficiency in data was a little higher than that determined from simulation as well as the electron misidentification rate being lower. The electron charge misidentification rate in data matched that calculated from simulation.

The studies presented here provide a solid starting point for a full fledged light stop search at ATLAS in the dileptonic decay mode.

There are two possible outcomes: if the result confirms the hypothesis, then you've made a measurement. If the result is contrary to the hypothesis, then you've made a discovery.

– Enrico Fermi

11

Conclusions and Outlook

The SM of particle physics provides an excellent description of three of the four fundamental forces of nature. However, its failure to account for two major cosmological observations, namely the existence of dark matter and the matter-antimatter asymmetry of the universe suggests that it is an incomplete theory. One popular extension of the SM is SUSY, in which a new symmetry between bosons and fermions is introduced. If SUSY is to provide a solution to both these aformentioned problems then it should also provide observable phenomenology in the TeV energy range accessible at the LHC, in particular a light stop quark which is lighter than the top quark.

This thesis began by exploring the bounds of the MSSM parameter space in which the matter-antimatter asymmetry of the universe is dynamically generated through electroweak baryogensis by executing a random MSSM parameter space scan using micrOmegas. It was found that the parameter space region is highly constrained by experimental limits on the EDM of the electron and the $b \to s\gamma$ branching ratio. If the additional requirement of matching the observed dark matter abundance by the relic density of the LSP is necessitated, the allowed MSSM parameter space is further reduced by results from direct dark matter detection experiments, though not ruled out.

The focus of the thesis then moved to the investigation of the collider phenomenology of supersymmetric electroweak baryogenesis, in particular, the evaluation of the discovery potential of light stop quark pair production at the ATLAS experiment. The analysis of light stop decays is a prime candidate for early supersymmetry searches at the LHC, due to its high production cross section and clean lepton based event topologies. The study assumed a light stop decay topology involving the lightest chargino and neutralino where the visible final state products mimic those from top quark pair production. Both the dileptonic and semileptonic decay modes were considered, where the charged leptons were electrons or muons.

For the dileptonic decay mode, two signal regions were defined to take into account the varying signal topologies caused by the numerous stop-chargino-neutralino mass difference possibilities. For proton-proton collisions at $\sqrt{s} = 10$ TeV and an integrated luminosity of 1 fb^{-1}, it was determined that signal points with low stop mass and high stop-neutralino mass differences had the greatest discovery potential. Future studies must look towards refining the techniques used for background subtraction from sideband information and on ensuring the analysis be robust against systematic uncertainties from the selection criteria for the signal region.

If evidence for new physics is found following the dileptonic search procedure, it will not necessarily indicate the presence of a light stop. Further information about the mass scale and nature of the underlying physics in the event must be extracted from measurements of the kinematic endpoints for example. This can be done using the semileptonic decay mode. However, it was concluded that for an integrated luminosity of 1 fb^{-1} at $\sqrt{s} = 10$ TeV, the semileptonic decay channel is overwhelmed by backgrounds and requires detailed understanding of the detector and backgrounds in order to extract a signal.

The final chapter of this thesis presented preliminary results for an integrated luminosity of 41.4 pb^{-1} of data collected at $\sqrt{s} = 7$ TeV. The study focused on understanding the selection variables and backgrounds in the dileptonic search channel where both leptons were electrons. It was found that the data were well modelled by simulation.

The studies presented provide a solid starting point for a full fledged light stop search at ATLAS in the dileptonic decay mode. With the LHC on track to provide experiments with over 1 fb^{-1} at collision energies of $\sqrt{s} = 7$ TeV by the end of 2011 and continuing to run through 2012, possibly at higher collision energies, there is much to look forward to.

Bibliography

[1] M. E. Peskin and D. V. Schroeder, *An Introduction To Quantum Field Theory*. Westview Press, 1995. 3

[2] D. Griffiths, *Introduction to Elementary Particles*. Wiley-VCH, 2008. 3

[3] G. L. Kane, *Modern Elementary Particle Physics*. Westview Press, 1993. 3

[4] Particle Data Group, K. Nakamura *et al.*, "Review of particle physics," *J. Phys.* **G37** (2010) 075021. 3, 4, 5, 15, 92

[5] GNO Collaboration, M. Altmann *et al.*, "Complete results for five years of GNO solar neutrino observations," *Phys. Lett.* **B616** (2005) 174–190, `arXiv:hep-ex/0504037`. 4

[6] Super-Kamiokande Collaboration, Y. Ashie *et al.*, "Evidence for an oscillatory signature in atmospheric neutrino oscillation," *Phys. Rev. Lett.* **93** (2004) 101801, `arXiv:hep-ex/0404034`. 4

[7] KamLAND Collaboration, T. Araki *et al.*, "Measurement of neutrino oscillation

with KamLAND: Evidence of spectral distortion," *Phys. Rev. Lett.* **94** (2005) 081801, `arXiv:hep-ex/0406035`. 4

[8] MINOS Collaboration, P. Adamson *et al.*, "Measurement of Neutrino Oscillations with the MINOS Detectors in the NuMI Beam," *Phys. Rev. Lett.* **101** (2008) 131802. 4

[9] S. L. Glashow, "Partial Symmetries of Weak Interactions," *Nucl. Phys.* **22** (1961) 579–588. 8

[10] S. Weinberg, "A Model of Leptons," *Phys. Rev. Lett.* **19** (1967) 1264–1266. 8

[11] A. Salam, "Gauge Unification of Fundamental Forces," *Rev. Mod. Phys.* **52** (1980) 525–538. 8

[12] G. 't Hooft, "Renormalization of Massless Yang-Mills Fields," *Nucl. Phys.* **B33** (1971) 173–199. 9

[13] P. W. Higgs, "Broken Symmetries and the Masses of Gauge Bosons," *Phys. Rev. Lett.* **13** (1964) 508–509. 9

[14] N. Cabibbo, "Unitary Symmetry and Leptonic Decays," *Phys. Rev. Lett.* **10** (1963) 531–533. 10

[15] M. Kobayashi and T. Maskawa, "CP Violation in the Renormalizable Theory of Weak Interaction," *Prog. Theor. Phys.* **49** (1973) 652–657. 10

[16] B. W. Lee, C. Quigg, and H. B. Thacker, "Strength of Weak Interactions at Very High Energies and the Higgs Boson Mass," *Phys. Rev. Lett.* **38** (1977) 883–885. 10

[17] LEP Working Group for Higgs Boson Searches, "Search for the standard model Higgs boson at LEP," *Phys. Lett.* **B565** (2003) 61–75, `arXiv:hep-ex/0306033`. 10

[18] Tevatron Higgs Working Group, "Combined CDF and DØ Upper Limits on Standard Model Higgs-Boson Production with up to 6.7 fb^{-1} of Data," `arXiv:1007.4587 [hep-ex]`. 10

[19] LEP, Tevatron and SLD Electroweak Working Groups, "Precision Electroweak Measurements and Constraints on the Standard Model," `arXiv:1012.2367 [hep-ex]`. 10

[20] H. Baer and X. Tata, *Weak Scale Supersymmetry: From Superfields to Scattering Events*. Cambridge University Press, first ed., 2006. 11

[21] S. P. Martin, "A Supersymmetry Primer," `arXiv:hep-ph/9709356`. 11, 13

[22] A. Bartl, S. Hesselbach, K. Hidaka, T. Kernreiter, and W. Porod, "Top squarks and bottom squarks in the MSSM with complex parameters," *Phys.Rev.* **D70** (2004) 035003, `arXiv:hep-ph/0311338 [hep-ph]`. 14

[23] S. Dimopoulos and D. W. Sutter, "The Supersymmetric flavor problem," *Nucl.Phys.* **B452** (1995) 496–512, `arXiv:hep-ph/9504415 [hep-ph]`. 16

[24] H. P. Nilles, "Dynamically Broken Supergravity and the Hierarchy Problem," *Phys.Lett.* **B115** (1982) 193. 16

[25] Super-Kamiokande Collaboration, M. Shiozawa *et al.*, "Search for Proton Decay via $p \to e + \pi^0$ in a Large Water Cherenkov Detector," *Phys. Rev. Lett.* **81** (1998) 3319–3323, `arXiv:hep-ex/9806014`. 16

[26] G. 't Hooft, "Symmetry Breaking through Bell-Jackiw Anomalies," *Phys. Rev. Lett.* **37** (1976) 8. 16

[27] R. Barbier *et al.*, "R-parity Violating Supersymmetry," *Phys. Rept.* **420** (2005) 1–202, `arXiv:hep-ph/0406039`. 17

[28] A. Borriello and P. Salucci, "The Dark Matter Distribution in Disk Galaxies," *Mon. Not. Roy. Astron. Soc.* **323** (2001) 285, `arXiv:astro-ph/0001082`. 17

[29] F. Zwicky, "Spectral displacement of extra galactic nebulae," *Helv. Phys. Acta* **6** (1933) 110–127. 17

[30] D. Clowe *et al.*, "A direct empirical proof of the existence of dark matter," *Astrophys. J.* **648** (2006) L109–L113, `arXiv:astro-ph/0608407`. 17

[31] E. Komatsu *et al.*, "Seven-Year Wilkinson Microwave Anisotropy Probe (WMAP) Observations: Cosmological Interpretation," *Astrophys. J. Supp.* **192** (2011) 18, `arXiv:1001.4538 [astro-ph]`. 17, 27, 28

[32] K. A. Olive, G. Steigman, and T. P. Walker, "Primordial Nucleosynthesis: Theory and Observations," *Phys. Rept.* **333** (2000) 389–407,

arXiv:astro-ph/9905320. 17

[33] SDSS Collaboration, M. Tegmark *et al.*, "The 3D power spectrum of galaxies from the SDSS," *Astrophys. J.* **606** (2004) 702–740, arXiv:astro-ph/0310725. 17

[34] A. Sakharov, "Violation of CP Invariance, C Asymmetry, and Baryon Asymmetry of the Universe," *Pisma Zh.Eksp.Teor.Fiz.* **5** (1967) 32–35. 19

[35] W. Bernreuther, "CP violation and baryogenesis," *Lect. Notes Phys.* **591** (2002) 237–293, arXiv:hep-ph/0205279. 19

[36] J. M. Carmona, J. L. Cortes, A. K. Das, J. Gamboa, and F. Mendez, "Matter-antimatter asymmetry without departure from thermal equilibrium," *Mod. Phys. Lett.* **A21** (2006) 883–892, arXiv:hep-th/0410143. 20

[37] M. Trodden, "Electroweak baryogenesis," *Rev.Mod.Phys.* **71** (1999) 1463–1500, arXiv:hep-ph/9803479 [hep-ph]. 20

[38] J. M. Cline, "Baryogenesis," arXiv:hep-ph/0609145 [hep-ph]. 20

[39] M. Carena, G. Nardini, M. Quiros, and C. E. M. Wagner, "The Baryogenesis Window in the MSSM," *Nucl. Phys.* **B812** (2009) 243–263, arXiv:0809.3760 [hep-ph]. 21

[40] W. Buchmuller, Z. Fodor, and A. Hebecker, "Thermodynamics of the electroweak phase transition," *Nucl. Phys.* **B447** (1995) 317–339, arXiv:hep-ph/9502321. 21

[41] M. Carena, G. Nardini, M. Quiros, and C. E. M. Wagner, "The Effective Theory of the Light Stop Scenario," *JHEP* **10** (2008) 062, arXiv:0806.4297 [hep-ph]. 21, 23

[42] C. Balazs, M. S. Carena, A. Menon, D. E. Morrissey, and C. E. M. Wagner, "The Supersymmetric Origin of Matter," *Phys. Rev.* **D71** (2005) 075002, arXiv:hep-ph/0412264. 21, 23, 27

[43] G. Belanger, F. Boudjema, S. Kraml, A. Pukhov, and A. Semenov, "Relic density of neutralino dark matter in the MSSM with CP violation," *Phys. Rev.* **D73** (2006) 115007, arXiv:hep-ph/0604150. 23

[44] G. Belanger, F. Boudjema, A. Pukhov, and A. Semenov, "Dark matter direct detection rate in a generic model with micrOMEGAs 2.2," *Comput. Phys. Commun.* **180** (2009) 747–767, `arXiv:0803.2360 [hep-ph]`. 23

[45] G. Degrassi, S. Heinemeyer, W. Hollik, P. Slavich, and G. Weiglein, "Towards high-precision predictions for the MSSM Higgs sector," *Eur. Phys. J.* **C28** (2003) 133–143, `arXiv:hep-ph/0212020`. 24

[46] C. Jarlskog, "Commutator of the Quark Mass Matrices in the Standard Electroweak Model and a Measure of Maximal CP Violation," *Phys.Rev.Lett.* **55** (1985) 1039. 25

[47] S. Abel, S. Khalil, and O. Lebedev, "EDM constraints in supersymmetric theories," *Nucl. Phys.* **B606** (2001) 151–182, `arXiv:hep-ph/0103320`. 25

[48] Y. Li, S. Profumo, and M. Ramsey-Musolf, "Higgs-Higgsino-Gaugino Induced Two Loop Electric Dipole Moments," *Phys.Rev.* **D78** (2008) 075009, `arXiv:0806.2693 [hep-ph]`. 25

[49] B. C. Regan, E. D. Commins, C. J. Schmidt, and D. DeMille, "New Limit on the Electron Electric Dipole Moment," *Phys. Rev. Lett.* **88** no. 7, (Feb, 2002) 071805. 25, 26

[50] H. Murayama and A. Pierce, "Signatures of Baryogenesis in the MSSM," *Phys. Rev.* **D67** (2003) 071702, `arXiv:hep-ph/0201261`. 25

[51] R. Barbieri and G. F. Giudice, "$b \to s\gamma$ decay and supersymmetry," *Phys. Lett.* **B309** (1993) 86–90, `arXiv:hep-ph/9303270`. 25

[52] Heavy Flavor Averaging Group, "Averages of b-hadron, c-hadron, and tau-lepton Properties," `arXiv:1010.1589 [hep-ex]`. 25, 26

[53] M. Misiak *et al.*, "The first estimate of $\mathcal{B}(\bar{B} \to X_s\gamma)$ at $\mathcal{O}(\alpha_s^2)$," *Phys. Rev. Lett.* **98** (2007) 022002, `arXiv:hep-ph/0609232`. 25, 26

[54] K. Garrett and G. Duda, "Dark Matter: A Primer," *Adv.Astron.* **2011** (2011) 968283, `arXiv:1006.2483 [hep-ph]`. 27, 29

[55] G. Jungman, M. Kamionkowski, and K. Griest, "Supersymmetric dark matter," *Phys. Rept.* **267** (1996) 195–373, `arXiv:hep-ph/9506380`. 28, 29

[56] B. C. Allanach *et al.*, "Les Houches 'Physics at TeV colliders 2005' Beyond the standard model working group: Summary report," `arXiv:hep-ph/0602198`. 29, 32, i

[57] XENON100 Collaboration, E. Aprile *et al.*, "First Dark Matter Results from the XENON100 Experiment," *Phys. Rev. Lett.* **105** (2010) 131302, `arXiv:1005.0380 [astro-ph]`. 29, 30

[58] CDMS-II Collaboration, Z. Ahmed *et al.*, "Dark Matter Search Results from the CDMS II Experiment," *Science* **327** (2010) 1619–1621, `arXiv:0912.3592 [astro-ph]`. 29, 30

[59] ZEPLIN-III Collaboration, V. N. Lebedenko *et al.*, "Results from the First Science Run of the ZEPLIN-III Dark Matter Search Experiment," *Phys. Rev.* **D80** (2009) 052010, `arXiv:0812.1150 [astro-ph]`. 29, 30

[60] R. Gaitskell, V. Mandic, and J. Filippini, "Dark Matter Tools." `http://dmtools.brown.edu/`. 30

[61] IceCube Collaboration, R. Abbasi *et al.*, "Limits on a muon flux from neutralino annihilations in the Sun with the IceCube 22-string detector," *Phys. Rev. Lett.* **102** (2009) 201302, `arXiv:0902.2460 [astro-ph]`. 30

[62] P. Salati, F. Donato, and N. Fornengo, "Indirect Dark Matter Detection with Cosmic Antimatter," `arXiv:1003.4124 [astro-ph]`. 30

[63] HESS Collaboration, A. Abramowski *et al.*, "H.E.S.S. constraints on Dark Matter annihilations towards the Sculptor and Carina Dwarf Galaxies," `arXiv:1012.5602 [astro-ph]`. 30

[64] O. Adriani *et al.*, "An anomalous positron abundance in cosmic rays with energies 1.5-100 GeV," *Nature* **458** (2009) 607–609, `arXiv:0810.4995 [astro-ph]`. 30

[65] J. Chang *et al.*, "An excess of cosmic ray electrons at energies of 300-800 GeV," *Nature* **456** (2008) 362–365. 30

[66] Fermi-LAT Collaboration, A. Abdo *et al.*, "Measurement of the Cosmic Ray e+ plus e- spectrum from 20 GeV to 1 TeV with the Fermi Large Area Telescope," *Phys.Rev.Lett.* **102** (2009) 181101, `arXiv:0905.0025 [astro-ph]`. 30

[67] D. Grasso *et al.*, "On possible interpretations of the high energy electron-positron spectrum measured by the Fermi Large Area Telescope," *Astropart.Phys.* **32** (2009) 140–151, `arXiv:0905.0636 [astro-ph]`. 30, 31

[68] A. Strong *et al.*, "The GALPROP Cosmic-Ray Propagation Code," `arXiv:0907.0559 [astro-ph]`. 31

[69] L. Evans and P. Bryant, "LHC Machine," *JINST* **3** (2008) S08001. 34

[70] M. Benedikt *et al.*, "LHC Design Report," *CERN-2004-003* (2004) . 34, 37

[71] ATLAS Collaboration, G. Aad *et al.*, "The ATLAS Experiment at the CERN Large Hadron Collider," *JINST* **3** (2008) S08003. 34, 38, 39, 42, 44, 45, 46, 58, 65, 75

[72] CMS Collaboration, S. Chatrchyan *et al.*, "The CMS experiment at the CERN Large Hadron Collider," *JINST* **3** (2008) S08004. 34

[73] LHCb Collaboration, A. Augusto Alves Jr *et al.*, "The LHCb Detector at the LHC," *JINST* **3** (2008) S08005. 34

[74] ALICE Collaboration, K. Aamodt *et al.*, "The ALICE experiment at the CERN Large Hadron Collider," *JINST* **3** (2008) S08002. 34

[75] CERN AC Term, "The four main LHC experiments," *CERN-AC-9906026* (1999) . 35

[76] CERN AC Team, "The LHC injection complex," *LHC-PHO-1993-008* (1993) . 35

[77] ATLAS Collaboration, A. Airapetian *et al.*, "ATLAS Detector and Physics Performance Technical design report," *CERN-LHCC-99-14* (1999) . 38, 48, iii

[78] ATLAS Collaboration, G. Aad *et al.*, "Expected Performance of the ATLAS Experiment - Detector, Trigger and Physics," `arXiv:0901.0512 [hep-ex]`. VII, 38, 55, 61, 62, 110, 123, iii

[79] R. K. Bock and A. Vasilescu, *The Particle Detector BriefBook*. Springer, 1998. 40

[80] ATLAS Collaboration, A. Airapetian *et al.*, "ATLAS Magnet System Technical Design Report," *CERN-LHCC-97-18* (1997) . 41

[81] "ATLAS Fact Sheet." `http://atlas.ch/fact-sheets.html`. 41

[82] ATLAS Collaboration, A. Airapetian *et al.*, "ATLAS Inner Detector Technical Design Report," *CERN-LHCC-97-16* (1997) . 42

[83] ATLAS Collaboration, A. Airapetian *et al.*, "ATLAS Calorimeter Performance Technical Design Report," *CERN-LHCC-96-40* (1996) . 43

[84] ATLAS Collaboration, A. Airapetian *et al.*, "ATLAS Muon Spectrometer Technical Design Report," *CERN-LHCC-97-22* (1997) . 46

[85] ATLAS Collaboration, P. Bright-Thomas *et al.*, "ATLAS First-Level Trigger Technical Design Report," *CERN-LHCC-98-14* (1998) . 47

[86] ATLAS Collaboration, B. Caron *et al.*, "ATLAS High-Level Trigger, Data Acquisition and Controls Technical Design Report," *CERN-LHCC-2003-022* (2003) . 47

[87] A. Barriuso Poy *et al.*, "The Detector Control System of the ATLAS experiment," *JINST* **3** (2008) P05006. 49

[88] ATLAS Collaboration, G. Aad *et al.*, "The ATLAS Simulation Infrastructure," `arXiv:1005.4568 [physics.ins-det]`. 49

[89] S. Agostinelli *et al.*, "GEANT4: A Simulation toolkit," *Nucl. Instrum. Meth.* **A506** (2003) 250–303. 49

[90] A. Kaidalov and K. Ter-Martirosyan, "Multihadron production at high energies in the model of quark gluon strings," *Sov.J.Nucl.Phys.* **40** (1984) 135–140. 49

[91] H. Bertini, A. Culkowski, O. Hermann, N. Gove, and M. Guthrie, "High-Energy (e ≤ 1000 GeV) Intranuclear Cascade Model for Nucleons and Pions Incident on Nuclei and Comparisons with Experimental Data," *Phys.Rev.* **C17** (1978) 1382–1394. 49

[92] S. Dean and P. Sherwood, "Athena-Atlfast." `www.hep.ucl.ac.uk/atlas/atlfast`, 2008. 50

[93] K. Edmonds *et al.*, "The Fast ATLAS Track Simulation (FATRAS)," *ATL-SOFT-PUB-2008-001. ATL-COM-SOFT-2008-002* . 50

[94] E. Barberio *et al.*, "The Geant4-Based ATLAS Fast Electromagnetic Shower Simulation," *ATL-SOFT-CONF-2007-002. ATL-COM-SOFT-2007-014* . 50

[95] T. Cornelissen *et al.*, "Concepts, Design and Implementation of the ATLAS New Tracking (NEWT)," *ATL-SOFT-PUB-2007-007. ATL-COM-SOFT-2007-002* . 51

[96] W. Lampl *et al.*, "Calorimeter Clustering Algorithms: Description and Performance," *ATL-LARG-PUB-2008-002. ATL-COM-LARG-2008-003* . 52

[97] C. Cojocaru *et al.*, "Hadronic calibration of the ATLAS liquid argon end-cap calorimeter in the pseudorapidity region $1.6 < |\eta| < 1.8$ in beam tests," *Nucl.Instrum.Meth.* **A531** (2004) 481–514, `arXiv:physics/0407009 [physics]`. 52, iv

[98] S. Hassani *et al.*, "A muon identification and combined reconstruction procedure for the ATLAS detector at the LHC using the (MUONBOY, STACO, MuTag) reconstruction packages," *Nucl. Instrum. Meth.* **A572** (2007) 77–79. 54

[99] M. Cacciari, G. P. Salam, and G. Soyez, "The Anti-k(t) jet clustering algorithm," *JHEP* **0804** (2008) 063, `arXiv:0802.1189 [hep-ph]`. 55, 146

[100] ATLAS Collaboration, G. Aad *et al.*, "The ATLAS Inner Detector commissioning and calibration," *Eur.Phys.J.* **C70** (2010) 787–821, `arXiv:1004.5293 [physics.ins-det]`. 58

[101] ATLAS Collaboration, G. Aad *et al.*, "Readiness of the ATLAS Liquid Argon Calorimeter for LHC Collisions," *Eur.Phys.J.* **C70** (2010) 723–753, `arXiv:0912.2642 [physics.ins-det]`. 58, 144

[102] ATLAS Collaboration, G. Aad *et al.*, "Readiness of the ATLAS Tile Calorimeter for LHC collisions," *Eur.Phys.J.* **C70** (2010) 1193–1236, `arXiv:1007.5423 [physics.ins-det]`. 58

[103] ATLAS Collaboration, G. Aad *et al.*, "Commissioning of the ATLAS Muon Spectrometer with Cosmic Rays," *Eur.Phys.J.* **C70** (2010) 875–916, `arXiv:1006.4384 [physics.ins-det]`. 58

[104] ATLAS Collaboration, G. Aad *et al.*, "Performance of the ATLAS Detector using First Collision Data," *JHEP* **09** (2010) 056, `arXiv:1005.5254 [hep-ex]`. 58

[105] R. Achenbach *et al.*, "The ATLAS level-1 calorimeter trigger," *JINST* **3** (2008) P03001. 64

[106] R. Fruhwirth, "Application of Kalman filtering to track and vertex fitting," *Nucl. Instrum. Meth.* **A262** (1987) 444–450. 69

[107] D. Emelyanov, "A probabilistic data association filter for fast tracking in the ATLAS transition radiation tracker," *Nucl. Instrum. Meth.* **A566** (2006) 50–53. 69

[108] ATLAS Collaboration, G. Aad *et al.*, "Performance of the Electron and Photon Trigger in p-p Collisions at a centre of mass energy of 900 GeV," *ATLAS-CONF-2010-022. ATLAS-COM-CONF-2010-022* . 78

[109] ATLAS Collaboration, G. Aad *et al.*, "Performance of the ATLAS Inner Detector Trigger algorithms in p-p collisions at $\sqrt{s}$=900 GeV," *ATLAS-CONF-2010-014. ATLAS-COM-CONF-2010-014* . 78

[110] ATLAS Collaboration, G. Aad *et al.*, "Electron and photon reconstruction and identification in ATLAS: expected performance at high energy and results at 900 GeV," *ATLAS-CONF-2010-005. ATLAS-COM-CONF-2010-005* . 78

[111] T. Han, Z. Si, K. M. Zurek, and M. J. Strassler, "Phenomenology of Hidden Valleys at Hadron Colliders," *JHEP* **07** (2008) 008, `arXiv:0712.2041 [hep-ph]`. 82

[112] W. Beenakker, M. Kramer, T. Plehn, M. Spira, and P. M. Zerwas, "Stop production at Hadron Colliders," *Nucl. Phys.* **B515** (1998) 3–14, `arXiv:hep-ph/9710451`. 84, 85

[113] W. Beenakker, R. Hopker, and M. Spira, "PROSPINO: A program for the PROduction of Supersymmetric Particles In Next-to-leading Order QCD," `arXiv:hep-ph/9611232`. 84

[114] P. M. Nadolsky *et al.*, "Implications of CTEQ global analysis for collider observables," *Phys. Rev.* **D78** (2008) 013004, `arXiv:0802.0007 [hep-ph]`. 84

[115] A. Bartl, H. Eberl, S. Kraml, W. Majerotto, W. Porod, *et al.*, "Search of stop, sbottom, tau sneutrino, and stau at an e^+e^- linear collider with $\sqrt{s}$ = 0.5 TeV - 2 TeV," *Z.Phys.* **C76** (1997) 549–560, `arXiv:hep-ph/9701336 [hep-ph]`. 85

[116] W. Porod and T. Wohrmann, "Higher order top squark decays," *Phys.Rev.* **D55** (1997) 2907–2917, `arXiv:hep-ph/9608472 [hep-ph]`. 85

[117] W. Porod, "More on higher order decays of the lighter top squark," *Phys.Rev.* **D59** (1999) 095009, `arXiv:hep-ph/9812230 [hep-ph]`. 85

[118] C. Boehm, A. Djouadi, and Y. Mambrini, "Decays of the lightest top squark," *Phys.Rev.* **D61** (2000) 095006, `arXiv:hep-ph/9907428 [hep-ph]`. 85

[119] J. F. Gunion and H. E. Haber, "Two-body decays of neutralinos and charginos," *Phys. Rev.* **D37** (1988) 2515. 86

[120] ALEPH Collaboration, A. Heister *et al.*, "Search for scalar quarks in e^+e^- collisions at $\sqrt{s}$ up to 209 GeV," *Phys.Lett.* **B537** (2002) 5–20, `arXiv:hep-ex/0204036 [hep-ex]`. 92

[121] DELPHI Collaboration, J. Abdallah *et al.*, "Searches for supersymmetric particles in e^+e^- collisions up to 208 GeV and interpretation of the results within the MSSM," *Eur.Phys.J.* **C31** (2003) 421–479, `arXiv:hep-ex/0311019 [hep-ex]`. 92

[122] L3 Collaboration, P. Achard *et al.*, "Search for scalar leptons and scalar quarks at LEP," *Phys.Lett.* **B580** (2004) 37–49, `arXiv:hep-ex/0310007 [hep-ex]`. 92

[123] OPAL Collaboration, G. Abbiendi *et al.*, "Search for scalar top and scalar bottom quarks at LEP," *Phys.Lett.* **B545** (2002) 272–284, `arXiv:hep-ex/0209026 [hep-ex]`. 92

[124] CDF Collaboration, T. Aaltonen *et al.*, "Search for scale top decaying into $c + \tilde{\chi}^0$ in the MET+jets sample," *CDF Note 9834* . 93, 94

[125] DØ Collaboration, V. M. Abazov *et al.*, "Search for scalar top quarks in the acoplanar charm jets and missing transverse energy final state in $p\bar{p}$ collisions at $\sqrt{s} = 1.96$ TeV," *Phys. Lett.* **B665** (2008) 1–8, `arXiv:0803.2263 [hep-ex]`. 93

[126] CDF Collaboration, T. Aaltonen *et al.*, "Search for the supersymmetric partner of the top quark in $p\bar{p}$ collisions at $\sqrt{s} = 1.96$ TeV," *Phys.Rev.* **D82** (2010) 092001, `arXiv:1009.0266 [hep-ex]`. 93

[127] DØ Collaboration, V. M. Abazov *et al.*, "Search for pair production of the scalar

top quark in the electron-muon final state," `arXiv:1009.5950 [hep-ex]`. 93, 94

[128] CDF Collaboration, T. Aaltonen *et al.*, "Search for Pair Production of Supersymmetric Top Quarks in Dilepton Events from p anti-p Collisions at $\sqrt{s}$ = 1.96 TeV," *Phys.Rev.Lett.* **104** (2010) 251801, `arXiv:0912.1308 [hep-ex]`. 93, 94

[129] DØ Collaboration, V. M. Abazov *et al.*, "Search for admixture of scalar top quarks in the $t\bar{t}$ lepton+jets final state at $\sqrt{s}$=1.96 TeV," *Phys. Lett.* **B674** (2009) 4–10, `arXiv:0901.1063 [hep-ex]`. 93

[130] W.-K. Tung, H. L. Lai, J. Pumplin, P. M. Nadolsky, and C. P. Yuan, "Global QCD Analysis and Collider Phenomenology - CTEQ," `arXiv:0707.0275 [hep-ph]`. 96

[131] T. Sjostrand, S. Mrenna, and P. Z. Skands, "PYTHIA 6.4 Physics and Manual," *JHEP* **0605** (2006) 026, `arXiv:hep-ph/0603175 [hep-ph]`. 96

[132] G. Corcella *et al.*, "HERWIG 6.5: an event generator for Hadron Emission Reactions With Interfering Gluons (including supersymmetric processes)," *JHEP* **01** (2001) 010, `arXiv:hep-ph/0011363`. 96

[133] M. L. Mangano, M. Moretti, F. Piccinini, R. Pittau, and A. D. Polosa, "ALPGEN, a generator for hard multiparton processes in hadronic collisions," *JHEP* **07** (2003) 001, `arXiv:hep-ph/0206293`. 96

[134] B. P. Kersevan and E. Richter-Was, "The Monte Carlo event generator AcerMC version 2.0 with interfaces to PYTHIA 6.2 and HERWIG 6.5," `arXiv:hep-ph/0405247`. 96

[135] S. Frixione and B. R. Webber, "Matching NLO QCD computations and parton shower simulations," *JHEP* **06** (2002) 029, `arXiv:hep-ph/0204244`. 96

[136] J. M. Butterworth, J. R. Forshaw, and M. H. Seymour, "Multiparton interactions in photoproduction at HERA," *Z. Phys.* **C72** (1996) 637–646, `arXiv:hep-ph/9601371`. 96

[137] CDF Collaboration, T. Aaltonen *et al.*, "The underlying event in hard interactions at the Tevatron $\bar{p}p$ collider," *Phys. Rev.* **D70** (2004) 072002, `arXiv:hep-ex/0404004`. 96

[138] E. Barberio, B. van Eijk, and Z. Was, "PHOTOS: A Universal Monte Carlo for QED radiative corrections in decays," *Comput. Phys. Commun.* **66** (1991) 115–128. 96

[139] P. Gondolo *et al.*, "DarkSUSY: Computing supersymmetric dark matter properties numerically," *JCAP* **0407** (2004) 008, `arXiv:astro-ph/0406204`. 96

[140] F. E. Paige, S. D. Protopopescu, H. Baer, and X. Tata, "ISAJET 7.69: A Monte Carlo event generator for pp, $\bar{p}p$, and e^+e^- reactions," `arXiv:hep-ph/0312045`. 96

[141] M. Muhlleitner, A. Djouadi, and Y. Mambrini, "SDECAY: A Fortran code for the decays of the supersymmetric particles in the MSSM," *Comput. Phys. Commun.* **168** (2005) 46–70, `arXiv:hep-ph/0311167`. 96

[142] S. Moretti, K. Odagiri, P. Richardson, M. H. Seymour, and B. R. Webber, "Implementation of supersymmetric processes in the HERWIG event generator," *JHEP* **04** (2002) 028, `arXiv:hep-ph/0204123`. 96

[143] S. Frixione, P. Nason, and B. R. Webber, "Matching NLO QCD and parton showers in heavy flavour production," *JHEP* **08** (2003) 007, `arXiv:hep-ph/0305252`. 99

[144] S. Moch and P. Uwer, "Theoretical status and prospects for top-quark pair production at hadron colliders," *Phys. Rev.* **D78** (2008) 034003, `arXiv:0804.1476 [hep-ph]`. 99

[145] U. Langenfeld, S. Moch, and P. Uwer, "New results for $t\bar{t}$ production at hadron colliders," `arXiv:0907.2527 [hep-ph]`. 99

[146] J. M. Campbell, R. K. Ellis, and F. Tramontano, "Single top production and decay at next-to-leading order," *Phys. Rev.* **D70** (2004) 094012, `arXiv:hep-ph/0408158`. 99

[147] J. M. Campbell and F. Tramontano, "Next-to-leading order corrections to W t production and decay," *Nucl. Phys.* **B726** (2005) 109–130, `arXiv:hep-ph/0506289`. 99

[148] S. Frixione, E. Laenen, P. Motylinski, and B. R. Webber, "Single-top production in MC@NLO," *JHEP* **03** (2006) 092, `arXiv:hep-ph/0512250`. 99

[149] S. Frixione, E. Laenen, P. Motylinski, B. R. Webber, and C. D. White, "Single-top hadron production in association with a W boson," *JHEP* **07** (2008) 029, `arXiv:0805.3067 [hep-ph]`. 99

[150] F. Caravaglios, M. L. Mangano, M. Moretti, and R. Pittau, "A new approach to multi-jet calculations in hadron collisions," *Nucl. Phys.* **B539** (1999) 215–232, `arXiv:hep-ph/9807570`. 100

[151] K. Melnikov and F. Petriello, "Electroweak gauge boson production at hadron colliders through $O(\alpha_s^2)$," *Phys. Rev.* **D74** (2006) 114017, `arXiv:hep-ph/0609070`. 100

[152] ATLAS Collaboration, G. Aad *et al.*, "Luminosity Determination Using the ATLAS Detector," *ATLAS-CONF-2010-060* . 104

[153] P. Urquijo and A. Phan, "Search for the light scalar top in the dilepton final state in ATLAS.," *ATL-PHYS-INT-2010-084* . VII, 107

[154] E. Barberio *et al.*, "First Observation of the process $Z \to \tau\tau \to e\mu + 4\nu$ with the ATLAS Detector," *ATLAS-COM-CONF-2011-040* . 120

[155] B. Acharya *et al.*, "Prospects for measuring the top quark pair production cross-section in the single lepton channel at ATLAS in 10 TeV pp Collisions," *ATL-PHYS-INT-2009-071* . 125, 129, 131, 134

[156] J. Adelman *et al.*, "Sensitivity of the top dilepton cross-section measurement at $\sqrt{s} = 10$ TeV," *ATL-PHYS-INT-2009-066* . 125, 129, 131

[157] S. Allwood-Spiers *et al.*, "Understanding Monte Carlo Generators for Top Physics," *ATL-COM-PHYS-2009-334* . 126

[158] R. D. Cousins, J. T. Linnemann, and J. Tucker, "Evaluation of three methods for calculating statistical significance when incorporating a systematic uncertainty into a test of the background-only hypothesis for a Poisson process," *Nucl. Instrum. Meth.* **A595** (2008) 480–501. 127

[159] M. Uslenghi, "Ricerche di supersimmetria con il rivelatore ATLAS," Master's thesis, University of Milan, 2008. 138, 139

[160] ATLAS Collaboration, G. Aad *et al.*, "Measurement of the $W \to \ell\nu$ and

$Z/\gamma^* \rightarrow \ell\ell$ production cross sections in *pp* collisions at $\sqrt{s} = 7$ TeV with the ATLAS detector," *JHEP* **12** (2010) 060, `arXiv:1010.2130 [hep-ex]`. 143

[161] ATLAS Collaboration, G. Aad *et al.*, "Measurement of the top quark pair production cross section with ATLAS in *pp* collisions at $\sqrt{s} = 7$ TeV," `arXiv:1012.1792 [hep-ex]`. 143

[162] ATLAS Collaboration, G. Aad *et al.*, "Search for supersymmetry using final states with one lepton, jets, and missing transverse momentum with the ATLAS detector in $\sqrt{s} = 7$ TeV *pp* collisions," `arXiv:1102.2357 [hep-ex]`. 143

[163] ATLAS Collaboration, G. Aad *et al.*, "SUSY searches with dileptons and high missing transverse momentum," *ATL-COM-PHYS-2010-1045* . 143

[164] F. Cerutti *et al.*, "Muon Momentum Resolution in First Pass Reconstruction of *pp* Collision Data Recorded by ATLAS in 2010," *ATLAS-COM-CONF-2011-003* . 146

[165] ATLAS Collaboration, G. Aad *et al.*, "Measurement of jet production in proton-proton collisions at 7 TeV centre-of-mass energy with the ATLAS Detector," *ATLAS-CONF-2010-050* . 146

[166] ATLAS Collaboration, G. Aad *et al.*, "Calibrating the *b*-Tag and Mistag Efficiencies of the SV0 *b*-Tagging Algorithm in 3 pb^{-1} of Data with the ATLAS Detector," *ATLAS-CONF-2010-099* . 147

[167] ATLAS Collaboration, G. Aad *et al.*, "Data-Quality Requirements and Event Cleaning for Jets and Missing Transverse Energy Reconstruction with the ATLAS Detector in Proton-Proton Collisions at a Center-of-Mass Energy of $\sqrt{s} = 7$ TeV," *ATLAS-CONF-2010-038* . 150

[168] C. Lester, M. A. Parker, and M. J. White, "Three body kinematic endpoints in SUSY models with non-universal Higgs masses," *JHEP* **0710** (2007) 051, `arXiv:hep-ph/0609298 [hep-ph]`. xxii

A

Light Stop Benchmark Parameters

Table A.1. MSSM parameters of the $\tilde{t}_1$ benchmark point *LHS*2 [56].

Squark Mass Parameters	**Slepton Mass Parameters**
$m_{\tilde{Q},\tilde{U},\tilde{D}_{1,2}} = 10\,000$ GeV	$m_{\tilde{L}_{1,2}} = 10\,000$ GeV
$m_{\tilde{Q}_3} = 1\,500$ GeV	$m_{\tilde{L}_3} = 1\,000$ GeV
$m_{\tilde{U}_3} = 0$ GeV	$m_{\tilde{E}_{1,2}} = 10\,000$ GeV
$m_{\tilde{D}_3} = 1\,000$ GeV	$m_{\tilde{E}_3} = 1\,000$ GeV
Higgs Sector Parameters	**Trilinear Interaction Parameters**
$\lvert\mu\rvert = 400$ GeV	$\lvert A_t\rvert = 643$ GeV
$\phi_\mu = \frac{\pi}{2}$	$\phi_{A_t} = -\frac{\pi}{2}$
$\tan\beta = 7$	$A_b = 0$
$m_A = 1000$ GeV	$A_{e,\mu,\tau} = 0$
Gaugino Mass Parameters	
$M_1 = 60$ GeV	
$M_2 = 121$ GeV	
$M_3 = 948$ GeV	

B

Missing Energy Reconstruction

Events with large $\not{E}_\mathrm{T}$ are a key signature for new physics such as supersymmetry. An accurate measurement of missing transverse energy ($\not{E}_\mathrm{T}$ in this chapter) is a crucial requirement for the study these events in ATLAS. This chapter describes a study of the expected performance of $\not{E}_\mathrm{T}$ reconstruction in minimum bias events at $\sqrt{s} = 14$ TeV, performed by the author and published in Reference [78].

B.1. Missing Transverse Energy Reconstruction Algorithm

The calculation of $\not{E}_\mathrm{T}$ is performed by imposing energy conservation: $\not{E}_\mathrm{T} = -E_\mathrm{T}^\mathrm{visible}$. However, complications arise from calorimeter coverage, calibration and noise which affect visible energy measurements. Therefore, the most important effects on good $\not{E}_\mathrm{T}$ reconstruction in ATLAS are [77]: the accurate tuning of electronic noise suppression; the use of all calorimeters cells; and accurate calorimeter calibration and intercalibration.

The cell-based $\not{E}_\mathrm{T}$ algorithm takes all these factors into account. The algorithm is based on the energy deposited in each calorimeter cell calibrated to an associated reconstructed particle and an estimate of energy lost by particles entering the cryostat between the electromagnetic and hadronic calorimeters. An additional correction is required for muons, which are minimum ionising particles and thus do not deposit much energy in the calorimeters. The x and y components of the final $\not{E}_{\mathrm{T}}$ can be defined as:

$$\not{E}_{x,y}^{\mathrm{Final}} = \not{E}_{x,y}^{\mathrm{CaloCalib}} + \not{E}_{x,y}^{\mathrm{Cryo}} + \not{E}_{x,y}^{\mathrm{Muon}} \tag{B.1}$$

In the following, the three terms in the above equation will be referred as the calorimeter, cryostat and muon terms respectively. They will be described in the following subsections.

Complementary to the reconstruction of the $\not{E}_{\mathrm{T}}$ is total transverse energy, ΣE_{T}, which is the scalar sum of the transverse energy and is calculated using the same quantities:

$$\Sigma E_{\mathrm{T}}^{\mathrm{Final}} = \Sigma E_{\mathrm{T}}^{\mathrm{CaloCalib}} + \Sigma E_{\mathrm{T}}^{\mathrm{Cryo}} + \Sigma E_{\mathrm{T}}^{\mathrm{Muon}}$$

B.1.1. Missing Transverse Energy Calorimeter Term

The ATLAS calorimeter has a large number of readout channels, so electronic and pileup noise can be significant contributions to energy measurements. Thus it is crucial to have a good calorimeter noise suppression algorithm. By only using cells in topoclusters, the $\not{E}_{\mathrm{T}}$ algorithm takes advantage of the 4/2/0 topocluster noise thresholds which are optimised to suppress electronic noise and pileup from minimum bias events, while keeping the single pion efficiency as high as possible [97].

The x and y components of the non-calibrated calorimeter $\not{E}_{\mathrm{T}}$ term are derived from the transverse energies deposited in calorimeter cells in topoclusters:

$$\not{E}_{x,y}^{\mathrm{Calo}} = -\sum_{\mathrm{cells}} E_{x,y} \quad \text{(only cells in topoclusters)}$$

As the ATLAS calorimeter is non-compensating, its energy response to electromagnetic and hadronic showers is different, so calorimeter cells must be calibrated accordingly. The calibration method used for the calorimeter $\not{E}_{\mathrm{T}}$ term is the so-called *Refined Calibration* where each calorimeter cell is calibrated according to the reconstructed particle it belongs to.

To apply this calibration method, the calorimeter cells selected have to be associated with reconstructed and identified physics objects in the event. This method begins with a loop over the reconstructed particles in the event in the following order: electrons/γs, tauons, b jets, jets and muons.

The association of calorimeter cells to particles is performed by filling an association map, starting from reconstructed particles in the chosen order, navigating back to their component clusters (sliding window clusters for electrons/γs, combined clusters for taus and topoclusters for jets and b jets) and back again to their cells. If a cell belongs to more than one kind of reconstructed particle, the first association is taken, in the chosen order of the reconstructed objects. If a cell belongs to more than one object of the same kind, all associations are taken and the geometrical weights are also included. Cells within topoclusters, but which are not associated to any reconstructed particle are calibrated using jet weights.

The contribution to $\not{E}_{\mathrm{T}}$ of all cells associated to the same kind of particles is saved separately and the Refined Calibrated $\not{E}_{\mathrm{T}}$ is calculated by summing all the separate contributions, for x component:

$$\begin{aligned} \not{E}_x^{\mathrm{CaloCalib}} &= \not{E}_x^{\mathrm{RefFinal}} \\ &= \not{E}_x^{\mathrm{RefEM}} + \not{E}_x^{\mathrm{RefTau}} + \not{E}_x^{\mathrm{RefBjet}} + \not{E}_x^{\mathrm{RefJet}} + \not{E}_x^{\mathrm{RefMuo}} + \not{E}_x^{\mathrm{CellOut}} \qquad \text{(B.2)} \end{aligned}$$

and similarly for the y component, where each term is calculated from the sum of calibrated cells for a specific particle type.

B.1.2. Missing Transverse Energy Cryostat Term

The thickness of the cryostat between the liquid argon barrel electromagnetic calorimeter and the tile barrel hadronic calorimeter is about half an interaction length. The $\not{E}_{\mathrm{T}}$ reconstruction recovers energy loss in the cryostat using the correlation between energies of the third layer of the liquid argon calorimeter and the first layer of the hadronic calorimeter. A similar correction is applied for the endcap cryostats.

The cryostat correction term in the $\not{E}_{\mathrm{T}}$ calculation in Equation B.1 is defined as:

$$\not{E}_{x,y}^{\mathrm{Cryo}} = -\sum_{\mathrm{jets}} E_{\mathrm{jet}_{\mathrm{x,y}}}^{\mathrm{Cryo}}$$

where the sum is done on all the reconstructed jets in the event, and:

$$E_{\text{jet}}^{\text{Cryo}} = w^{\text{Cryo}} \times \sqrt{E_{\text{EM3}} \times E_{\text{HAD}}}$$

where w^{Cryo} is the cryostat correction factor, and E_{EM3} and E_{HAD} are the jet energies in the third layer of the electromagnetic calorimeter and the first layer of the hadronic calorimeter respectively.

This correction term is non-negligible for p_{T} jets; it represents a ~5% contribution per jet for $p_{\text{T}} > 500$ GeV.

B.1.3. Missing Transverse Energy Muon Term

The $\not{E}_{\text{T}}$ muon term in the $\not{E}_{\text{T}}$ calculation in Equation B.1 is calculated as:

$$\not{E}_{x,y}^{\text{Muon}} = -\sum_{\text{muons}} E_{x,y}^{\text{muon}}$$

which is a sum over all reconstructed muons where the energies are taken from the muon spectrometer only. This insures that energy lost by muons in the calorimeter is not double counted since that is already taken into account in the calorimeter term.

The request of having an actual reconstructed muon, with a matching track in the inner detector reduces the probability of having fake muons. To decrease the possibility of double muons or muons with bad associations between the inner and the external muon spectrometer detector only good quality muons are used, applying a cutoff on the combination χ^2.

The $\not{E}_{\text{T}}$ resolution is dominated by the calorimeter term; the muon term does not contribute much to the $\not{E}_{\text{T}}$ resolution, but unmeasured, badly measured and misidentified muons can be a source of fake $\not{E}_{\text{T}}$.

B.2. Evaluating Missing Transverse Energy Reconstruction

The $\not{E}_{\text{T}}$ reconstruction performance is evaluated by comparing the final reconstructed $\not{E}_{\text{T}}^{\text{Final}}$ with $\not{E}_{\text{T}}^{\text{True}}$, calculated from the momentum of the stable and non-interacting particles, such as neutrinos, in terms of resolution, tails and bias.

The final $\not{E}_{\mathrm{T}}$ performance is evaluated from the distribution:

$$\not{E}_{\mathrm{T}}^{\mathrm{Final}} - \not{E}_{\mathrm{T}}^{\mathrm{True}} \quad or \quad \not{E}_{x,y}^{\mathrm{Final}} - \not{E}_{x,y}^{\mathrm{True}} \quad \text{(for each component)} \tag{B.3}$$

The $\not{E}_{\mathrm{T}}$ resolution is defined as the σ of a Gaussian fit to the distribution of Equation B.3. The calorimeter $\not{E}_{\mathrm{T}}$ resolution is well described by the simple formula $a \times \sqrt{\Sigma E_{\mathrm{T}}}$ where the parameter a quantifies the resolution. As the final $\not{E}_{\mathrm{T}}$ resolution is dominated by calorimeter measurements, in events where the activity outside η coverage is not very large, that formula is also valid for the final $\not{E}_{\mathrm{T}}$ resolution. $\not{E}_{\mathrm{T}}$ resolution is affected mainly affected by calorimeter noise suppression and calibration.

The $\not{E}_{\mathrm{T}}$ tail is defined as the fraction of events outside 3σ of the distribution of Equation B.3. Tails in $\not{E}_{\mathrm{T}}$ are caused by abnormalities in energy measurements, such as hot or dead calorimeter cells, large losses in inactive detector material or jet energy fluctuations.

The $\not{E}_{\mathrm{T}}$ bias is the mean value of the distribution of Equation B.3. In events without $\not{E}_{\mathrm{T}}^{\mathrm{True}}$, a positive bias is expected by definition.

B.3. Missing Transverse Energy Performance in Minimum Bias Events

The validation of the $\not{E}_{\mathrm{T}}$ reconstruction and calibration in ATLAS described in the previous sections can be performed using minimum bias events. These can be used to verify the $\not{E}_{\mathrm{T}}$ reconstruction procedure and to estimate the $\not{E}_{\mathrm{T}}$ resolution of low energy events.

B.3.1. Simulation of Minimum Bias Events

This study has been performed using fully simulated non-diffractive minimum bias events which have been generated with PYTHIA where the underlying event has been tuned to fit previous experiments. Details of the data sample used are given in Table B.1.

Table B.1. Details of the minimum bias dataset used in the minimum bias $\not\!\!E_{\mathrm{T}}$ study. Events were generated using PYTHIA.

Process	Events	σ (mb)	$\int \mathcal{L}$ (pb^{-1})
Non-Diffractive	4 016 250	80	5.0×10^{-5}

Minimum bias events are also comprised of inelastic single diffractive and double diffractive events. Their contributions and the backgrounds of beam gas and halo are expected to be negligible after trigger and event selection and thus have not been included in this study.

B.3.2. Selection of Minimum Bias Events

In the early stages of the experiment, minimum bias events will be selected by three types of trigger: random L1 trigger only, random L1 trigger with additional track trigger requirement, and L1 scintillator trigger with possible verification at the HLT. During initial running these triggers will be used in a 1:50:50 ratio. The output of each of the triggers will be prescaled such that the total minimum bias trigger rate at the EF will either be 1, 10 or 20 Hz. These triggers have been chosen to reduce any bias introduced in the event selection.

For the study of $\not\!\!E_{\mathrm{T}}$ in minimum bias events, high signal efficiency and background rejection is required, while the composition of the signal, meaning the fraction of non-diffractive, single diffractive and double diffractive events in the sample is unimportant. The selection criteria for such events is:

1. The number of SCT spacepoints greater than 40 to reject empty events; and

2. At least one good reconstructed track to reject beam gas and halo events. The standard selection of a good track is N(SCT+pixel) spacepoints ≥ 7, $|d_0| < 2$ mm and $|z_0 \sin\theta| < 10$mm. No cut is applied on the number of hits on the innermost pixel layer.

Figure B.1 shows event selection efficiency as a function of ΣE_{T}. The efficiency of the SCT spacepoint selection is almost 100% for $\Sigma E_{\mathrm{T}} > 20$ GeV. Overall spacepoint efficiency is 96.8% and track selection is 80.6%, respectively and total selection efficiency is 78.0%. To keep enough statistics, all plots shown hereafter are made without selection since no clear selection bias is seen.

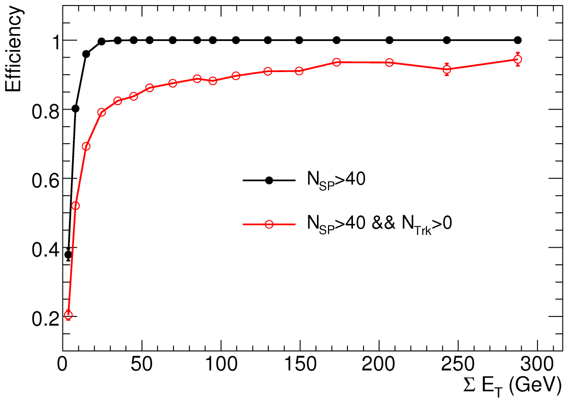

Figure B.1. Event selection efficiency as a function of ΣE_T in minimum bias events. Closed circles show the SCT spacepoint selection efficiency and the open circles display the track selection efficiency.

B.3.3. Characteristics of Minimum Bias Events

Minimum bias interactions at the LHC are dominated by soft interactions of the two proton beams. These low energy interactions produce spherically distributed low p_T hadrons, the majority being pions, the lightest known meson. These particles are produced with very low momentum, in fact so low that most of these hadrons will not be identified within ATLAS, since there is a minimum p_T cut on reconstructed particles of the order of 5 GeV.

Figure B.2 shows the number of reconstructed jets and their p_T for different ΣE_T regions. Note that jets are the only particles reconstructed in minimum bias events as only hadrons are produced in the interactions. It is clear that there is a lower limit on the p_T of a reconstructed jet of 5 GeV and that jets are rarely reconstructed depending on ΣE_T.

The $\not{E}_\mathrm{T}$ and ΣE_T distributions of the non-diffractive minimum bias events are depicted in Figure B.3. The $\not{E}_\mathrm{T}$ in the events is fairly low as expected, with a mean of 4.3 GeV. Fake $\not{E}_\mathrm{T}$ is mainly caused by the calorimeter energy resolution (82%) and acceptance (18%) and while the truth $\not{E}_\mathrm{T}$ originates from the inflight decays of K or π mesons and the decay of charm and bottom quarks, and is 0.06 GeV on average. The non-diffractive minimum bias events are comparatively of low energy with a mean ΣE_T of 49.0 GeV.

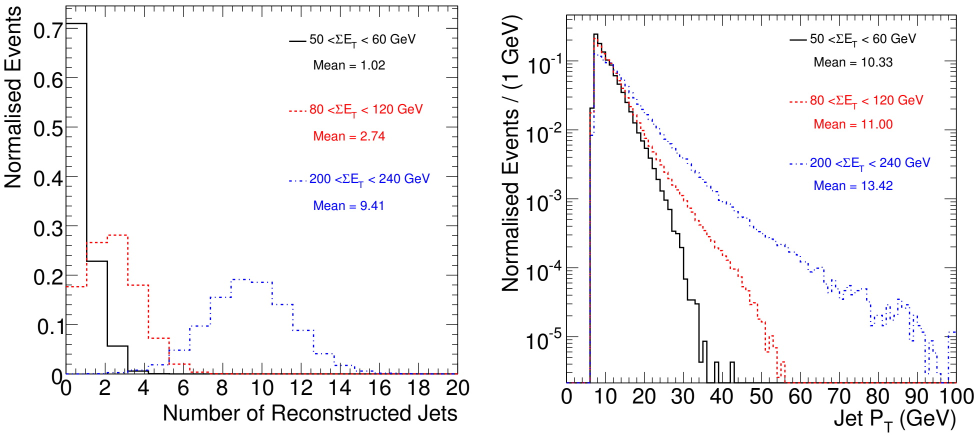

(a) Number of reconstructed jets **(b)** Jet p_{T}

Figure B.2. Jet reconstruction in minimum bias events for different ΣE_{T} regions, $50\ \mathrm{GeV} < \Sigma E_{\mathrm{T}} < 60\ \mathrm{GeV}$ (solid lines), $80\ \mathrm{GeV} < \Sigma E_{\mathrm{T}} < 120\ \mathrm{GeV}$ (dashed lines) and $200\ \mathrm{GeV} < \Sigma E_{\mathrm{T}} < 240\ \mathrm{GeV}$ (dotted lines).

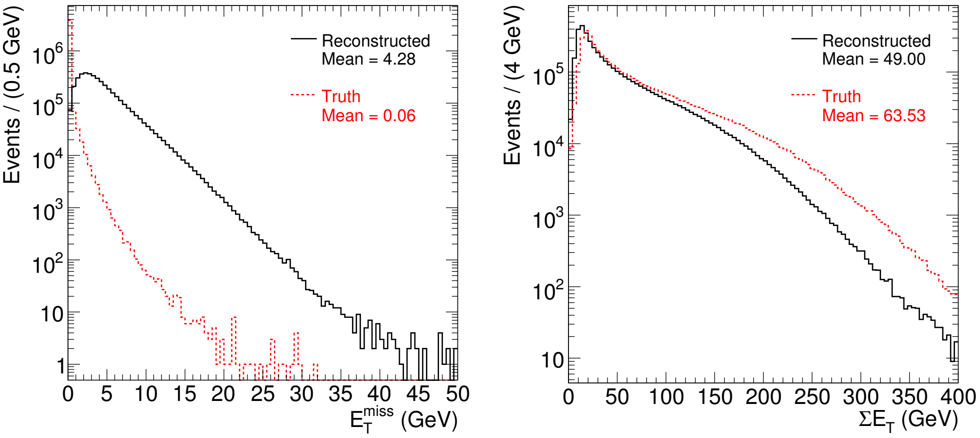

(a) $\not\!\!E_{\mathrm{T}}$ **(b)** ΣE_{T}

Figure B.3. The $\not\!\!E_{\mathrm{T}}$ (left) and ΣE_{T} (right) distributions for minimum bias events. The solid lines are the reconstructed distributions while the dashed lines are the true distributions. No event selection is applied.

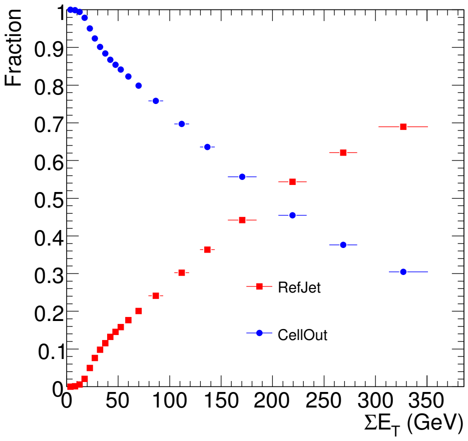

Figure B.4. The fraction of reconstructed $\not\!\!E_{\mathrm{T}}$ coming from jets (solid squares) and cells outside of objects (solid circles) in minimum bias events.

Figure B.4 shows the fraction of the reconstructed $\not\!\!E_{\mathrm{T}}$ coming from jets and cells outside of objects, ($\not\!\!E_x^{\mathrm{RefJets}}$ and $\not\!\!E_x^{\mathrm{RefOut}}$ in Equation B.2). As minimum bias events are dominated by soft interactions and jets are rarely reconstructed, the $\not\!\!E_{\mathrm{T}}$ will be dominated by the $\not\!\!E_x^{\mathrm{RefOut}}$ for low ΣE_{T}.

B.3.4. Missing Transverse Energy Performance in Minimum Bias Events

The $\not\!\!E_{\mathrm{T}}$ performance is evaluated comparing the final reconstructed $\not\!\!E_{\mathrm{T}}^{\mathrm{Final}}$ with the $\not\!\!E_{\mathrm{T}}^{\mathrm{True}}$, in terms of bias, resolution and tails, as mentioned earlier. As minimum bias events contain very little $\not\!\!E_{\mathrm{T}}$, looking at the bias does not describe $\not\!\!E_{\mathrm{T}}$ performance, only resolution and tails will be discussed.

Figure B.5(a) depicts the difference $\not\!\!E_{\mathrm{T}}^{\mathrm{Final}} - \not\!\!E_{\mathrm{T}}^{\mathrm{True}}$ in minimum bias events for different ΣE_{T} regions. These distributions are well fitted by Gaussian functions, with offsets of zero and resolutions which increase with ΣE_{T}, $\sigma_{x,y} = 3.92$ (5.10) (7.08) GeV for $\Sigma E_{\mathrm{T}} = 0$ - 40 (100-140) (200-240) GeV. Note the lack of tails on the distributions, which means the $\not\!\!E_{\mathrm{T}}$ in minimum bias events is not very affected by fake muons, jets pointing to cracks or losses in dead materials.

The $\not\!\!E_{\mathrm{T}}$ resolution in minimum bias events is expected to scale as $\sqrt{\Sigma E_{\mathrm{T}}}$. This is because the stochastic term of the calorimeter resolution is dominant for low ΣE_{T} regions. The $\not\!\!E_{x,y}$ resolution as a function of ΣE_{T} is shown in Figure B.5(b). This distribution is fitted by functions of the forms: $p1\sqrt{\Sigma E_{\mathrm{T}}}$ and $p0 + p1\sqrt{\Sigma E_{\mathrm{T}}}$, where $p1$ and $p0$ represent

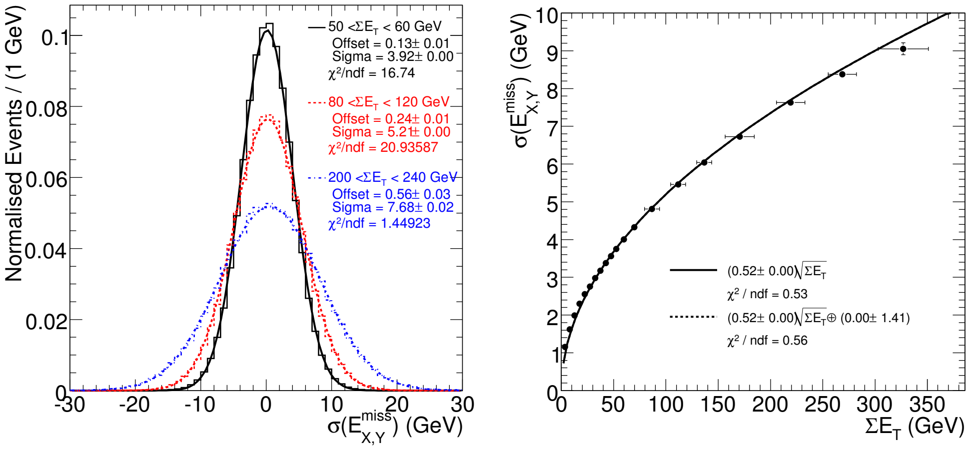

(a) $\not\!\!E_{\mathrm{T}}$ resolution for x and y components for different ΣE_{T} regions, 50 GeV $< \Sigma E_{\mathrm{T}} <$ 60 GeV (solid lines), 80 GeV $< \Sigma E_{\mathrm{T}} <$ 120 GeV (dashed lines) and 200 GeV $< \Sigma E_{\mathrm{T}} <$ 240 GeV (dotted lines).

(b) ΣE_{T} scaling of the $\not\!\!E_{\mathrm{T}}$ resolution, fitted with two different functions: $p1\sqrt{\Sigma E_{\mathrm{T}}}$ (solid line) and $p0 + p1\sqrt{\Sigma E_{\mathrm{T}}}$ (dashed line).

Figure B.5. The $\not\!\!E_T$ resolution in minimum bias events.

the stochastic and noise terms of the calorimeter energy resolution, respectively. The scaling is well-described with a stochastic term of 0.51 and noise term of ~ 0 GeV.

Figure B.6 shows the validity of $\not\!\!E_{\mathrm{T}}$ resolution evaluated by this study in a higher ΣE_{T} region (300 GeV $< \Sigma E_{\mathrm{T}} <$ 600 GeV). The $\not\!\!E_{\mathrm{T}}$ resolution in QCD multijet events are well on the the resolution curve obtained by minimum bias events. Details of the QCD multijet datasets used in this comparison can be found in Table B.2. For direct evaluation of $\not\!\!E_{\mathrm{T}}$ performance in higher ΣE_{T} regions, more statistics or other schemes using well known physics processes are required.

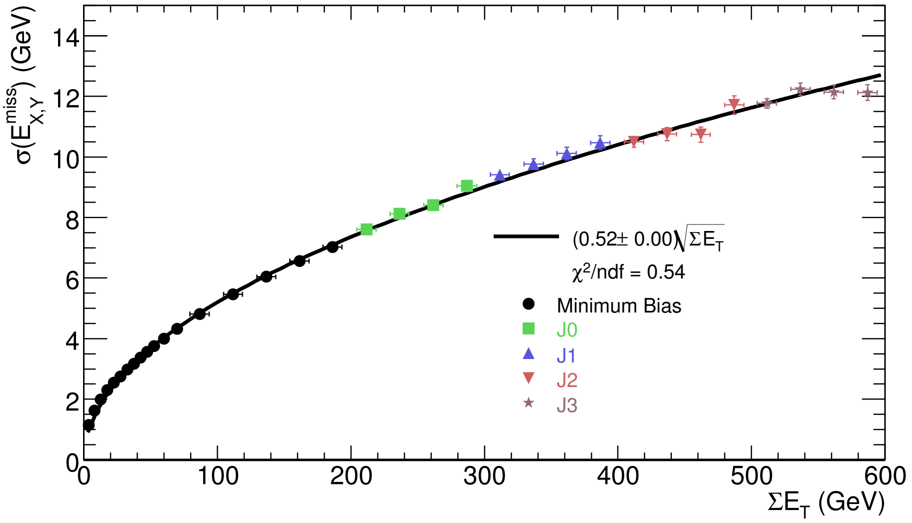

Figure B.6. The $\not{E}_{\mathrm{T}}$ resolution in QCD multijet events (solid squares, triangles and stars) are shown together with a $\not{E}_{\mathrm{T}}$ resolution obtained from this study (solid circles) and obtained resolution curve (solid line) as a function of ΣE_{T}.

Table B.2. Details of QCD multijet datasets used in the minimum bias $\not{E}_{\mathrm{T}}$ study. Datasets were all generated using PYTHIA.

Process	p_{T} Range	Events	σ (pb)
QCD Multijet	8 – 17 GeV	147 000	1.7×10^{10}
	17 – 35 GeV	135 000	1.4×10^{9}
	35 – 70 GeV	320 000	9.3×10^{7}
	70 – 140 GeV	231 000	5.9×10^{6}

C

Dileptonic Light Stop Grid Results

This chapter provides results for the full signal grid from the dileptonic stop analysis at $\sqrt{s} = 10$ TeV. Table C.1 links the full result tables in this chapter to their summarised versions in Chapter 8.

Table C.1. Dileptonic 10 TeV signal grid result tables.

Summarised Table	Full Table
8.4	C.2
8.6	C.3
8.9	C.4
8.10	C.5
8.13	C.6

Table C.2. Dileptonic event yields at 10 TeV for the b jet and high $E_{\mathrm{T}}^{\mathrm{miss}}$ signal regions for 1 fb^{-1} with the signal grid points. Errors are statistical only.

$m_{\tilde{t}_1}/m_{\tilde{\chi}_1^\pm}/m_{\tilde{\chi}_1^0}$ **(GeV)**	b **jet region**	**high** $E_{\mathrm{T}}^{\mathrm{miss}}$ **region**
95/95/45	90 ± 50	1 000 ± 200
95/95/85	0	0
95/135/45	50 ± 30	800 ± 100
95/135/85	0	0
105/95/45	70 ± 30	480 ± 80
105/95/85	10 ± 10	60 ± 30
105/135/45	20 ± 20	500 ± 90
105/135/85	10 ± 10	130 ± 40
115/95/45	380 ± 60	390 ± 60
115/95/85	0	70 ± 30
115/135/45	10 ± 10	420 ± 60
115/135/85	20 ± 20	270 ± 60
120/95/45	450 ± 60	320 ± 50
120/155/45	0	470 ± 60
120/155/105	0	10 ± 10
120/215/45	20 ± 10	320 ± 50
120/215/105	0	40 ± 20
150/95/45	59 ± 9	60 ± 10
150/155/45	220 ± 20	140 ± 20
150/155/105	5 ± 4	150 ± 20
150/215/45	10 ± 5	270 ± 30
150/215/105	0	190 ± 30
180/95/45	5 ± 4	270 ± 30
180/155/45	60 ± 9	180 ± 20
180/155/105	76 ± 10	130 ± 10
180/215/45	0	150 ± 10
180/215/105	0	140 ± 10
180/215/165	0	4 ± 2
240/95/45	3 ± 1	27 ± 3
240/155/45	7 ± 1	40 ± 3
240/155/105	13 ± 2	32 ± 2
240/215/45	6 ± 1	62 ± 4
240/215/105	15 ± 2	56 ± 4
240/215/165	17 ± 2	34 ± 3

Table C.3. Dileptonic event yields at 10 TeV for the *t* and *Z* sideband regions for both signal regions for 1 fb^{-1} with the signal grid points. Errors are statistical only.

$m_{\tilde{t}_1}/m_{\tilde{\chi}_1^\pm}/m_{\tilde{\chi}_1^0}$	**b jet signal region**		**high E_T^{miss} signal region**	
(GeV)	***t* sideband**	***Z* sideband**	***t* sideband**	***Z* sideband**
95/95/45	20 ± 20	0	110 ± 50	310 ± 80
95/95/85	0	0	0	0
95/135/45	50 ± 30	20 ± 20	50 ± 30	500 ± 100
95/135/85	0	0	0	0
105/95/45	30 ± 20	60 ± 30	70 ± 30	240 ± 60
105/95/85	0	10 ± 10	10 ± 10	10 ± 10
105/135/45	20 ± 20	20 ± 20	60 ± 30	320 ± 70
105/135/85	0	0	0	10 ± 10
115/95/45	10 ± 10	120 ± 30	90 ± 30	330 ± 60
115/95/85	0	20 ± 10	20 ± 10	0
115/135/45	10 ± 10	20 ± 10	0	310 ± 60
115/135/85	10 ± 10	0	20 ± 20	20 ± 20
120/95/45	20 ± 10	100 ± 30	110 ± 30	150 ± 30
120/155/45	10 ± 10	20 ± 10	40 ± 20	280 ± 50
120/155/105	0	0	7 ± 7	0
120/215/45	7 ± 7	0	10 ± 10	210 ± 40
120/215/105	0	0	7 ± 7	0
150/95/45	70 ± 9	35 ± 7	23 ± 5	35 ± 7
150/155/45	50 ± 10	40 ± 10	40 ± 10	40 ± 10
150/155/105	5 ± 4	0	10 ± 5	34 ± 9
150/215/45	3 ± 3	0	217 ± 7	150 ± 20
150/215/105	0	0	4 ± 4	360 ± 10
180/95/45	5 ± 4	5 ± 4	10 ± 5	140 ± 20
180/155/45	13 ± 4	41 ± 7	47 ± 8	90 ± 10
180/155/105	4 ± 2	17 ± 5	40 ± 7	42 ± 7
180/215/45	2 ± 2	2 ± 2	7 ± 3	90 ± 10
180/215/105	0	1 ± 1	10 ± 3	36 ± 6
180/215/165	0	0	0	0
240/95/45	17 ± 2	7 ± 1	18 ± 2	7 ± 1
240/155/45	13 ± 2	15 ± 2	25 ± 2	16 ± 2
240/155/105	11 ± 2	5 ± 1	20 ± 2	6 ± 1
240/215/45	1 ± 1	6 ± 1	20 ± 2	17 ± 2
240/215/105	2 ± 1	8 ± 1	17 ± 2	16 ± 2
240/215/165	2 ± 1	5 ± 1	11 ± 1	8 ± 1

Table C.4. Discovery potential at 10 TeV for the *b* jet signal region with 1 fb^{-1} for the signal grid points.

$m_{\tilde{t}_1}/m_{\tilde{\chi}_1^\pm}/m_{\tilde{\chi}_1^0}$ (GeV)	**Yield (events)**	**Statistical Error (%)**	**Systematic Error (%)**	**Significance**
95/95/45	90	29	61	1.4
95/95/85	0	–	–	–
95/135/45	45	57	130	0.6
95/135/85	0	–	–	–
105/95/45	74	35	74	1.1
105/95/85	14	170	370	0.2
105/135/45	15	170	360	0.2
105/135/85	15	170	360	0.2
115/95/45	374	8.3	14	10.4
115/95/85	0	–	–	–
115/135/45	10	250	540	0.1
115/135/85	11	220	480	0.1
120/95/45	451	7.2	12	12.4
120/155/45	0	–	–	–
120/155/105	0	–	–	–
120/215/45	22	120	250	0.3
120/215/105	0	–	–	–
150/95/45	61	40	95	0.9
150/155/45	210	14	27	3.0
150/155/105	5	470	1 030	0.0
150/215/45	10	240	515	0.1
150/215/105	0	–	–	–
180/95/45	5	470	1 000	0.0
180/155/45	57	45	95	0.9
180/155/105	74	35	72	1.2
180/215/45	0	–	–	–
180/215/105	0	–	–	–
180/215/165	0	–	–	–
240/95/45	2	1 000	2 200	0.0
240/155/45	7	350	740	0.0
240/155/105	12	200	440	0.1
240/215/45	6	410	890	0.0
240/215/105	15	170	360	0.2
240/215/165	17	150	320	0.2

Table C.5. Discovery potential at 10 TeV for the high $E_{\mathrm{T}}^{\mathrm{miss}}$ signal region with 1 fb^{-1} for the signal grid points.

$m_{\tilde{t}_1}/m_{\tilde{\chi}_1^\pm}/m_{\tilde{\chi}_1^0}$ (GeV)	Yield (events)	Statistical Error (%)	Systematic Error (%)	Significance
95/95/45	697	7.1	8.6	12.1
95/95/85	0	–	–	–
95/135/45	562	8.2	9.9	10.6
95/135/85	0	–	–	–
105/95/45	238	18	24	3.2
105/95/85	29	140	190	0.4
105/135/45	360	12	16	4.7
105/135/85	29	130	180	0.4
115/95/45	268	17	22	3.5
115/95/85	30	130	180	0.4
115/135/45	239	17	22	3.4
115/135/85	193	21	28	2.8
120/95/45	180	25	33	2.4
120/155/45	303	14	18	4.1
120/155/105	7	530	740	0.1
120/215/45	209	20	26	3.0
120/215/105	22	175	240	0.3
150/95/45	36	110	150	0.5
150/155/45	83	49	67	1.2
150/155/105	109	36	50	1.6
150/215/45	215	19	25	3.1
150/215/105	130	31	41	1.9
180/95/45	214	19	25	3.1
180/155/45	128	32	44	1.8
180/155/105	78	52	72	1.1
180/215/45	131	31	41	1.9
180/215/105	100	39	54	1.5
180/215/165	5	780	1 100	0.0
240/95/45	20	190	270	0.3
240/155/45	31	130	180	0.4
240/155/105	23	170	240	0.3
240/215/45	44	90	130	0.6
240/215/105	39	100	140	0.6
240/215/165	22	180	250	0.3

Table C.6. Top basic selection event yields at 10 TeV for 1 fb^{-1} with the signal grid points. Errors are statistical only.

$m_{\tilde{t}_1}/m_{\tilde{\chi}^\pm_1}/m_{\tilde{\chi}^0_1}$ (GeV)	**Semileptonic Selection**	**Dileptonic Selection**
95/95/45	5 000 ± 1 000	1 000 ± 200
95/95/85	4 000 ± 1 000	0
95/135/45	100 ± 200	900 ± 100
95/135/85	4 000 ± 1 000	0
105/95/45	100 ± 200	800 ± 100
105/95/85	4100 ± 300	10 ± 10
105/135/45	800 ± 100	700 ± 100
105/135/85	2 900 ± 200	10 ± 10
115/95/45	900 ± 300	780 ± 90
115/95/85	2 900 ± 200	0
115/135/45	2 940 ± 70	680 ± 80
115/135/85	2 570 ± 70	90 ± 30
120/95/45	1 120 ± 40	780 ± 10
120/155/45	1 910 ± 60	710 ± 70
120/155/105	1 010 ± 40	0
120/215/45	23 ± 7	530 ± 60
120/215/105	1 020 ± 4	7 ± 7
150/95/45	1 390 ± 5	230 ± 20
150/155/45	681 ± 4	360 ± 30
150/155/105	760 ± 3	100 ± 20
150/215/45	570 ± 3	450 ± 30
150/215/105	250 ± 2	80 ± 20
180/95/45	6 000 ± 8 000	440 ± 30
180/155/45	0	370 ± 20
180/155/105	5 000 ± 8 000	160 ± 10
180/215/45	70 ± 900	240 ± 20
180/215/105	5 000 ± 4 000	180 ± 20
180/215/165	400 ± 1 000	0
240/95/45	5 000 ± 4 000	57 ± 4
240/155/45	600 ± 1 000	131 ± 6
240/155/105	5 000 ± 2 000	48 ± 3
240/215/45	300 ± 500	88 ± 5
240/215/105	5 000 ± 2 000	85 ± 5
240/215/165	1 000 ± 1 000	32 ± 3

D

Sparticle Mass Calculation

For particular sparticle mass spectra and light stop decay modes, it may be possible to extract the sparticle masses by measuring the kinematic endpoints of invariant mass distributions from the semileptonic decay channel.

The light stop decay mode in which this may be possible is shown in Figure D.1, where the light stop undergoes a two body decay into a b quark and a chargino, which subsequently undergoes a three body decay via a virtual W boson into a neutralino and fermion pair.

By taking different combinations of the visible decay products, the following invariant masses can be formed: m_{qq}, m_{bqq} and $m_{b\ell}$. These will have maxima resulting from

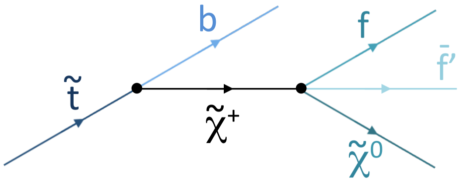

Figure D.1. Light stop decay chain allowing for sparticle mass extraction.

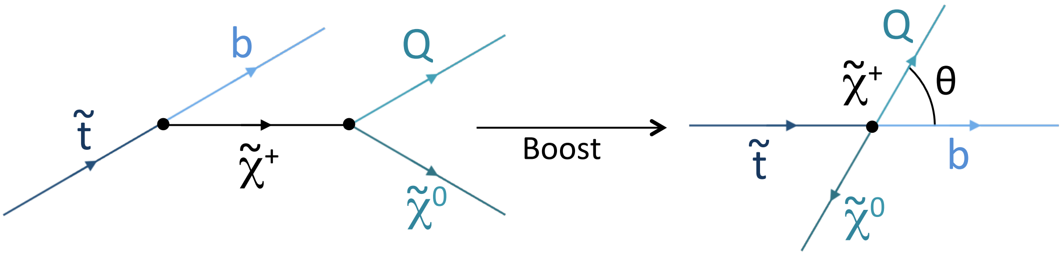

Figure D.2. Light stop hadronic decay branch and rest frame involved in invariant mass kinematic endpoint calculation.

kinematic limits whose position is given by a function of $m_{\tilde{t}_1}$, $m_{\tilde{\chi}_1^\pm}$ and $m_{\tilde{\chi}_1^0}$, each of which will be derived below using the formalism of Reference [168].

For the hadronic branch $\tilde{t}_1 \rightarrow b\tilde{\chi}_1^+ \rightarrow b\tilde{\chi}_1^0 W^+ \rightarrow b\tilde{\chi}_1^0 q\bar{q}'$, the endpoint of the m_{qq} distribution results from the three body decay of the $\tilde{\chi}_1^\pm$ and is trivially given by the mass difference between the $\tilde{\chi}^\pm$ and the $\tilde{\chi}_1^0$:

$$m_{qq}^{max} = m_{\tilde{\chi}_1^\pm} - m_{\tilde{\chi}_1^0} \tag{D.1}$$

In calculating the m_{bqq} endpoint, the three body $\tilde{\chi}_1^\pm$ decay is treated as a two body decay where the quarks are combined into a single particle, Q, as shown in Figure D.2. The mass of this Q particle, $m_Q \equiv m_{qq}$ must lie in within a specific range:

$$m_Q = \lambda(m_{\tilde{\chi}_1^\pm} - m_{\tilde{\chi}_1^0}),\ \lambda \in [0, 1] \tag{D.2}$$

To evaluate the maximum invariant mass which may be attained by the b quark and Q particle, it is best to move into the rest frame of the decaying $\tilde{\chi}_1^\pm$, also shown in Figure D.2. In this frame, it is clear that the only kinematic freedom is the angle θ between the b quark and Q particle. The momenta and energies of the particles may be obtained by four-momentum conservation, and are given by:

$$\begin{aligned} \mathbf{Q}^2 &= (\boldsymbol{\tilde{\chi}_1^0})^2 = [m_Q^2, m_{\tilde{\chi}_1^\pm}^2, m_{\tilde{\chi}_1^0}^2] \qquad & E_Q^2 &= m_Q^2 + \mathbf{Q}^2 \\ \mathbf{b}^2 &= (\boldsymbol{\tilde{t}_1})^2 = [m_b^2, m_{\tilde{\chi}_1^\pm}^2, m_{\tilde{t}_1}^2] \qquad & E_b^2 &= m_b^2 + \mathbf{b}^2 \end{aligned} \tag{D.3}$$

where

$$[x, y, z] \equiv \frac{x^2 + y^2 + z^2 - 2(xy + xz + yz)}{4y}$$

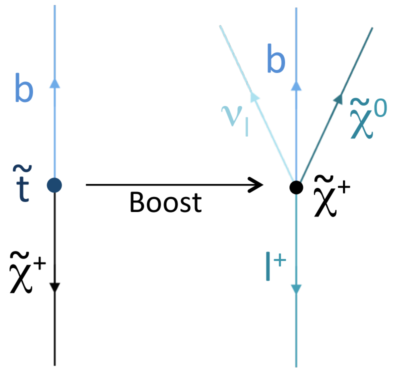

Figure D.3. Light stop leptonic decay branch and rest frames involved in invariant mass kinematic endpoint calculation.

The invariant mass of the b quark and Q particle is given by:

$$\begin{aligned} m_{bQ}^2 &= (b+Q)^2 \\ &= m_b^2 + m_Q^2 + 2b^\mu Q_\mu \\ &= m_b^2 + m_Q^2 + 2(E_b E_Q - |\mathbf{b}||\mathbf{Q}|\cos\theta) \\ &\simeq m_Q^2 + 2|\mathbf{b}|(E_Q - |\mathbf{Q}|\cos\theta) \qquad\qquad ;\text{ taking } m_b \simeq 0 \end{aligned}$$

The maximum of m_{bQ} will occur when $\cos\theta = -1$, that is, the b quark and Q particle are back to back in the $\tilde\chi_1^\pm$ rest frame. Combining this with Equation D.3, an expression for the endpoint of m_{bqq} distribution can be obtained in terms of m_q:

$$(m_{bqq})^2 = m_Q^2 + \frac{m_{\tilde t_1} - m_{\tilde\chi_1^\pm}}{2m_{\tilde\chi_1^\pm}}\left[m_Q^2 - (m_{\tilde\chi_1^0} - m_{\tilde\chi_1^\pm}) + \sqrt{((m_{\tilde\chi_1^\pm} + m_{\tilde\chi_1^0}) - m_Q)^2 - 4m_{\tilde\chi_1^\pm} m_{\tilde\chi_1^0}}\right]$$

The maximum of m_{bqq} can be found by considering the boundaries of possible m_Q values given by Equation D.2, that is, where $\lambda = 0$ and $\lambda = 1$. This gives two possible expressions:

$$(m_{bqq}^{max})^2 = \begin{cases} (m_{\tilde t_1} - m_{\tilde\chi_1^0})^2 & ;\text{if } m_{\tilde\chi_1^\pm}^2 > m_{\tilde t_1} m_{\tilde\chi_1^0} \\ (m_{\tilde t_1}^2 - m_{\tilde\chi_1^\pm}^2)(m_{\tilde\chi_1^\pm}^2 - m_{\tilde\chi_1^0}^2)/m_{\tilde\chi_1^\pm}^2 & ;\text{otherwise} \end{cases} \tag{D.4}$$

For the leptonic branch $\tilde t_1 \to b\tilde\chi_1^+ \to b\tilde\chi_1^0 W^+ \to b\tilde\chi_1^0 \ell^+\nu_l$, the two sequential reference frames under consideration are shown in Figure D.3. Any maximum in the $m_{b\ell}$ invariant mass must arise from the b quark and charged lepton being back to back in the $\tilde\chi_1^\pm$ rest frame. This configuration can occur in two different ways:

1. The neutralino is produced at rest, and the charged lepton is antiparallel to the b quark; or

2. None of the particles from the three body decay is produced at rest, but the charged lepton is antiparallel to the b quark and the neutrino and neutralino are travelling in the same direction as the b quark.

The maximum of these two cases provides the $m_{b\ell}$ endpoint:

$$(m_{bl}^{max})^2 = (m_{\tilde{t}_1}^2 - m_{\tilde{\chi}_1^\pm}^2)(m_{\tilde{\chi}_1^\pm}^2 - m_{\tilde{\chi}_1^0}^2)/m_{\tilde{\chi}_1^\pm}^2 \tag{D.5}$$

Figure D.4 shows the discussed invariant mass distributions and with corresponding analytically calculated endpoints for semileptonic *LHS*2 stop decays using generator level information. Note that in the *LHS*2 benchmark, $m_{\tilde{\chi}_1^\pm}^2 > m_{\tilde{t}_1} m_{\tilde{\chi}_1^0}$, so the first case for the m_{bqq} endpoint in Equation D.4 applies.

The system of the three endpoint equations, namely Equations D.1, D.4 and D.5, contains three unknown sparticle masses: $m_{\tilde{t}}$, $m_{\tilde{\chi}_1^\pm}$ and $m_{\tilde{\chi}_1^0}$. This system of three equations should be solvable for the three sparticle masses assuming that the invariant mass endpoints can be found from the distributions. However due to the quadratic nature of both Equations D.4 and D.5, there could be multiple sets of sparticle mass solutions, and thus additional constraints need to be applied, such as the physical constraints of $m_{\tilde{t}} > m_{\tilde{\chi}_1^\pm} > m_{\tilde{\chi}_1^0}$ and $m_{\tilde{t}}, m_{\tilde{\chi}_1^\pm}, m_{\tilde{\chi}_1^0} > 0$ and/or the grand unification motivated constraint of $m_{\tilde{\chi}_1^\pm} \simeq 2m_{\tilde{\chi}_1^0}$.

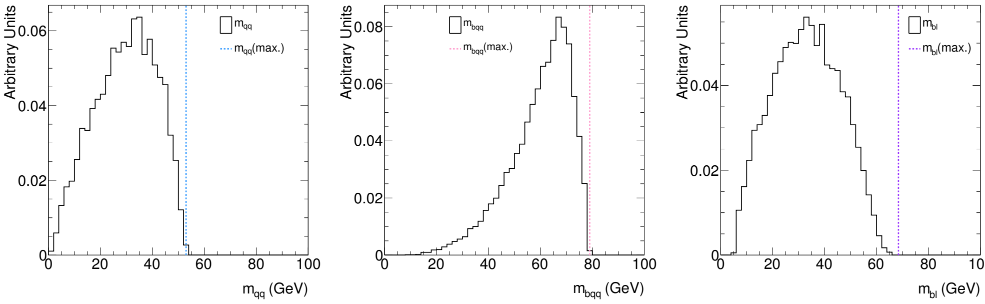

(a) m_{qq} **(b)** m_{bqq} **(c)** $m_{b\ell}$

Figure D.4. Truth distributions (solid, hollow histograms) for m_{qq}, m_{qq} and m_{qq} invariant masses for semileptonic *LHS*2 stop decays with corresponding analytically calculated endpoints (dashed lines).

E

Neutrino Momentum Calculation

For the semileptonic top pair background $t\bar{t} \rightarrow b\bar{b}W^{+}W^{-} \rightarrow b\bar{b}\bar{q}ql\nu$, the only missing energy in the final state comes from the neutrino, and due to the mass difference between the top and bottom quarks, the W bosons should be created onshell. Thus it should be possible to calculate the z component of the neutrino momentum p_{ν_z}, by looking at the leptonic leg of the decay $t \rightarrow bW^{+} \rightarrow l^{+}\nu$ and using the W mass constraint.

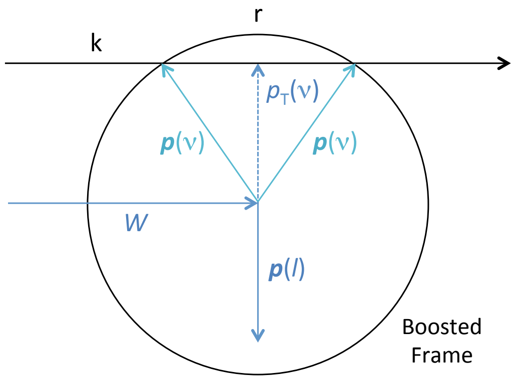

Figure E.1. Diagramatic description of neutrino momentum calculation.

This can be seen diagrammatically in Figure E.1, where the system is boosted into a reference frame where the lepton has a momentum orthogonal to the decaying W boson direction. Due to energy conservation, the allowed neutrino momentum must lie on a circle of radius r. From momentum conservation the allowed neutrino momentum lies on the straight line k. The intersection in the following system of equations yields two solutions.

Mathematically, this involves manipulating the W mass constraint to become a quadratic in p_{ν_z}:

$$\begin{aligned} m_W^2 &= E_W^2 - p_W^2 \\ &= (E_\ell + E_\ell)^2 - (p_{\nu_\mathrm{x}} + p_{\nu_\mathrm{x}})^2 - (p_{\ell_\mathrm{y}} + p_{\nu_\mathrm{y}})^2 - (p_{\ell_\mathrm{z}} + p_{\nu_\mathrm{z}})^2 \\ \therefore m_W^2 + (p_{\ell_\mathrm{x}} + p_{\nu_\mathrm{x}})^2 + (p_{\ell_\mathrm{y}} + p_{\nu_\mathrm{y}})^2 - E_\ell^2 &= 2E_\ell E_\nu + E_\nu^2 - p_{\ell_\mathrm{z}}^2 - 2p_{\ell_\mathrm{z}} p_{\nu_\mathrm{z}} - p_{\nu_\mathrm{z}}^2 \\ \therefore \alpha &= 2E_\ell E_\nu + p_{\nu_\mathrm{T}}^2 + p_{\nu_\mathrm{z}}^2 - p_{\ell_\mathrm{z}}^2 - 2p_{\ell_\mathrm{z}} p_{\nu_\mathrm{z}} - p_{\nu_\mathrm{z}}^2 \end{aligned}$$

where $\alpha \equiv m_W^2 + (p_{\ell_\mathrm{x}} + p_{\nu_\mathrm{x}})^2 + (p_{\ell_\mathrm{y}} + p_{\nu_\mathrm{y}})^2 - E_\ell^2$ and $E_\nu^2 = p_{\nu_\mathrm{T}}^2 + p_{\nu_\mathrm{z}}^2$ since $m_\nu^2 = E_\nu^2 - p_{\nu_\mathrm{T}}^2 - p_{\nu_\mathrm{z}}^2 = 0$.

$$\begin{aligned} \therefore \frac{1}{2}(\alpha - p_{\nu_\mathrm{T}}^2 + p_{\ell_\mathrm{z}}^2) &= E_\ell E_\nu - p_{\ell_\mathrm{z}} p_{\nu_\mathrm{z}} \\ \therefore \beta &= E_\ell \sqrt{p_{\nu_\mathrm{T}}^2 + p_{\nu_\mathrm{z}}^2} - p_{\ell_\mathrm{z}} p_{\nu_\mathrm{z}} \end{aligned}$$

where $\beta \equiv \frac{1}{2}(\alpha - p_{\nu_\mathrm{T}}^2 + p_{\ell_\mathrm{z}}^2)$.

$$\begin{aligned} \therefore \beta + p_{\ell_\mathrm{z}} p_{\nu_\mathrm{z}} &= E_\ell \sqrt{p_{\nu_\mathrm{T}}^2 + p_{\nu_\mathrm{z}}^2} \\ \therefore \beta^2 + 2\beta p_{\ell_\mathrm{z}} p_{\nu_\mathrm{z}} + p_{\ell_\mathrm{z}}^2 p_{\nu_\mathrm{z}}^2 &= E_\ell^2 (p_{\nu_\mathrm{T}}^2 + p_{\nu_\mathrm{z}}^2) \\ \therefore \beta^2 - E_\ell^2 p_{\nu_\mathrm{T}}^2 &= -2\beta p_{\ell_\mathrm{z}} p_{\nu_\mathrm{z}} + p_{\nu_\mathrm{z}}^2 (E_\ell^2 - p_{\ell_\mathrm{z}}) \\ \therefore 0 &= p_{\nu_\mathrm{z}}^2 - \frac{2\beta p_{\ell_\mathrm{z}}}{E_\ell^2 - p_{\ell_\mathrm{z}}} p_{\nu_\mathrm{z}} - \frac{\beta^2 - E_\ell^2 p_{\nu_\mathrm{T}}^2}{E_\ell^2 - p_{\ell_\mathrm{z}}} \end{aligned}$$

This equation is solvable for p_{ν_z} if $\Delta \geq 0$ where $\gamma \equiv -\frac{\beta^2 - E_\ell^2 p_{\nu_\mathrm{T}}^2}{E_\ell^2 - p_{\ell_\mathrm{z}}}$ and $\lambda \equiv \frac{2\beta p_{\ell_\mathrm{z}}}{E_\ell^2 - p_{\ell_\mathrm{z}}}$ and $\Delta \equiv \lambda^2 - 4\gamma$. This condition is equivalent to $m_\mathrm{T} \leq m_W$, where the transverse mass of the lepton and the $E_\mathrm{T}^\mathrm{miss}$ is defined as, $m_\mathrm{T} \equiv 2|p_{\ell_\mathrm{T}}||E_\mathrm{T}^\mathrm{miss}| - 2\vec{p}_{\ell_\mathrm{T}} \cdot \vec{E}_\mathrm{T}^\mathrm{miss}$. If this condition is satisfied then $p_{\nu_\mathrm{z}} = \frac{1}{2}(\lambda \pm \sqrt{\Delta})$ where the smallest absolute value is chosen. If this condition is not satisfied, then $p_{\nu_\mathrm{z}} = \frac{p_{\ell_\mathrm{z}} p_{\nu_\mathrm{T}}}{p_{\ell_\mathrm{T}}}$.

F

Dileptonic Same Sign Results

This chapter presents supplementary results to those in found in Section 10.3. Those results were for events containing two electrons of opposite sign. These results are for events containing two electrons of same sign.

Table F.1. Dileptonic same sign event yields at 7 TeV in data and simulation for 31.7 pb^{-1}. Errors are purely statistical.

Dataset	**Yield**
Data	75 ± 9
Simulation	78 ± 3
$t\bar{t}$	0.5 ± 0.1
single t	0.03 ± 0.02
$W \rightarrow \ell\nu + j$	1.4 ± 0.4
$Z \rightarrow \ell\ell + j$	68 ± 3
$\gamma^* \rightarrow \ell\ell + j$	0.7 ± 0.2
Diboson	0.49 ± 0.02
QCD multijet	6.7 ± 1.9

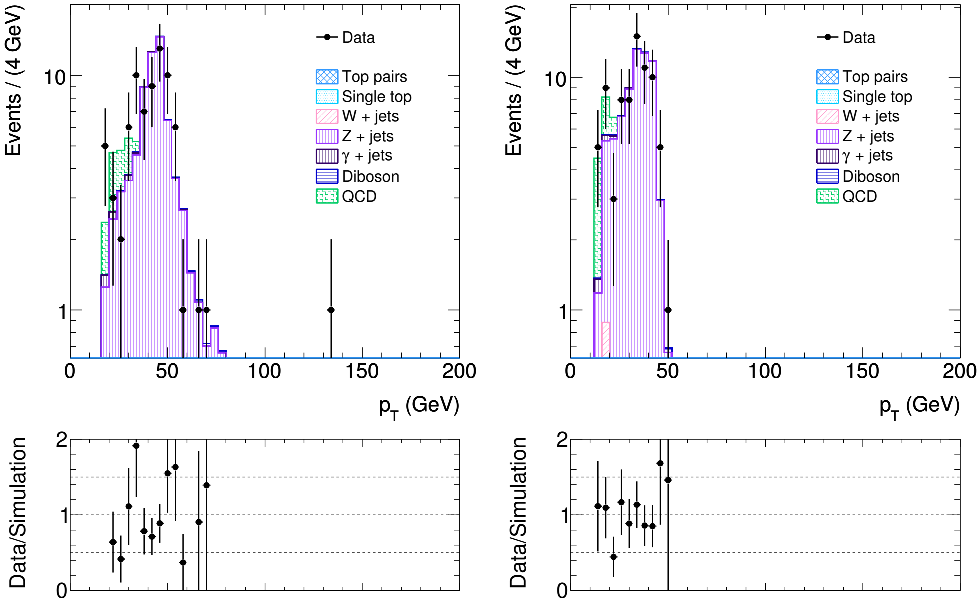

(a) $p_{\mathrm{T}}(e_1^{\pm})$ **(b)** $p_{\mathrm{T}}(e_2^{\pm})$

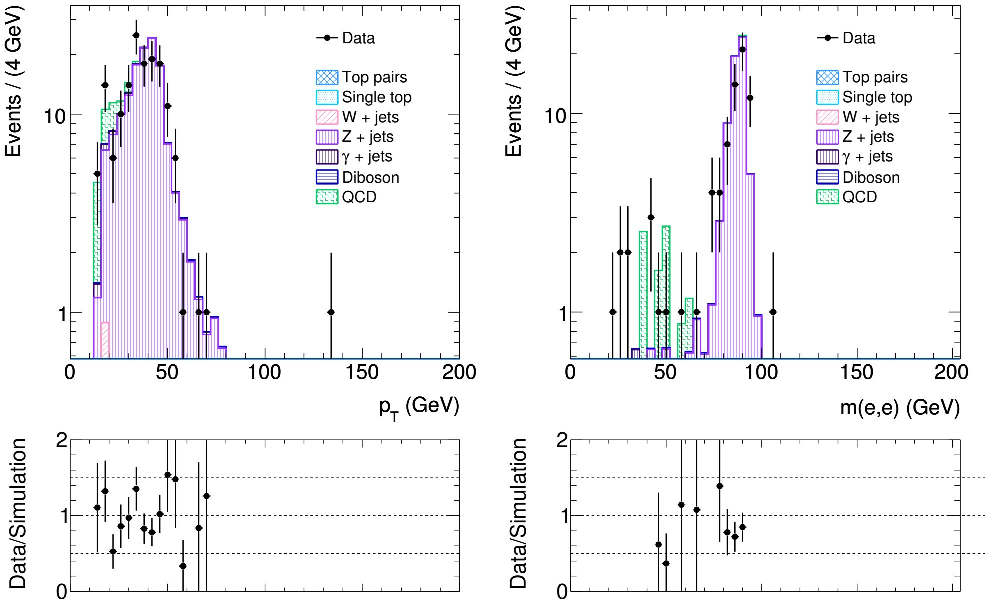

(c) $p_{\mathrm{T}}(e)$ **(d)** $m(e_1^{\pm}, e_2^{\mp})$

Figure F.1. Dileptonic same sign observables at 7 TeV in (solid circles) and simulation (patterned histograms) for 31.7 pb^{-1}. Data errors are purely statistical. No errors are shown for simulation. Ratio errors are statistical.

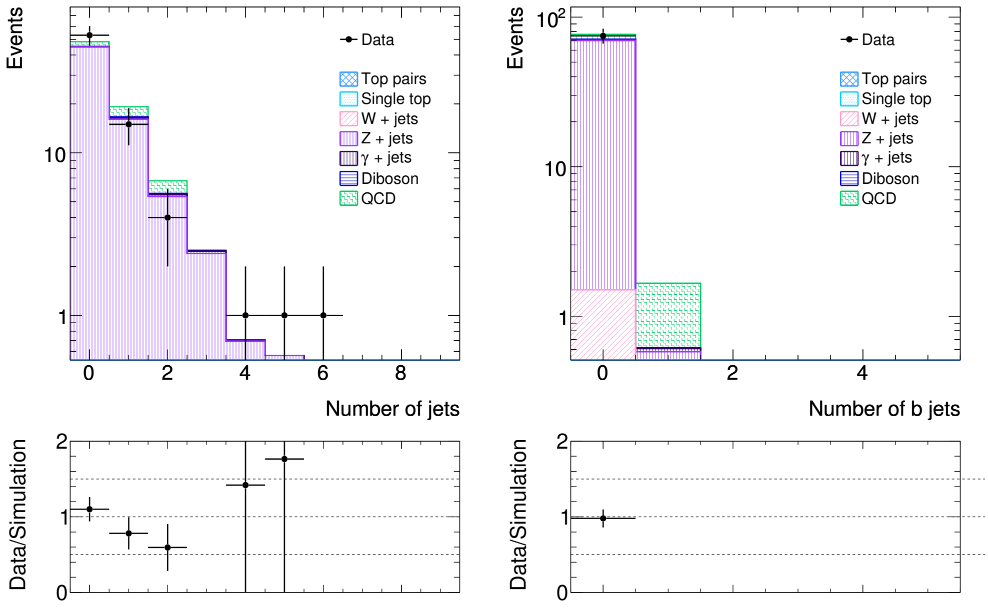

(a) Number of jets **(b)** Number of b jets

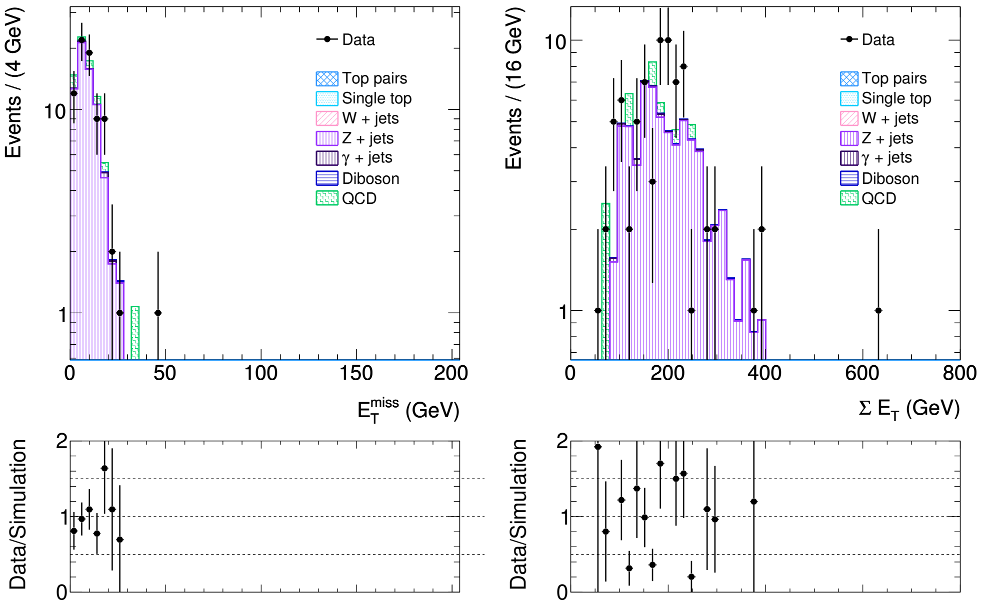

(c) $E_{\mathrm{T}}^{\mathrm{miss}}$ **(d)** ΣE_{T}

Figure F.2. More dileptonic same sign observables at 7 TeV in (solid circles) and simulation (patterned histograms) for 31.7 pb^{-1}. Data errors are purely statistical. No errors are shown for simulation. Ratio errors are statistical.